

## ABSTRACT

HU, XINFANG. Investigation of Growth and Degradation Behaviors of Biodegradable Polyester Brushes and Their Applications. (Under the direction of Christopher B. Gorman)

Polymer brushes fabricated from degradable polyesters including poly(lactic acid) (PLA), poly(glycolic acid) (PGA) and poly( $\epsilon$ -caprolactone) (PCL) were prepared via ring opening polymerization (ROP) on silicon substrates. These are proposed as a possible, dynamic layer that might gradually expose and activate an array of biosensors. The growth conditions for PGA and PCL brushes were investigated by varying the temperature and solvent. Different optimal conditions were established for growth of PGA and PCL brushes. These differences were explained by (1) the different activation barriers for the ring opening step (2) and the position of the polymerization/depolymerization equilibrium. Similar degradation behaviors of both PGA and PCL brushes to the previously studied PLA brushes were demonstrated. Only neutral or basic conditions were applicable for brush degradation which was consistent with a backbiting mechanism. CV experiments provided comparable results to ellipsometry measurements: PGA brushes degraded faster than PCL brushes under similar conditions. The antifouling property of these brushes were tested using a single protein buffer solution containing bovine serum albumin (BSA) under physiological conditions. The degradation and protein adsorption behaviors of PLA, PGA, PCL brushes and their co-polymer brushes with oligo(ethylene glycol) (OEG) and poly(ethylene glycol) (PEG) were studied. Fabrication of degradable polyester brushes with moderate protein resistance was demonstrated. Furthermore, characterization methods including ellipsometry, ATR-FTIR spectroscopy and a protein assay were applied to monitor the adsorbed protein on flat substrates.

A strategy for improving the properties of polymer (i.e. molecular weight distribution: PDI) synthesized via free radical polymerization (FRP) was proposed and investigated. The local heating effect of microwave absorbers under microwave irradiation was tested in order to achieve an accelerated initiation rate close to the surface compared to the propagation rate

presumably farther from the surface, which might lead to a lower PDI of the resulting polymer. Surface initiated free radical polymerization (SI-FRP) of styrene was performed on azo initiator (ATCS) modified  $\text{Fe}_2\text{O}_3$  nanoparticles by microwave irradiation under different working modes and conditions. Under the SPS working mode, both low monomer conversion (<20%) and small PDI (<1.5) were obtained. These results were explained by (1) a reduced propagation rate due to the fast formation and decomposition of radical initiators (2) and the reduced chain transfer effect under low monomer conversion. Neither results obtained from experiment nor from a model calculation supported the local heating effect of  $\text{Fe}_2\text{O}_3$  nanoparticles. Furthermore, the reproducibility of SI-FRP on another microwave absorber, silicon, was found to be poor. The variation of temperature across a silicon sample under same conditions was monitored by an external IR camera and underestimation of the surface temperature is likely to be the cause of the problem. The local heating effect of Si sample was probed by coating the substrate with an insulator layer ( $\text{SiO}_x$ ) and by placing the sample in different positions. The results indicate the surface temperature of the substrate was higher than the bulk solution due to a saturation of heat transfer in the open-vessel system. However, this might deviate from results obtained under the actual experimental conditions where the system was sealed. Furthermore, the surface temperature of silicon was shown to be poorly controlled under practical conditions. A thick insulator layer attached to the silicon surface might alleviate these problems.

© Copyright 2013 Your Name

All Rights Reserved

Investigation of Growth and Degradation Behaviors of Biodegradable Polyester Brushes and  
Their Applications

by  
Xinfang Hu

A dissertation submitted to the Graduate Faculty of  
North Carolina State University  
in partial fulfillment of the  
requirements for the degree of  
Doctor of Philosophy

Chemistry

Raleigh, North Carolina

2013

APPROVED BY:

---

Christopher B. Gorman  
Committee Chair

---

Jan Genzer

---

Lin He

---

Edmond F. Bowden

## **BIOGRAPHY**

Xinfang Hu graduated from Beijing Normal University with a B.S. degree in Chemistry in 2008. She then began her Ph.D. program in Chemistry Department at North Carolina State University in the fall of 2008. There she joined the research group of Dr. Christopher B. Gorman where she had the opportunity to work on two research projects.

## **ACKNOWLEDGMENTS**

I would like to first thank my advisor, Professor Gorman and my co-advisor, Professor Genzer for their continuous guidance and help throughout my work during these five years. I also want to thank my committee members, Professor He and Professor Bowden, for giving me helpful advice on my research. I thank Gongfang Hu for his work on the growth of PCL brushes. I thank Dr. Erich Bain and Dr. Bill Behof for working on the microwave project. I am grateful to the current and former group members in both Dr. Gorman and Dr. Genzer's group for sharing their helpful ideas on my research. Last but not least, I thank my family for their support.

# TABLE OF CONTENTS

LIST OF TABLES .....	vii
LIST OF SCHEMES.....	viii
LIST OF FIGURES .....	x
Chapter 1 Introduction .....	1
1.1 Stimuli-Responsive Surfaces .....	1
1.1.1. Introduction to Stimuli-Responsive Surfaces .....	1
1.1.2. Types of Stimuli-Responsive Surfaces .....	1
1.1.3. Applications of Stimuli-Responsive Surfaces .....	4
1.2. Protein Adsorption .....	6
1.2.1. Desirable and Undesirable Immobilization of Protein on Surface .....	6
1.2.2. Study of the Mechanisms of Protein Adsorption .....	7
1.2.3. Characterization of Protein Adsorption .....	8
1.2.4. Efforts towards Reducing Protein Adsorption .....	9
1.3. Polymer Brushes .....	11
1.3.1. Introduction to Polymer Brushes .....	11
1.3.2. Preparation Methods for Polymer Brushes .....	13
1.3.3. Applications of Polymer Brushes .....	16
1.4. Biodegradable Polyesters .....	16
1.4.1. Introduction to Biodegradable Polyesters: Poly(lactic acid), Poly(glycolic acid) and Poly( $\epsilon$ -caprolactone) .....	16
1.4.2. Synthesis of Poly(lactic acid), Poly(glycolic acid) and Poly( $\epsilon$ -caprolactone) and Their Copolymers.....	18
1.4.3. Degradation of Poly(lactic acid), Poly(glycolic acid) and Poly( $\epsilon$ -caprolactone) and Their Copolymers .....	20
1.4.4. Applications of Poly(lactic acid), Poly(glycolic acid) and Poly( $\epsilon$ -caprolactone) and Their copolymers.....	22
1.5. Proposed Anti-fouling Dynamic Surface.....	23
REFERENCES .....	24
Chapter 2 Growth and Degradation of PGA and PCL Brushes.....	39
2.1 Introduction .....	39
2.2 Results and Discussion.....	40
2.2.1 Reproducibility and Modified Conditions of PLA Brush Growth.....	40
2.2.2 Study of the Growth of PGA and PCL Brushes.....	48

2.2.3 Degradation Study of PGA and PCL Brushes .....	60
2.2.4 Comparison of the Degradation of Spin Coated and Grafted Brushes .....	69
2.3 Conclusions .....	80
2.4 Experimental .....	80
2.4.1 Preparation of Silicon and Gold Substrates .....	80
2.4.2 Preparation of Reactants .....	81
2.4.3 Preparation of Brushes on Silicon and Gold Substrates .....	81
2.4.4 Preparation of Spin Coated Brushes .....	81
2.4.5 Degradation of Brushes.....	82
2.4.6 Ellipsometry Measurements.....	82
2.4.7 Cyclic Voltammetry Measurements .....	82
2.4.8 Contact Angle Measurements .....	83
2.4.9 ATR-FTIR Measurements.....	83
REFERENCES .....	84
Chapter 3 Protein Adsorption on Biodegradable Polyester and OEG Incorporated Co-polymer Brushes .....	88
3.1 Introduction .....	88
3.2 Results and Discussion.....	89
3.2.1 BSA Adsorption on PLA, PGA and PCL Brushes .....	89
3.2.2 BSA Adsorption on OEG Incorporated Co-polymer Brushes .....	98
3.2.3 BSA Adsorption on PEG Modified Brushes.....	116
3.2.4 Quantitative Characterization of BSA Adsorption on Brushes.....	121
3.3 Conclusions .....	130
3.4 Experimental .....	132
3.4.1 Preparation of Co-polymer Brushes.....	132
3.4.2 PEGylation of Brushes with Synthesized PEG Derivatives .....	132
3.4.3 Adsorption of Protein on Brush Substrates and Degradation of Brushes .....	133
3.4.4 Protein Desorption via Sonication .....	133
3.4.5 Ellipsometry Measurements.....	134
3.4.6 BCA Protein Assay Measurements .....	134
3.4.7 ATR-FTIR Measurements.....	135
3.4.8 NMR .....	135
REFERENCES .....	136
Chapter 4 Further Study on Microwave Induced Free Radical Polymerization on Nanoparticles .....	140
4.1 Introduction .....	140

4.1.1 Free Radical Polymerization.....	140
4.1.2 Conventional Heating and Microwave Heating.....	144
4.1.3 Microwave Assisted Polymerization.....	146
4.1.4 Other Applications of Microwave Heating.....	148
4.1.5 Our Hypothesis .....	149
4.2 Results and Discussion.....	150
4.2.1 Preliminary Results .....	150
4.2.2 Further Study .....	175
4.3 Conclusions .....	208
4.4 Experimental .....	210
4.4.1 Materials .....	210
4.4.2 Synthesis of Asymmetric Azo Initiators .....	210
4.4.3 Initiator Deposition .....	214
4.4.4 Microwave Induced and FRP on Substrate.....	215
4.4.5 Thermal FRP on Substrate .....	216
4.4.6 Characterization .....	216
REFERENCES .....	218

## LIST OF TABLES

Table 2.2.1 Table of deionized water contact angles collected on grafted PLA, PGA and PCL brushes under different conditions.....	72
Table 4.1.1 Rate constant of dissociation and half lives of initiators in benzene. <sup>7</sup> .....	142
Table 4.2.1 GPC results for polystyrene synthesized in the presence of azo initiator modified Fe <sub>2</sub> O <sub>3</sub> nanoparticles using thermal heating (60 °C, 17 h ). .....	156
Table 4.2.2 Conditions for FRP of styrene in the presence of ATCS modified Fe <sub>2</sub> O <sub>3</sub> nanoparticles using duty cycle mode (1 <sub>st</sub> set). Values in the parenthesis represent the standard deviation of measured temperatures between two samples.....	158
Table 4.2.3 Conditions for FRP of styrene in the presence of ATCS modified Fe <sub>2</sub> O <sub>3</sub> nanoparticles using duty cycle mode (2 <sub>nd</sub> set). Values in the parenthesis represent the standard deviation of measured temperatures between two samples.....	159
Table 4.2.4 GPC results for polystyrene synthesized in the presence of ATCS modified Fe <sub>2</sub> O <sub>3</sub> nanoparticles using SPS mode. Values in the parenthesis represent the standard deviation of results between two samples.....	160
Table 4.2.5 Conditions for FRP of styrene in the presence of ATCS modified Fe <sub>2</sub> O <sub>3</sub> nanoparticles using SPS mode. ....	161
Table 4.2.6 Conditions for FRP of styrene in the presence of free AIBN using SPS mode.	164
Table 4.2.7 Heat capacity of different solvents. <sup>44</sup> .....	205

## LIST OF SCHEMES

Scheme 1.1 (top) SI-ATRP of OEGMA on initiator modified substrates to build a non-fouling surface; <sup>42</sup> (bottom) UV induced graft polymerization of PEGMA on a SAM-modified gold surface pretreated with argon plasma. <sup>43</sup> .....	10
Scheme 1.2 Molecular structures of zwitterionic monomers: (from left to right) sulfobetaine methacrylate (SBMA), carboxybetaine methacrylate (CBMA) and carboxybetaine acrylamides (CBAA). .....	11
Scheme 1.3 Molecular structure of an azo initiator reported by Rhe et al. <sup>58</sup> .....	14
Scheme 1.4 SI-ROP of p-DO, LA and $\epsilon$ -CL from surfaces with hydroxyl terminal groups. <sup>64</sup>	15
Scheme 1.5 Polymerization of PLLA by two approaches: condensation polymerization and ring opening polymerization. ....	17
Scheme 1.6 Synthesis of PCL under (1) anionic ROP, (2) cationic ROP and (3) coordination-insertion ROP mechanisms. ....	19
Scheme 1.7 Chain-end scission hydrolysis and backbiting process of PLA. ....	21
Scheme 2.1.1 Degradation of PLA under (1) random chain scission mechanism and (2) backbiting mechanism. ....	39
Scheme 2.2.1 SI-ROP and bulk ROP of PLA. ....	43
Scheme 2.2.2 Formation of initiators. ....	45
Scheme 2.2.3 Hydrolysis of (A) PGA and (B) PCL brushes under basic conditions via backbiting mechanism. ....	62
Scheme 2.2.4 Modification of terminal hydroxy groups of (A) PGA and (B) PCL brushes using succinic anhydride. ....	63
Scheme 3.2.1 Synthesis of PGA and OEG co-polymer brushes with OEG as an outside layer. ....	102
Scheme 3.2.2 Synthesis of PGA and OEG co-polymer brushes with OEG as the substrate layer. ....	105

Scheme 3.2.3 Synthesis of multilayer Si-(OEG-PGA) <sub>2</sub> -OEG co-polymer brushes. ....	114
Scheme 3.2.4 Synthesis of SC activated mPEG <sub>2000</sub> and PEGylation of PGA brushes with mPEG <sub>2000</sub> -SC. ....	117
Scheme 3.2.5 PEGylation of SC modified PGA brushes with mPEG <sub>5000</sub> -NH <sub>2</sub> and PEGylation of PLA brushes with mPEG <sub>2000</sub> silanes.....	118
Scheme 4.1.1 Initiation step of free radical polymerization. ....	140
Scheme 4.1.2 Proposed mechanism for SI-FRP under microwave irradiation.....	149
Scheme 4.2.1 Deposition of ATCS on Fe <sub>2</sub> O <sub>3</sub> nanoparticles.....	157

## LIST OF FIGURES

- Figure 1.1 (top) Two association/dissociation equilibria of orthophosphoric acid in PMEP brushes; (bottom) Depiction of the advancing contact angles of DI water on PMEP brush surface under different pH environments: (from left to right) pH<1, 65 °; pH=4, 49 °; pH>10, 13 °.<sup>12</sup> ..... 3
- Figure 1.2 Depiction of the reversible structure changes of PS/P2VP mixed brush system under different solvent environments: (left) in toluene and (right) in acidic water and ethanol.<sup>13</sup> ..... 4
- Figure 1.3 (left) Depiction of the switching swelling effects of P2VP and PAA domains under different pH environments: (top) pH 1.2 and (bottom) 8.6 respectively; (right) Fluorescence graphs depicting FITC-casein adsorbed (a) on PAA and (b) on P2VP domains. .... 5
- Figure 1.4 Depiction of the conformational change of BSA molecules adsorbed on the surface.<sup>33</sup> ..... 8
- Figure 1.5 Depiction of polymer brushes on various surfaces with different structures: (left to right) a polymer brush grafted from a flat solid substrate, a polymer micelle and block copolymer at fluid-fluid interfaces.<sup>49</sup> ..... 12
- Figure 1.6 Depiction of methods for preparing polymer brushes.<sup>52</sup> ..... 13
- Figure 2.2.1 Plots of ellipsometric thicknesses of PLA brushes versus growth time at room temperature. Error bars represent the magnitude of the 90% confidence interval for ten measurements on two samples. .... 41
- Figure 2.2.2 Plots of ellipsometric thicknesses of PLA brushes versus growth time at different temperatures. Reaction conditions: [L-lactide] = 0.1 M, [Sn(Oct)<sub>2</sub>] = 0.001 M, 24 h. Error bars represent the magnitude of the 90% confidence interval for five measurements on one samples.<sup>3</sup> ..... 42
- Figure 2.2.3 Plots of ellipsometric thicknesses of PLA brushes versus growth time at room temperature with and without addition of droplet of DI water. Error bars represent the magnitude of the 90% confidence interval for ten measurements on two samples. .... 44
- Figure 2.2.4 Plots of ellipsometric thicknesses of PLA brushes versus growth time at room temperature with addition 10 µL of 1 N NaOH (aq), 1 N HCl (aq) and DI water.

Error bars represent the magnitude of the 90% confidence interval for ten measurements on two samples. ....	46
Figure 2.2.5 Plots of ellipsometric thicknesses of PLA brushes versus growth time at room temperature with addition of 10 $\mu$ L ethanol and DI water. Error bars represent the magnitude of the 90% confidence interval for ten measurements on two samples. ....	47
Figure 2.2.6 Plots of ellipsometric thicknesses of PLA brushes versus growth time at room temperature on silicon and gold substrates. Error bars represent the magnitude of the 90% confidence interval for ten measurements on two samples. ....	48
Figure 2.2.7 Plots of ellipsometric thicknesses of PGA and PCL brushes versus growth time at room temperature. Error bars represent the magnitude of the 90% confidence interval for ten measurements on two samples. ....	49
Figure 2.2.8 Plots of ellipsometric thicknesses of PGA brushes versus growth time at different temperatures. Error bars represent the magnitude of the 90% confidence interval for ten measurements on two samples. ....	50
Figure 2.2.9 Photograph of the reaction vials used for the growth of PGA brushes at (left to right) 25 $^{\circ}$ C, 40 $^{\circ}$ C and 60 $^{\circ}$ C for 1 h.....	51
Figure 2.2.10 Plots of ellipsometric thicknesses of PCL brushes versus growth time at different temperatures. Error bars represent the magnitude of the 90% confidence interval for ten measurements on two samples. ....	53
Figure 2.2.11 Plots of ellipsometric thicknesses of PCL brushes versus growth time at different temperatures. Error bars represent the magnitude of the 90% confidence interval for ten measurements on two samples. ....	54
Figure 2.2.12 Plots of ellipsometric thicknesses of PCL brushes versus growth time at room temperature in (top) THF and (bottom) toluene added with 20 $\mu$ L catalyst (dissolved in THF) solution. Error bars represent the magnitude of the 90% confidence interval for ten measurements on two samples.....	56
Figure 2.2.13 Photographs of the reaction vials used for the growth of PCL brushes at 25 $^{\circ}$ C for 48 h in (left )THF and (right) toluene.....	57
Figure 2.2.14 Plot of ellipsometric thicknesses of PCL brushes versus growth time at room temperature in toluene added with 20 $\mu$ L catalyst (dissolved in toluene) solution.	

Error bars represent the magnitude of the 90% confidence interval for ten measurements on two samples. ....	58
Figure 2.2.15 Plots of ellipsometric thicknesses of PCL brushes versus growth time at different temperatures in toluene added with 20 $\mu\text{L}$ catalyst (dissolved in THF) solution. Error bars represent the magnitude of the 90% confidence interval for ten measurements on two samples. ....	59
Figure 2.2.16 Plots of ellipsometric thicknesses of (top) PGA and (bottom) PCL brushes versus degradation time at different pH values. Error bars represent the magnitude of the 90% confidence interval for five measurements on one sample. ....	61
Figure 2.2.17 Plots of ellipsometric thicknesses of SA blocked and unblocked (top) PGA and (bottom) PCL brushes versus degradation time under pH 8.0 at 37 $^{\circ}\text{C}$ . Error bars represent the magnitude of the 90% confidence interval for five measurements on one sample. ....	64
Figure 2.2.18 Plots of ellipsometric thicknesses of (top) PGA and (bottom) PCL brushes versus degradation time at different temperatures. Error bars represent the magnitude of the 90% confidence interval for five measurements on one sample. ....	66
Figure 2.2.19 Plots of maximum current densities versus time at different pH values for grafted (A) PGA, (B) PLA and (C) PCL brushes. These current densities are uncorrected for capacitance (e.g. non-Faradaic) effects. ....	68
Figure 2.2.20 Plots of ellipsometric thicknesses of grafted and spin coated PGA brushes versus degradation time at different pH values. Error bars represent the magnitude of the 90% confidence interval for five measurements on one sample. ....	70
Figure 2.2.21 Plots of ellipsometric thicknesses of grafted and spin coated PCL brushes versus degradation time under different pH values. Error bars represent the magnitude of the 90% confidence interval for five measurements on one sample. ....	71
Figure 2.2.22 Plots of DI water contact angles on (top) grafted PGA and PCL brushes versus time sitting in air and (bottom) grafted PGA and PCL brushes versus time in contact with DI water. Error bars represent the magnitude of the 90% confidence interval for six measurements on two samples. ....	73

Figure 2.2.23 Plots of DI water contact angles on grafted PLA brushes versus time contacting with DI water. Error bars represent the magnitude of the 90% confidence interval for six measurements on two samples. Figure taken from reference.<sup>4</sup> ..... 75

Figure 2.2.24 Plots of DI water contact angles on spin coated PLA brushes with and without annealing versus time contacting with DI water. Error bars represent the magnitude of the 90% confidence interval for six measurements on two samples. .... 76

Figure 2.2.25 Plots of DI water contact angles on spin coated PGA and PCL brushes versus time contacting with DI water. Error bars represent the magnitude of the 90% confidence interval for six measurements on two samples..... 77

Figure 2.2.26 Plots of maximum current densities versus time under different pH values for spin coated (A) PGA, (B) PLA and (C) PCL brushes. These current densities are uncorrected for capacitance (e.g. non-Faradaic) effects. .... 79

Figure 3.2.1 Plots of ellipsometric thicknesses of adsorbed BSA on bare Si versus incubation time in BSA(PBS, pH 7.4, 10 mM ionic strength, 37 °C) solutions with different concentrations. Error bars represent the magnitude of the 90% confidence interval for five measurements on one sample. Lines are drawn merely as guides to the eye. .... 91

Figure 3.2.2 Plots of ellipsometric thicknesses of adsorbed BSA on grafted PLA brushes versus incubation time in BSA(PBS, pH 7.4, 10 mM ionic strength, 37 °C) solutions with different concentrations. Error bars represent the magnitude of the 90% confidence interval for five measurements on one sample. Lines are drawn merely as guides to the eye. .... 92

Figure 3.2.3 Plots of ellipsometric thicknesses of adsorbed BSA on grafted (top) PLA, (center) PGA and (bottom) PCL brushes versus incubation time in BSA (PBS, pH 7.4, 100 mM ionic strength, 37 °C) solutions with different concentrations. Error bars represent the magnitude of the 90% confidence interval for five measurements on one sample. Lines are drawn merely as guides to the eye..... 94

Figure 3.2.4 Plot of ellipsometric thicknesses of adsorbed BSA on bare Si versus incubation time in 4.5 mg/mL BSA(PBS, pH 7.4, 100 mM ionic strength, 37 °C) solutions. Error bars represent the magnitude of the 90% confidence interval for five measurements on one sample..... 95

Figure 3.2.5 Plots of ellipsometric thicknesses of PLA, PGA and PCL brushes versus

incubation time in 4.5 mg/mL BSA(PBS, pH 7.4, 100 mM ionic strength, 37 °C) solutions. Adsorbed BSA was removed by sonication in 5 wt% SDS(aq). Error bars represent the magnitude of the 90% confidence interval for five measurements on one sample..... 97

Figure 3.2.6 Plots of ellipsometric thicknesses of adsorbed BSA on Si-OEG brushes versus incubation time in BSA (PBS, pH 7.4, 10 mM ionic strength, 37 °C) solutions with different concentrations. Error bars represent the magnitude of the 90% confidence interval for five measurements on one sample. Lines are drawn merely as guides to the eye. .... 99

Figure 3.2.7 Plots of ellipsometric thicknesses of adsorbed BSA on Si-OEG<sub>mix</sub> brushes (mixed OEG substrate layer: 90% : 10% methoxy and hydroxy terminated OEG) versus incubation time in 4.5 mg/mL BSA (PBS, pH 7.4, 10 mM ionic strength, 37 °C) solutions. Error bars represent the magnitude of the 90% confidence interval for five measurements on one sample..... 100

Figure 3.2.8 Plots of CV curves taken with OEG<sub>mix</sub> covered gold working electrodes of varying composition after incubating in 1 mM K<sub>3</sub>(Fe(CN)<sub>6</sub>) (100 mM PBS, pH 8.0) for 10 min. These current densities are uncorrected for capacitance (e.g. non-Faradaic) effects. .... 101

Figure 3.2.9 Plots of ellipsometric thicknesses of (top) adsorbed BSA on Si-PLA-OEG, Si-PGA-OEG and Si-PCL-OEG brushes and (bottom) Si-PLA-OEG, Si-PGA-OEG and Si-PCL-OEG brushes after BSA was removed by sonication in 5 wt% SDS(aq) versus incubation time in 4.5 mg/mL BSA(PBS, pH 7.4, 100 mM ionic strength, 37 °C) solutions. Error bars represent the magnitude of the 90% confidence interval for five measurements on one sample. .... 103

Figure 3.2.10 Plots of ellipsometric thicknesses of (top) adsorbed BSA on Si-OEG-PLA, Si-OEG-PGA and Si-OEG-PCL brushes and (bottom) Si-OEG-PLA, Si-OEG-PGA and Si-OEG-PCL brushes after BSA was removed by sonication in 5 wt% SDS(aq) versus incubation time in 4.5 mg/mL BSA(PBS, pH 7.4, 100 mM ionic strength, 37 °C) solutions. Error bars represent the magnitude of the 90% confidence interval for five measurements on one sample. .... 106

Figure 3.2.11 Plots of ellipsometric thicknesses of (top) adsorbed BSA on Si-OEG<sub>mix</sub>-PGA brushes and (bottom) Si-OEG<sub>mix</sub>-PGA brushes (mixed OEG substrate layer: 50% : 50% methyl and hydroxy terminated OEG) after BSA was removed by sonication in 5 wt% SDS(aq) versus incubation time in 4.5 mg/mL BSA (PBS, pH 7.4, 10 mM ionic strength, 37 °C) solutions. Error bars represent the magnitude of the

90% confidence interval for five measurements on one sample..... 108

Figure 3.2.12 Plots of ellipsometric thicknesses of (top) adsorbed BSA on Si-OEG<sub>mix</sub>-PGA brushes and (bottom) bare Si-OEG<sub>mix</sub>-PGA brushes (mixed OEG substrate layer: 90% : 10% methyl and hydroxy terminated OEG) after BSA was removed by sonication in 5 wt% SDS(aq) versus incubation time in 4.5 mg/mL BSA (PBS, pH 7.4, 10 mM ionic strength, 37 °C) solutions. Error bars represent the magnitude of the 90% confidence interval for five measurements on one sample. .... 109

Figure 3.2.13 Plots of ellipsometric thicknesses of (top) adsorbed BSA on Si-OEG<sub>mix</sub>-PGA brushes and (bottom) Si-OEG<sub>mix</sub>-PGA brushes (mixed OEG substrate layer: 50% : 50% methyl and hydroxy terminated OEG) after BSA was removed by sonication in 5 wt% SDS(aq) versus incubation time in 4.5 mg/mL BSA (PBS, pH 7.4, 100 mM ionic strength, 37 °C) solutions. Error bars represent the magnitude of the 90% confidence interval for five measurements on one sample.....111

Figure 3.2.14 Plots of ellipsometric thicknesses of (top) adsorbed BSA on Si-OEG<sub>mix</sub>-PCL brushes and (bottom) Si-OEG<sub>mix</sub>-PCL brushes (mixed OEG substrate layer: 50% : 50% methyl and hydroxy terminated OEG) after BSA was removed by sonication in 5 wt% SDS(aq) versus incubation time in 4.5 mg/mL BSA (PBS, pH 7.4, 100 mM ionic strength, 37 °C) solutions. Error bars represent the magnitude of the 90% confidence interval for five measurements on one sample.....112

Figure 3.2.15 Plot of ellipsometric thicknesses after the growth of each segment in multilayer Si-(OEG-PGA)<sub>2</sub>-OEG brushes. Error bars represent the magnitude of the 90% confidence interval for ten measurements on two sample. ....115

Figure 3.2.16 Plots of ellipsometric thicknesses of Si-(OEG-PGA)<sub>2</sub>-OEG brushes versus incubation time in PBS (pH 7.4) and 4.5 mg/mL BSA(PBS, pH 7.4, 10 mM ionic strength, 37 °C) solutions. Error bars represent the magnitude of the 90% confidence interval for five measurements on one sample. ....116

Figure 3.2.17 Plots of ellipsometric thicknesses of (top) adsorbed BSA on mPEG<sub>2000</sub> brushes and mPEG<sub>2000</sub> modified PLA brushes and (bottom) bare mPEG<sub>2000</sub> modified PLA brushes versus incubation time in 4.5 mg/mL BSA(PBS, pH 7.4, 10 mM ionic strength, 37 °C) solutions. Error bars represent the magnitude of the 90% confidence interval for five measurements on one sample. .... 120

Figure 3.2.18 (top) Weighted with standard errors and (bottom) non-weighted calibration curves of BCA protein assay over 0-2000 ug/mL BSA (aq) range. Error bars

represent (top) the relative errors and (bottom) the magnitude of the 90% confidence interval for five readings on one sample. ....	123
Figure 3.2.19 (top) Weighted with standard errors and (bottom) non-weighted calibration curves of BCA protein assay over 0-5 $\mu\text{g/mL}$ BSA (aq) range. Error bars represent (top) the relative errors and (bottom) the magnitude of the 90% confidence interval for five readings on one sample. ....	124
Figure 3.2.20 Linearity of BCA protein assay calibration curves versus incubation time over different BSA (aq) concentration ranges. Measurements were taken every ten minutes until two hours (trial 12) and then every four hours.....	126
Figure 3.2.21 Plots of ellipsometric thicknesses and BCA protein assay calculated adsorbed BSA on grafted PGA brushes versus incubation time in 4.5 mg/mL BSA(PBS, pH 7.4, 10 mM ionic strength, 37 °C) solutions. Error bars represent the magnitude of the 90% confidence interval for five measurements on one sample.....	127
Figure 3.2.22 Plot of ATR-FTIR spectrum of PLA brushes after adsorption with BSA. ....	128
Figure 3.2.23 Plot of ATR-FTIR spectrum of bulk BSA. Inset shows characteristic amide I and II peaks of surface adsorbed BSA from the literature. <sup>22a</sup> .....	129
Figure 3.2.24 Plots of ATR-FTIR spectra of BSA from aqueous solution to gelation state.	129
Figure 3.2.25 Plot of linear regression of quantity ratio between BSA and PLA brushes calculated based on ellipsometric thickness and ATR-FTIR spectra. ....	130
Figure 3.4.1 Photograph (left) and design scheme (right) of a plastic vial used as a sample container during sonication. ....	134
Figure 4.1.1 Depiction of a more efficient stabilization of a more polar transition state compared to the ground state under microwave irradiation. <sup>21</sup> .....	147
Figure 4.2.1 Plots of temperature profiles of toluene containing a stir bar versus time under different powers induced by microwave heating measured by the microwave IR sensor. Error bars represent the standard deviation of three measurements over three samples.....	151
Figure 4.2.2 Plots of temperature profiles of toluene containing $\text{Fe}_2\text{O}_3$ particles with different sizes versus time under different powers induced by microwave heating measured by microwave IR sensor. Error bars represent the standard deviation of three	

measurements over three samples.....	153
Figure 4.2.3 Plots of temperature profiles of toluene containing SiO <sub>2</sub> particles with different sizes versus time under different powers induced by microwave heating measured by microwave IR sensor. Error bars represent the standard deviation of three measurements over three samples.....	154
Figure 4.2.4 Plot of ATR-FTIR spectrum of ATCS modified Fe <sub>2</sub> O <sub>3</sub> nanoparticles. ....	155
Figure 4.2.5 Plots of GPC results (M <sub>n</sub> & PDI versus reaction temperature) for polystyrene synthesized using SPS mode in the presence of ATCS modified Fe <sub>2</sub> O <sub>3</sub> nanoparticles. Error bars represent the standard deviation of two measurements over two samples.....	162
Figure 4.2.6 Plots of GPC results (M <sub>n</sub> & PDI versus reaction temperature) for polystyrene synthesized using SPS mode using free AIBN as initiators. Error bars represent the standard deviation of two measurements over two samples. ....	163
Figure 4.2.7 Plots of GPC results (M <sub>n</sub> & PDI versus reaction time) for polystyrene synthesized at 60 °C using (top) microwave heating and (bottom) thermal heating with free AIBN as initiators. Error bars represent the standard deviation of two measurements over two samples.....	165
Figure 4.2.8 Plots of GPC results (M <sub>n</sub> & PDI versus reaction time) of polystyrene synthesized at 70 °C using (top) microwave heating and (bottom) thermal heating with free AIBN as initiators. Error bars represent the standard deviation of two measurements over two samples.....	166
Figure 4.2.9 Plots of monomer conversions at different temperatures versus reaction time using different heating methods with free AIBN as initiator. Error bars represent the standard deviation of two measurements over two samples. ....	167
Figure 4.2.10 Picture of heat transfer process of microwave irradiated reactions.....	168
Figure 4.2.11 Picture of heat conservation in Fe <sub>2</sub> O <sub>3</sub> nanoparticles .....	171
Figure 4.2.12 Plot of radius of particles versus temperature gradient. ....	175
Figure 4.2.13 Plots of UV-Vis spectra of styrene and toluene.....	177
Figure 4.2.14 Plots of UV-Vis spectra of styrene/toluene solutions at different volume ratios.	

.....	177
Figure 4.2.15 (top) Weighted with standard errors and (bottom) non-weighted calibration curves of UV-Vis spectra using styrene/toluene solution system. Error bars represent (top) the relative errors and (bottom) the magnitude of the 90% confidence interval for five readings on one sample. ....	179
Figure 4.2.16 Linear range of calibration curves of UV-Vis spectra (top) weighted with standard errors and (bottom) non-weighted using styrene/toluene solution system. Error bars represent (top) the relative errors and (bottom) the magnitude of the 90% confidence interval for five readings on one sample. ....	180
Figure 4.2.17 (top) Weighted with standard errors and (bottom) non-weighted calibration curves of GC using styrene/methanol solution system with benzene as the internal standard. Error bars represent (top) the relative errors and (bottom) the magnitude of the 90% confidence interval for six readings on one sample. ....	182
Figure 4.2.18 (top) Weighted with standard errors and (bottom) non-weighted calibration curves of GC using styrene/methanol solution system with benzyl chloride as the internal standard. Error bars represent (top) the relative errors and (bottom) the magnitude of the 90% confidence interval for four readings on one sample.....	184
Figure 4.2.19 Plots of styrene monomer conversions calculated by GC calibration curve versus reaction time for microwave and thermal induced FRP at different temperatures. Error bars represent the magnitude of the 90% confidence interval for nine readings on three sample. ....	185
Figure 4.2.20 Plots of ellipsometric thickness of (top) PMMA and (bottom) PS and maximum system temperature versus reaction power for microwave induced FRP on silicon surface using power time mode. Error bars represent the magnitude of the 90% confidence interval for ten measurements on two samples.....	187
Figure 4.2.21 Plots of ellipsometric thickness of PS versus reaction time at (top) 100 °C and (bottom) 120 °C using different powers for microwave induced FRP on silicon surfaces using SPS mode. Error bars represent the magnitude of the 90% confidence interval for ten measurements on two samples.....	189
Figure 4.2.22 Plots of ellipsometric thickness of PMMA versus reaction time at (top) 100 °C and (bottom) 120 °C using different powers for microwave induced FRP on silicon surfaces using SPS mode. Error bars represent the magnitude of the 90% confidence interval for ten measurements on two samples.....	190

Figure 4.2.23 Plots of temperature profiles of a toluene solution versus time at different powers induced by microwave heating measured by a microwave IR sensor. ..	192
Figure 4.2.24 Plots of temperature profiles of a toluene solution containing a quartz substrate versus time at different powers induced by microwave heating measured by a microwave IR sensor. ....	193
Figure 4.2.25 Plots of temperature profiles of a toluene solution containing a silicon substrate versus time at different powers induced by microwave heating measured by a microwave IR sensor. ....	194
Figure 4.2.26 Depiction of a setup where a tilted silicon sample was placed in a microwave tube and the temperature profile was monitored by an IR camera from the top and a microwave IR sensor from the bottom in parallel. ....	196
Figure 4.2.27 Plots of temperature profiles of tilted silicon substrates in air and toluene versus time at different powers induced by microwave heating measured by an IR camera and a microwave IR sensor. ....	197
Figure 4.2.28 Depiction of a setup where pieces of crushed silicon wafer were placed in a microwave tube (right) with and (left) without addition of toluene. The temperature profile was monitored by an IR camera from the top and a microwave IR sensor from the bottom in parallel. ....	198
Figure 4.2.29 Plots of temperature profiles of crushed silicon substrates placed in air and toluene versus time at different powers induced by microwave heating measured by an IR camera and a microwave IR sensor. ....	199
Figure 4.2.30 Depiction of a setup where silicon wafer was horizontally placed in a microwave tube (right) with and (left) without addition of toluene. The temperature was monitored by an IR camera from the top and a microwave IR sensor from the bottom in parallel. ....	200
Figure 4.2.31 Plots of temperature profiles of silicon substrates horizontally placed at bottom of microwave tube in air and toluene versus time at different powers induced by microwave heating measured by an IR camera and a microwave IR sensor. ....	201
Figure 4.2.32 Depiction of a TEOS coated silicon sample placed (1) in air, (2) above toluene with the bottom face contacting with toluene (3) and below toluene for just 1~2 mm in a microwave tube. ....	202

Figure 4.2.33 Temperature profiles of microwave heated (1) Si in air, (2) Si/SiO<sub>x</sub> in air, (3) Si/SiO<sub>x</sub> above toluene with the bottom face contacting with toluene (4) and Si/SiO<sub>x</sub> below toluene for just 1~2 mm at different powers monitored by an IR camera. .... 203

Figure 4.2.34 A cartoon illustrating the "saturation of heat transfer" between Si/SiO<sub>x</sub> and toluene under unpressurized atmosphere. .... 204

Figure 4.2.35 Temperature profiles of microwave heated Si/SiO<sub>x</sub> sample placed above CCl<sub>4</sub>, toluene and water with the bottom face contacting with solvents at different powers monitored by an IR camera. .... 206

Figure 4.2.36 Temperature profiles of microwave heated silicon sample with a PDMS layer attached to the surface monitored by an IR camera. .... 207

# Chapter 1 Introduction

## 1.1 Stimuli-Responsive Surfaces

### 1.1.1. Introduction to Stimuli-Responsive Surfaces

Stimuli-responsive surfaces, also referred to as smart surfaces, have been of extensive research interest recently because of their various potential applications, especially in the biological fields.<sup>1</sup> Under an external stimulus, such as temperature, solvent or pH, surface properties (such as wettability) or structures can be changed, and these changes are usually reversible.<sup>2</sup> Surfaces with such tunable properties can be utilized in diverse applications such as microfluidic and sensor devices, drug delivery systems and micromechanical systems.<sup>3</sup> Most of the smart surfaces are prepared with self-assembled monolayers (SAMs) and polymer layers that have stimuli-responsive properties.

### 1.1.2. Types of Stimuli-Responsive Surfaces

SAMs which are employed to prepare a stimuli-responsive surface consist of anchoring groups (head groups) that can form covalent bonds between the SAMs molecules and the substrate. The most widely used anchoring groups are thiol and silane groups which can bind to gold and silica surfaces.<sup>4</sup> The tail groups of the SAM molecules are usually functional groups that can respond to external stimuli. For instance, thiol terminated SAMs on gold substrates have been prepared where the molecules are spaced out relatively sparsely on the surface. This low density SAM was formed by assembly of cyclodextrin (CD)-wrapped 16-mercaptohexadecanoic acid (MHA) on the surface followed by the dissociation of CD from SAM using ethanol. Another work prepared similar low density MHA SAM through assembly of MHA derivative with a bulky end group, (16-mercapto)hexadecanoic acid (2-chlorophenyl) diphenylmethyl ester (MHAE).<sup>5</sup> The bulky end group was then removed through hydrolysis. The resulting carboxylic acid tail groups show reversible conformational changes under different potentials.<sup>6</sup> Under a negative potential (-0.3 V), the chains are relatively stretched due to the electrostatic repulsion between the carboxylate ion and the substrate. In contrast, under a positive potential (0.3 V),

the chains are bent due to the attraction between the negatively charged tail groups and the positively charged substrate. It was also shown that the amount of positively charged avidin assembled on the SAMs surface was higher (almost 5 times) under negative potential compared to under positive potential. This was caused by the more exposure of carboxylate ions under negative potential leading to more assembly of the protein molecules.

Other stimuli can be applied as driving forces leading to conformational reorientation of SAMs. For example, it was demonstrated that thiol terminated SAMs with oligo(ethylene glycol) (OEG) and methyl mixed tail groups can undergo conformational changes at different temperatures (room temperature and 37 °C). This behavior was proposed to be the main reason for reversible adsorption of protein on the surface.<sup>7</sup>

Another category of stimuli-responsive surfaces can be fabricated by depositing a polymer layer on the substrate via either physical or chemical approaches.<sup>8</sup> The polymer layer can be cross-linked polymer films, hydrogels, homo- or co-polymer brushes.<sup>9</sup> Polymer brushes can be covalently bonded to the substrate via various techniques such as "grafting to" and "grafting from" methods. Using the grafting from method, polymer brushes are usually formed through a surface initiated polymerization process (SIP) which can result in brushes with high grafting densities. The stimuli responsive properties can be introduced either through the end functional groups of the brush or through the brush backbones. Diverse approaches have been investigated to build stimuli-responsive surfaces using polymer brushes. For example, a theoretical study by Wu et al. indicated that a surface with reversible conformational changes can be obtained through modifying the end groups (end monomer unit) of homopolymer brushes with a high grafting density.<sup>10</sup> In this work, simulations suggested that both percentage of end groups modified and the size of the end groups were important factors to attain switchable reorientation of the brush under the influence of temperature and solvent.

Similar to SAM-modified smart surfaces, the stimuli responsive properties of surfaces grafted with polymer brushes also can be driven by various stimulations. For instance, poly(N-isopropylacrylamide) (PNIPAM) brushes are well known to have switchable surface

wettability due to chain reorientation induced by changes in temperature.<sup>11</sup> The reversible conformational changes are caused by (1) the formation of hydrogen bonds between PNIPAM chains and water molecules below the critical solution temperature (LCST) of PNIPAM leading to relatively stretched structure and hydrophilic property of the brushes and (2) the formation of hydrogen bonds between C=O and N-H groups on the polymer backbones resulting in compact and hydrophobic brushes. It is also reported that the surface roughness can even enhance this temperature-induced reversible changes in wettability of PNIPAM brushes.<sup>11a</sup>

Polyelectrolyte brushes are also widely employed in preparing smart surfaces which are responsive to pH. As shown in Figure 1.1, it was shown that poly[2-(methacryloyloxy) ethyl] phosphate (PMEP) brushes can undergo two surface wettability change processes induced by pH due to the two association/dissociation equilibria (two pKa values: 1~2 & 6~7) of orthophosphoric acid.<sup>12</sup> The enhanced hydrophilicity and swelling of the brush surface was caused by the electrostatic repulsion between chains due to the formation of phosphonate groups at higher pH values (larger than pKa<sub>1</sub> and pKa<sub>2</sub>).

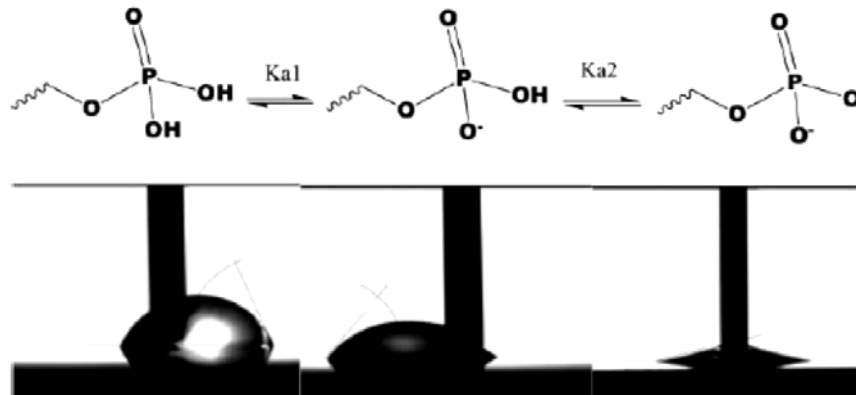


**Figure 1.1 (top) Two association/dissociation equilibria of orthophosphoric acid in PMEP brushes; (bottom) Depiction of the advancing contact angles of DI water on PMEP brush surface under different pH environments: (from left to right) pH<1, 65 °; pH=4, 49 °; pH>10, 13 °.<sup>12</sup>**

Solvent can also act as an external stimulus to cause a morphology change of smart surface modified with polymer brushes. It was shown that when exposing a mixed brush system containing polystyrene (PS) and poly(2-vinylpyridine) (P2VP) (1:1) to different solvents (toluene and acidic water), the dominant component on the outer layer of the brush can be changed (Figure 1.2).<sup>13</sup> The hydrophilicity of the surface can then be tuned due to the different degree of swelling and hydrophilicity of the two polymer components.

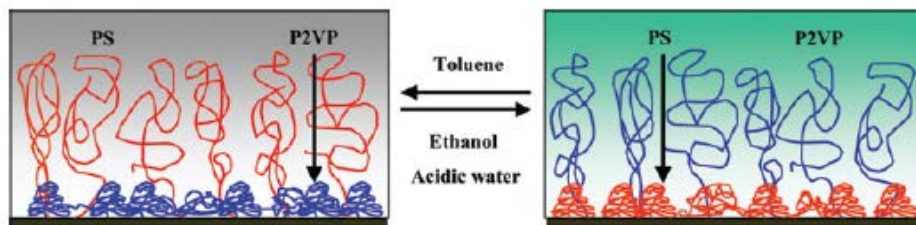


**Figure 1.2 Depiction of the reversible structure changes of PS/P2VP mixed brush system under different solvent environments: (left) in toluene and (right) in acidic water and ethanol.**<sup>13</sup>

In addition to the external stimuli mentioned above, the properties of smart surfaces can also be adjusted through other approaches such as using photochemical and electrical potential methods,<sup>14</sup> and by varying counter ions of polyelectrolyte brushes.<sup>15</sup> Some polymer brush modified smart surfaces can even respond to multiple stimuli instead of a single stimulus.<sup>16</sup>

### 1.1.3. Applications of Stimuli-Responsive Surfaces

In addition to the wide study of stimuli responsive behaviors of smart surfaces, the applications of these surfaces have also drawn tremendous research interest. The most popular bio-applications include drug delivery, biosensors and control of biomolecule adsorption. A polypyrrole brush, a type of conductive polymer brush, was utilized as a substrate responsive to changes in electrical potential to release incorporated drugs (i.e. nerve growth factor) under electrical stimulation.<sup>17</sup> Mixed SAMs of ferrocenylalkanethiol and

encapsulated horseradish peroxidase on gold substrate have been utilized as a hydrogen peroxide detecting sensor through electron transfer between the two SAMs components.<sup>18</sup>

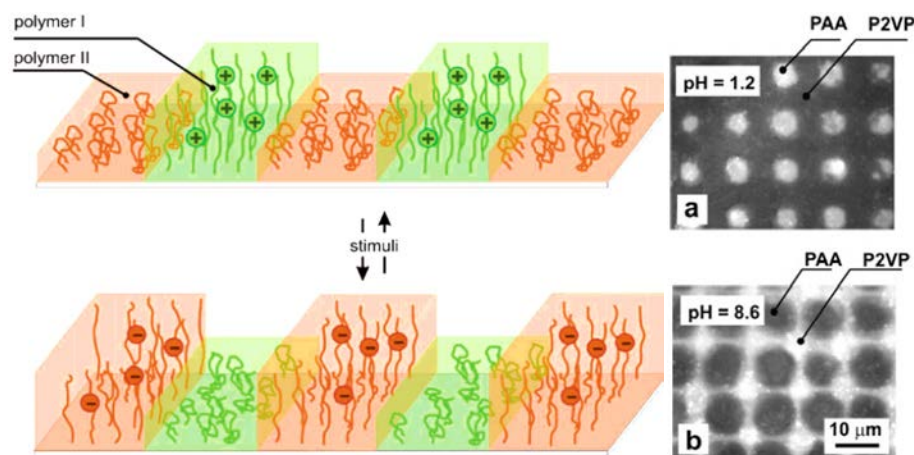


**Figure 1.3 (left) Depiction of the switching swelling effects of P2VP and PAA domains under different pH environments: (top) pH 1.2 and (bottom) 8.6 respectively; (right) Fluorescence graphs depicting FITC-casein adsorbed (a) on PAA and (b) on P2VP domains.**

The conformational change of stimuli-responsive polymer brushes can be exploited to control biomolecule adsorption. Thermally responsive polymers such as PNIPAM which was discussed in the last section, can experience surface wettability changes at different temperatures. The resulting reduced hydration at elevated temperatures ( $>LCST$ ) and enhanced hydration at lower temperatures ( $<LCST$ ) can lead to changes in the tendency of adsorption and desorption of cells and protein molecules.<sup>19</sup> The adsorption of protein molecules on substrates can also be altered by changes in pH using polyelectrolyte brushes induced by pH. The adsorption of a fluorescently-labeled protein, casein fluorescein isothiocyanate (FITC-casein), was examined on a mixed polymer brush system consisting of P2VP and poly(acrylic acid) (PAA).<sup>20</sup> It was demonstrated that the FITC-casein selectively adsorbed (1) on PAA domains at low pH (1.2) when protein molecules and the swollen P2VP

domains were positively charged and (2) on P2VP domains at high pH (8.6) when both protein molecules and the swollen PAA chains were negatively charged (Figure 1.3).

## **1.2. Protein Adsorption**

Protein adsorption on various types of surfaces has been the subject of a lot of attention recently due to its significant impact in many application areas.<sup>21</sup> Efforts have been spent on understanding and controlling this process. The mechanism of protein adsorption is complicated and has not been fully understood, but studies have been performed to understand different aspects such as the properties of proteins and surfaces, and the types of interactions between them. Substrates modified with polymer brushes, SAMs etc. have been utilized to conduct investigations aiming at controlling protein adsorption.<sup>22</sup>

### **1.2.1. Desirable and Undesirable Immobilization of Protein on Surface**

Protein adsorption can be regarded as a desirable or undesirable process. Fabrication of biomaterials used for tissue engineering processes is a good example where protein adsorption is desirable. Immobilization of cell-adhesion proteins is a typical first step in this process.<sup>23</sup> Various approaches have been applied to achieve the immobilization of biomolecules on these biomaterials including physisorption and chemical methods.<sup>24</sup> Although physisorption is relatively easier to conduct than chemical immobilization, several problems usually exist when using this method. For example, the conformation of the adsorbed materials on surfaces is difficult to control, and the molecules can desorb from substrates over time. Therefore, chemical methods are more frequently adopted to achieve a more controllable and stable immobilization of the biomolecules. For instance, in order to improve cell adhesion, fibronectin was used to covalently attach the surface of poly(vinyl alcohol) (PVA) hydrogels which were pre-modified with long chain carboxylic acids.<sup>25</sup> Arginine-glycine-aspartic acid (RGD) peptides were immobilized on the surface of poly(dimethylsiloxane) (PDMS) through photochemical methods to promote the adhesion and proliferation of human skin fibroblasts.<sup>26</sup> Collagen was bonded to the surface of poly(L-lactic acid) which was pre-grafted with poly(methacrylic acid) aiming at enhancing cell spreading and growth.<sup>27</sup>

Nevertheless, in many other applications, protein adsorption is an undesirable process and is defined as a biofouling problem. Many areas such as in the food and marine industries suffer from biofouling problems. In addition, many blood-contacting implanted devices can have thrombosis problems due to the adsorption of protein on the surface. Therefore, research has been focused on the pre-treatment of the surface with materials which resist biomolecule adhesion.<sup>28</sup> A detailed discussion related to improving protein resistance of surfaces is provided in Section 1.2.4 below.

### **1.2.2. Study of the Mechanisms of Protein Adsorption**

In order to control the protein adsorption process, it is essential to understand the interaction mechanisms between the protein molecule and the substrates. Although this issue has not been fully addressed, a lot of experimental and theoretical investigations have been performed. It is generally concluded that properties such as surface charge, wettability and morphology, conformation and grafting density of the modified layer (polymer or SAMs) can influence the adsorption process.<sup>29</sup> For instance, protein adsorption was tested on surface modified with alkanethiol SAMs with different terminal groups. It was found that more protein adsorbed on less hydrophilic surfaces due to increased hydrophobic interactions between protein and the surface.<sup>29b, 30</sup> It was also demonstrated that surface modified with poly(ethylene glycol) (PEG) could better resist protein adsorption when the grafting density of PEG was increased, leading to higher steric repulsion between protein and the surface.<sup>29c</sup> In addition, a theoretical study showed that the conformation of densely packed oligo(ethylene glycol) (OEG) terminated alkanethiol SAMs contributes a lot to resisting protein adsorption. It was calculated that OEG terminated SAMs with a helical conformation have stronger interaction with water molecules than a SAM with a "all-trans" planar conformation, which can cause reduced hydrophobic interactions between protein and the surface.<sup>31</sup> Another study revealed that nanostructured titania surfaces had more protein adsorption when surface roughness was increased because of the enhanced protein nucleation inside the nanopores.<sup>32</sup>

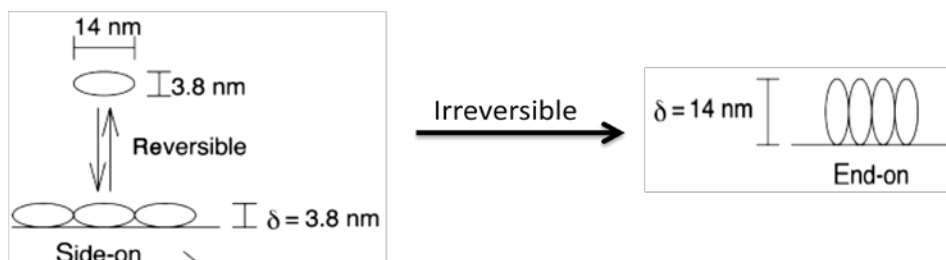


**Figure 1.4** Depiction of the conformational change of BSA molecules adsorbed on the surface.<sup>33</sup>

In addition to surface properties, the adsorption modes of protein on surfaces have also been investigated. Taking bovine serum albumin (BSA) as an example, it was suggested that the adsorption of BSA on surfaces such as nanoparticles, usually follows two binding modes: side-on and end-on binding conformations.<sup>33</sup> BSA molecules adsorb on a surface primarily via a reversible side-on conformation. This is followed by an irreversible end-on orientation when unfolding or denaturation of the protein molecules occur leading to more interaction between the densely packed protein molecules (Figure 1.4). For example, it was shown that BSA attached to citrate coated gold nanoparticles with the end-on orientation resulted in a high surface coverage of the protein molecules.<sup>34</sup> Also, PEG brushes with different degrees of polymerization can also affect the adsorption modes of BSA molecules (primary and ternary adsorptions).<sup>35</sup>

### 1.2.3. Characterization of Protein Adsorption

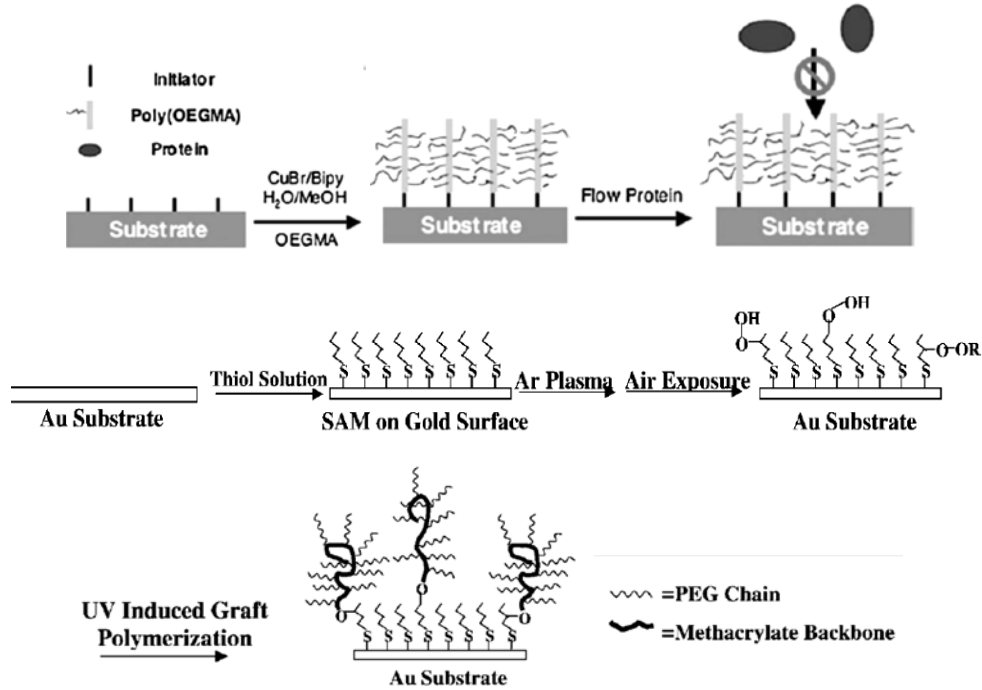
Various techniques have been utilized to characterize the adsorption of protein on different surfaces. For instance, quartz crystal microbalance (QCM) and QCM with dissipation factor monitoring (QCM-D) have been widely used in determining the mass and viscoelasticity of adsorbed protein layers on flat substrates by relating the decrease of oscillating frequency of the quartz crystal with the change of mass on the substrate.<sup>36</sup> Surface plasmon resonance (SPR) can be employed to monitor the adsorption profile of proteins on flat substrates by measuring the change of SPR angle.<sup>37</sup> Confocal laser scanning

microscopy (CLSM) can be used to evaluate the surface coverage of biomolecules adsorbed on surfaces.<sup>38</sup> Furthermore, various types of protein assays have also been applied to quantitatively measure the adsorbed proteins on substrates.<sup>39</sup>

#### **1.2.4. Efforts towards Reducing Protein Adsorption**

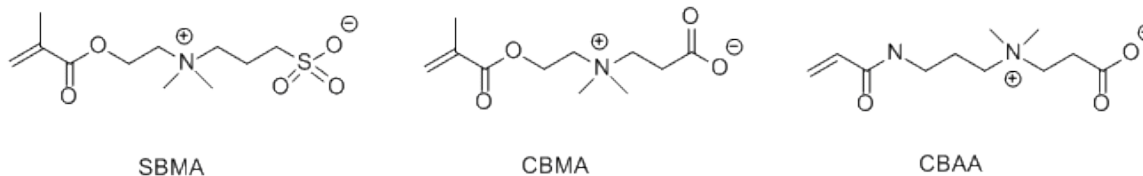
Due to the problems associated with of protein adsorption mentioned previously, research has been dedicated to engineer protein resistant surfaces and coatings. Among all the materials, PEG and OEG are the most prevalent coatings used for preventing non-specific adsorption of protein.<sup>40</sup> Various methodologies have been investigated to fabricate SAMs and polymer brushes consisting of PEG and OEG components, including physisorption and chemical grafting methods.<sup>41</sup> For example, poly(OEG-methacrylate) (POEGMA) was grafted on gold and silica substrates via surface initiated atom transfer radical polymerization (SI-ATRP) as a protein-resistant layer as shown in Scheme 1.1 (top).<sup>42</sup> Another report showed that via UV-induced graft polymerization, poly(ethylene glycol) methacrylate (PEGMA) can be grafted from SAM-modified gold surfaces which were pre-treated with argon plasma (Scheme 1.1 bottom).<sup>43</sup>

Scheme 1.1 (top) SI-ATRP of OEGMA on initiator modified substrates to build a non-fouling surface;<sup>42</sup> (bottom) UV induced graft polymerization of PEGMA on a SAM-modified gold surface pretreated with argon plasma.<sup>43</sup>



Synthesis of tissue engineering biomaterials modified with PEG components and biodegradable materials were also reported. For example, poly(ethylene glycol)-block - poly(D,L-lactide) (PEG-b-PDLLA) was synthesized and attached to fiber surfaces through electrospinning to improve the protein resisting properties of the fibers.<sup>44</sup> Poly(D,L-lactide-co-glycolide) fibers modified with star-shaped PEG also showed enhanced biofouling properties.<sup>45</sup>

**Scheme 1.2 Molecular structures of zwitterionic monomers: (from left to right) sulfobetaine methacrylate (SBMA), carboxybetaine methacrylate (CBMA) and carboxybetaine acrylamides (CBAA).**



The antifouling properties of other materials such as peptides and zwitterionic materials also have been widely explored. Gold surfaces modified with amino acid L-cysteine were shown to have slightly improved antifouling property than bare gold substrates.<sup>46</sup> Gold surfaces modified with SAMs of 3-mercaptopropionyl-leucinyl-histidinyl-aspartic acid (3-MPA-(Leu-His-Asp)<sub>2</sub>-OH) showed enhanced protein resisting properties.<sup>47</sup> Also, zwitterionic polymers such as poly(carboxybetaine methacrylate) (polyCBMA), poly(sulfobetaine methacrylate) (polySBMA) and poly(carboxybetaine acrylamides) (polyCBAA) (Scheme 1.2) have been synthesized on surfaces through ATRP to reduce non-specific protein adsorption.<sup>48</sup>

### 1.3. Polymer Brushes

#### 1.3.1. Introduction to Polymer Brushes

Fabrication of biodegradable polymer brushes and examination of their bio-applications are a research interest in the project described in this thesis. Polymer brushes can be generally defined as a layer of polymer chains with one end attached to a surface. The attachment of polymer chains on the surface can be via physical or chemical methods as described further in the next section. There are various types of surfaces where polymer chains can be tethered such as a solid and the interface between liquids; therefore, the structure of polymer brushes can be very different (Figure 1.5).<sup>49</sup> Polymer brushes usually display properties different from bulk polymers and polymers in solution due to surface confinement.<sup>50</sup> Therefore, they are of great interest in basic research and applications.

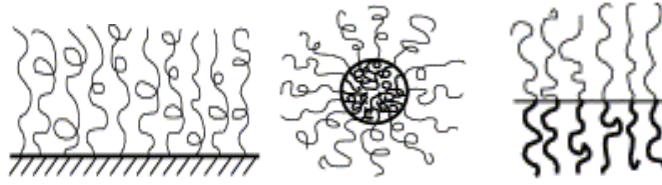


**Figure 1.5 Depiction of polymer brushes on various surfaces with different structures: (left to right) a polymer brush grafted from a flat solid substrate, a polymer micelle and block copolymer at fluid-fluid interfaces.<sup>49</sup>**

The structure of a polymer brush can be determined by parameters including brush thickness ( $h$ ), reduced tethered density ( $\Sigma$ ) and grafting density ( $\sigma$ ). The equation describing the grafting density of polymer brushes is as follows:

$$\sigma \text{ (nm}^{-2}\text{)} = \frac{h \text{ (nm)}\rho \left(\frac{\text{g}}{\text{cm}^3}\right) N_A \text{ (mol}^{-1}\text{)}}{M_n \left(\frac{\text{g}}{\text{mol}}\right)} \times 10^{-21} \left(\frac{\text{cm}^3}{\text{nm}^3}\right)$$

where  $\rho$  is the density of the polymer component,  $M_n$  is the molecular weight of the polymer chains and  $N_A$  is the Avogadro's number. For example, when depositing pre-formed polymer chains on a surface such as using "grafting to" method, the grafting density can be calculated if the molecular weight of the polymer is known and the thickness of the brush is measured. A reduced tethered density is defined as the number of polymer chains occupying the region that a single polymer chain takes up without interference with other chains under the same conditions. It can be described in the following equation:

$$\Sigma = \sigma \Pi R_g^2$$

where  $R_g$  is the gyration radius of a polymer chain. The reduced tethered density has been usually used to determine the structure of polymer brushes. It is considered that three main regimes of a polymer brush can exist: mushroom conformation ( $\Sigma < 1$ ), mushroom to brush transition conformation ( $\Sigma \approx 1$ ) and brush conformation ( $\Sigma > 1$ ). However, this statement is

relatively idealized. In most of the cases, the three conformational regimes do not exactly follow the reduced tethered density range as mentioned above due to different brush properties and environmental conditions.<sup>51</sup> Therefore, a revised model is more frequently used instead, to illustrate the three structures: mushroom conformation ( $\Sigma < 1$ ), mushroom to brush transition conformation ( $1 < \Sigma < 5$ ) and brush conformation ( $\Sigma > 5$ ).

### 1.3.2. Preparation Methods for Polymer Brushes

Polymer brushes can be prepared through physical and chemical methods including physisorption, "grafting to" and "grafting from" approaches (Figure 1.6).<sup>52</sup> For physisorption, a solution containing diblock copolymer is deposited on the substrate. This method is relatively easy to conduct; however, drawbacks of this process exist such as desorption of the polymers that can occur under certain conditions.<sup>53</sup> Therefore, a more stable way to attach the polymer chains on surfaces through covalent bonding by "grafting to" or "grafting from" method is more preferable.

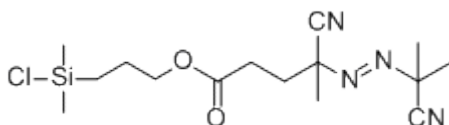


**Figure 1.6 Depiction of methods for preparing polymer brushes.**<sup>52</sup>

Polymer brushes prepared through a "grafting to" method usually require pre-formed polymer with functional end groups that can work as anchoring groups on a surface. For example, PS with thiol terminal groups (in toluene) synthesized through anionic polymerization has been grafted to gold substrates.<sup>54</sup> PS modified with hydroxy terminal groups through living free radical polymerization using 2,2,6,6-tetramethylpiperidinyloxy (TEMPO) as the initiator has been grafted to silicon surfaces containing a native oxide

layer.<sup>55</sup> Also, carboxy terminated PS was grafted to trimethoxysilane modified silicon surface with gradually changing thicknesses using a gradient heating stage.<sup>56</sup> Polymer brushes obtained by "grafting to" method usually have lower grafting densities than using "grafting from" method.<sup>57</sup> Also, polymer brushes can be prepared by many different polymerization methods using "grafting from" approach. Therefore, "grafting from" method is a more attractive and superior way to make densely packed polymer brushes compared to the "grafting to" method.

**Scheme 1.3 Molecular structure of an azo initiator reported by R  he et al.<sup>58</sup>**

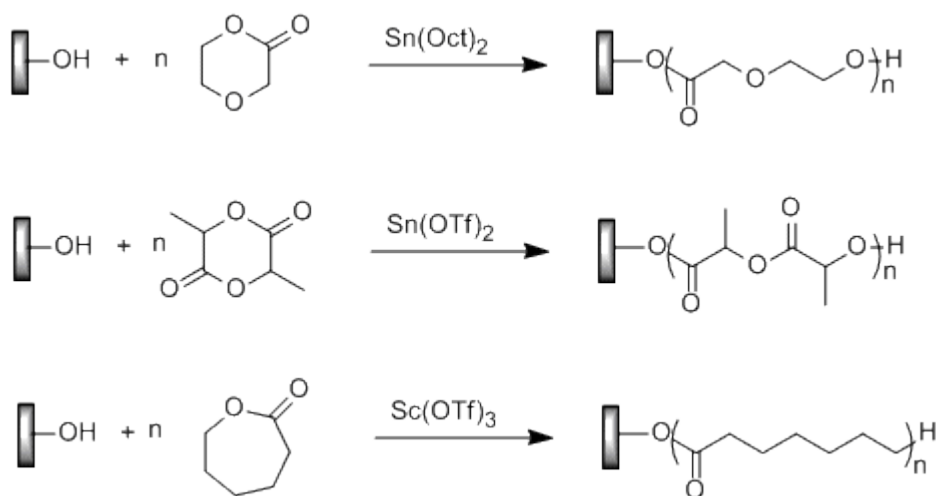


The "grafting from" approach is also known as surface initiated polymerization (SIP). Initiators can be the native layer on a surface such as the oxide layer on silicon wafer, or can be immobilized through various methods on the surface. Many different polymerization schemes such as free radical polymerization (FRP), atom transfer radical polymerization (ATRP), ionic polymerization and ring opening polymerization (ROP) can be utilized to synthesize polymer brushes. For instance, FRP has been applied in synthesizing PS on initiator modified silica gel surface.<sup>58</sup> In the structure of the azo initiator synthesized by R  he et al., there are three important components: a silane anchoring group, a cleavable ester group and an initiator group. After the SI-FRP of PS, the polymer brushes can be cleaved off from the surface by acid catalyzed hydrolysis of the ester group. Using this approach, more characterization methods of the grafted polymer brushes are available.

ATRP is also reported in preparing various types of polymer brushes through SIP. For example, a triblock copolymer consisting of poly(methyl acrylate) (PMA), poly(methyl methacrylate) (PMMA) and poly(2-hydroxyethyl methacrylate) (PHEMA) was synthesized

on gold and silicon substrates modified with (2-bromopropionyl bromide) initiator through SI-ATRP.<sup>59</sup> Poly(N,N-dimethyl -acrylamide) (PDMA) was grafted from polystyrene latex through SI-ATRP in aqueous environment.<sup>60</sup> In addition, polyelectrolyte brushes such as poly(2-(methacryloyloxy)ethyl trimethylammonium chloride)-b-PMMA-b-poly(sodium methacrylate), could also be synthesized through SI-ATRP on gold substrates modified with initiator SAMs.<sup>61</sup> Anionic and cationic polymerization methods were also employed for preparing polymer brushes via SIP. It was shown that, through anionic polymerization, PS was grafted from gold and silicon surfaces which were modified with n-butyl lithium activated diphenylethylene initiator.<sup>62</sup> Another work demonstrated that PS brushes can be grafted from silicate substrate modified with various carbocationic initiators via cationic polymerization.<sup>63</sup>

**Scheme 1.4 SI-ROP of p-DO, LA and  $\epsilon$ -CL from surfaces with hydroxyl terminal groups.<sup>64</sup>**



ROP is another widely used method to fabricate polymer brushes using cyclic monomers. Numerous types of biodegradable polymers, such as poly(p-dioxanone) (PPDO),

poly(lactic acid) (PLA) and poly( $\epsilon$ -caprolactone) (PCL) have been prepared via SI-ROP.<sup>64-65</sup> Usually, organometallic catalysts such as tin(II) octanoate, tin(II) trifluoromethane sulfonate and scandium (III) trifluoromethane sulfonate were applied to assist the SI-ROP of these cyclic monomers on surfaces with hydroxyl or amino functional groups. Examples of SI-ROP of p-DO, LA and  $\epsilon$ -CL are shown in Scheme 1.4.

### **1.3.3. Applications of Polymer Brushes**

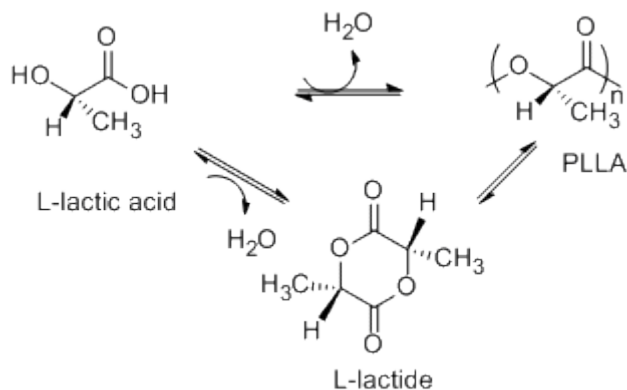
Due to the distinctive properties of polymer brushes, they have raised a lot of research interest in their applications. As mentioned previously, various types of polymer brushes have been employed as stimuli-responsive surfaces. In addition to modulate the adhesion of biomolecules, they can also be utilized in stabilizing colloidal particles<sup>66</sup>, supporting metallic nanoparticles<sup>67</sup> and modifying membranes.<sup>68</sup> In this project, research interest is mainly focused on the anti-biofouling properties of polymer brushes as described in section 1.5.

## **1.4. Biodegradable Polyesters**

### **1.4.1. Introduction to Biodegradable Polyesters: Poly(lactic acid), Poly(glycolic acid) and Poly( $\epsilon$ -caprolactone)**

Biodegradable polymers including natural and synthetic polymers, have attracted a lot of attention due to their numerous bio-applications.<sup>69</sup> Various types of biodegradable polymers such as polysaccharides, polypeptides and polyesters, have been studied and utilized as biomedical materials.<sup>70</sup> For example, a chitosan- thioethylamidine derivative exhibiting increased mucoadhesion properties was synthesized and demonstrated to have potential application for drug release.<sup>71</sup> Gelatin has been very widely used as a hemostat for tens of years.<sup>72</sup> PCL and its copolymers have been employed as suture coatings.<sup>73</sup> As the result of the research goals of this project, polyesters including poly(lactic acid) (PLA), poly(glycolic acid) (PGA) and poly( $\epsilon$ -caprolactone) (PCL) are mainly studied in the following chapters.

**Scheme 1.5 Polymerization of PLLA by two approaches: condensation polymerization and ring opening polymerization.**



PLA is a well-studied and widely used biodegradable polyester. It has low toxicity and is generated from renewable natural sources. The basic monomer for PLA, lactic acid, can be produced by fermentation from natural materials such as corn and sugar beets.<sup>74</sup> PLA can be synthesized either via condensation polymerization of lactic acid or through ROP of lactide, the cyclic dimer of lactic acid (Scheme 1.5).<sup>75</sup> The monomer, lactide, has three different stereoisomer structures: L-lactide, D-lactide and meso-lactide, among which L-lactide is the most common natural form. The crystallinity of PLA is mainly determined by the stereopurity of the structure of its backbone. Pure PLLA and PDLA are semicrystalline polymers while PDLLA and PLA prepared from meso-lactide monomer are usually amorphous materials. The degradation or hydrolysis of PLA can be either enzymatically or chemically catalyzed.<sup>76</sup> Usually, PLA molecules with high molecular weight first degrade into low molecular weight oligomers which then further degrade into lactic acid.<sup>77</sup> The degradation rate is dependent on many factors such as pH, temperature, molecular weight and crystallinity of PLA.<sup>78</sup> PLA is commonly synthesized with other cyclic monomers (GA and  $\epsilon$ -CL) to form block or random copolymers in order to adjust the degradation rate and other properties (i.e. tensile strength) of the polymer.

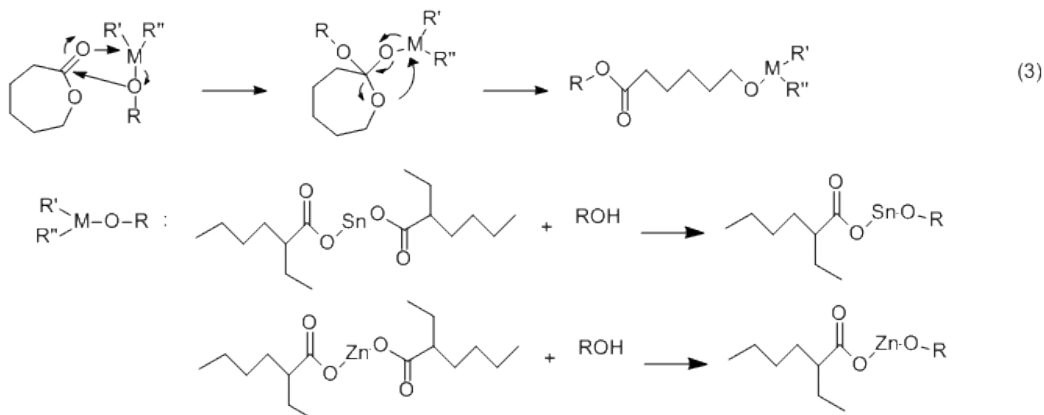
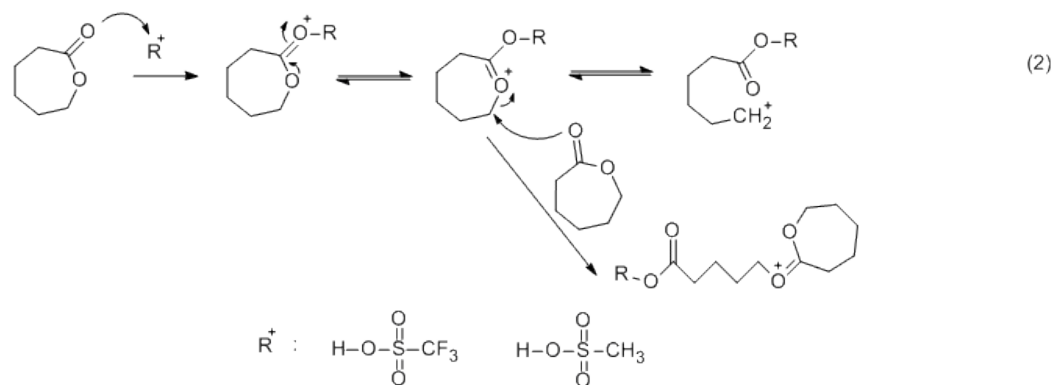
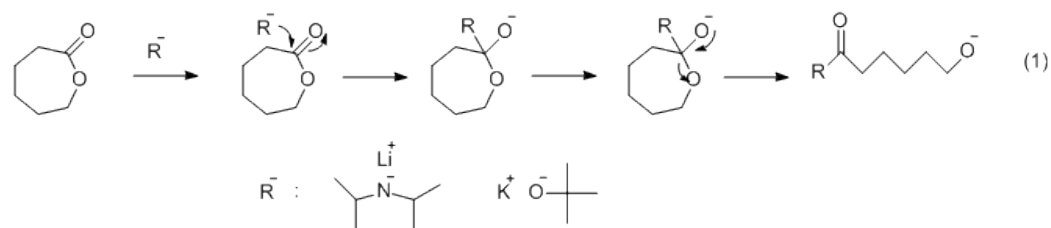
Similar to PLA, PGA is another biodegradable polymer with good biocompatibility. It can also be produced by polycondensation reaction of glycolic acid and by ROP of glycolide monomer both of which can be obtained from renewable resources.<sup>79</sup> PGA is a semicrystalline polymer with better mechanical properties (i.e. tensile modulus of 6~7 GPa) than PLA (i.e. tensile modulus of 3 GPa) and PCL (i.e. tensile modulus of 0.21-0.44 GPa).<sup>80</sup> Due to the rigidity, copolymers of PGA with PLA and PCL are usually fabricated in order to tune their mechanical properties for different applications.<sup>81</sup> Also, it is worth noting that the solubility of PGA in most organic solvents is rather poor except in fluorinated solvents such as hexafluoroisopropanol.<sup>82</sup>

The other biodegradable polymer studied in this work is PCL. PCL is more frequently prepared via ROP of  $\epsilon$ -CL than by a polycondensation reaction using  $\omega$ -hydroxyhexanoic acid to give high molecular weight PCL with low polydispersity.<sup>83</sup> Similar to PLA and PGA, both hydrolytic and enzymatic degradations can occur with PCL.<sup>84</sup> PCL is soluble in most solvents such as chloroform, dichloromethane, benzene and toluene at room temperature. PCL has a relatively slow degradation rate and is more ductile than PLA.<sup>80a</sup> As mentioned above, it is usually used to form copolymers with other biodegradable components.

#### **1.4.2. Synthesis of Poly(lactic acid), Poly(glycolic acid) and Poly( $\epsilon$ -caprolactone) and Their Copolymers**

Instead of using polycondensation reactions to make PLA, PGA and PCL which requires continuous water removal, ROP is more widely employed as the synthesis method. The three polyesters can be prepared using various catalysts following different mechanisms including anionic ROP, cationic ROP and coordination-insertion ROP. ROP of PCL under different mechanisms using typical catalysts is shown in Scheme 1.6 as an example.<sup>85</sup>

**Scheme 1.6 Synthesis of PCL under (1) anionic ROP, (2) cationic ROP and (3) coordination-insertion ROP mechanisms.**



Catalysts employed during the ROP of LA, GA and  $\epsilon$ -CL can be generally classified into two main groups: metal-based catalysts and enzyme catalysts. Among all the metal catalysts such as alkali-based, alkaline earth-based and poor metal-based catalysts, tin-based catalysts (i.e. tin(II) octanoate) are used and reported most frequently in the literature due to

their high reactivity.<sup>86</sup> For tin(II) octanoate catalyzed ROP, a coordination-insertion mechanism has been proposed.<sup>87</sup> Usually, co-catalysts such as alcohols (or amines) are added to react with tin(II) octanoate to form the actual initiator, tin(II) alkoxide (eq. 3 in Scheme 1.6). ROP catalyzed by enzymes has also been investigated. For instance, a *Pseudomonas* sp. lipase was utilized to catalyze ROP of  $\epsilon$ -CL resulting in higher molecular weight and monomer conversion than polycondensation reaction.<sup>88</sup> The reaction rate and the properties of the resulting polyester such as molecular weight and polydispersity, can be varied by using different catalysts.<sup>89</sup>

Other reaction conditions such as solvent and temperature also have been shown to affect the reaction rate and polymer properties. For example, synthesis of PCL was reported to be faster in toluene than in dioxane using tin(II) octanoate as catalyst.<sup>90</sup> The conversion of L-LA during solution polymerization in dioxane also using tin(II) octanoate as catalyst increased faster at elevated temperatures.<sup>91</sup> Furthermore, a decreased molecular weight of PGA prepared through bulk ROP using Maghnite-H<sup>+</sup> as catalyst was observed at elevated temperatures.<sup>82</sup> Another work also showed that the molecular weight of PLA synthesized under higher temperatures was decreased which was attributed to the depolymerization of the resulting polymer.<sup>92</sup>

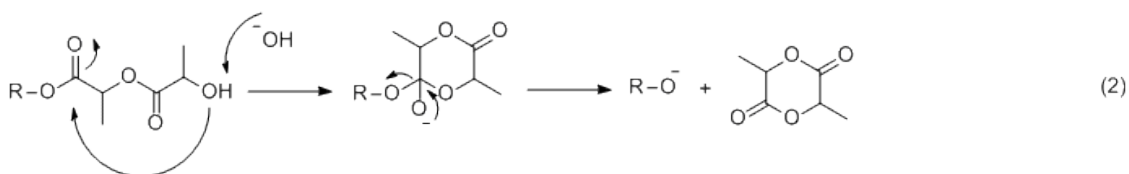
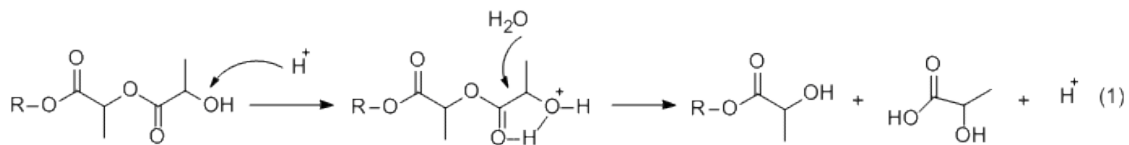
In addition to single polyesters, synthesis of various types of copolymers using the three polyester components and other polymers such as PEG have been established.<sup>93</sup> As mentioned in the previous section, surface grafted polyesters through ROP reaction was also demonstrated.<sup>94</sup>

#### **1.4.3. Degradation of Poly(lactic acid), Poly(glycolic acid) and Poly( $\epsilon$ -caprolactone) and Their Copolymers**

Degradation of PLA, PGA and PCL and their copolymers can be both acid and base catalyzed.<sup>95</sup> In aqueous media, degradation of these polyesters usually follows two steps: solvation of the polymer and the hydrolysis of ester groups. The mechanisms accounting for the degradation of polyesters have been studied in several ways and can be generally classified into two types: chain scission and backbiting.<sup>95a, 96</sup> The chain scission process of all

three polyesters can be catalyzed by both acid and base while the backbiting process is only seen in base-catalyzed reactions.

**Scheme 1.7 Chain-end scission hydrolysis and backbiting process of PLA.**



Hydrolysis of ester groups on the polymer backbones can occur at any random position leading to random chain scission and at the end group position resulting in chain-end scission (eq.1 in Scheme 1.7). In some reports about the degradation of PLA and its oligomers, a faster hydrolysis rate was seen for chain-end scission than random scission process. This behavior was not the case for PCL.<sup>97</sup> Also, the end groups of polyesters such as carboxylic acid and hydroxyl groups can also act as catalysts for the hydrolysis reaction. Therefore, an auto-catalysis behavior is often observed during degradation. For example, the interior of bulk polyester degrades faster than at the surface due to the auto-catalysis process caused by the increased number of end groups of oligomers accumulated inside the matrix.<sup>98</sup>

During the backbiting process which is catalyzed by hydroxyl ions, cyclic monomer is formed and cleaved off from the polymer chain. As can be seen from Scheme 1.7 (eq. 2), the backbiting process of PLA takes place by intramolecular transesterification resulting in lactide monomer. The backbiting of lactic acid oligomers was studied in alkaline medium by

characterizing the degradation products using HPLC and MS.<sup>96c</sup> However, this mechanism has been less studied and documented than the chain scission mechanism.<sup>96a</sup>

The rate of degradation of these polyesters can be affected by many factors such as degradation environment including temperature and pH, and crystallinity of the materials. For instance, degradation of PLA and its oligomers was observed to be more rapid at elevated temperatures.<sup>99</sup> PLA and PCL copolymers with varying components of each polyester and PLGA copolymer annealed at different temperatures have different degradation rates under the same conditions due to different sample morphologies.<sup>100</sup> PLGA films degrade faster under static environment because of the auto-catalysis inside the polymer under undisturbed conditions than under a dynamic situation.<sup>101</sup>

#### **1.4.4. Applications of Poly(lactic acid), Poly(glycolic acid) and Poly( $\epsilon$ -caprolactone) and Their copolymers**

In both the industrial and biomedical fields, applications of PLA, PGA, PCL and their copolymers have been extensively investigated. They can be fabricated as plastic fibers, paper coating, films and packaging materials. For instance, PCL foams with thermal insulation and packaging applications have been generated using supercritical carbon dioxide.<sup>102</sup> They can also be used in drug delivery, or as implant materials due to their good biocompatibility.<sup>103</sup> For example, PLGA copolymers are commonly used in the microsphere or nanoparticle forms for drug delivery. PEG components are frequently introduced to reduce coagulation on the surface of the particles.<sup>104</sup>

As can be seen, the importance of these applications has been a driving force for research on these polyesters. However, attention is mainly focused on investigation of bulk polymers. Research on surface grafted polyesters such as their growth, degradation and applications has rarely been demonstrated. Therefore, the aim of this project is to study the growth and degradation behaviors of surface grafted PLA, PGA and PCL brushes and probe their application as antifouling surfaces which is further discussed in the next section.

## 1.5. Proposed Anti-fouling Dynamic Surface

The long term goal of this project is to fabricate an anti-fouling dynamic surface prepared by coating biodegradable and biocompatible polymer brushes on substrates. It is proposed that the degradable polymer brushes can be utilized as a protecting layer that can degrade off from the substrate under suitable conditions to eventually expose the substrate. This dynamic surface can have potential applications such as a biosensor. For example, sensor arrays on a substrate coated with a biodegradable polymer brush with gradient thickness can be gradually activated upon the degradation of the brush. At the same time, resisting nonspecific biomolecule adsorption on the surface is also important for this dynamic surface. Surface grafted biodegradable polyesters, PLA, PGA and PCL are explored as the protecting layers.

In order to achieve the goal, it is essential to have fundamental knowledge about the growth, degradation behaviors of these polyester brushes. Previously, the growth and degradation of PLA brushes have been systematically studied by Xu and coworkers.<sup>105</sup> In this project, the growth and degradation behaviors of PGA and PCL brushes were further tested. Optimal growth conditions for both polyester brushes were established. Degradation of grafted polyester brush and spin coated polyester thin film was investigated under various conditions. In addition, protein adsorption on these three polyester brush surfaces including their co-polymer brushes with OEG and PEG components was examined using BSA as a model protein. Fabrication of polyester brush with both degradability and anti-fouling properties was demonstrated.

## REFERENCES

1. (a) Lue, S. J.; Hsu, J.-J.; Wei, T.-C., Drug permeation modeling through the thermo-sensitive membranes of poly(N-isopropylacrylamide) brushes grafted onto micro-porous films. *J. Membr. Sci.* 2008, *321* (2), 146-154; (b) Nagase, K.; Kobayashi, J.; Kikuchi, A.; Akiyama, Y.; Kanazawa, H.; Okano, T., Preparation of thermoresponsive cationic copolymer brush surfaces and application of the surface to separation of biomolecules. *Biomacromolecules* 2008, *9* (4), 1340-7; (c) Zhang, Z.; Chen, S.; Jiang, S., Dual-functional biomimetic materials: Nonfouling poly(carboxybetaine) with active functional groups for protein immobilization. *Biomacromolecules* 2006, *7* (12), 3311-3315.
2. Chen, T.; Ferris, R.; Zhang, J.; Ducker, R.; Zauscher, S., Stimulus-responsive polymer brushes on surfaces: Transduction mechanisms and applications. *Prog. Polym. Sci.* 2010, *35* (1-2), 94-112.
3. (a) Ahn, S.-k.; Kasi, R. M.; Kim, S.-C.; Sharma, N.; Zhou, Y., Stimuli-responsive polymer gels. *Soft Matter* 2008, *4* (6), 1151-1157; (b) Tokarev, I.; Minko, S., Stimuli-responsive hydrogel thin films. *Soft Matter* 2009, *5* (3), 511-524.
4. Schreiber, F., Self-assembled monolayers: from 'simple' model systems to biofunctionalized interfaces. *J. Phys.: Condens. Matter* 2004, *16* (28), R881-R900.
5. Lahann, J.; Mitragotri, S.; Tran, T. N.; Kaido, H.; Sundaram, J.; Choi, I. S.; Hoffer, S.; Somorjai, G. A.; Langer, R., A reversibly switching surface. *Science (New York, N.Y.)* 2003, *299* (5605), 371-4.
6. Liu, Y.; Mu, L.; Liu, B. H.; Zhang, S.; Yang, P. Y.; Kong, J. L., Controlled protein assembly on a switchable surface. *Chem. Commun.* 2004, (10), 1194-1195.
7. Balamurugan, S.; Ista, L. K.; Yan, J.; López, G. P.; Fick, J.; Himmelhaus, M.; Grunze, M., Reversible protein adsorption and bioadhesion on monolayers terminated with mixtures of oligo(ethylene glycol) and methyl groups. *J. Am. Chem. Soc.* 2005, *127* (42), 14548-14549.
8. (a) Norrman, K.; Ghanbari-Siahkali, A.; Larsen, N. B., 6 Studies of spin-coated polymer films. *Annu. Rep. Prog. Chem., Sect. C: Phys. Chem.* 2005, *101* (0), 174-201; (b)

Zhou, F.; Huck, W. T. S., Surface grafted polymer brushes as ideal building blocks for "smart" surfaces. *Phys. Chem. Chem. Phys.* 2006, 8 (33), 3815-3823.

9. Ionov, L., Actively-moving materials based on stimuli-responsive polymers. *J. Mater. Chem.* 2010, 20 (17), 3382-3390.

10. Merlitz, H.; He, G.-L.; Wu, C.-X.; Sommer, J.-U., Nanoscale brushes: How to build a smart surface coating. *Phys. Rev. Lett.* 2009, 102 (11), 115702.

11. (a) Sun, T.; Wang, G.; Feng, L.; Liu, B.; Ma, Y.; Jiang, L.; Zhu, D., Reversible Switching between Superhydrophilicity and Superhydrophobicity. *Angew. Chem. Int. Ed.* 2004, 43 (3), 357-360; (b) Schild, H. G., Poly(N-isopropylacrylamide): experiment, theory and application. *Prog. Polym. Sci.* 1992, 17 (2), 163-249.

12. Zhou, F.; Huck, W. T. S., Three-stage switching of surface wetting using phosphate-bearing polymer brushes. *Chem. Commun.* 2005, (48), 5999-6001.

13. Kumar Vyas, M.; Schneider, K.; Nandan, B.; Stamm, M., Switching of friction by binary polymer brushes. *Soft Matter* 2008, 4 (5), 1024-1032.

14. (a) Higuchi, A.; Hamamura, A.; Shindo, Y.; Kitamura, H.; Yoon, B. O.; Mori, T.; Uyama, T.; Umezawa, A., Photon-modulated changes of cell attachments on poly(spiropyran-co-methyl methacrylate) membranes. *Biomacromolecules* 2004, 5 (5), 1770-1774; (b) Miller, L. L.; Zhou, X. Q., Poly(N-methylpyrrolylium) poly(styrenesulfonate) - a conductive, electrically switchable cation exchanger that cathodically binds and anodically releases dopamine. *Macromolecules* 1987, 20 (7), 1594-1597.

15. Azzaroni, O.; Brown, A. A.; Huck, W. T. S., Tunable wettability by clicking counterions into polyelectrolyte brushes. *Adv. Mater.* 2007, 19 (1), 151-154.

16. Xia, F.; Ge, H.; Hou, Y.; Sun, T.; Chen, L.; Zhang, G.; Jiang, L., Multiresponsive surfaces change between superhydrophilicity and superhydrophobicity. *Adv. Mater.* 2007, 19 (18), 2520-2524.

17. George, P. M.; LaVan, D. A.; Burdick, J. A.; Chen, C. Y.; Liang, E.; Langer, R., Electrically controlled drug delivery from biotin-doped conductive polypyrrole. *Adv. Mater.* 2006, *18* (5), 577-581.
18. Peng, Y.; Jiang, D.; Su, L.; Zhang, L.; Yan, M.; Du, J.; Lu, Y.; Liu, Y.-N.; Zhou, F., Mixed monolayers of ferrocenylalkanethiol and encapsulated horseradish peroxidase for sensitive and durable electrochemical detection of hydrogen peroxide. *Anal. Chem.* 2009, *81* (24), 9985-9992.
19. Kushida, A.; Yamato, M.; Konno, C.; Kikuchi, A.; Sakurai, Y.; Okano, T., Decrease in culture temperature releases monolayer endothelial cell sheets together with deposited fibronectin matrix from temperature-responsive culture surfaces. *J. Biomed. Mater. Res.* 1999, *45* (4), 355-62.
20. Synytska, A.; Stamm, M.; Diez, S.; Ionov, L., Simple and fast method for the fabrication of switchable bicomponent micropatterned polymer surfaces. *Langmuir* 2007, *23* (9), 5205-5209.
21. (a) Franz, S.; Rammelt, S.; Scharnweber, D.; Simon, J. C., Immune responses to implants – A review of the implications for the design of immunomodulatory biomaterials. *Biomaterials* 2011, *32* (28), 6692-6709; (b) Shen, M.; Martinson, L.; Wagner, M. S.; Castner, D. G.; Ratner, B. D.; Horbett, T. A., PEO-like plasma polymerized tetraglyme surface interactions with leukocytes and proteins: in vitro and in vivo studies. *J. Biomater. Sci., Polym. Ed.* 2002, *13* (4), 367-390.
22. (a) Nath, N.; Hyun, J.; Ma, H.; Chilkoti, A., Surface engineering strategies for control of protein and cell interactions. *Surf. Sci.* 2004, *570* (1–2), 98-110; (b) Blaszykowski, C.; Sheikh, S.; Thompson, M., Surface chemistry to minimize fouling from blood-based fluids. *Chem. Soc. Rev.* 2012, *41* (17), 5599-5612.
23. Chen, R.; Hunt, J. A., Biomimetic materials processing for tissue-engineering processes. *J. Mater. Chem.* 2007, *17* (38), 3974-3979.
24. Vladkova, T. G., Surface engineered polymeric biomaterials with improved biocontact properties. *Int. J. Polymer. Sci.* 2010, 2010.

25. Nuttelman, C. R.; Mortisen, D. J.; Henry, S. M.; Anseth, K. S., Attachment of fibronectin to poly(vinyl alcohol) hydrogels promotes NIH3T3 cell adhesion, proliferation, and migration. *J. Biomed. Mater. Res.* 2001, *57* (2), 217-223.
26. Li, B.; Chen, J.; Wang, J. H., RGD peptide-conjugated poly(dimethylsiloxane) promotes adhesion, proliferation, and collagen secretion of human fibroblasts. *J. Biomed. Mater. Res., Part A* 2006, *79* (4), 989-98.
27. Ma, Z.; Gao, C.; Gong, Y.; Shen, J., Cartilage tissue engineering PLLA scaffold with surface immobilized collagen and basic fibroblast growth factor. *Biomaterials* 2005, *26* (11), 1253-9.
28. (a) Jenney, C. R.; Anderson, J. M., Effects of surface-coupled polyethylene oxide on human macrophage adhesion and foreign body giant cell formation in vitro. *J. Biomed. Mater. Res.* 1999, *44* (2), 206-216; (b) Deible, C. R.; Petrosko, P.; Johnson, P. C.; Beckman, E. J.; Russell, A. J.; Wagner, W. R., Molecular barriers to biomaterial thrombosis by modification of surface proteins with polyethylene glycol. *Biomaterials* 1998, *19* (20), 1885-1893; (c) Tseng, Y. C.; Park, K., Synthesis of photoreactive poly(ethylene glycol) and its application to the prevention of surface-induced platelet activation. *J. Biomed. Mater. Res.* 1992, *26* (3), 373-391.
29. (a) Jager, M.; Zilkens, C.; Zanger, K.; Krauspe, R., Significance of nano- and microtopography for cell-surface interactions in orthopaedic implants. *J BIOMED BIOTECHNOL* 2007, *2007* (8), 69036; (b) Sigal, G. B.; Mrksich, M.; Whitesides, G. M., Effect of surface wettability on the adsorption of proteins and detergents. *J. Am. Chem. Soc.* 1998, *120* (14), 3464-3473; (c) Malmsten, M.; Emoto, K.; Van Alstine, J. M., Effect of chain density on inhibition of protein adsorption by poly(ethylene glycol) based coatings. *J. Colloid Interface Sci.* 1998, *202* (2), 507-517.
30. Ostuni, E.; Chapman, R. G.; Holmlin, R. E.; Takayama, S.; Whitesides, G. M., A Survey of structure-property relationships of surfaces that resist the adsorption of protein. *Langmuir* 2001, *17* (18), 5605-5620.
31. Wang, R. L. C.; Kreuzer, H. J.; Grunze, M., Molecular Conformation and Solvation of Oligo(ethylene glycol)-Terminated Self-Assembled Monolayers and Their Resistance to Protein Adsorption. *J. Phys. Chem. B* 1997, *101* (47), 9767-9773.

32. Scopelliti, P. E.; Borgonovo, A.; Indrieri, M.; Giorgetti, L.; Bongiorno, G.; Carbone, R.; Podestà, A.; Milani, P., The effect of surface nanometre-scale morphology on protein adsorption. *PLoS ONE* 2010, 5 (7), e11862.
33. Kim J, Y. J., Protein adsorption on polymer particles. In *Encyclopedia of surface and colloid science*, Hubbard, A. T., Ed. Marcel Dekker: New York, 2002; Vol. 4, pp 4373-4381.
34. Brewer, S. H.; Glomm, W. R.; Johnson, M. C.; Knag, M. K.; Franzen, S., Probing BSA binding to citrate-coated gold nanoparticles and surfaces. *Langmuir* 2005, 21 (20), 9303-9307.
35. Halperin, A.; Fragneto, G.; Schollier, A.; Sferrazza, M., Primary versus ternary adsorption of proteins onto PEG brushes. *Langmuir* 2007, 23 (21), 10603-17.
36. (a) Molino, P. J.; Higgins, M. J.; Innis, P. C.; Kapsa, R. M.; Wallace, G. G., Fibronectin and bovine serum albumin adsorption and conformational dynamics on inherently conducting polymers: a QCM-D study. *Langmuir* 2012, 28 (22), 8433-45; (b) Park, J.; Park, J.-H.; Ock, K.-S.; Ganbold, E.-O.; Song, N. W.; Cho, K.; Lee, S. Y.; Joo, S.-W., Preferential adsorption of fetal bovine serum on bare and aromatic thiol-functionalized gold surfaces in cell culture media. *J. Colloid Interface Sci.* 2011, 363 (1), 105-113.
37. (a) Wang, R.; Lajevardi-Khosh, A.; Choi, S.; Chae, J., Regenerative surface plasmon resonance (SPR) biosensor: real-time measurement of fibrinogen in undiluted human serum using the competitive adsorption of proteins. *Biosens Bioelectron* 2011, 28 (1), 304-7; (b) Chang, Y.; Chu, W. L.; Chen, W. Y.; Zheng, J.; Liu, L.; Ruan, R. C.; Higuchi, A., A systematic SPR study of human plasma protein adsorption behavior on the controlled surface packing of self-assembled poly(ethylene oxide) triblock copolymer surfaces. *J. Biomed. Mater. Res., Part A* 2010, 93 (1), 400-8.
38. (a) Kim, T.; Kang, J.; Lee, J. H.; Yoon, J., Influence of attached bacteria and biofilm on double-layer capacitance during biofilm monitoring by electrochemical impedance spectroscopy. *Water Res* 2011, 45 (15), 4615-22; (b) Lata, S.; Piehler, J., Stable and functional immobilization of histidine-tagged proteins via multivalent chelator headgroups on a molecular poly(ethylene glycol) brush. *Anal Chem* 2005, 77 (4), 1096-105.

39. (a) Lei, L.; Li, C.; Yang, P.; Huang, N., Photo-immobilized heparin micropatterns on Ti–O surface: preparation, characterization, and evaluation in vitro. *J. Mater. Sci.* 2011, *46* (21), 6772-6782; (b) Kitano, H.; Kondo, T.; Kamada, T.; Iwanaga, S.; Nakamura, M.; Ohno, K., Anti-biofouling properties of an amphoteric polymer brush constructed on a glass substrate. *Colloids Surf., B* 2011, *88* (1), 455-62; (c) Zhang, Z.; Chao, T.; Chen, S.; Jiang, S., Superlow fouling sulfobetaine and carboxybetaine polymers on glass slides. *Langmuir* 2006, *22* (24), 10072-10077; (d) Holmberg, M.; Hou, X., Competitive protein adsorption--multilayer adsorption and surface induced protein aggregation. *Langmuir* 2009, *25* (4), 2081-9.
40. (a) Banerjee, I.; Pangule, R. C.; Kane, R. S., Antifouling coatings: recent developments in the design of surfaces that prevent fouling by proteins, bacteria, and marine organisms. *Adv. Mater.* 2011, *23* (6), 690-718; (b) Zhao, C.; Li, L.-Y.; Guo, M.-M.; Zheng, J., Functional polymer thin films designed for antifouling materials and biosensors. *Chem. Pap.* 2012, *66* (5), 323-339.
41. (a) Lee, J. H.; Kopeckova, P.; Kopecek, J.; Andrade, J. D., Surface properties of copolymers of alkyl methacrylates with, methoxy (polyethylene oxide) methacrylates and their application as protein-resistant coatings. *Biomaterials* 1990, *11* (7), 455-464; (b) Park, K. D.; Kim, W. G.; Jacobs, H.; Okano, T.; Kim, S. W., Blood compatibility of SUUU-PEO-heparin graft copolymers. *J. Biomed. Mater. Res.* 1992, *26* (6), 739-756; (c) Harder, P.; Grunze, M.; Dahint, R.; Whitesides, G. M.; Laibinis, P. E., Molecular conformation in oligo(ethylene glycol)-terminated self-assembled monolayers on gold and silver surfaces determines their ability to resist protein adsorption. *J. Phys. Chem. B* 1998, *102* (2), 426-436.
42. Hucknall, A.; Rangarajan, S.; Chilkoti, A., In pursuit of zero: polymer brushes that resist the adsorption of proteins. *Adv. Mater.* 2009, *21* (23), 2441-2446.
43. Zhang, F.; Kang, E. T.; Neoh, K. G.; Huang, W., Modification of gold surface by grafting of poly(ethylene glycol) for reduction in protein adsorption and platelet adhesion. *J. Biomater. Sci., Polym. Ed.* 2001, *12* (5), 515-31.
44. Grafahrend, D.; Calvet, J. L.; Klinkhammer, K.; Salber, J.; Dalton, P. D.; Moller, M.; Klee, D., Control of protein adsorption on functionalized electrospun fibers. *Biotechnol Bioeng* 2008, *101* (3), 609-21.

45. Grafahrend, D.; Heffels, K. H.; Beer, M. V.; Gasteier, P.; Moller, M.; Boehm, G.; Dalton, P. D.; Groll, J., Degradable polyester scaffolds with controlled surface chemistry combining minimal protein adsorption with specific bioactivation. *Nat Mater* 2011, *10* (1), 67-73.
46. Lestelius, M.; Tengvall, P.; Lundström, I., Features of plasma protein adsorption onto glutathione immobilized on gold. *J. Colloid Interface Sci.* 1995, *171* (2), 533-535.
47. Bolduc, O. R.; Lambert-Lanteigne, P.; Colin, D. Y.; Zhao, S. S.; Proulx, C.; Boeglin, D.; Lubell, W. D.; Pelletier, J. N.; Fethiere, J.; Ong, H.; Masson, J.-F., Modified peptide monolayer binding His-tagged biomolecules for small ligand screening with SPR biosensors. *Analyst* 2011, *136* (15), 3142-3148.
48. (a) Ladd, J.; Zhang, Z.; Chen, S.; Hower, J. C.; Jiang, S., Zwitterionic polymers exhibiting high resistance to nonspecific protein adsorption from human serum and plasma. *Biomacromolecules* 2008, *9* (5), 1357-1361; (b) Chang, Y.; Shu, S.-H.; Shih, Y.-J.; Chu, C.-W.; Ruaan, R.-C.; Chen, W.-Y., Hemocompatible mixed-charge copolymer brushes of pseudozwitterionic surfaces resistant to nonspecific plasma protein fouling. *Langmuir* 2009, *26* (5), 3522-3530; (c) Vaisocherová, H.; Yang, W.; Zhang, Z.; Cao, Z.; Cheng, G.; Piliarik, M.; Homola, J. i.; Jiang, S., Ultralow fouling and functionalizable surface chemistry based on a zwitterionic polymer enabling sensitive and specific protein detection in undiluted blood plasma. *Anal. Chem.* 2008, *80* (20), 7894-7901.
49. Zhao, B.; Brittain, W. J., Polymer brushes: surface-immobilized macromolecules. *Prog. Polym. Sci.* 2000, *25* (5), 677-710.
50. (a) Netz, R. R.; Schick, M., Polymer brushes: From self-consistent field theory to classical theory. *Macromolecules* 1998, *31* (15), 5105-5122; (b) Ismagilov, R. F.; Rosmarin, D.; Kenis, P. J. A.; Chiu, D. T.; Zhang, W.; Stone, H. A.; Whitesides, G. M., Pressure-driven laminar flow in tangential microchannels: an elastomeric microfluidic switch. *Anal. Chem.* 2001, *73* (19), 4682-4687; (c) Raviv, U.; Giasson, S.; Kampf, N.; Gohy, J. F.; Jerome, R.; Klein, J., Lubrication by charged polymers. *Nature* 2003, *425* (6954), 163-165.
51. (a) Kent, M. S., A quantitative study of tethered chains in various solution conditions using Langmuir diblock copolymer monolayers. *Macromol. Rapid Commun.* 2000, *21* (6), 243-270; (b) Zheng, J. X.; Xiong, H.; Chen, W. Y.; Lee, K.; Van Horn, R. M.; Quirk, R. P.; Lotz, B.; Thomas, E. L.; Shi, A.-C.; Cheng, S. Z. D., Onsets of tethered chain overcrowding

and highly stretched brush regime via crystalline–amorphous diblock copolymers. *Macromolecules* 2005, 39 (2), 641-650; (c) Wu, T.; Efimenko, K.; Genzer, J., Combinatorial study of the mushroom-to-brush crossover in surface anchored polyacrylamide. *J. Am. Chem. Soc.* 2002, 124 (32), 9394-9395.

52. Brittain, W. J.; Minko, S., A structural definition of polymer brushes. *J. Polym. Sci., Part A: Polym. Chem.* 2007, 45 (16), 3505-3512.

53. Yerushalmi-Rozen, R.; Klein, J.; Fetters, L. J., Suppression of rupture in thin, nonwetting liquid films. *Science (New York, N.Y.)* 1994, 263 (5148), 793-5.

54. Koutsos, V.; van der Vegte, E. W.; Hadziioannou, G., Direct view of structural regimes of end-grafted polymer monolayers: a scanning force microscopy study. *Macromolecules* 1999, 32 (4), 1233-1236.

55. Mansky, P.; Liu, Y.; Huang, E.; Russell, T. P.; Hawker, C. J., Controlling polymer-surface interactions with random copolymer brushes. *Science (New York, N.Y.)* 1997, 275 (5305), 1458-1460.

56. Ionov, L.; Zdyrko, B.; Sidorenko, A.; Minko, S.; Klep, V.; Luzinov, I.; Stamm, M., Gradient polymer layers by “grafting To” approach. *Macromol. Rapid Commun.* 2004, 25 (1), 360-365.

57. Zana, R., Dimeric and oligomeric surfactants. Behavior at interfaces and in aqueous solution: a review. *Adv. Colloid Interface Sci.* 2002, 97 (1–3), 205-253.

58. Prucker, O.; Rühle, J., Synthesis of poly(styrene) monolayers attached to high surface area silica gels through self-assembled monolayers of azo initiators. *Macromolecules* 1998, 31 (3), 592-601.

59. Kim, J.-B.; Huang, W.; Bruening, M. L.; Baker, G. L., Synthesis of triblock copolymer brushes by surface-initiated atom transfer radical polymerization. *Macromolecules* 2002, 35 (14), 5410-5416.

60. Jayachandran, K. N.; Takacs-Cox, A.; Brooks, D. E., Synthesis and characterization of polymer brushes of poly(N,N-dimethylacrylamide) from polystyrene latex by aqueous atom transfer radical polymerization. *Macromolecules* 2002, 35 (11), 4247-4257.
61. Osborne, V. L.; Jones, D. M.; Huck, W. T. S., Controlled growth of triblock polyelectrolyte brushes. *Chem. Commun.* 2002, (17), 1838-1839.
62. Advincula, R.; Zhou, Q.; Park, M.; Wang, S.; Mays, J.; Sakellariou, G.; Pispas, S.; Hadjichristidis, N., Polymer brushes by living anionic surface initiated polymerization on flat silicon (SiO<sub>x</sub>) and gold surfaces: homopolymers and block copolymers. *Langmuir* 2002, 18 (22), 8672-8684.
63. Zhao, B.; Brittain, W. J., Synthesis of polystyrene brushes on silicate substrates via carbocationic polymerization from self-assembled monolayers. *Macromolecules* 1999, 33 (2), 342-348.
64. (a) Möller, M.; Nederberg, F.; Lim, L. S.; Kånge, R.; Hawker, C. J.; Hedrick, J. L.; Gu, Y.; Shah, R.; Abbott, N. L., Stannous(II) trifluoromethane sulfonate: a versatile catalyst for the controlled ring-opening polymerization of lactides: Formation of stereoregular surfaces from polylactide "brushes". *J. Polym. Sci., Part A: Polym. Chem.* 2001, 39 (20), 3529-3538; (b) Yoon, K.; Kim, Y.; Choi, I., Mechanistic study on Sn(Oct)<sub>2</sub>-catalyzed, ring-opening polymerization of p-dioxanone by surface-initiated polymerization and x-ray photoelectron spectroscopy. *J. Polym. Res.* 2005, 11 (4), 265-268.
65. (a) Moon, J.-H.; Ramaraj, B.; Lee, S. M.; Yoon, K. R., Direct grafting of  $\epsilon$ -caprolactone on solid core/mesoporous shell silica spheres by surface-initiated ring-opening polymerization. *J. Appl. Polym. Sci.* 2008, 107 (4), 2689-2694; (b) Husemann, M.; Mecerreyes, D.; Hawker, C. J.; Hedrick, J. L.; Shah, R.; Abbott, N. L., Surface-initiated polymerization for amplification of self-assembled monolayers patterned by microcontact printing. *Angew. Chem. Int. Ed.* 1999, 38 (5), 647-649.
66. (a) Radhakrishnan, B.; Ranjan, R.; Brittain, W. J., Surface initiated polymerizations from silica nanoparticles. *Soft Matter* 2006, 2 (5), 386-396; (b) Ranjan, R.; Brittain, W. J., Synthesis of high density polymer brushes on nanoparticles by combined RAFT polymerization and click chemistry. *Macromol. Rapid Commun.* 2008, 29 (12-13), 1104-1110.

67. (a) Azzaroni, O.; Brown, A. A.; Cheng, N.; Wei, A.; Jonas, A. M.; Huck, W. T. S., Synthesis of gold nanoparticles inside polyelectrolyte brushes. *J. Mater. Chem.* 2007, *17* (32), 3433-3439; (b) Santer, S.; R uhe, J., Motion of nano-objects on polymer brushes. *Polymer* 2004, *45* (25), 8279-8297.
68. (a) Bruening, M. L.; Dotzauer, D. M.; Jain, P.; Ouyang, L.; Baker, G. L., Creation of functional membranes using polyelectrolyte multilayers and polymer brushes. *Langmuir* 2008, *24* (15), 7663-7673; (b) Jain, P.; Baker, G. L.; Bruening, M. L., Applications of polymer brushes in protein analysis and purification. *Annu. Rev. Anal. Chem.* 2009, *2* (1), 387-408.
69. (a) Tuzlakoglu, K.; Reis, R. L., Biodegradable polymeric fiber structures in tissue engineering. *Tissue Eng Part B Rev* 2009, *15* (1), 17-27; (b) Chiellini, F.; Piras, A. M.; Errico, C.; Chiellini, E., Micro/nanostructured polymeric systems for biomedical and pharmaceutical applications. *Nanomedicine (London, England)* 2008, *3* (3), 367-93; (c) Heller, J., Biodegradable polymers in controlled drug delivery. *Crit Rev Ther Drug Carrier Syst* 1984, *1* (1), 39-90; (d) Ratcliffe, A., Tissue engineering of vascular grafts. *Matrix Biol* 2000, *19* (4), 353-7.
70. Jain, J. P.; Yenet Ayen, W.; Domb, A. J.; Kumar, N., Biodegradable Polymers in Drug Delivery. In *Biodegradable Polymers in Clinical Use and Clinical Development*, John Wiley & Sons, Inc.: 2011; pp 1-58.
71. Kafedjiiski, K.; Krauland, A. H.; Hoffer, M. H.; Bernkop-Schnurch, A., Synthesis and in vitro evaluation of a novel thiolated chitosan. *Biomaterials* 2005, *26* (7), 819-26.
72. (a) Weaver, F. A.; Hood, D. B.; Zatina, M.; Messina, L.; Badduke, B., Gelatin-thrombin-based hemostatic sealant for intraoperative bleeding in vascular surgery. *Annals of vascular surgery* 2002, *16* (3), 286-93; (b) Szpalski, M.; Gunzburg, R.; Sztern, B., An overview of blood-sparing techniques used in spine surgery during the perioperative period. *Eur Spine J* 2004, *13 Suppl 1*, S18-27.
73. Jarrett, P. K.; Casey, D. J.; Lehmann, L. T. Bioabsorbable coating for a surgical article. U.S. Pat. 4791929, December, 20th, 1986.

74. Melzoch, K.; Votruba, J.; Habova, V.; Rychtera, M., Lactic acid production in a cell retention continuous culture using lignocellulosic hydrolysate as a substrate. *J. Biotechnol.* 1997, *56* (1), 25-31.
75. (a) Shogren, R. L.; Thompson, A. R.; Felker, F. C.; Harry-Ókuru, R. E.; Gordon, S. H.; Greene, R. V.; Gould, J. M., Polymer compatibility and biodegradation of starch–poly(ethylene-co-acrylic acid)–polyethylene blends. *J. Appl. Polym. Sci.* 1992, *44* (11), 1971-1978; (b) Kolstad, J. J., Crystallization kinetics of poly(L-lactide-co-meso-lactide). *J. Appl. Polym. Sci.* 1996, *62* (7), 1079-1091.
76. (a) Tsuji, H.; Miyauchi, S., Poly(l-lactide): 7. Enzymatic hydrolysis of free and restricted amorphous regions in poly(l-lactide) films with different crystallinities and a fixed crystalline thickness. *Polymer* 2001, *42* (9), 4463-4467; (b) Tsuji, H.; Nakahara, K., Poly(L-lactide). IX. Hydrolysis in acid media. *J. Appl. Polym. Sci.* 2002, *86* (1), 186-194.
77. Lunt, J., Large-scale production, properties and commercial applications of polylactic acid polymers. *Polym. Degrad. Stab.* 1998, *59* (1–3), 145-152.
78. (a) Kimura, T.; Ihara, N.; Ishida, Y.; Saito, Y.; Shimizu, N., Hydrolysis characteristics of biodegradable plastic (Poly Lactic Acid). *J JPN SOC FOOD SCI* 2002, *49* (9), 598-604; (b) Mauduit, J.; Perouse, E.; Vert, M., Hydrolytic degradation of films prepared from blends of high and low molecular weight poly(DL-lactic acid)s. *J. Biomed. Mater. Res.* 1996, *30* (2), 201-7.
79. Varadarajan, S.; Miller, D. J., Catalytic upgrading of fermentation-derived organic acids. *Biotechnol Prog* 1999, *15* (5), 845-854.
80. (a) Södergård, A.; Stolt, M., Properties of lactic acid based polymers and their correlation with composition. *Prog. Polym. Sci.* 2002, *27* (6), 1123-1163; (b) Montes de Oca, H.; Ward, I. M.; Chivers, R. A.; Farrar, D. F., Structure development during crystallization and solid-state processing of poly(glycolic acid). *J. Appl. Polym. Sci.* 2009, *111* (2), 1013-1018; (c) Van de Velde, K.; Kiekens, P., Biopolymers: overview of several properties and consequences on their applications. *Polym. Test.* 2002, *21* (4), 433-442.
81. (a) Vieira, A. C.; Vieira, J. C.; Guedes, R. M.; Marques, A. T., Degradation and Viscoelastic Properties of PLA-PCL, PGA-PCL, PDO and PGA Fibres. In *Advanced*

*Materials Forum V, Pt 1 and 2*, Rosa, L. G.; Margarido, F., Eds. 2010; Vol. 636-637, pp 825-832; (b) Emerich, D. F.; Tracy, M. A.; Ward, K. L.; Figueiredo, M.; Qian, R.; Henschel, C.; Bartus, R. T., Biocompatibility of poly (DL-lactide-co-glycolide) microspheres implanted into the brain. *Cell transplantation* 1999, 8 (1), 47-58; (c) Athanasiou, K. A.; Niederauer, G. G.; Agrawal, C. M., Sterilization, toxicity, biocompatibility and clinical applications of polylactic acid/polyglycolic acid copolymers. *Biomaterials* 1996, 17 (2), 93-102.

82. Amine, H.; Karima, O.; Amine, B.; Belbachir, M.; Meghabar, R., Cationic ring opening polymerization of glycolide catalysed by a montmorillonite clay catalyst. *J. Polym. Res.* 2005, 12 (5), 361-365.

83. (a) Braud, C.; Devarieux, R.; Atlan, A.; Ducos, C.; Michel, V., Capillary zone electrophoresis in normal or reverse polarity separation modes for the analysis of hydroxy acid oligomers in neutral phosphate buffer. *J Chromatogr B Biomed Sci App* 1998, 706 (1), 73-82; (b) Stridsberg, K. M.; Ryner, M.; Albertsson, A. C., Controlled ring-opening polymerization: Polymers with designed macromolecular architecture. In *Degradable Aliphatic Polyesters*, Albertsson, A. C., Ed. Springer-Verlag Berlin: Berlin, 2002; Vol. 157, pp 41-65.

84. Hou, Y.; Chen, J.; Sun, P.; Gan, Z.; Zhang, G., In situ investigations on enzymatic degradation of poly( $\epsilon$ -caprolactone). *Polymer* 2007, 48 (21), 6348-6353.

85. (a) Khanna, A.; Sudha, Y.; Pillai, S.; Rath, S., Molecular modeling studies of poly lactic acid initiation mechanisms. *J Mol Model* 2008, 14 (5), 367-374; (b) Labet, M.; Thielemans, W., Synthesis of polycaprolactone: a review. *Chem Soc Rev* 2009, 38 (12), 3484-504.

86. (a) Möller, M.; Kånge, R.; Hedrick, J. L., Sn(OTf)<sub>2</sub> and Sc(OTf)<sub>3</sub>: Efficient and versatile catalysts for the controlled polymerization of lactones. *J. Polym. Sci., Part A: Polym. Chem.* 2000, 38 (11), 2067-2074; (b) Dechy-Cabaret, O.; Martin-Vaca, B.; Bourissou, D., Controlled ring-opening polymerization of lactide and glycolide. *Chem. Rev.* 2004, 104 (12), 6147-6176.

87. (a) Kowalski, A.; Libiszowski, J.; Biela, T.; Cypryk, M.; Duda, A.; Penczek, S., Kinetics and mechanism of cyclic esters polymerization initiated with tin(II) octoate. Polymerization of  $\epsilon$ -caprolactone and 1,l-lactide co-initiated with primary amines. *Macromolecules* 2005, 38 (20), 8170-8176; (b) Kowalski, A.; Duda, A.; Penczek, S.,

Mechanism of cyclic ester polymerization initiated with tin(II) octoate. 2.† Macromolecules fitted with tin(II) alkoxide species observed directly in MALDI–TOF spectra. *Macromolecules* 2000, 33 (3), 689-695; (c) Jiang, G.; Jones, I. A.; Rudd, C. D.; Walker, G. S., Mechanistic study of Sn(Oct)<sub>2</sub>-catalyzed ε-caprolactone polymerization using Sn(Oct)<sub>2</sub>/BF<sub>3</sub> dual catalyst. *J. Appl. Polym. Sci.* 2009, 114 (1), 658-662.

88. Dong, H.; Wang, H.-d.; Cao, S.-g.; Shen, J.-c., Lipase-catalyzed polymerization of lactones and linear hydroxyesters. *Biotechnol. Lett.* 1998, 20 (10), 905-908.

89. (a) Wang, Y.; Kunioka, M., Ring-opening polymerization of cyclic monomers with aluminum triflate. *Macromol. Symp.* 2005, 224 (1), 193-206; (b) Ko, B.-T.; Lin, C.-C., Efficient “living” and “immortal” polymerization of lactones and diblock copolymer of ε-CL and δ-VL catalyzed by aluminum alkoxides. *Macromolecules* 1999, 32 (25), 8296-8300.

90. Bhaw-Luximon, A.; Jhurry, D.; Motala-Timol, S.; Lochee, Y., Polymerization of ε-caprolactone and its copolymerization with γ-butyrolactone using metal complexes. *Macromol. Symp.* 2005, 231 (1), 60-68.

91. Duda, A.; Penczek, S., Thermodynamics of L-lactide polymerization. Equilibrium monomer concentration. *Macromolecules* 1990, 23 (6), 1636-1639.

92. Hyon, S.-H.; Jamshidi, K.; Ikada, Y., Synthesis of polylactides with different molecular weights. *Biomaterials* 1997, 18 (22), 1503-1508.

93. (a) Wang, Z.; Yu, L.; Ding, M.; Tan, H.; Li, J.; Fu, Q., Preparation and rapid degradation of nontoxic biodegradable polyurethanes based on poly(lactic acid)-poly(ethylene glycol)-poly(lactic acid) and L-lysine diisocyanate. *Polym. Chem.* 2011, 2 (3), 601-607; (b) Gilding, D.; Reed, A., Biodegradable polymers for use in surgery—polyglycolic/poly(lactic acid) homo- and copolymers: 1. *Polymer* 1979, 20 (12), 1459-1464; (c) Li, Y.; Volland, C.; Kissel, T., Biodegradable brush-like graft polymers from poly(D,L-lactide) or poly(D,L-lactide-coglycolide) and charge-modified, hydrophilic dextrans as backbone—in-vitro degradation and controlled releases of hydrophilic macromolecules. *Polymer* 1998, 39 (14), 3087-3097.

94. Choi, I. S.; Langer, R., Surface-initiated polymerization of L-lactide: Coating of solid substrates with a biodegradable polymer. *Macromolecules* 2001, 34 (16), 5361-5363.

95. (a) Jung, J. H.; Ree, M.; Kim, H., Acid- and base-catalyzed hydrolyses of aliphatic polycarbonates and polyesters. *Catal. Today* 2006, *115* (1-4), 283-287; (b) Yoo, J. Y.; Kim, J. M.; Seo, K. S.; Jeong, Y. K.; Lee, H. B.; Khang, G., Characterization of degradation behavior for PLGA in various pH condition by simple liquid chromatography method. *Biomed Mater Eng* 2005, *15* (4), 279-88.
96. (a) van Nostrum, C. F.; Veldhuis, T. F. J.; Bos, G. W.; Hennink, W. E., Hydrolytic degradation of oligo(lactic acid): a kinetic and mechanistic study. *Polymer* 2004, *45* (20), 6779-6787; (b) Schliecker, G.; Schmidt, C.; Fuchs, S.; Kissel, T., Characterization of a homologous series of D,L-lactic acid oligomers; a mechanistic study on the degradation kinetics in vitro. *Biomaterials* 2003, *24* (21), 3835-44; (c) de Jong, S. J.; Arias, E. R.; Rijkers, D. T. S.; van Nostrum, C. F.; Kettenes-van den Bosch, J. J.; Hennink, W. E., New insights into the hydrolytic degradation of poly(lactic acid): participation of the alcohol terminus. *Polymer* 2001, *42* (7), 2795-2802.
97. (a) Shih, C., Chain-end scission in acid catalyzed hydrolysis of poly (d,l-lactide) in solution. *J. Controlled Release* 1995, *34* (1), 9-15; (b) Batycky, R. P.; Hanes, J.; Langer, R.; Edwards, D. A., A theoretical model of erosion and macromolecular drug release from biodegrading microspheres. *J. Pharm. Sci.* 1997, *86* (12), 1464-1477.
98. (a) Li, S.; Garreau, H.; Vert, M., Structure-property relationships in the case of the degradation of massive aliphatic poly-( $\alpha$ -hydroxy acids) in aqueous media. *J. Mater. Sci.: Mater. Med.* 1990, *1* (3), 123-130; (b) Zhang, X. C.; Wyss, U. P.; Pichora, D.; Goosen, M. F. A., An investigation of poly(lactic acid) degradation. *J. Bioact. Compat. Polym* 1994, *9* (1), 80-100; (c) Li, S., Hydrolytic degradation characteristics of aliphatic polyesters derived from lactic and glycolic acids. *J. Biomed. Mater. Res.* 1999, *48* (3), 342-53.
99. (a) Li, S.; McCarthy, S., Further investigations on the hydrolytic degradation of poly (DL-lactide). *Biomaterials* 1999, *20* (1), 35-44; (b) Codari, F.; Lazzari, S.; Soos, M.; Storti, G.; Morbidelli, M.; Moscatelli, D., Kinetics of the hydrolytic degradation of poly(lactic acid). *Polym. Degrad. Stab.* 2012, *97* (11), 2460-2466.
100. (a) Fernández, J.; Larrañaga, A.; Etxeberría, A.; Sarasua, J. R., Effects of chain microstructures and derived crystallization capability on hydrolytic degradation of poly(l-lactide/ $\epsilon$ -caprolactone) copolymers. *Polym. Degrad. Stab.* 2013, *98* (2), 481-489; (b) Loo, S. C.; Ooi, C. P.; Wee, S. H.; Boey, Y. C., Effect of isothermal annealing on the hydrolytic degradation rate of poly(lactide-co-glycolide) (PLGA). *Biomaterials* 2005, *26* (16), 2827-33.

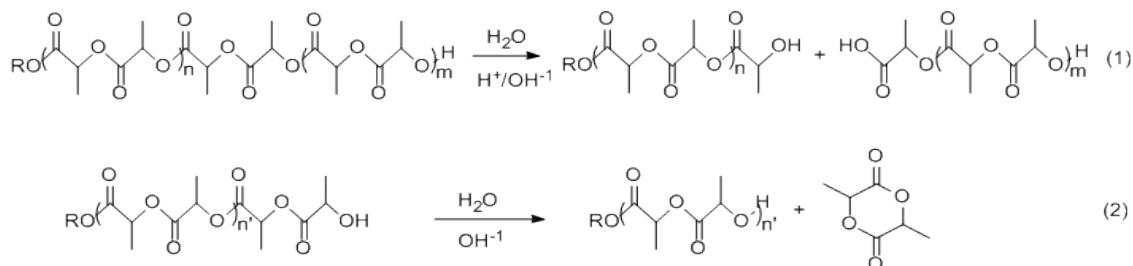
101. Huang, Y.-y.; Qi, M.; Zhang, M.; Liu, H.-z.; Yang, D.-z., Degradation mechanisms of poly (lactic-co-glycolic acid) films in vitro under static and dynamic environment. *Transactions of Nonferrous Metals Society of China* 2006, *16*, Supplement 1, s293-s297.
102. YU, L., Generation of biodegradable polycaprolactone foams in supercritical carbon dioxide. In *Biodegradable polymers for industrial applications*, Smith, R., Ed. CRC Press: Washington, DC, 2005.
103. (a) Jostel, A.; Mukherjee, A.; Alenfall, J.; Smethurst, L.; Shalet, S. M., A new sustained-release preparation of human growth hormone and its pharmacokinetic, pharmacodynamic and safety profile. *Clinical endocrinology* 2005, *62* (5), 623-7; (b) de Medinaceli, L.; al Khoury, R.; Merle, M., Large amounts of polylactic acid in contact with divided nerve sheaths have no adverse effects on regeneration. *J Reconstr Microsurg.* 1995, *11* (1), 43-9; (c) Gautier, S. E.; Oudega, M.; Fragoso, M.; Chapon, P.; Plant, G. W.; Bunge, M. B.; Parel, J. M., Poly(alpha-hydroxyacids) for application in the spinal cord: resorbability and biocompatibility with adult rat Schwann cells and spinal cord. *J. Biomed. Mater. Res.* 1998, *42* (4), 642-54.
104. (a) Jain, R.; Shah, N. H.; Malick, A. W.; Rhodes, C. T., Controlled drug delivery by biodegradable poly(ester) devices: different preparative approaches. *Drug Dev Ind Pharm* 1998, *24* (8), 703-27; (b) Plard, J.-P.; Bazile, D., Comparison of the safety profiles of PLA50 and Me.PEG-PLA50 nanoparticles after single dose intravenous administration to rat. *Colloids Surf., B* 1999, *16* (1-4), 173-183.
105. (a) Xu, L.; Gorman, C. B., Poly(lactic acid) brushes grow longer at lower temperatures. *J. Polym. Sci., Part A: Polym. Chem.* 2010, *48* (15), 3362-3367; (b) Xu, L.; Crawford, K.; Gorman, C. B., Effects of temperature and pH on the degradation of poly(lactic acid) brushes. *Macromolecules* 2011, *44* (12), 4777-4782.

## Chapter 2 Growth and Degradation of PGA and PCL Brushes

### 2.1 Introduction

Polyesters including PLA, PGA and PCL have been very well studied regarding to their synthesis and degradation in solution and in bulk state.<sup>1</sup> However, relatively little effort has been dedicated to the investigation of their brush forms.<sup>2</sup> As polymer brushes are surface-confined structures, they might have distinct properties leading to potential bio-applications. As proposed in Chapter 1, an array of biosensors covered by polyester brushes with gradient thickness might be gradually exposed and activated upon the brush degradation. In order to achieve these applications, it is essential to have basic knowledge about these polyester brushes. For example, it is necessary to establish controllable and reproducible methods for preparing the brushes and methods to detect their degradability under various conditions.

#### Scheme 2.1.1 Degradation of PLA under (1) random chain scission mechanism and (2) backbiting mechanism.



Previously, Xu et al. explored the growth and degradation behaviors of PLA brushes. Controllable growth of PLA brushes through surface initiated ring opening polymerization (SI-ROP) on silicon and gold surfaces was established at room temperature using tin octanoate as the catalyst.<sup>3</sup> PLA brushes were found to be only degradable under neutral and basic conditions.<sup>4</sup> This behavior is different from the degradation of bulk PLA and PLA in solution which can occur under both acidic and basic conditions.<sup>5</sup> Although random chain

scission as described in Chapter 1, is applicable under both acidic and basic conditions (eq. 1, Scheme 2.1); the rate of this process is slower than backbiting process (eq. 2, Scheme 2.1).<sup>6</sup> Also, in Xu's work, the end hydroxyl groups of PLA brushes were shown to be very important during the degradation procedure. Therefore, the backbiting mechanism was proposed for the degradation of PLA brushes.

In this chapter, the reproducibility of growth of PLA brushes under previously optimized conditions was first tested. The effort was then focused on studying the growth of PGA and PCL brushes under varying conditions such as temperature and solvent in order to find the best conditions for growing each type of brush. Furthermore, the effect of pH and temperature on the degradation of PGA and PCL brushes was probed. The degradation mechanism was also investigated. Lastly, the degradation behavior was compared between grafted polyester brushes and spin coated brushes.

## **2.2 Results and Discussion**

### **2.2.1 Reproducibility and Modified Conditions of PLA Brush Growth**

#### **i. PLA Brush Growth under Standardized Conditions**

Before probing the growth and degradation of PGA and PCL brushes, the growth of PLA brushes that had been previously reported was reexamined.<sup>3</sup> PLA brushes were reported to have a controllable and reproducible growth using tin octanoate as the catalyst via SI-ROP at room temperature by Xu et al.<sup>3</sup> Two separate trials were conducted under identical conditions to those previously reported.

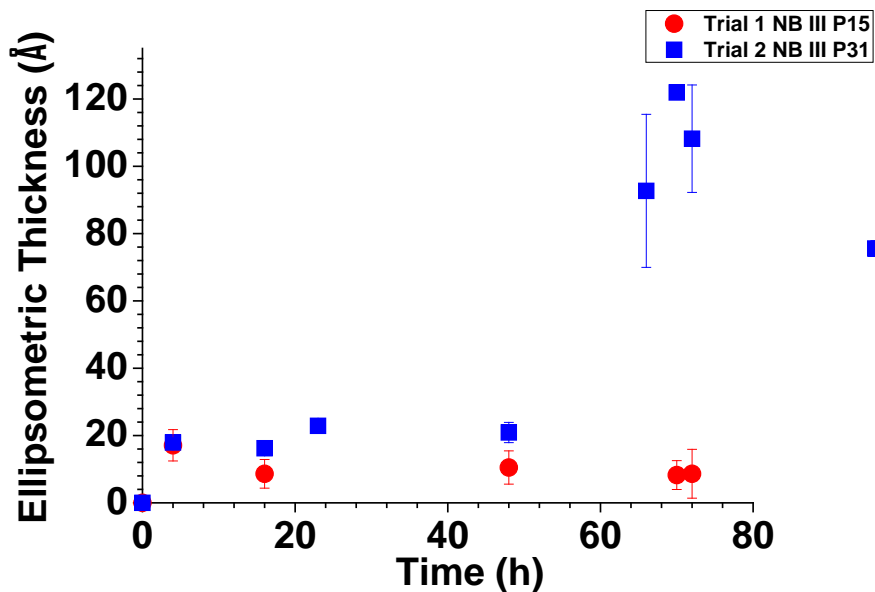


**Figure 2.2.1 Plots of ellipsometric thicknesses of PLA brushes versus growth time at room temperature. Error bars represent the magnitude of the 90% confidence interval for ten measurements on two samples.**

The ellipsometric thicknesses of the PLA brushes with time as the polymerization was carried out are shown in Figure 2.2.1. No significant growth was observed up to almost 60 h reaction for both trials. This contradicts with the previously reported results (Figure 2.2.2). Xu showed a maximum of around ca. 9 nm thickness of PLA brushes after 12 h reaction at room temperature. Before performing the experiment, all the chemicals used for the reaction were carefully purified and characterized with NMR. The reaction procedure was also carefully followed in order to obviate differences in the experimental techniques.

It was hypothesized that the lack of success in reproducing the growth curve of the PLA brushes was resulted from very small differences in the reaction environment. For example, the amount of impurities such as water left in the chemicals after purification or

during the preparation procedure might vary with runs. Thus, more trials were run by adjusting the reaction conditions very cautiously in the following work.

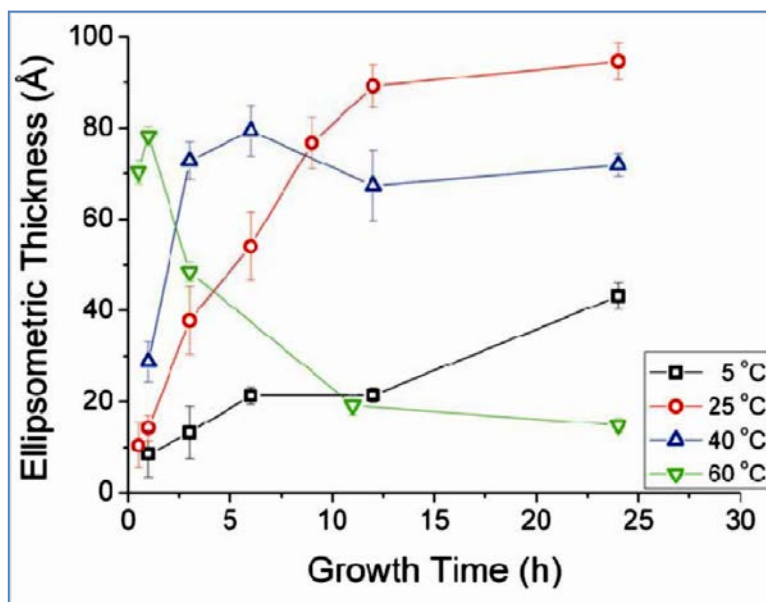
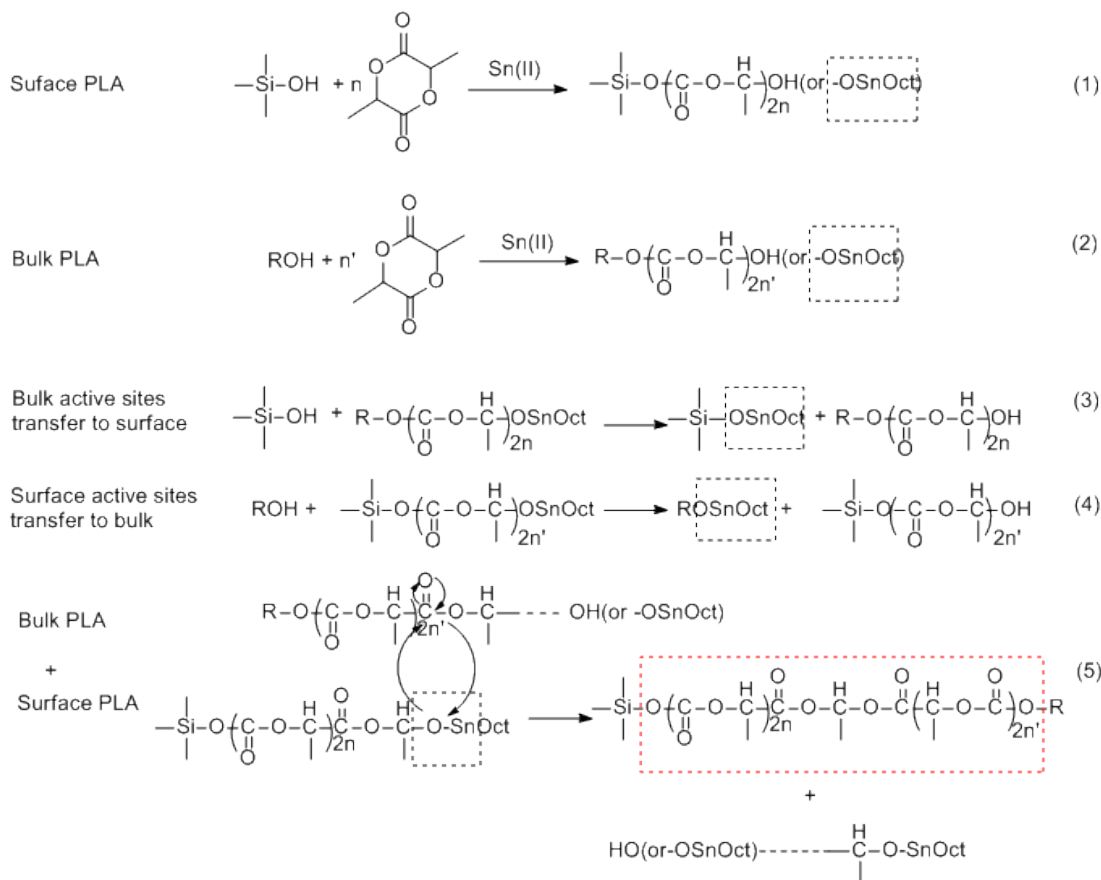


**Figure 2.2.2 Plots of ellipsometric thicknesses of PLA brushes versus growth time at different temperatures. Reaction conditions: [L-lactide] = 0.1 M, [Sn(Oct)<sub>2</sub>] = 0.001 M, 24 h. Error bars represent the magnitude of the 90% confidence interval for five measurements on one samples.<sup>3</sup>**

## ii. PLA Brush Growth under Modified Conditions

The growth of PLA brushes was repeated with the same preparation scheme except that a small amount of deionized (DI) water was added to the reaction vial before it was capped and transferred from the dry box to the incubator. The amount of DI water added to the reaction ranged from 10  $\mu$ L to 1 mL. Comparison of PLA growth with and without addition of water was made by monitoring the thickness of the brush using ellipsometry.

### Scheme 2.2.1 SI-ROP and bulk ROP of PLA.



The growth curve obtained when adding 10  $\mu\text{L}$  DI water replicated the reported results by Xu very well (Figure 2.2.3). However, addition of more than 100  $\mu\text{L}$  DI water resulted in the hindrance of the brush growth which indicates the sensitivity of the SI-ROP to the environmental moisture. The reason for the better growth of PLA brushes upon addition of 10  $\mu\text{L}$  DI water compared to those obtained when either a larger amount of water was added or when water was not added might be explained by the reaction mechanism shown in Scheme 2.2.1. Addition of DI water provided initiators for bulk ROP of PLA that can coexist with SI-ROP (eqs. 1 & 2). If the amount of bulk initiators were larger than the surface silanol initiators such as addition of more than 100  $\mu\text{L}$  DI water, the competition between SI-ROP

and bulk ROP would favor the latter process and the active sites on surface would transfer to bulk (eq. 4). This would end up resulting in more bulk PLA than surface PLA which corresponds to poor growth of PLA brushes with 100  $\mu$ L and 1 mL water added as shown in Figure 2.2.3. However, if the amount of added water was low enough to obviate the equilibrium between SI-ROP and bulk ROP shifting forwards, the transfer of active sites between bulk and surface might be under equilibrium (eqs. 3 & 4). Based on the coordination-insertion mechanism, tin octanoate must be converted into tin alkoxide to initiate the ROP of lactide.<sup>7</sup> Thus, the coexistence of bulk active sites and surface active sites upon polymerization (eqs. 1 & 2) would increase the opportunity of the transfer of bulk PLA to surface PLA (eq. 5). This behavior, in the end, could assist in better growth of the PLA brushes.

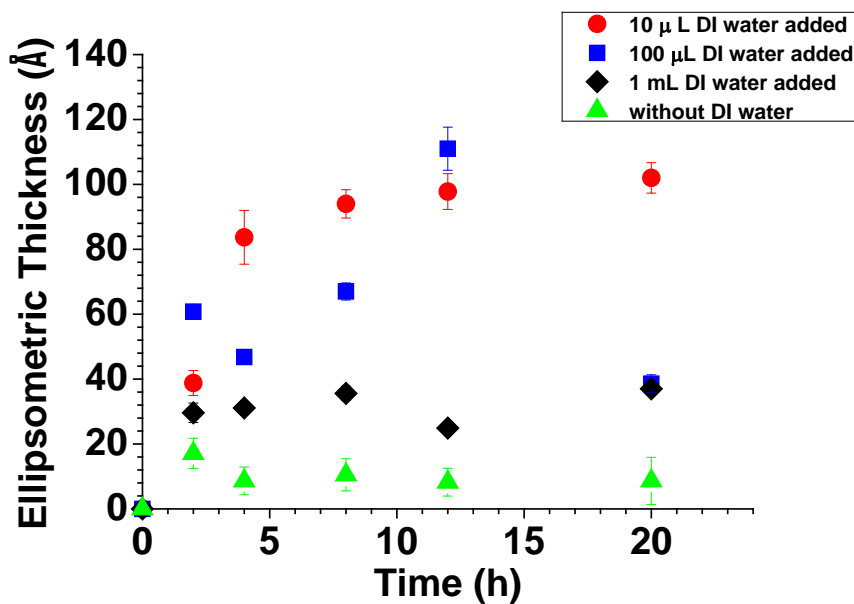
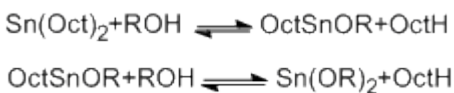


**Figure 2.2.3** Plots of ellipsometric thicknesses of PLA brushes versus growth time at room temperature with and without addition of droplet of DI water. Error bars represent the magnitude of the 90% confidence interval for ten measurements on two samples.

### Scheme 2.2.2 Formation of initiators.



The growth of PLA brushes was also tested under different pH environments. After determining that 10  $\mu\text{L}$  of DI water was the upper limit to assist the growth of PLA brushes, the standard growth conditions were modified by adding 10  $\mu\text{L}$  1 N HCl (aq) or 1 N NaOH (aq) to the reaction vial. The growth of PLA brushes under different pH environments was monitored and compared as shown in Figure 2.2.4. Addition of 10  $\mu\text{L}$  of acid to the reaction completely hindered the PLA growth while addition of base greatly slowed down the process compared to the growth of PLA under neutral conditions. Acid was reported to interfere with the tin(II) catalyst<sup>8</sup> and can suppress the formation of active tin(II) alkoxide. (Scheme 2.2.2) Thus acidic environment was not suitable for the growth of PLA brushes. The addition of base might result in catalyzing the ring opening process of lactide and the degradation of PLA, both of which could lead to slow growth of PLA brushes.

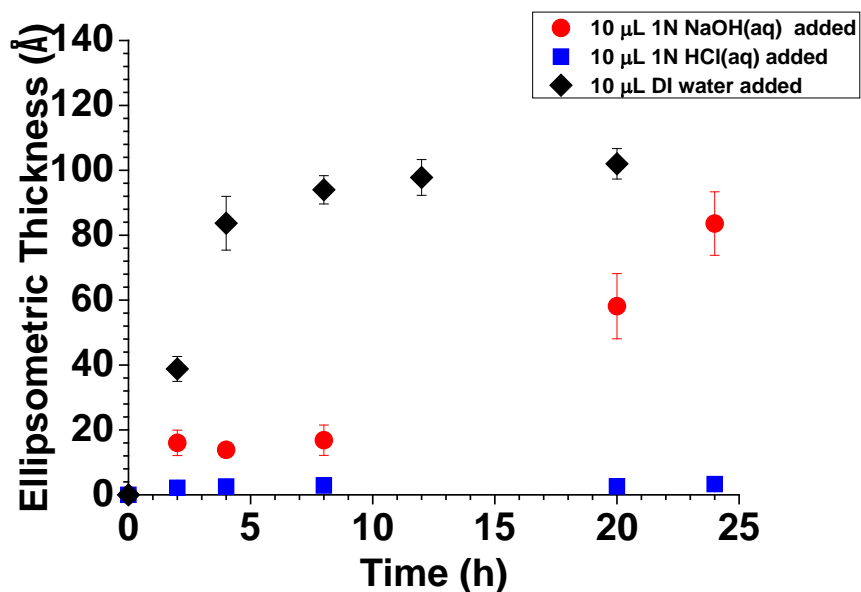


**Figure 2.2.4** Plots of ellipsometric thicknesses of PLA brushes versus growth time at room temperature with addition 10  $\mu\text{L}$  of 1 N NaOH (aq), 1 N HCl (aq) and DI water. Error bars represent the magnitude of the 90% confidence interval for ten measurements on two samples.

Besides water, other nucleophiles such as ethanol was also tested. An aliquot of 10  $\mu\text{L}$  of ethanol was added to the reaction mixture and the growth of PLA brushes was compared as shown in Figure 2.2.5. According to the results, both DI water and ethanol assisted the growth of PLA in a similar fashion which could be explained by the proposed mechanism in Scheme 2.2.1.

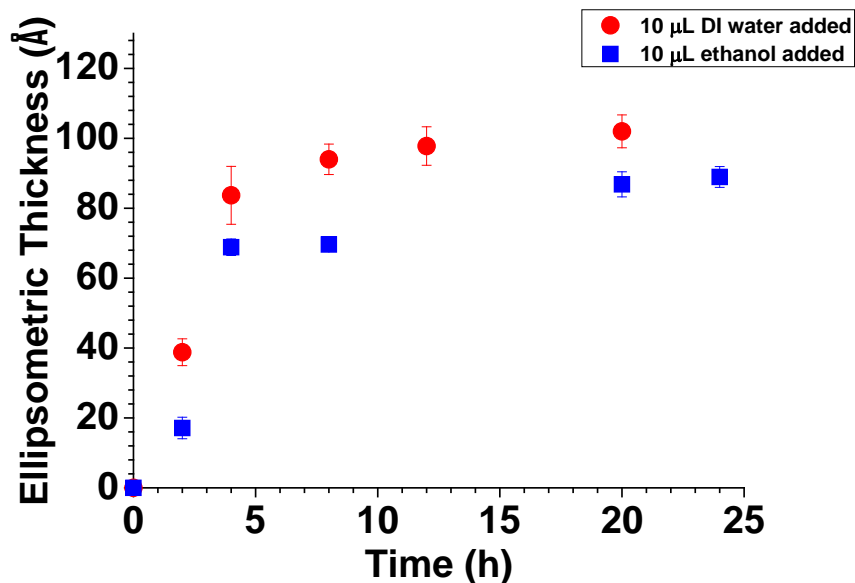


**Figure 2.2.5** Plots of ellipsometric thicknesses of PLA brushes versus growth time at room temperature with addition of 10  $\mu\text{L}$  ethanol and DI water. Error bars represent the magnitude of the 90% confidence interval for ten measurements on two samples.

### iii. PLA Brush Growth on Silicon and Gold Substrates

The growth of PLA brushes was also performed on gold surfaces. These surfaces are better candidates for subsequent electrochemical tests which will be described below. The gold surface was first modified with a SAM of 2-mercaptoethanol to introduce an initiator layer. Then the same conditions as described by Xu were applied for the growth of PLA brushes on gold. According to the results (Figure 2.2.6), the reproducibility of PLA growth on gold was easier to control and it also coincided well with the PLA growth on silicon with addition of 10  $\mu\text{L}$  of DI water. The good reproducibility of PLA growth on gold might be due to the uniformity of the SAM initiators on the surface.<sup>9</sup> The silanol groups on silicon surface were introduced by oxidizing the substrate using UV ozone reactor. The thickness of the oxidized layer was around 17  $\text{\AA}$  indicating multiple oxidized layers. In addition, the cross

linkages between silanols might also increase the porosity of the oxidized layer and reduce the surface uniformity.<sup>10</sup>

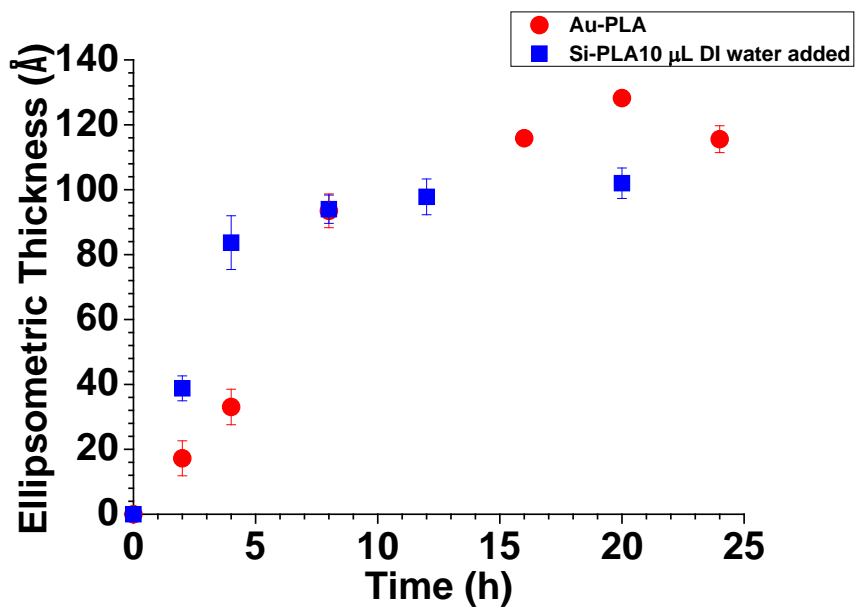


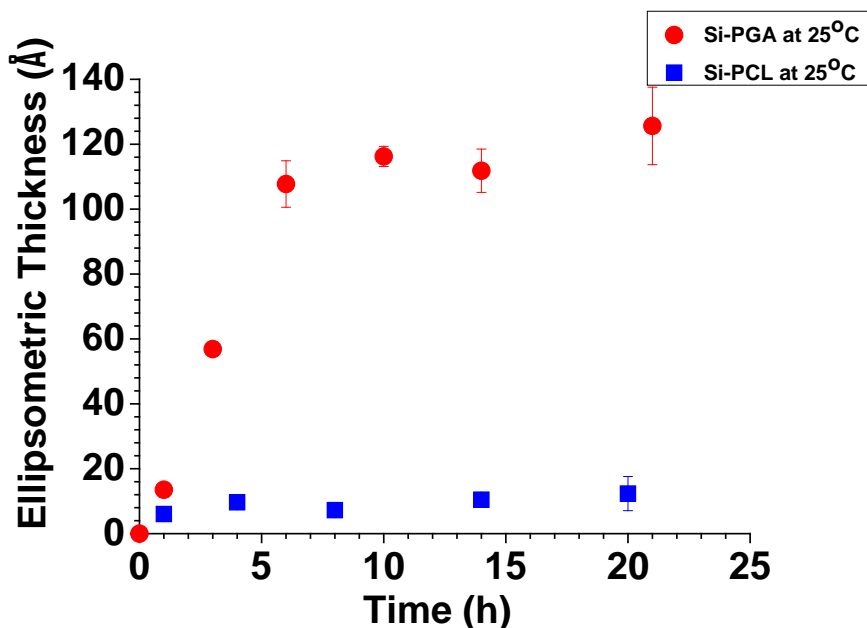
**Figure 2.2.6** Plots of ellipsometric thicknesses of PLA brushes versus growth time at room temperature on silicon and gold substrates. Error bars represent the magnitude of the 90% confidence interval for ten measurements on two samples.

## 2.2.2 Study of the Growth of PGA and PCL Brushes

### i. Growth of PGA and PCL Brushes under Previously Optimized Conditions for PLA Brushes

After the growth trends of PLA brushes on gold and silicon surfaces were successfully reproduced using reported and slightly modified conditions, the growth of PGA and PCL brushes was attempted. The optimal conditions for PLA growth were applied except using GA and  $\epsilon$ -CL as monomers. The purification of these monomers was also different from LA. GA was recrystallized using anhydrous ethyl acetate due to its lower melting point (ca. 81-86 °C) than LA (ca. 95-99 °C).<sup>11</sup> The  $\epsilon$ -CL monomer was distilled under reduced

pressure after being dried over calcium hydride for 24 h at room temperature. All the chemicals were confirmed to be dry by NMR before use. The growth of PGA and PCL was monitored using ellipsometry as a function of growth time at 25 °C.



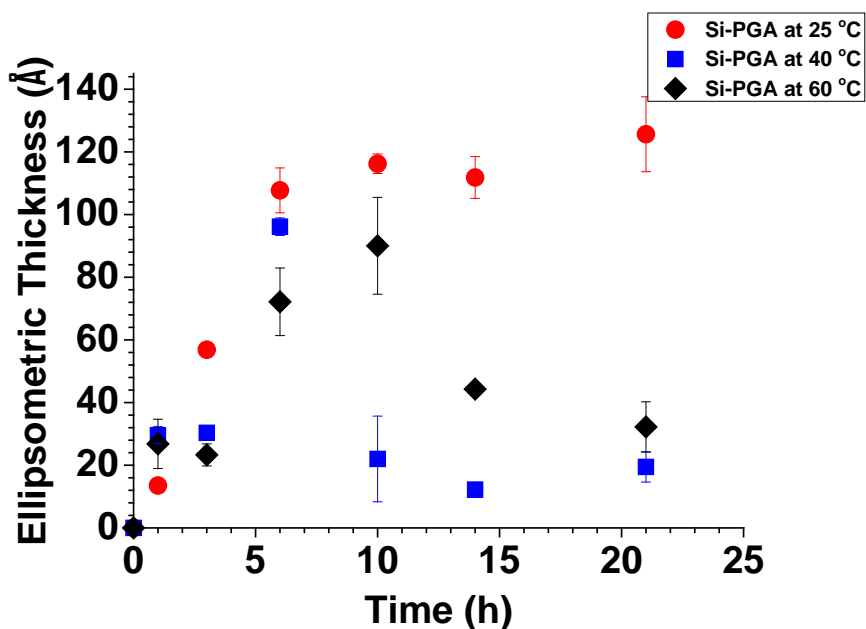
**Figure 2.2.7** Plots of ellipsometric thicknesses of PGA and PCL brushes versus growth time at room temperature. Error bars represent the magnitude of the 90% confidence interval for ten measurements on two samples.

Figure 2.2.7 shows the change in ellipsometric thicknesses of PGA and PCL brushes with growth time under the conditions optimized for the growth of PLA brushes. PGA brushes grew in the same manner as PLA brushes as shown in Figure 2.2.6. The thickness of PGA brushes reached a maximum around 120 Å after 20 h which is only slightly higher than that found for PLA brushes, about 20 Å. Thus the optimal conditions for the growth of PLA brushes are also applicable for growing PGA brushes. However, PCL brushes didn't show any growth at 25 °C. This result might be due to the higher activation barrier of ROP of  $\epsilon$ -CL

than LA and GA which is discussed in detail in the following section.

## ii. Effect of Temperature on the Growth of PGA and PCL Brushes.

After preliminary attempts at growing PGA and PCL brushes under the conditions optimized for PLA brushes, more conditions were investigated by varying the temperature, reaction time and solvent. Since PGA brushes were already shown to have a controllable growth at room temperature within 20 h in THF (Figure 2.2.7), only the reaction temperature was varied (ranging from 25 °C to 60 °C) to confirm this optimal condition. However, PCL brushes were studied at a wider range of temperature (23-100 °C) and a longer reaction time in order to determine the best growth conditions. The growth of both brushes was monitored by measuring the thickness with ellipsometry as the polymerization was carried out.



**Figure 2.2.8 Plots of ellipsometric thicknesses of PGA brushes versus growth time at different temperatures. Error bars represent the magnitude of the 90% confidence interval for ten measurements on two samples.**

Figure 2.2.8 shows the growth of PGA brushes at various temperatures. At elevated

temperatures, such as 40 and 60 °C, an initial increase in thickness followed by a decreasing thickness at longer polymerization times was observed. This phenomenon was very similar to the growth trend of PLA studied by Xu (Figure 2.2.2). It was explained by the shift of equilibrium between polymerization and depolymerization towards the latter process that is favored at elevated temperatures.<sup>4</sup> The similar behavior for PLA and PGA, decreased molecular weight at higher temperatures, was also observed and reported in solution and bulk.<sup>12</sup>

Another observation differentiating the growth of PGA brushes from PLA brushes was that the solution used to prepare the PGA brushes became increasingly cloudy as polymerization proceeded - specifically at longer reaction time and/or at elevated temperatures (Figure 2.2.9). Eventually, noticeable white precipitates were produced, fell on and covered the silicon samples. Although this process occurred more slowly at 25 °C, precipitate can still be formed after a longer reaction time (> 20 h). The precipitate was confirmed to be bulk PGA with IR.

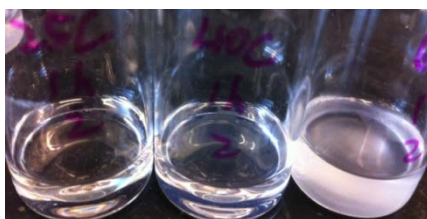
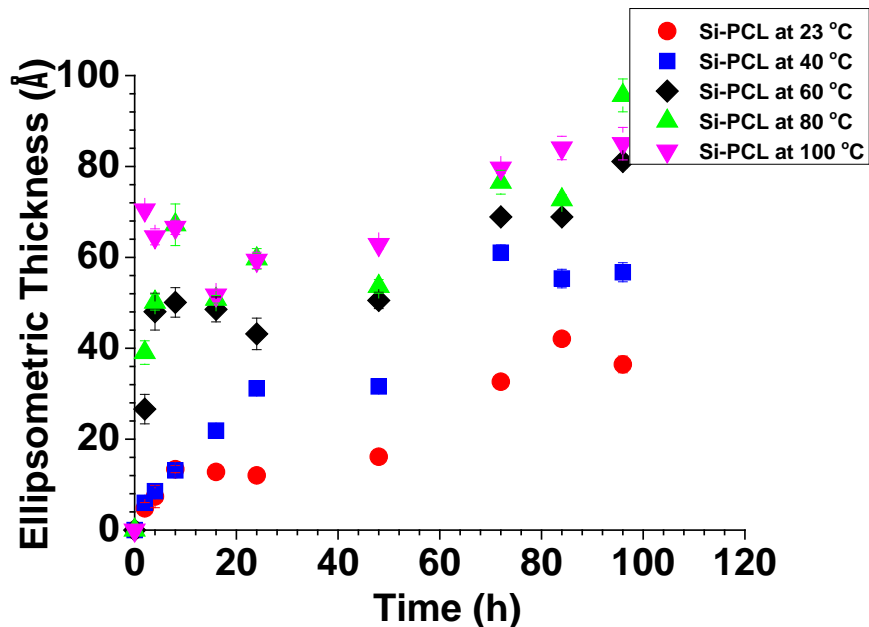


**Figure 2.2.9 Photograph of the reaction vials used for the growth of PGA brushes at (left to right) 25 °C, 40 °C and 60 °C for 1 h.**

This unusual observation can be explained by the poor solubility of bulk PGA in most organic solvents.<sup>13</sup> PGA was reported with a high degree of crystallinity resulting its low solubility in most organic solvents except highly fluorinated organic solvents such as hexafluoroisopropanol.<sup>12a, 14</sup> Its poor solubility might also be due to its hydrophilic nature. Characterization of PGA such as using GPC and NMR is often carried out using these

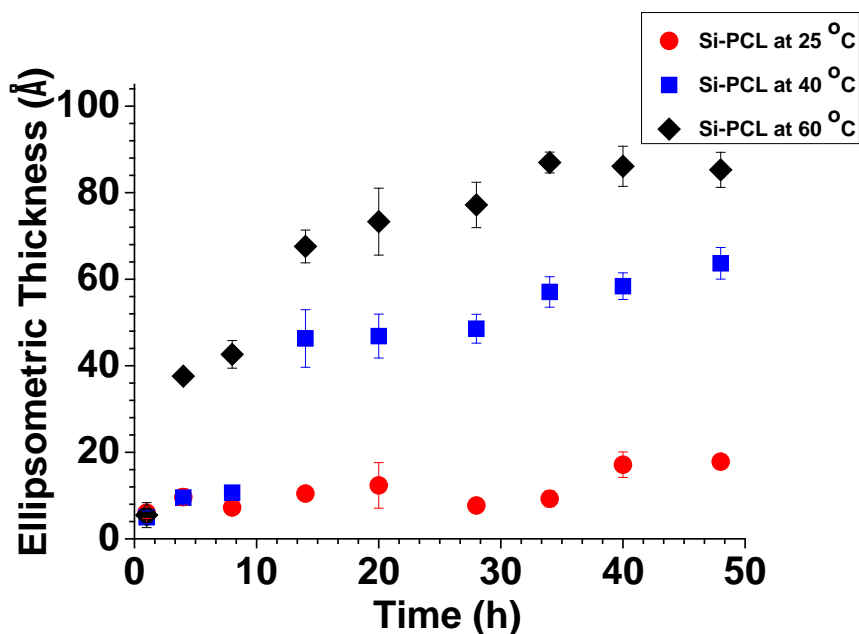
fluorinated organic solvents.<sup>12a, 14</sup> For example, trifluoroacetic acid-d (TFAD) was added to chloroform-d (1:3 weight ratio) in order to dissolve PGA for NMR analysis.<sup>14</sup> The increased solubility of PGA was caused by the coverage of hydrophobic (CF<sub>3</sub>) end on PGA chains through the hydrogen bonding between TFAD and carbonyl oxygen of PGA. This would increase the hydrophobic character of PGA and assist its solubility in chloroform-d. According to these reported observations, the cloudy bulk solution and resulting precipitate at elevated temperatures or longer reaction time at room temperature in our case is reasonable. Moreover, these conditions should be avoided for controllable growth of PGA brushes since further brush growth could be inhibited by the coverage of the bulk precipitate on the surface initiators or active sites.

Figure 2.2.10 shows the preliminary result of ellipsometric thicknesses of PCL brushes with time at various temperatures ranging from 23 °C to 100 °C. A reasonable growth of PCL brushes was only observed when the temperature was raised to 60 °C. A maximum thickness of the resulting brushes, around 80 Å, was achieved after a much longer reaction time than PLA and PGA brushes. After the initial attempt of probing the optimal temperature range of growing PCL brushes, another trial was tested at a smaller temperature range (from 25 °C to 60 °C) to confirm the best growth condition.



**Figure 2.2.10** Plots of ellipsometric thicknesses of PCL brushes versus growth time at different temperatures. Error bars represent the magnitude of the 90% confidence interval for ten measurements on two samples.

As is shown in Figure 2.2.11, the same maximum thickness of PCL brushes (80 Å) was achieved at 60 °C after around 30 h and the result was reproducible. The growth rate was still much slower comparing to PLA and PGA brushes. In addition, the bulk solution prepared for the growth of PCL brushes was clear at all reaction temperatures. No cloudiness or white precipitate was observed as was seen during the growth of PGA brushes.



**Figure 2.2.11** Plots of ellipsometric thicknesses of PCL brushes versus growth time at different temperatures. Error bars represent the magnitude of the 90% confidence interval for ten measurements on two samples.

The slower growth rate of PCL brushes compared to PLA and PGA brushes can be explained by the higher activation barrier for ROP of  $\epsilon$ -CL than LA and GA monomers. Previously, calculations of the kinetics of ROP of  $\epsilon$ -CL and LA monomers using scandium alkoxide as initiators have been performed and reported.<sup>15</sup> The  $\epsilon$ -CL monomer required a higher activation energy, about ca. 6 kcal/mol, than LA to polymerize via ROP. Other researchers concluded that the bulk polymerization of  $\epsilon$ -CL took a much longer reaction time (32 fold) than LA to achieve the same conversion under the same conditions.<sup>16</sup> Therefore, conclusion can be made that LA is more reactive than  $\epsilon$ -CL. Furthermore, GA was reported to be even more active (40%) than LA at the coordination insertion step while using aluminum alkoxides as initiators.<sup>17</sup> Thus, it can be generally stated that  $\epsilon$ -CL is the least reactive among the three monomers. The requirement for higher temperatures and longer

reaction time to achieve a reasonable brush growth is rational.

Different from the growth trend of PLA and PGA brushes at elevated temperatures, no thickness decrease was observed for the growth of PCL brushes. This behavior can be attributed to the larger free enthalpy of polymerization ( $\Delta G_p$ ) of  $\epsilon$ -CL. Based on calculations, the  $\Delta G_p$  of  $\epsilon$ -CL is -12.7 kJ/mol and -10.9 kJ/mol at 25 °C and 60 °C respectively while the  $\Delta G_p$  of LA is only -10.7 kJ/mol at 25 °C and -9.7 kJ/mol at 60 °C. The larger  $\Delta G_p$  of  $\epsilon$ -CL compared to LA can lead to a more unfavorable equilibrium between depolymerization and polymerization.<sup>18</sup> Thus PCL brushes are more stable at elevated temperatures compared to PLA and PGA brushes. The similar trend was also observed for bulk PCL under elevated temperatures. Under these conditions, the molecular weight of PCL also increased.<sup>19</sup>

### **iii. Effect of Solvent on the Growth of PCL Brushes**

In addition to establishing the optimal growth condition for PCL brushes using THF, other solvent systems such as toluene were also investigated. The growth of PCL brushes was first tested at room temperature using monomer/toluene solution. However, the tin (II) catalyst solution was the same as that in previously performed experiments. It was dissolved in anhydrous THF and 20  $\mu$ L of the catalyst solution was added to each reaction vial. Therefore, the reaction system was composed with 5 mL of 0.1 M monomer (in toluene) solution and 20  $\mu$ L of 0.5 M catalyst (in THF) solution. The growth of PCL brushes in toluene at room temperature was monitored with ellipsometry and compared with the growth in THF.

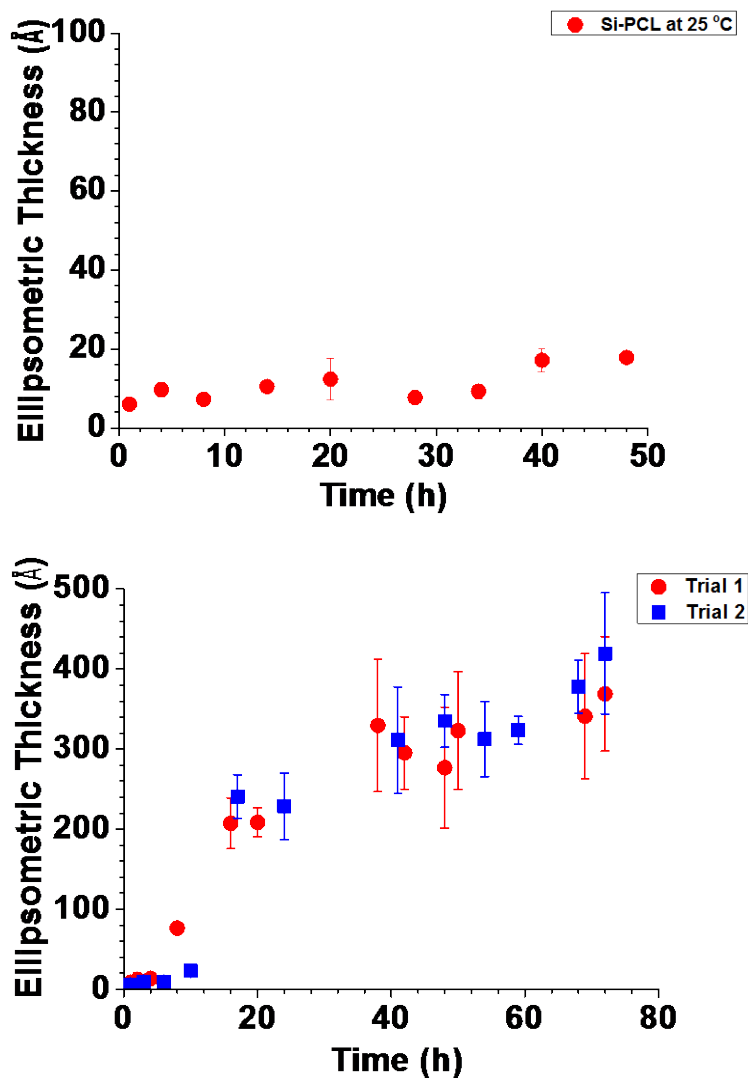


Figure 2.2.12 Plots of ellipsometric thicknesses of PCL brushes versus growth time at room temperature in (top) THF and (bottom) toluene added with 20  $\mu\text{L}$  catalyst (dissolved in THF) solution. Error bars represent the magnitude of the 90% confidence interval for ten measurements on two samples.

Very distinctive results were obtained as shown in Figure 2.2.12. While no growth

was seen after long reaction time in THF at room temperature, PCL showed very dramatic growth in toluene. Separate trials were performed to confirm the reproducibility. As can be seen from Figure 2.2.12, a maximum thickness of PCL brushes, around 400 Å was reached after about 60 h in toluene. This was significantly higher than the maximum thickness of PCL in THF at the corresponding optimal temperature (60 °C). Another different observation was made that the toluene solution used for growing PCL brushes became increasingly cloudy and eventually resulted in white precipitate as seen in Figure 2.2.13. This was confirmed to be bulk PCL using IR. In order to rule out the effect of water contamination, both purified solvents and monomer were examined by NMR, and the results indicated that all chemicals were dry enough for the reactions. Therefore, the different growth result of PCL brushes in toluene from THF was not due to environmental moisture.



**Figure 2.2.13 Photographs of the reaction vials used for the growth of PCL brushes at 25 °C for 48 h in (left )THF and (right) toluene.**

The other difference between reaction of PCL in THF and toluene was the composition of the solutions. The previously used THF solution system was more

homogenous compared to the toluene solution system (mixed with 20  $\mu\text{L}$  of THF) used in this test. In order to verify if the addition of small amount of THF would make such great difference, another trial using just toluene as solvent for dissolving both monomer and catalyst was tested. The result is shown in Figure 2.2.14.

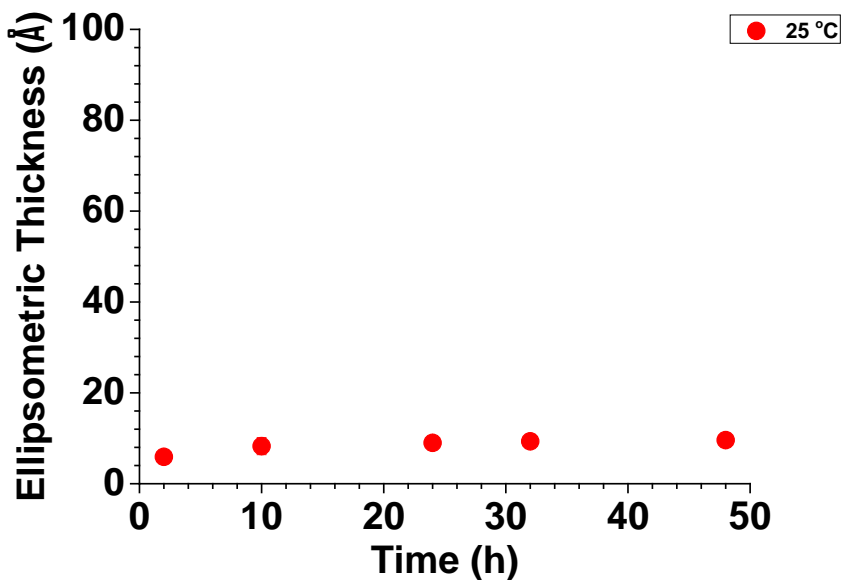


**Figure 2.2.14** Plot of ellipsometric thicknesses of PCL brushes versus growth time at room temperature in toluene added with 20  $\mu\text{L}$  catalyst (dissolved in toluene) solution. Error bars represent the magnitude of the 90% confidence interval for ten measurements on two samples.

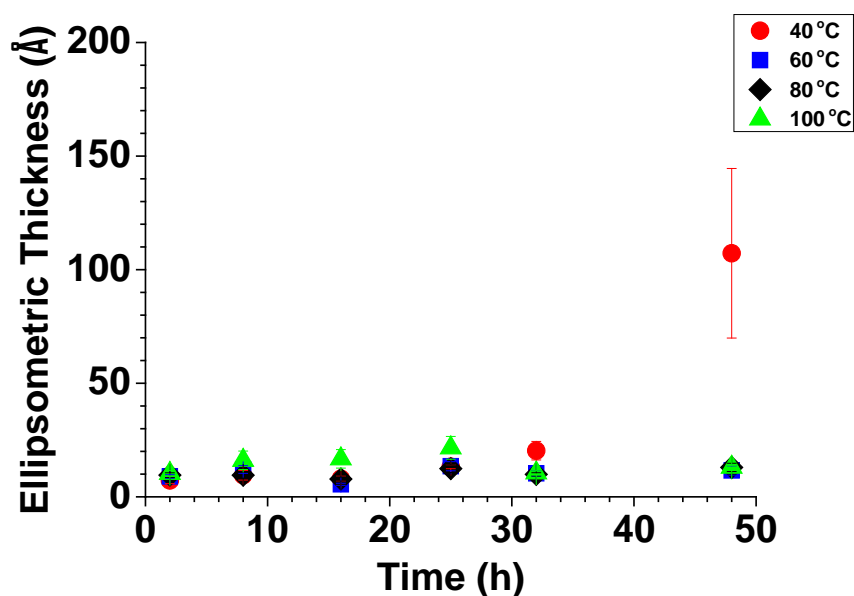


**Figure 2.2.15** Plots of ellipsometric thicknesses of PCL brushes versus growth time at different temperatures in toluene added with 20  $\mu\text{L}$  catalyst (dissolved in THF) solution. Error bars represent the magnitude of the 90% confidence interval for ten measurements on two samples.

After changing the entire solvent system to toluene, no obvious growth of PCL brushes was observed at room temperature up to 50 h. This behavior was similar to the results when growing PCL brushes in pure THF solution at room temperature (Figure 2.2.12). The very distinct result indicated the important role of solvent and temperature in the growth of PCL brushes. As stated previously, elevated temperature was optimal for PCL growth in THF solution. However, room temperature and addition of very small amount of THF were desired for a better growth of PCL brushes in toluene. Elevated temperatures were not suitable for the growth of PCL brushes in toluene as was shown in Figure 2.2.15. The influence of additional THF in toluene on the growth of PCL brushes possibly originated from the reactivity difference of catalyst in different environment. Many different aspects

such as solvent polarity and geometry might affect the catalyst reactivity and conclusion was difficult to make using only one factor.<sup>20</sup> The reason that this mixed solvent system only worked at room temperature might be due to the volatilization of THF (20  $\mu\text{L}$ ) at higher temperatures. Further investigation of PCL growth using toluene as solvent was not performed due to the large variation of the sample thickness in different trials and because the optimal conditions were already established using THF.

### **2.2.3 Degradation Study of PGA and PCL Brushes**

#### **i. Effect of pH on the Degradation of PGA and PCL Brushes**

Degradation of PGA and PCL brushes was first investigated under different pH conditions. Brush samples with similar thicknesses were prepared. Degradation experiments were performed by incubating the brush samples in phosphate buffer solutions (PBS) with adjusted pH values ranging from 3.0 to 8.0 at 37 °C. Periodically samples were removed from the buffer and rinsed thoroughly with DI water. Brush thicknesses were monitored by ellipsometry and results are shown in Figure 2.2.16.

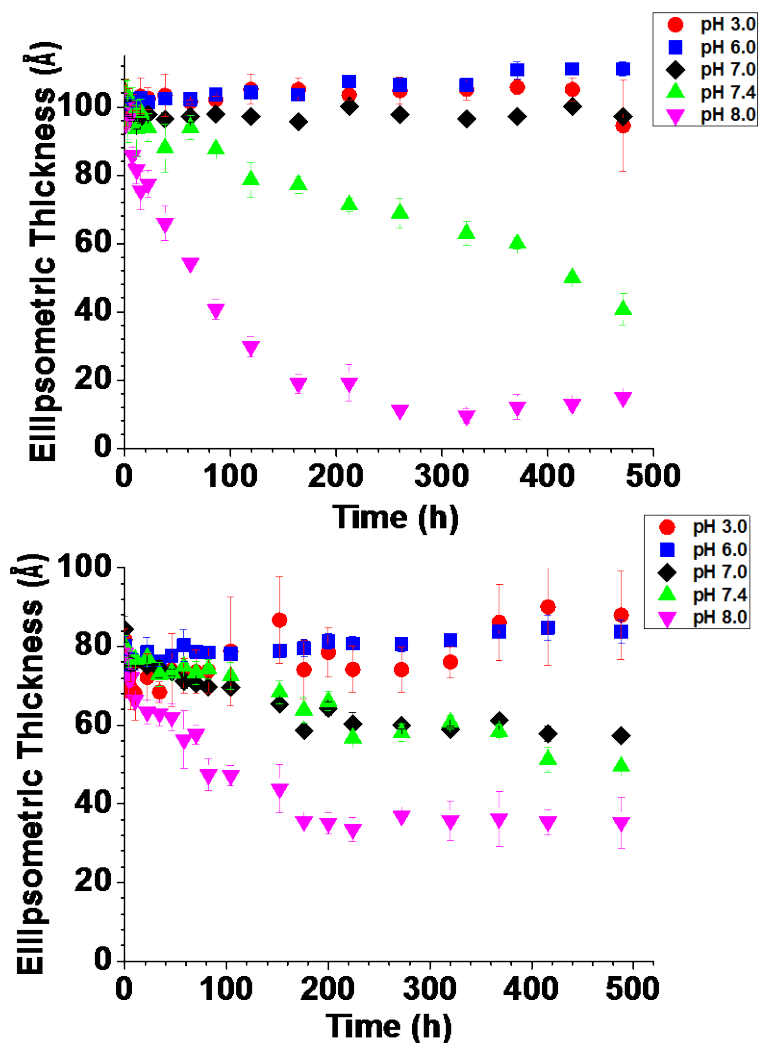
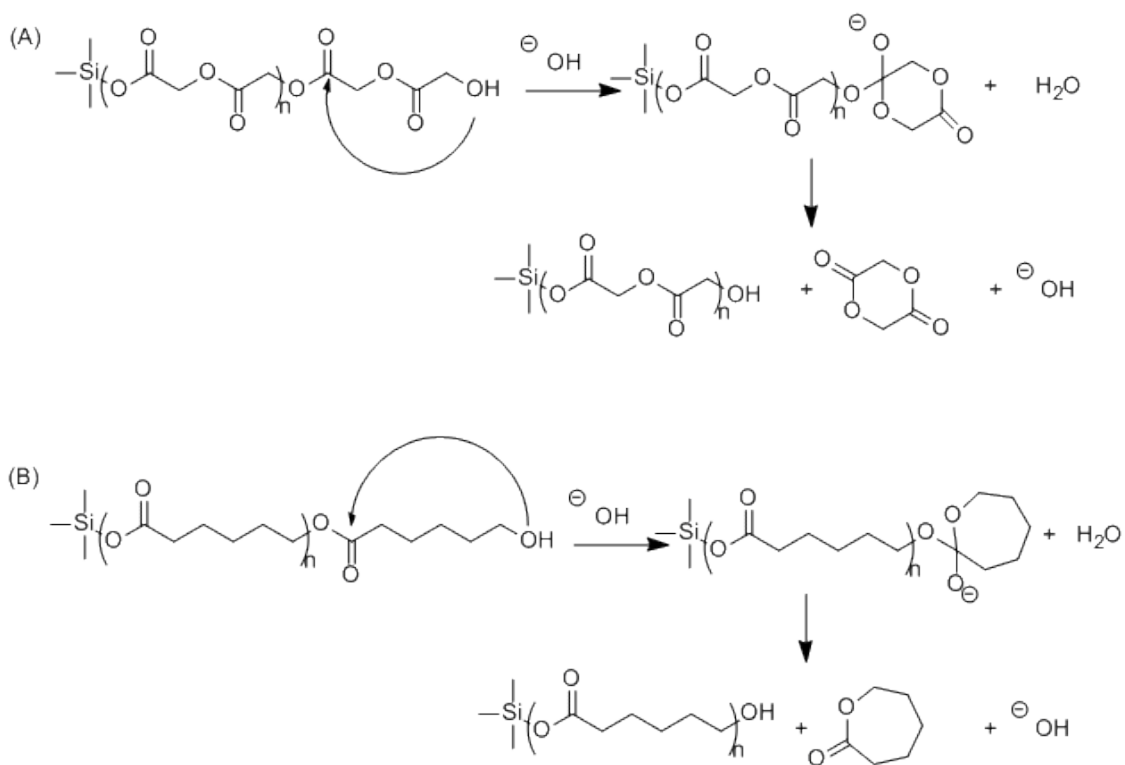


**Figure 2.2.16** Plots of ellipsometric thicknesses of (top) PGA and (bottom) PCL brushes versus degradation time at different pH values. Error bars represent the magnitude of the 90% confidence interval for five measurements on one sample.

The degradation behavior of PGA and PCL brushes was very similar to that of the previously reported PLA brushes.<sup>4</sup> A decrease in thickness was only observed under neutral or

basic pH conditions for both PGA and PCL brushes. In the previous work, this base catalyzed hydrolysis of the polyester brushes was explained by a backbiting mechanism (Scheme 2.2.3).<sup>4</sup> Although random chain scission mechanism is applicable under both acidic and basic catalysis,<sup>5</sup> the rate of this process is much slower than the backbiting.<sup>1d</sup> Therefore, the preferential degradation of PLA, PGA and PCL brushes under basic conditions was mainly attributed to the backbiting mechanism. Further evidence is provided in subsequent work described below.

**Scheme 2.2.3 Hydrolysis of (A) PGA and (B) PCL brushes under basic conditions via backbiting mechanism.**

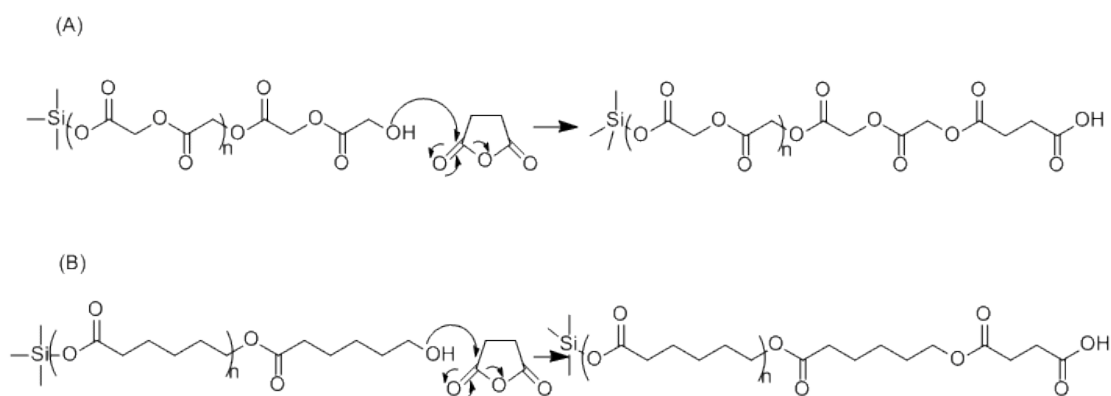


It was noticeable that PGA showed a faster degradation rate than PCL at pH 7.4 and 8.0. For example, PGA showed a decrease in thickness of ca. 6.0 nm after 500 h while PCL

brushes only decreased in thickness by ca. 3.0 nm at pH 7.4. Although the degradation rate of both PGA and PCL brushes increased when pH was raised to 8.0, PGA brushes still showed a more rapid degradation rate than PCL brushes. A ca. 8.0 nm decrease in thickness after 150 h was obtained for PGA brushes compared to a ca. 3.0 nm decrease for PCL brushes. The slower degradation rate of PCL brushes can be ascribed to the larger  $\Delta G_p$  of  $\epsilon$ -CL as described previously. This would result in an unfavorable depolymerization process which led to a slower degradation rate. Different from PCL and PLA brushes that can degrade at pH 7.0, PGA brushes showed no degradation at pH 7.0 after 500 h (Figure 2.2.16). This is possibly due to the rigid property of PGA as stated elsewhere,<sup>13, 21</sup> resulting in the reluctant degradation under milder, basic conditions.

In order to further prove that the backbiting mechanism was the main reason accounting for the degradation of PGA and PCL brushes under basic conditions, a blocking experiment was performed. The end hydroxy groups of PGA and PCL brushes were protected using succinic anhydride (SA) as previously reported (scheme 2.4).<sup>22</sup> Degradation of protected brush samples was then performed under pH 8.0 at 37 °C. Degradation results were compared with non-protected samples as shown in Figure 2.2.17.

**Scheme 2.2.4 Modification of terminal hydroxy groups of (A) PGA and (B) PCL brushes using succinic anhydride.**



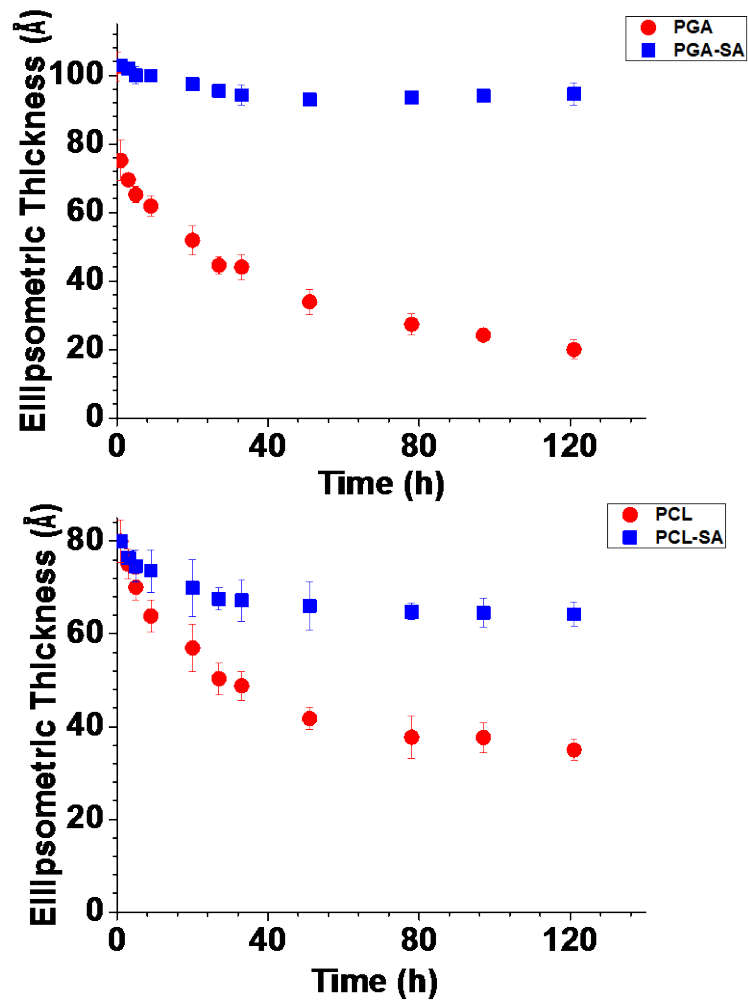


**Figure 2.2.17** Plots of ellipsometric thicknesses of SA blocked and unblocked (top) PGA and (bottom) PCL brushes versus degradation time under pH 8.0 at 37 °C. Error bars represent the magnitude of the 90% confidence interval for five measurements on one sample.

Degradation behaviors of both SA blocked PGA and PCL brushes compared to unblocked brushes were obtained. No obvious thickness decrease was observed for blocked

PGA brushes after 120 h degradation compared to the unblocked PGA brushes, which degraded by ca. 8.0 nm. The thickness of SA blocked PCL brushes decreased around ca. 1 nm after 30 h and then remained constant after 120 h compared to a continuous decrease in thickness of unblocked PCL brushes (ca. 4.0 nm). The reduced degradation rate of both SA blocked PGA and PCL brushes indicated the essential role of the terminal hydroxy groups in basic hydrolysis. The initial thickness decrease of SA blocked PCL brushes might be due to the incomplete coverage of end groups with SA. Nevertheless, backbiting mechanism was shown to be most consistent with the main process of brush degradation under basic conditions.

## **ii. Effect of Temperature on the Degradation of PGA and PCL Brushes**

The effect of temperature on the degradation of PGA and PCL brushes was studied under pH 7.4 at three different temperatures. Thickness of PGA and PCL brushes monitored by ellipsometry over time is shown in Figure 2.2.18. More rapid degradation for both PGA and PCL brushes was observed at elevated temperatures. As expected, under the same temperatures such as physiological conditions (37 °C) and higher temperatures, PCL brushes degraded slower than PGA brushes. This behavior is again ascribed to the larger  $\Delta G_p$  of  $\epsilon$ -CL, resulting in a more unfavorable depolymerization process than PGA.

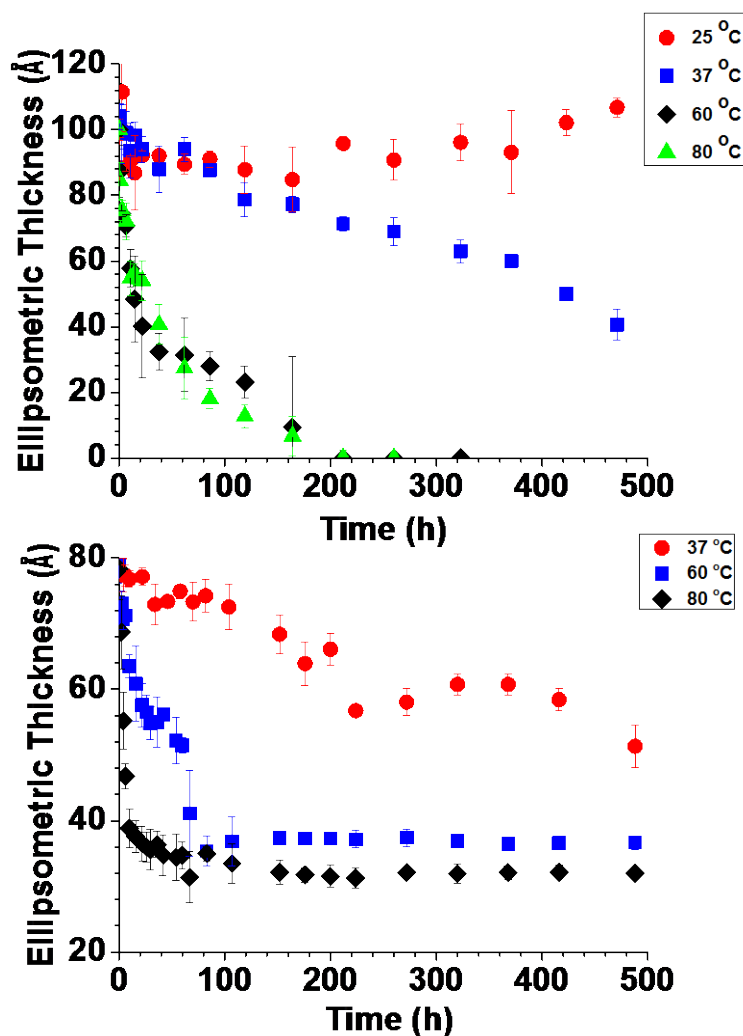


Figure 2.2.18 Plots of ellipsometric thicknesses of (top) PGA and (bottom) PCL brushes versus degradation time at different temperatures. Error bars represent the magnitude of the 90% confidence interval for five measurements on one sample.

### iii. Surface Defects and Degradation Monitored by Cyclic Voltammetry

Besides ellipsometry, cyclic voltammetry (CV) was also conducted to provide complementary information about change in surface properties during the degradation of

grafted PGA, PLA and PCL brushes. Polyester brushes were prepared on gold surface which was then utilized as the working electrode for CV experiments. The brush modified electrode was incubated in pH adjusted electrolyte containing ferricyanide as a redox probe. Peak current density was collected during the linear sweep voltammogram with time as the degradation was proceeded under acidic and basic conditions. Results are shown in Figure 2.2.19.

Under basic conditions, increased peak current density with time was detected for all three polymer brushes. However, little change in peak current density was obtained under acidic conditions. The CV results thus correspond well with conclusions drawn from ellipsometry measurements. The degradation of these polymer brushes led to a gradual exposure of the working electrode surface to the redox probe resulting in increased CV signals. Under acidic conditions, no degradation of the polymer brushes occurred. Thus, the polymer brushes covered on the electrode surface remained unchanged. This behavior results in blocking of the contact of the electrode with the redox couple which leads to little or no change in the CV signals.

The slopes of the peak current density curves under basic conditions indicated the relative degradation rates of the different polymer brushes. The CV curve of PGA brushes showed the steepest slope suggested the largest and fastest increase in peak current density due to degradation. The PCL brushes showed the smallest increase in signal for the same amount of time. This behavior was similar to the degradation result monitored by ellipsometry. In each case, the degradation rate of PGA brushes was faster than that of PCL brushes.

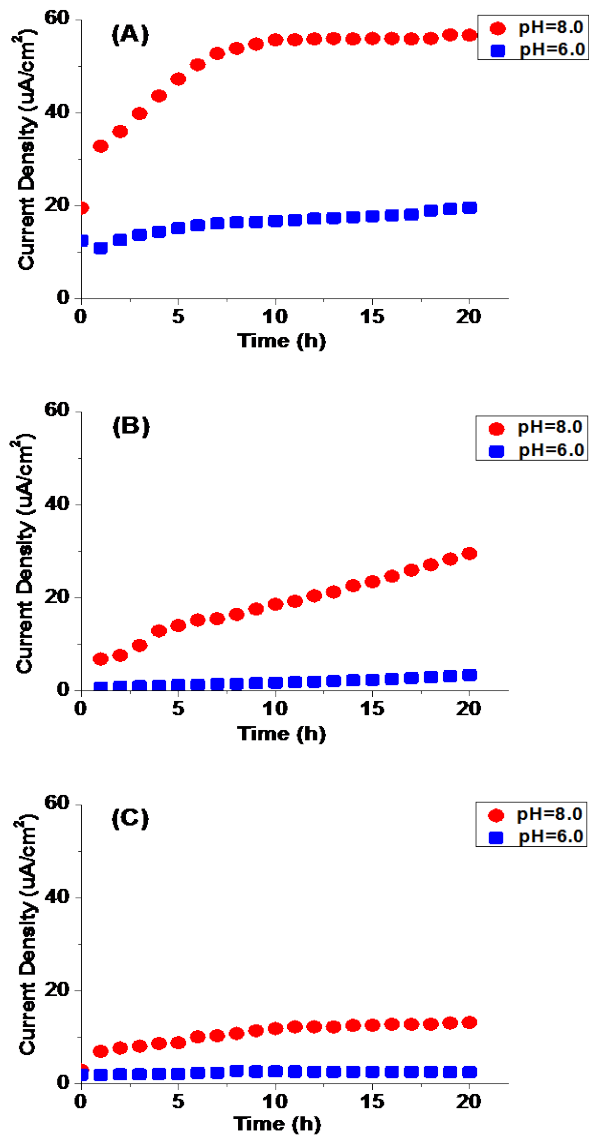


Figure 2.2.19 Plots of maximum current densities versus time at different pH values for grafted (A) PGA, (B) PLA and (C) PCL brushes. These current densities are uncorrected for capacitance (e.g. non-Faradaic) effects.

The electrochemistry results provide additional information during the degradation of polymer brushes. For example, although ellipsometric thickness indicated that PGA brushes degraded completely after about 200 h under pH 8.0, a saturation of increased CV signal was detected after only 8 h. This behavior can result from possible defects on the PGA brush surface such as incomplete coverage of the polymer chains. The existence of the defects on PGA brushes is also indicated by the measurement of a redox current at PGA covered electrode even before any degradation occurred (e.g. under acidic conditions or for very short degradation time under basic conditions). It was noticeable that under acidic conditions, even though the signal was not changed upon time because no degradation occurred, the initial value of the signal was not zero. This behavior is attributed to the much smaller length scale that is probed by a redox probe compared to ellipsometry. The thickness of polymer brushes monitored by ellipsometry was measured over millimeter length scale on the surface while CV detected the accessibility of the polymer brush covered electrode to the redox probe molecules. Thus, the sensitivity of CV is much higher than ellipsometry in monitoring surface morphology and defects.

#### **2.2.4 Comparison of the Degradation of Spin Coated and Grafted Brushes**

##### **i. Effect of pH**

After establishing optimal conditions for the growth of PGA and PCL brushes and probing their degradation behavior at various conditions, further effort was devoted to the study of the degradation behavior of spin coated PGA and PCL brushes. PGA and PCL layers with similar thicknesses to the grafted brushes were prepared via spin coating. Degradation was carried out in both acidic and basic phosphate buffer solutions. The change in brush thickness was monitored by ellipsometry and result was compared with the degradation of grafted brushes.(Figure 2.2.20 and 2.2.21)

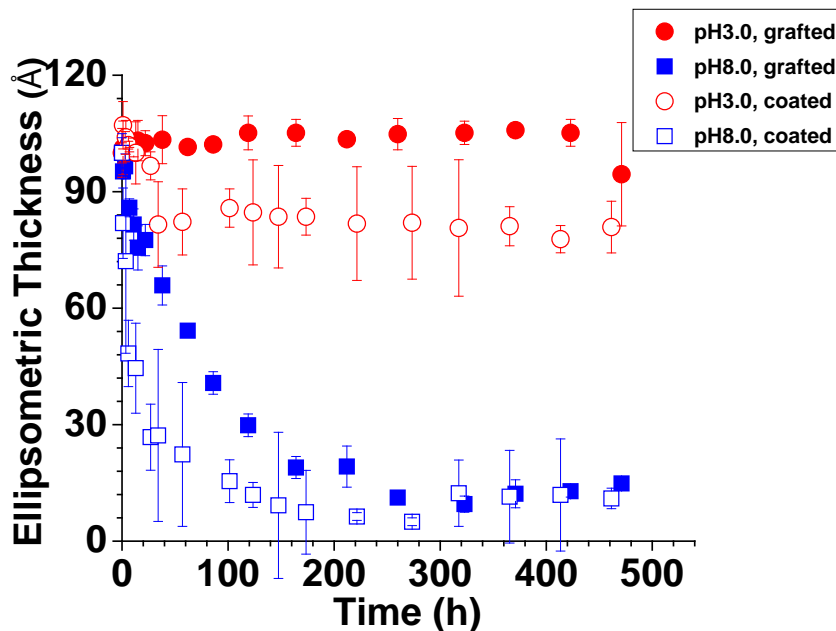


**Figure 2.2.20** Plots of ellipsometric thicknesses of grafted and spin coated PGA brushes versus degradation time at different pH values. Error bars represent the magnitude of the 90% confidence interval for five measurements on one sample.

Spin coated PGA brushes showed a faster degradation under basic conditions (ca. 8.0 nm after 50 h) compared to grafted brushes (ca. 4.5 nm after 50 h). The different degradation behavior between spin coated thin film and grafted brushes can mainly be explained by the different surface morphology.<sup>9a</sup> Grafted brushes are considered to be more orderly oriented than spin coated brushes. During spin coating, the bulk polyesters randomly pack and physisorb on the silicon surface. A randomly packed layer might solvate and desorb faster than a grafted brush which must degrade by breaking covalent bonds.

The degradation behavior of spin coated PGA was assumed to be similar to bulk PGA in PBS.<sup>1f</sup> Thus, both acid and base catalyzed hydrolysis were expected to occur for spin coated brushes. However, under acidic conditions, spin coated PGA brushes only showed a decrease in thickness of approximately 3.0 nm after 40 h. After that period, no further

degradation was observed. This behavior might be explained by the stiffness of bulk PGA polymers and slow solvation process under acidic conditions.<sup>13, 23</sup>

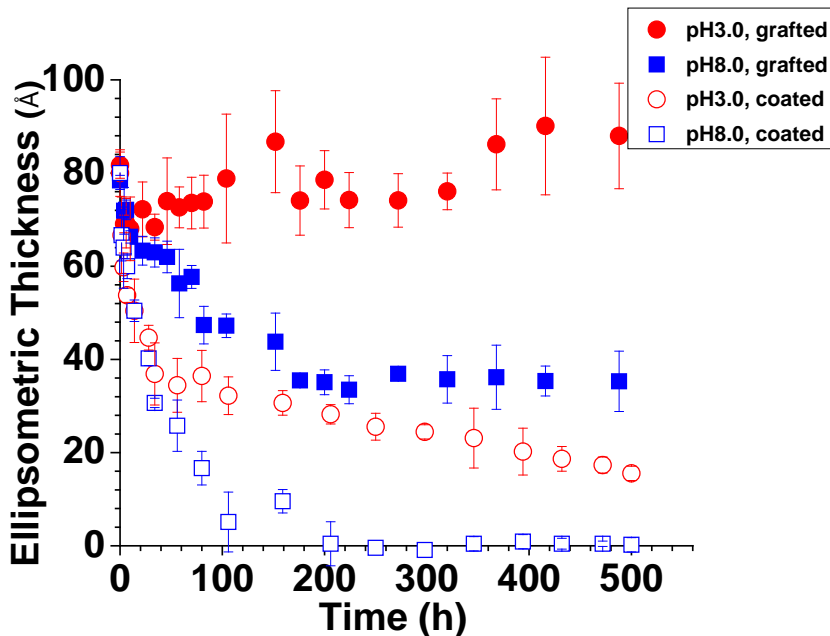


**Figure 2.2.21** Plots of ellipsometric thicknesses of grafted and spin coated PCL brushes versus degradation time under different pH values. Error bars represent the magnitude of the 90% confidence interval for five measurements on one sample.

Spin coated PCL brushes degraded faster in both acidic and basic conditions compared to grafted PCL brushes. This behavior may also be explained by rapid desorption of the spin coated brushes compared to degradation of the grafted brushes. However, the degradation of both spin coated PGA and PCL brushes examined here was different from the previously examined PLA brushes.<sup>4</sup> Spin coated PLA brushes were reported to degrade more slowly than grafted PLA brushes under basic conditions. In order to explain this apparent discrepancy, further experiments were performed and discussion is provided in the following section.

## ii. Study of Brush Morphology using Contact Angle Goniometry

Initially, the reason accounting for the different degradation behavior of spin coated PGA and PCL brushes compared to PLA brushes was proposed to be the different abilities of the polymer chains to reorient. Since grafted PLA brushes showed a faster degradation rate than spin coated PLA, the chain reorientation of grafted brushes to let the terminal hydroxy groups come into contact with the brush/water interface was assumed to be faster than grafted PGA and PCL brushes. If this was true, the reorientation should result in a large change in water contact angle.

**Table 2.2.1 Table of deionized water contact angles collected on grafted PLA, PGA and PCL brushes under different conditions.**

DI water contact angle	Freshly prepared	1 Day in air	5 Days in air	H <sub>2</sub> O soaked
PLA (°)	20	46	62	<5
PGA (°)	<5	18	38	<5
PCL (°)	30	50	42	<5

Grafted PLA, PGA and PCL brushes of similar thicknesses were prepared and the change in hydrophobicity of the surfaces upon sitting in air was compared (Table 2.2.1). After sitting in air for 1 day or 5 days, all three grafted brushes showed increased hydrophobicity. The increase in contact angle was quite similar. Furthermore, all brushes became hydrophilic after incubating in DI water for 1 h. These result do not indicate much difference in their ability to reorient. This behavior might be due to the large time interval between measurements. Therefore, another set of experiments was performed by continuously monitoring the contact angle change on grafted PGA and PCL brushes exposed to air and water.

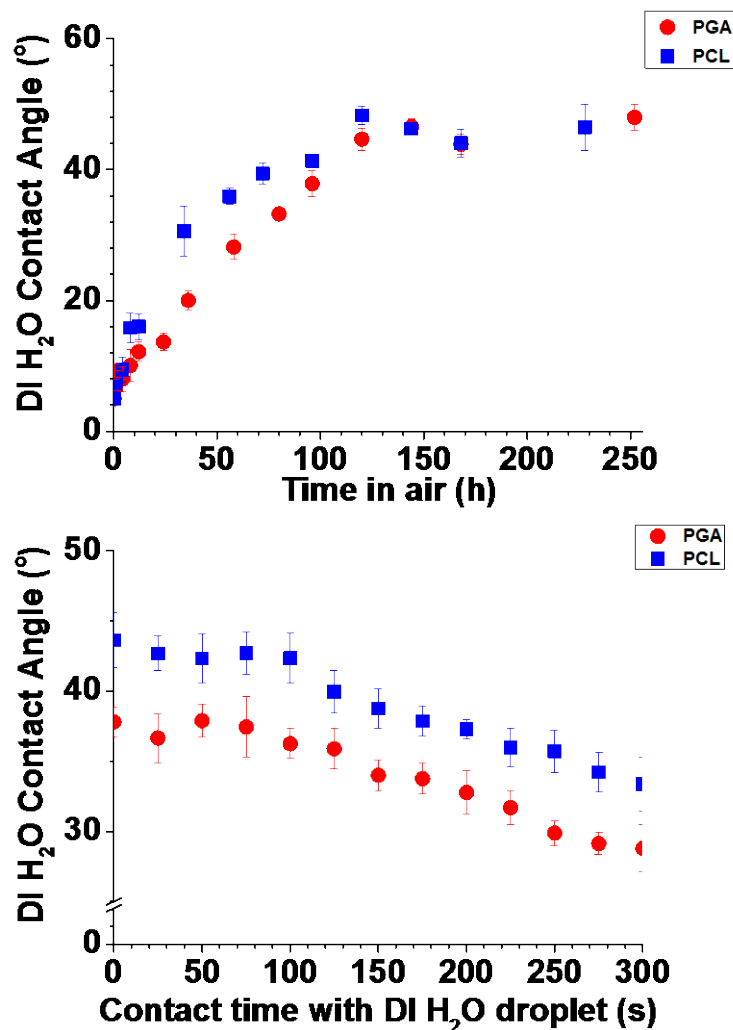
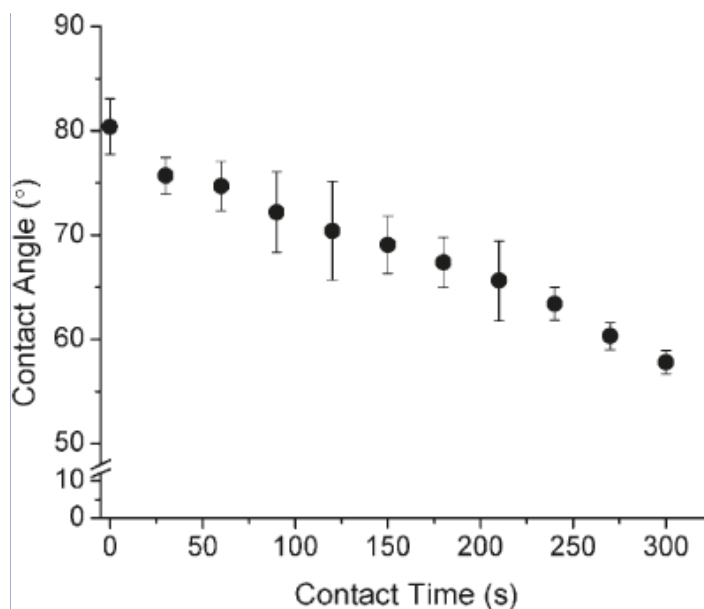


Figure 2.2.22 Plots of DI water contact angles on (top) grafted PGA and PCL brushes versus time sitting in air and (bottom) grafted PGA and PCL brushes versus time in contact with DI water. Error bars represent the magnitude of the 90% confidence interval for six measurements on two samples.

As is shown in Figure 2.2.22, both grafted PGA and PCL brushes displayed a similar

change in water contact angles with time. This behavior is consistent with a similar ability to reorient the polymer chains between the two polymer brushes. The increase in surface hydrophilicity of PGA and PCL brushes upon contacting with DI water (around ca. 10 ° decrease of contact angle) was smaller than the previously reported PLA brushes (around ca. 20 ° decrease of contact angle) (Figure 2.2.23). This behavior seems to indicate a different ability for the PLA brushes to reorient compared to the PGA and PCL brushes. It is important to note, however, that the PLA samples used to perform the test sat in air for a month after preparation. This longer time might result in a very hydrophobic surface of PLA brushes compared to the PGA and PCL brushes which were left in air for only a couple of days. The difference in relative hydrophobicity is reflected in the initial contact angles of the brushes. PLA brushes showed a contact angle of ca. 80 ° at the beginning while PGA and PCL brushes only had contact angles around 40 °. Thus, these results do not adequately indicate that relative ability for the chains to reorient is the main reason for the different degradation behavior of spin coated PGA and PCL from PLA when compared to grafted brushes.



**Figure 2.2.23** Plots of DI water contact angles on grafted PLA brushes versus time contacting with DI water. Error bars represent the magnitude of the 90% confidence interval for six measurements on two samples. Figure taken from reference.<sup>4</sup>

Another possibility for the degradation difference may be due to different preparation methods for the different, spin coated samples. As mentioned in the previous work by Xu,<sup>4</sup> no annealing procedure was followed after spin coating the PLA layer. However, all the spin coated PGA and PCL samples tested in this work were briefly annealed at around 60 °C for several hours. The annealing procedure can result in variations in surface morphology and different solvation behaviors. To probe this issue further, a comparison of the changes in water contact angle upon contacting with DI water droplet between spin coated PLA sample with and without annealing was made and is shown in Figure 2.2.24.

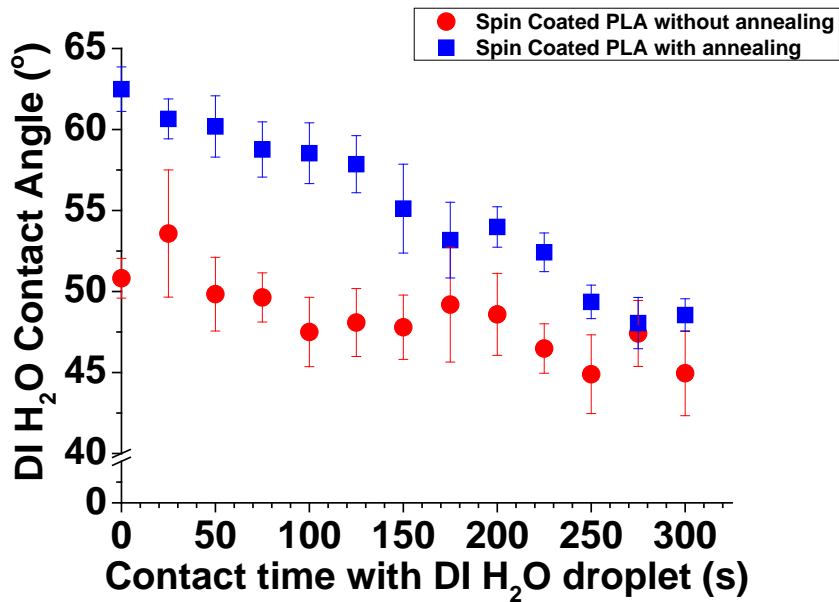


**Figure 2.2.24 Plots of DI water contact angles on spin coated PLA brushes with and without annealing versus time contacting with DI water. Error bars represent the magnitude of the 90% confidence interval for six measurements on two samples.**

From these results, one can see very little change in water contact angle for the non-annealed PLA sample indicating important changes in surface dynamics compared to the annealed sample. Indeed, different preparation methods can cause variation in surface morphology. Because different preparation methods may lead to different morphologies, and these morphologies are difficult to distinguish, it is difficult to fully understand and explain the different degradation behavior of spin coated PGA and PCL brushes presented here with the spin coated PLA samples examined earlier.

Figure 2.2.25 shows the change in DI water contact angle for spin coated PGA and PCL layers that were annealed. Both of these layers also showed continuous increase in surface hydrophilicity when exposed to water. It is possible that the annealing process reduced the water content in the brush and also resulted in voids on the surface. These

changes would lead to faster solvation by water. Similar to the degradation behavior of bulk polyesters, the increased surface heterogeneity and hydrophilicity can enhance the auto catalysis process and the solubility of the oligomers.<sup>22, 24</sup> Therefore, a fast degradation combined with desorption process would occur for the spin coated layers. While a complete understanding is not possible from these experiments, these rationales would explain the faster degradation rate of spin coated layers compared to grafted brushes.

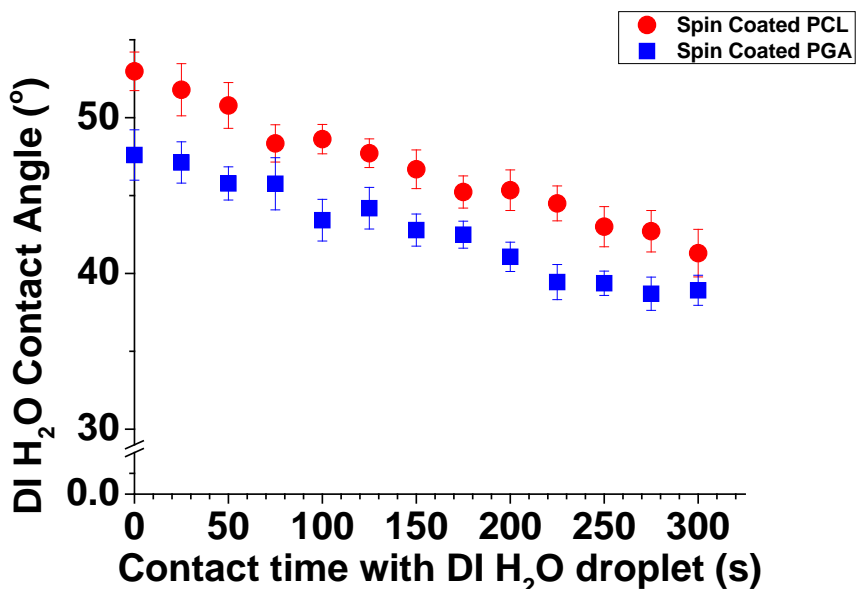


**Figure 2.2.25** Plots of DI water contact angles on spin coated PGA and PCL brushes versus time contacting with DI water. Error bars represent the magnitude of the 90% confidence interval for six measurements on two samples.

### iii. Degradation monitored by Cyclic Voltammetry

Besides using ellipsometry, CV was also applied here to monitor the degradation process of spin coated polyester brushes. The same procedure was employed to prepare the samples except using gold as the substrate which functioned as the working electrode.

Similar to the previously illustrated CV test on grafted brushes, electrolyte (pH 6.0 and 8.0) containing ferricyanide as a redox probe was utilized to incubate the electrode coated with the polyester layers. Peak current density was collected during the linear sweep voltammogram with time as the degradation proceeded.

Compared to the results on grafted polyester brushes, the change in peak current density of spin coated brushes was less controllable. For example, the increase of CV signal showed an abrupt increase at one point for the spin coated PGA brush sample at pH 8. A different type of abrupt increase of peak current density was seen for PGA brush degradation under acidic conditions. In addition, a non-zero signal was observed before brush degradation could occur. All this information implied a lack of homogeneity of the spin coated layers compared to the grafted brushes. Different domains and even voids due to randomly packing of the polymer chains might exist on spin coated surfaces. Nevertheless, a larger CV signal under basic conditions compared to acidic conditions was obtained for all three coated brushes indicating increased accessibility of the redox probe presumably due to the faster solvation or desorption of brushes under basic conditions. The increase in peak current density under both acidic and basic conditions was observed for spin coated PLA and PCL brushes. These results were consistent with which corresponded with the ellipsometric measurements.

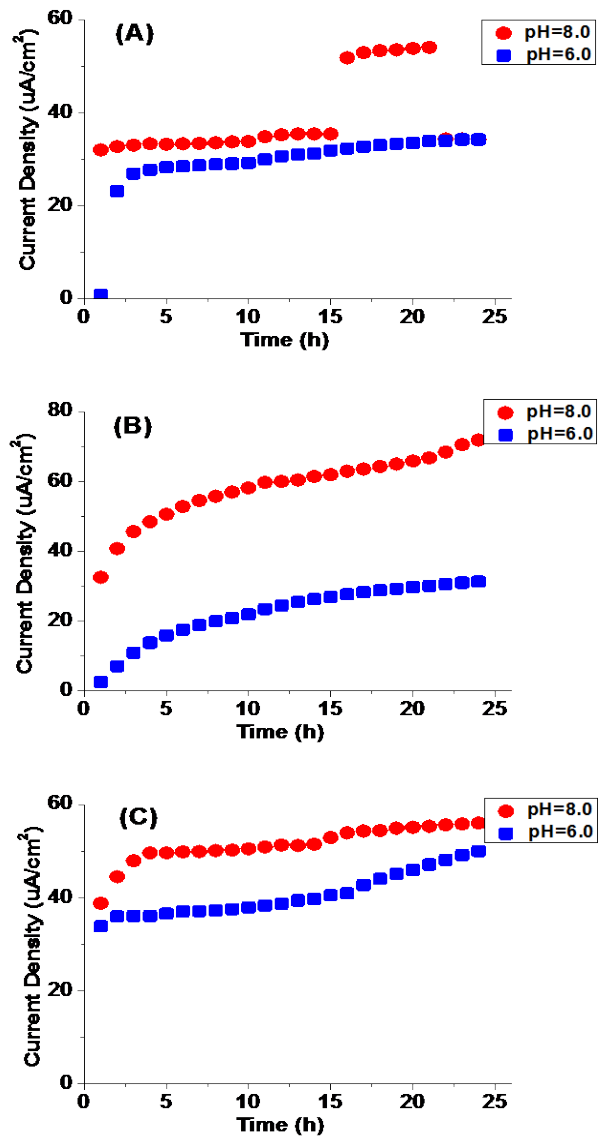


**Figure 2.2.26** Plots of maximum current densities versus time under different pH values for spin coated (A) PGA, (B) PLA and (C) PCL brushes. These current densities are uncorrected for capacitance (e.g. non-Faradaic) effects.

## 2.3 Conclusions

The growth and degradation behaviors of PGA and PCL brushes have been thoroughly investigated. Similar to the previously reported PLA brushes, PGA brushes also grew thicker at room temperature compared to elevated temperature. However, higher temperatures were optimal for the growth of PCL brushes which was explained by the higher activation barrier for the insertion step of  $\epsilon$ -CL than LA and GA. PCL brushes were more stable than PLA and PGA brushes at higher temperatures due to the unfavorable depolymerization of PCL caused by a larger  $\Delta G_p$  for  $\epsilon$ -CL. The poor growth trends of PGA brushes at elevated temperatures were also likely due to the poor solubility of the resulting bulk PGA which covered the surface active sites and prohibited the further growth of the brush.

Both PGA and PCL brushes degraded in a manner similar to that studied previously for PLA brushes that degradation was only observed under neutral or basic conditions. The reduced degradation rate of both PGA and PCL brushes after the protection of the end hydroxy groups with succinic anhydride suggested an important role of these groups in the hydrolysis process. These results were consistent with a proposed backbiting mechanism. In addition, CV experiments provided comparable degradation results with ellipsometry measurements that PGA brushes degraded faster than PCL brushes under basic conditions. The CV results also indicated the existence of defects on PGA brush surface.

Different from the degradation behavior of spin coated PLA brushes, both spin coated PGA and PCL brushes degraded faster than grafted brushes. This result was likely due to the different preparation methods of the brush. However, further investigation is necessary to fully understand this difference.

## 2.4 Experimental

### 2.4.1 Preparation of Silicon and Gold Substrates

The silicon and gold-coated glass slides were first cut into 1 cm  $\times$  1 cm pieces. The substrates were then cleaned by sonication in ethanol for 5 min and dried with a stream of

nitrogen. This was followed by oxidizing the samples under ultraviolet-generated ozone (UVO) for 30 min. After these cleaning treatments, the silicon samples were used directly for growing brushes. However, the gold-coated glass samples were first incubated in 1 mM solution of 2-mercaptoethanol in ethanol overnight before growing brushes.

#### **2.4.2 Preparation of Reactants**

Before performing the reactions, all chemicals including monomers, catalyst and solvents were carefully purified. GA and LA were recrystallized twice from anhydrous ethyl acetate and toluene respectively and then dried under vacuum (5 millitorr) overnight.  $\epsilon$ -CL was dried over calcium hydride overnight and then distilled under vacuum (5 millitorr). Tin octanoate was stirred and dried under vacuum (5 millitorr) overnight. THF was distilled over sodium/benzophenone. All chemicals were stored in a dinitrogen-filled dry box after purification. All the glassware was dried in an oven overnight before use.

#### **2.4.3 Preparation of Brushes on Silicon and Gold Substrates**

The preparation of all three polyester brushes were carried out in the dinitrogen-filled dry box. Each of the pre-treated substrates was placed in a 20 mL glass vial and transferred in to the dry box. Each sample was first covered with 20  $\mu$ L of 1 mM tin octanoate (in THF) solution. This was followed by the slow addition of 5 mL of monomer (0.1 M in THF) solutions. Afterwards, sample vials were sealed tightly with Teflon caps and transferred to an incubator at a given temperature with a rotation speed of 100 rpm.

#### **2.4.4 Preparation of Spin Coated Brushes**

The polyesters used for spin coating were collected from the reaction solutions in which the brush samples were prepared. The reaction solution was first concentrated and then the polymer was precipitated out in methanol. The collected polymer was dried under vacuum (5 millitorr) overnight before use. A stock solution of each polyester (1 mg/mL) was prepared by dissolving the pre-dried polymer in anhydrous THF. The silicon and gold substrates were pre-treated as described above and then incubated in 1% (v/v) N-hexadecyl trichlorosilane (Gelest, USA) in anhydrous toluene for 1 h. The spin coating process was conducted both on a spin coater (Laurell Technologies Corporation, WS-400B-6NPP/LITE)

and a home built spin coater as previously described.<sup>25</sup> While using the Laurell spin coater, the maximum rotation speed and acceleration rate were set to be 3000 rpm and 250 rpm/s. The polymer solution was added dropwise to the substrate during the acceleration stage. After reaching the maximum rotation speed, the sample was rotated for 3 min to allow the solvent to completely evaporate. Same procedure was followed when using the home built spin coater.<sup>4</sup> After the spin coating process, the samples was placed under vacuum (5 millitorr) and then annealed in an oven at a given temperature.

#### **2.4.5 Degradation of Brushes**

Degradation of both grafted and spin coated PGA, PLA and PCL brushes were conducted by immersing the sample in 10 mL freshly prepared PBS buffer at a given pH value in a 20 mL glass vial. The vial was placed in an incubator at a given temperature and a rotation speed of 100 rpm. At various time points, the sample was removed from the buffer and rinsed with excess amount of DI water, then dried with a stream of nitrogen.

#### **2.4.6 Ellipsometry Measurements**

The thickness of brushes was measured using a single-wavelength ellipsometer at a 70 degree angle (AutoEL-III, Rudolph Research, Flanders, NJ). All measurements were taken on dry samples. Five measurements, four at the corners and one at the center, were taken on each sample. Each sample was measured after treatment under UVO in order to obtain an initial silica thickness before growing brushes. The thickness of each polymer brush sample was calculated by subtracting the initial silica thickness from the thickness after modification with brush.

#### **2.4.7 Cyclic Voltammetry Measurements**

Cyclic voltammetry was performed using a cell fashioned as described by Bowden et al.<sup>26</sup> A gold substrate, Ag/AgCl and platinum wire were used as the working electrode, standard reference electrolyte and counter electrode, respectively. A 1 mM solution of  $K_3Fe(CN)_6$  in 100 mM phosphate buffer with pH 8.0 or pH 6.0 were used in these experiments. The scanning rate was 50 mV/s. All cyclic voltammetry measurements were performed at room temperature. The data were collected using a potentiostat (Model 273A,

Princeton Applied Research) controlled by a computer (Model 250 Research Electrochemistry Software, M270, 4.41, Princeton Applied Research). The current density was calculated from the current divided by working area of the electrode and was uncorrected for non-Faradaic processes.

#### **2.4.8 Contact Angle Measurements**

The DI water contact angle was measured on home-made setup. A droplet of about 5  $\mu$ L DI water was placed on the sample using a micro syringe. The image of the water droplet was collected by a video camera (Panasonic GP-KR222). Then the image was analyzed by ImageJ software (Image J 1.32j, Wayne Rasband, National Institutes of Health, USA) to determine the contact angle value.

#### **2.4.9 ATR-FTIR Measurements**

ATR-FTIR spectra were collected on the Excalibus Series bench (Varian) with the MIRacle Single Reflection ATR kits (PIKE). The ATR crystal was a germanium crystal. The pressure to hold the sample was 530 lb. The background scans were collected in air.

## REFERENCES

1. (a) Albertsson, A.-C.; Varma, I. K., Recent developments in ring opening polymerization of lactones for biomedical applications. *Biomacromolecules* 2003, 4 (6), 1466-1486; (b) Kaihara, S.; Matsumura, S.; Mikos, A. G.; Fisher, J. P., Synthesis of poly(L-lactide) and polyglycolide by ring-opening polymerization. *Nat Protoc* 2007, 2 (11), 2767-71; (c) Dobrzynski, P.; Li, S.; Kasperczyk, J.; Bero, M.; Gasc, F.; Vert, M., Structure-property relationships of copolymers obtained by ring-opening polymerization of glycolide and epsilon-caprolactone. Part 1. Synthesis and characterization. *Biomacromolecules* 2005, 6 (1), 483-8; (d) Xichen, Z.; Wyss, U. P.; Pichora, D.; Goosen, M. F. A., An investigation of poly(lactic acid) degradation. *J. Bioact. Compat. Polym* 1994, 9 (1), 80-100; (e) Jung, J. H.; Ree, M.; Kim, H., Acid- and base-catalyzed hydrolyses of aliphatic polycarbonates and polyesters. *Catal. Today* 2006, 115 (1-4), 283-287; (f) Ginde, R. M.; Gupta, R. K., In vitro chemical degradation of poly(glycolic acid) pellets and fibers. *J. Appl. Polym. Sci.* 1987, 33 (7), 2411-2429.
2. (a) Choi, I. S.; Langer, R., Surface-initiated polymerization of L-lactide: coating of solid substrates with a biodegradable polymer. *Macromolecules* 2001, 34 (16), 5361-5363; (b) Li, Y.; Volland, C.; Kissel, T., Biodegradable brush-like graft polymers from poly(D,L-lactide) or poly(D,L-lactide-coglycolide) and charge-modified, hydrophilic dextrans as backbone—in-vitro degradation and controlled releases of hydrophilic macromolecules. *Polymer* 1998, 39 (14), 3087-3097.
3. Xu, L.; Gorman, C. B., Poly(lactic acid) brushes grow longer at lower temperatures. *J. Polym. Sci., Part A: Polym. Chem* 2010, 48 (15), 3362-3367.
4. Xu, L.; Crawford, K.; Gorman, C., Effects of temperature and pH on the degradation of poly(lactic acid) brushes. *Macromolecules* 2011, 44 (12), 4777-4782.
5. Jung, J. H.; Ree, M.; Kim, H., Acid- and base-catalyzed hydrolyses of aliphatic polycarbonates and polyesters. *Catal. Today* 2006, 115 (1-4), 283-287.
6. van Nostrum, C. F.; Veldhuis, T. F. J.; Bos, G. W.; Hennink, W. E., Hydrolytic degradation of oligo(lactic acid): a kinetic and mechanistic study. *Polymer* 2004, 45 (20), 6779-6787.

7. Kowalski, A.; Duda, A.; Penczek, S., Kinetics and mechanism of cyclic esters polymerization initiated with tin(II) octoate. 3. Polymerization of L,L-dilactide. *Macromolecules* 2000, 33 (20), 7359-7370.
8. Zhang, X. C.; Macdonald, D. A.; Goosen, M. F. A.; McAuley, K. B., Mechanism of lactide polymerization in the presence of stannous octoate: the effect of hydroxy and carboxylic-acid substances. *J. Polym. Sci., Part A: Polym. Chem* 1994, 32 (15), 2965-2970.
9. (a) Zhao, B.; Brittain, W. J., Polymer brushes: surface-immobilized macromolecules. *Prog. Polym. Sci.* 2000, 25 (5), 677-710; (b) Love, J. C.; Estroff, L. A.; Kriebel, J. K.; Nuzzo, R. G.; Whitesides, G. M., Self-assembled monolayers of thiolates on metals as a form of nanotechnology. *Chem. Rev.* 2005, 105 (4), 1103-1169; (c) Raynor, J. E.; Capadona, J. R.; Collard, D. M.; Petrie, T. A.; Garcia, A. J., Polymer brushes and self-assembled monolayers: Versatile platforms to control cell adhesion to biomaterials (Review). *Biointerphases* 2009, 4 (2), FA3-FA16.
10. Wang, M. J.; Liechti, K. M.; Wang, Q.; White, J. M., Self-assembled silane monolayers: Fabrication with nanoscale uniformity. *Langmuir* 2005, 21 (5), 1848-1857.
11. Vanhummel, G. J.; Harkema, S.; Kohn, F. E.; Feijen, J., Structure of 3,6-Dimethyl-1,4-Dioxane-2,5-Dione [D-,D-(L-,L-)Lactide]. *Acta Crystallogr., Sect. B: Struct. Sci* 1982, 38 (5), 1679-1681.
12. (a) Amine, H.; Karima, O.; El Amine, B. M.; Belbachir, M.; Meghabar, R., Cationic ring opening polymerization of glycolide catalysed by a montmorillonite clay catalyst. *J. Polym. Res.* 2005, 12 (5), 361-365; (b) Hyon, S. H.; Jamshidi, K.; Ikada, Y., Synthesis of polylactides with different molecular weights. *Biomaterials* 1997, 18 (22), 1503-1508.
13. Middleton, J. C.; Tipton, A. J., Synthetic biodegradable polymers as orthopedic devices. *Biomaterials* 2000, 21 (23), 2335-2346.
14. Hariharan, R.; Pinkus, A. G., Useful NMR solvent mixture for polyesters - trifluoroacetic acid-D/chloroform-D. *Polym. Bull.* 1993, 30 (1), 91-95.
15. Ling, J.; Shen, J. G.; Hogen-Esch, T. E., A density functional theory study of the

mechanisms of scandium-alkoxide initiated coordination-insertion ring-opening polymerization of cyclic esters. *Polymer* 2009, 50 (15), 3575-3581.

16. Broderick, E. M.; Diaconescu, P. L., Cerium(IV) catalysts for the ring-opening polymerization of lactide. *Inorg. Chem.* 2009, 48 (11), 4701-4706.

17. (a) Dechy-Cabaret, O.; Martin-Vaca, B.; Bourissou, D., Controlled ring-opening polymerization of lactide and glycolide. *Chem. Rev.* 2004, 104 (12), 6147-6176; (b) von Schenck, H.; Ryner, M.; Albertsson, A. C.; Svensson, M., Ring-opening polymerization of lactones and lactides with Sn(IV) and Al(III) initiators. *Macromolecules* 2002, 35 (5), 1556-1562; (c) Eguiburu, J. L.; Fernandez-Berridi, M. J.; Cossio, F. P.; San Roman, J., Ring-opening polymerization of L-lactide initiated by (2-methacryloxy)ethoxy-aluminum trialkoxides. 1. Kinetics. *Macromolecules* 1999, 32 (25), 8252-8258; (d) Gilding, D. K.; Reed, A. M., Biodegradable polymers for use in surgery - polyglycolic-poly(lactic acid) homopolymers and copolymers .1. *Polymer* 1979, 20 (12), 1459-1464.

18. Duda, A.; Kowalski, A., Thermodynamics and Kinetics of Ring-Opening Polymerization. In *Handbook of Ring-Opening Polymerization*, Wiley-VCH Verlag GmbH & Co. KGaA: Weinheim, 2009; pp 1-51.

19. (a) Kricheldorf, H. R.; Langanke, D., Polylactones 54: ring-opening and ring-expansion polymerizations of epsilon-caprolactone initiated by germanium alkoxides. *Polymer* 2002, 43 (6), 1973-1977; (b) Liao, L. Q.; Liu, L. J.; Zhang, C.; He, F.; Zhuo, R. X., Heating characteristics and polymerization of epsilon-caprolactone under microwave irradiation. *J. Appl. Polym. Sci.* 2003, 90 (10), 2657-2664.

20. Kumar, A.; Gross, R. A., Candida antarctica lipase B catalyzed polycaprolactone synthesis: Effects of organic media and temperature. *Biomacromolecules* 2000, 1 (1), 133-138.

21. Vieira, A. C.; Vieira, J. C.; Guedes, R. M.; Marques, A. T., Degradation and Viscoelastic Properties of PLA-PCL, PGA-PCL, PDO and PGA Fibres. In *Advanced Materials Forum V, Pt 1 and 2*, Rosa, L. G.; Margarido, F., Eds. Trans Tech Publications Ltd: Stafa-Zurich, 2010; Vol. 636-637, pp 825-832.

22. de Jong, S. J.; Arias, E. R.; Rijkers, D. T. S.; van Nostrum, C. F.; Kettenes-van den

Bosch, J. J.; Hennink, W. E., New insights into the hydrolytic degradation of poly(lactic acid): participation of the alcohol terminus. *Polymer* 2001, 42 (7), 2795-2802.

23. Lee, W. K.; Gardella, J. A., Hydrolytic kinetics of biodegradable polyester monolayers. *Langmuir* 2000, 16 (7), 3401-3406.

24. Loo, S. C. J.; Ooi, C. P.; Wee, S. H. E.; Boey, Y. C. F., Effect of isothermal annealing on the hydrolytic degradation rate of poly(lactide-co-glycolide) (PLGA). *Biomaterials* 2005, 26 (16), 2827-2833.

25. Xu, L. Poly(lactic acid) Polymer Brushes as Dynamic Surfaces. Ph.D Dissertation, North Carolina State University, Raleigh, NC, 2011.

26. Clark, R. A.; Bowden, E. F., Voltammetric peak broadening for cytochrome c/alkanethiolate monolayer structures: Dispersion of formal potentials. *Langmuir* 1997, 13 (3), 559-565.

## Chapter 3 Protein Adsorption on Biodegradable Polyester and OEG Incorporated Co-polymer Brushes

### 3.1 Introduction

The growth and degradation of PGA and PCL brushes have been demonstrated in the previous chapter. In order to achieve the long term goal as mentioned in Chapter 1, the antifouling property of the proposed biosensor surface modified with degradable polyester brushes is also desirable and important to maintain the viability of the sensors. The polyester brushes have been shown to be degradable in pure buffer solutions. This environment is relatively simple. Whether the brush can degrade in a more complicated system such as in protein buffer solutions, is tested here.

Before performing the degradation and biofouling experiments *in vivo*, it is necessary to conduct these tests primarily *in vitro*. In this chapter, a single protein buffer solution containing bovine serum albumin (BSA) was employed as the *in vitro* environment and all tests were run under physiological conditions. According to the reaction conditions reported in literatures, BSA buffer solutions with concentrations ranging from 0.5 mg/mL to 4.5 mg/mL were adopted.<sup>1</sup>

PEG is a well known material that has substantial protein resisting properties. Recently, copolymers consisting of PLA or PLGA and PEG have been prepared. Reduced protein adsorption was observed on these copolymers compared to pure biodegradable polyesters (PLA and PLGA). These copolymers were reported to be degradable under physiological conditions.<sup>2</sup> In this chapter, in addition to assessing the degradation and protein adsorption behaviors of PLA, PGA and PCL brushes, modification methods of these polyester brushes with OEG and PEG were also investigated. The degradability and protein resistance of co-polymer brushes were tested under the same conditions as single polyester brushes. Fabrication of degradable polyester brushes with moderate protein resisting property was demonstrated.

Lastly, characterization methods for monitoring the adsorbed protein were studied. A variety of techniques have been reported to quantitatively and qualitatively characterize protein adsorption.<sup>3</sup> Here, ellipsometry, ATR-FTIR spectroscopy and a protein assay method were applied to measure the adsorbed protein on flat substrates.

## **3.2 Results and Discussion**

### **3.2.1 BSA Adsorption on PLA, PGA and PCL Brushes**

#### **i. BSA Adsorption on Respective Brushes**

Before assessing protein adsorption on grafted polyester brushes, experiments were performed on bare silicon surfaces as a background test. BSA(PBS) solutions with different concentrations, ranging from 0.5 mg/mL to 4.5 mg/mL were prepared for sample incubation. The adsorption process was monitored using ellipsometry with incubation time under physiological conditions (37 °C, pH 7.4). The results are shown in Figure 3.2.1.

Instant protein adsorption was observed on bare silicon surface in all five concentration BSA(PBS) solutions. According to the ellipsometric thickness (ca. 14 nm), at least a monolayer of BSA(dimensions:  $14 \times 4 \times 4 \text{ nm}^3$ ) was adsorbed on the surface after 1 h incubation. Although the amount of adsorbed protein was seen to fluctuate with incubation time, at least a 10 nm thick protein layer stayed on the surface during 50 h incubation.

The fast adsorption behavior was mainly ascribed to the low ionic strength of the protein buffer solution, which is around 10 mM modified with NaCl. This ionic strength value happens to be within the range when maximum binding between BSA and hydrophobic polymers occurs due to hydrophobic interactions and minimum electrostatic repulsions.<sup>4</sup> The employment of such low ionic strength here might enhance the opportunity for BSA to adsorb on the surface. Moreover, the conformation of BSA can be changed upon interaction with surface due to (1) reorientation (from side-on to end-on) that increases hydrophobic interaction between protein molecules followed by (2) unfolding that leads to denaturation.<sup>5</sup> Thus the effect of low ionic strength on protein adsorption can accelerate the conformational distortion of BSA which is irreversible as can be seen from the plateau of the adsorption curve. The entropy gain during this process leads to a negative Gibbs free energy change.<sup>6</sup>

This gain can overcome unfavorable interactions including electrostatic repulsion and using relatively hydrophilic surfaces such as the hydrated silicon surface.<sup>7</sup>

In addition to bare silicon surface, BSA adsorption was also conducted on PLA brush surfaces under the same conditions. Instant fouling behavior was also seen and the reason accounting for this phenomenon might be (1) the low ionic strength as mentioned above and (2) the more hydrophobic surface property of PLA brushes than hydrated silicon surface.<sup>8</sup> The thickness of adsorbed BSA on brush after 1 h incubation (10~14 nm) is similar to that on silicon indicating a quick formation of at least a monolayer of protein on the brush surface. A gradual increase in thickness was not observed. The degradation of the brushes was also completely hindered upon the fast attachment of the protein layer (results not shown, but experimental details for making this determination are provided later in this chapter). The slow decrease in protein thickness after maximum adsorption might be the slow penetration of deformed proteins into the brushes.

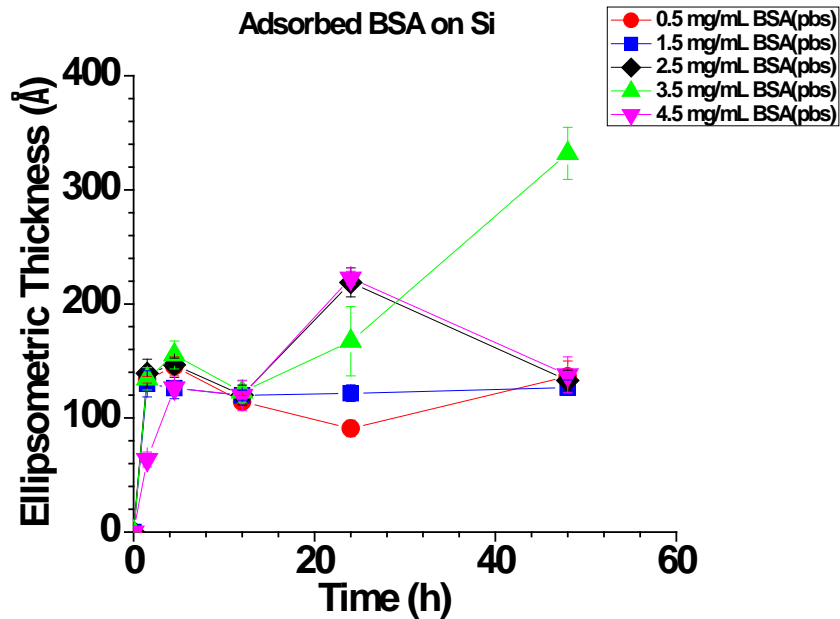
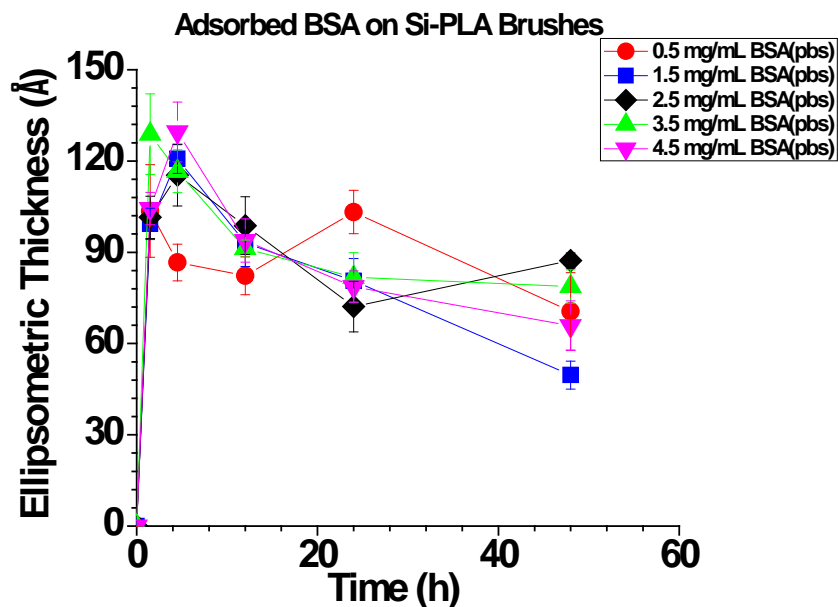


Figure 3.2.1 Plots of ellipsometric thicknesses of adsorbed BSA on bare Si versus incubation time in BSA(PBS, pH 7.4, 10 mM ionic strength, 37 °C) solutions with different concentrations. Error bars represent the magnitude of the 90% confidence interval for five measurements on one sample. Lines are drawn merely as guides to the eye.



**Figure 3.2.2** Plots of ellipsometric thicknesses of adsorbed BSA on grafted PLA brushes versus incubation time in BSA(PBS, pH 7.4, 10 mM ionic strength, 37 °C) solutions with different concentrations. Error bars represent the magnitude of the 90% confidence interval for five measurements on one sample. Lines are drawn merely as guides to the eye.

Since the low ionic strength can't be ruled out as a reason for fast fouling, a more suitable salt concentration was explored. BSA was shown to have a relatively strong affinity to polymers when the Debye length is close to the radius of the protein molecule which is ca. 2~4 nm.<sup>4</sup> The corresponding ionic strength is within the range of 6~20 mM. Increasing the concentration further to 100~200 mM can result in a reduced binding effect due to the more preserved and stable conformation of BSA in solution with most hydrophobes buried inside. This concentration is far below the point of intensive hydrophobic binding between protein molecules and even precipitation caused by charge neutralization under high ionic shielding conditions.<sup>9</sup> Thus, in the following work, modified protein buffer with ionic strength of

100 mM was applied in cases where quick adsorption was detected using a low ionic strength solution.

The adsorption of BSA on polyester brushes was reexamined using modified protein buffer solution. Ellipsometric thicknesses of adsorbed protein were measured as a function of incubation time, and results are shown in Figure 3.2.3.

After modifying the ionic strength of the protein-buffer solution, the instant adsorption effect was reduced. As can be seen from the adsorption curves of all three brush surfaces, the thickness of adsorbed BSA was less than 10~14 nm until almost 20 h of incubation. This result indicates the rapid adsorption and irreversible conformational change of protein caused by low salt concentration was relatively obviated. As a result, the interaction between protein molecules and polyester brushes (partial and full insertion) was slower as can be seen from the gradually increased thickness of adsorbed BSA. Moreover, the adsorption effect under various protein concentrations can be differentiated more obviously compared to the previous results (Figure 3.2.2). For example, the thickness of adsorbed BSA on three brushes reached above 10 nm in 4.5 mg/mL BSA solution after 34 h incubation while nearly no adsorption occurred in 0.5 mg/mL BSA solution.

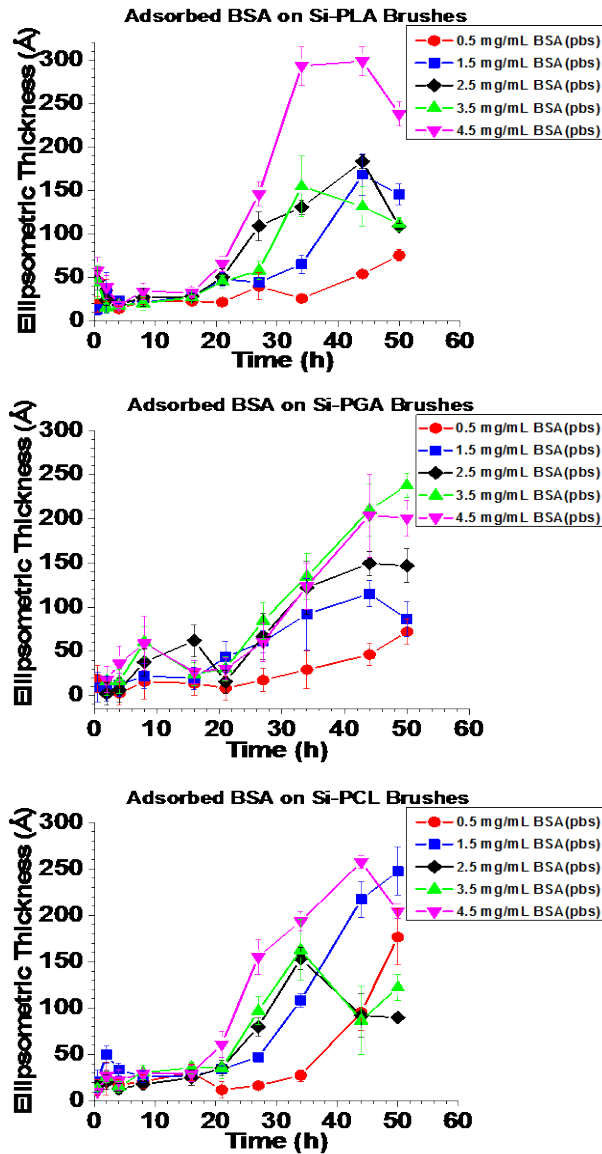
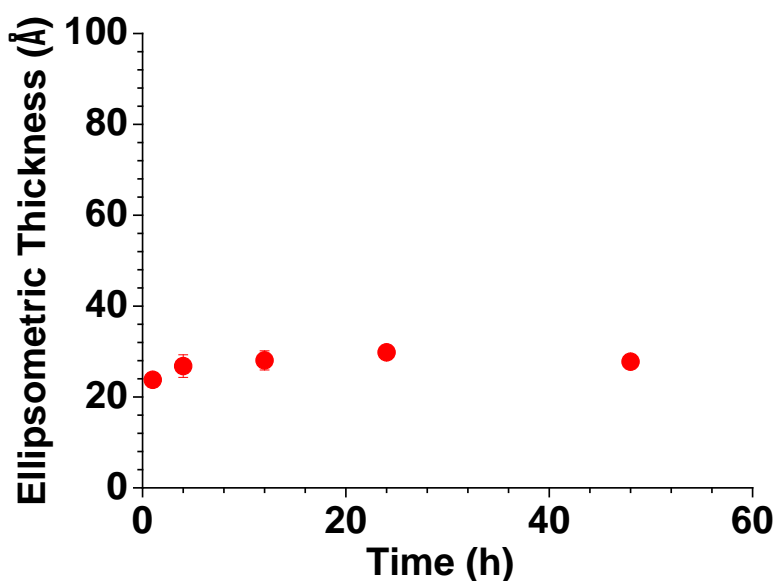


Figure 3.2.3 Plots of ellipsometric thicknesses of adsorbed BSA on grafted (top) PLA, (center) PGA and (bottom) PCL brushes versus incubation time in BSA (PBS, pH 7.4, 100 mM ionic strength, 37 °C) solutions with different concentrations. Error bars represent the magnitude of the 90% confidence interval for five measurements on one sample. Lines are drawn merely as guides to the eye.



**Figure 3.2.4** Plot of ellipsometric thicknesses of adsorbed BSA on bare Si versus incubation time in 4.5 mg/mL BSA(PBS, pH 7.4, 100 mM ionic strength, 37 °C) solutions. Error bars represent the magnitude of the 90% confidence interval for five measurements on one sample.

The adsorption behavior of BSA on all three polyester brushes was similar. The accumulation of protein on these brushes took place after 20 h and the amount of the adsorbed protein was continually increased. The heavier adsorption on the brushes than on bare silicon (Figure 3.2.4) might be due to the increased hydrophobic property of the surface after modification with polyesters. Small difference in the adsorption rate among the three brushes was observed. For instance, both PLA and PCL brushes displayed a faster adsorption rate compared to PGA brush in 4.5 mg/mL BSA(PBS) solutions as can be seen from the slopes of the curves after 20 h. This behavior was attributed to the relatively higher hydrophobicity of PLA and PCL than PGA. Towards the end of the test (after 40 h), there

were some fluctuations of the protein thickness on these brushes under several conditions. This is possibly due to desorption of the outer layer of protein molecules.

## **ii. Degradation of Brushes upon Adsorption**

The degradation of the three polyester brushes was monitored in parallel with the protein adsorption process. In order to determine the changes in the thickness of brush, it was first necessary to remove the adsorbed proteins. To remove adsorbed protein, the brush samples were sonicated thoroughly in 5 wt% sodium dodecyl sulfate (SDS) aqueous solutions after incubation. Ellipsometric thicknesses of the brushes were measured as a function of incubation time. The degradation of all three polyester brushes in 4.5 mg/mL BSA(PBS) solutions is shown in Figure 3.2.5.

The thickness of all three polyester brushes did not change much during 50 h incubation indicating no degradation occurred. Compared to the previous results where brushes were degraded (Figure 2.2.16), this process was interrupted when immersing the brushes in buffers containing proteins. This result suggests the protein adsorption inhibited brush degradation under these conditions. The hindered brush degradation can be explained by the blocking of the end hydroxy groups by protein molecules. Once the irreversible conformational change of proteins occurs on the surface, the covered hydroxy end groups of the brushes might be completely obstructed from contacting with the water layer.

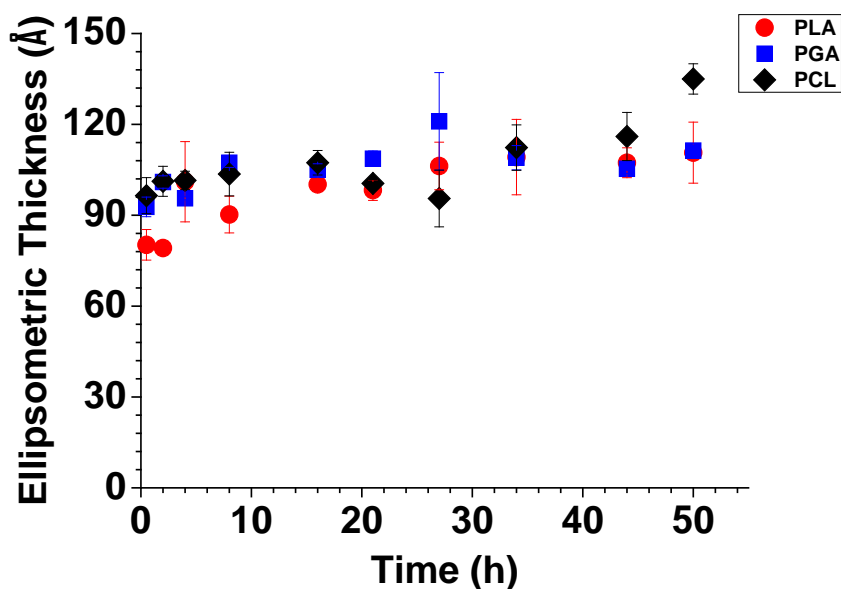


**Figure 3.2.5** Plots of ellipsometric thicknesses of PLA, PGA and PCL brushes versus incubation time in 4.5 mg/mL BSA(PBS, pH 7.4, 100 mM ionic strength, 37 °C) solutions. Adsorbed BSA was removed by sonication in 5 wt% SDS(aq). Error bars represent the magnitude of the 90% confidence interval for five measurements on one sample.

As can be seen from the adsorption curves (Figure 3.2.4), all three polyester brushes showed significant adsorption of BSA especially after 30 h when incubated in 4.5 mg/mL BSA(PBS) solutions. The result implies these polyester brushes are too prone to binding proteins and as a result, the brush degradation is greatly affected. In order to improve both protein resistance and brush degradation, modifications of these brushes with relatively hydrophilic components were performed as described in the next section.

### **3.2.2 BSA Adsorption on OEG Incorporated Co-polymer Brushes**

#### **i. BSA Adsorption on Hydroxy and Methoxy Terminated OEG Brushes**

PEG and OEG have been widely used as protein resisting materials.<sup>10</sup> In order to attempt to increase the protein resistance of the polyester brushes, OEG silanes (from Gelest) with methoxy (OEG-OMe) and hydroxy (OEG-OH) end groups were incorporated as a co-layer of the brush. OEG can be grafted to the surface either as a substrate layer to grow the polyester brushes or as an outer layer on top of the polyester brushes. The hydroxy end groups of OEG-OH were utilized as initiators for growing polyester brushes. Also, mixtures of OEG-OH and OEG-OMe were used to adjust the surface density of the subsequently grown polyester layers.

First, BSA adsorption was conducted on OEG-OH grafted silicon surfaces. The results are shown in Figure 3.2.6. Although this trial was run at low ionic strength (where protein adsorption was rapid for the unmodified polyester brushes), the OEG-OH modified silicon surface still reveals substantial protein resistance. No evident thickness increase due to protein adsorption was detected up to almost 50 h incubation. This behavior is consistent with previous reports. The ability of OEG-OMe modified silicon surface in resisting proteins is very similar to OEG-OH grafted surfaces (results not shown). Thus, the hydroxy end group plays a relatively small role in the overall protein resistance of these groups.

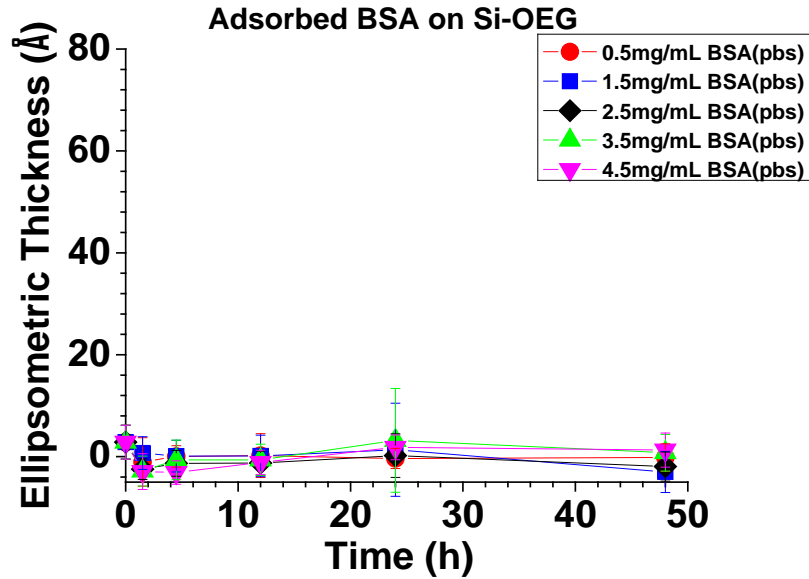


**Figure 3.2.6** Plots of ellipsometric thicknesses of adsorbed BSA on Si-OEG brushes versus incubation time in BSA (PBS, pH 7.4, 10 mM ionic strength, 37 °C) solutions with different concentrations. Error bars represent the magnitude of the 90% confidence interval for five measurements on one sample. Lines are drawn merely as guides to the eye.

Protein adsorption was also carried out on silicon surface modified with mixtures of OEG-OH and OEG-OMe. Figure 3.2.7 shows the BSA adsorption result on surface modified with 90% to 10% molar ratio of OEG-OMe and OEG-OH. No obvious protein adsorption was detected during the 50 h incubation. This again implies the similar hydrophilic and protein resistance of the two OEG components.

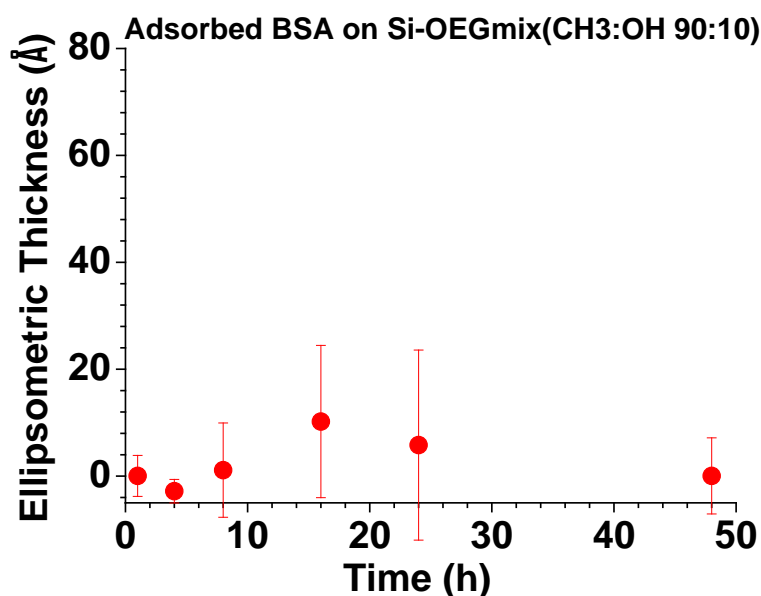


**Figure 3.2.7** Plots of ellipsometric thicknesses of adsorbed BSA on Si-OEG<sub>mix</sub> brushes (mixed OEG substrate layer: 90% : 10% methoxy and hydroxy terminated OEG) versus incubation time in 4.5 mg/mL BSA (PBS, pH 7.4, 10 mM ionic strength, 37 °C) solutions. Error bars represent the magnitude of the 90% confidence interval for five measurements on one sample.

Previously, CV was conducted on polyester grafted gold electrodes. Under basic conditions, the electrode can be gradually exposed to the redox couple upon degradation of the brushes as indicated by the increased current signal. In order to check if the intensity of current signal is affected by introducing a substrate layer that is less degradable compared to the polyesters, CV was performed on OEG mixture modified gold working electrodes. Current density was monitored during the linear sweep voltammogram and the results are shown in Figure 3.2.8.

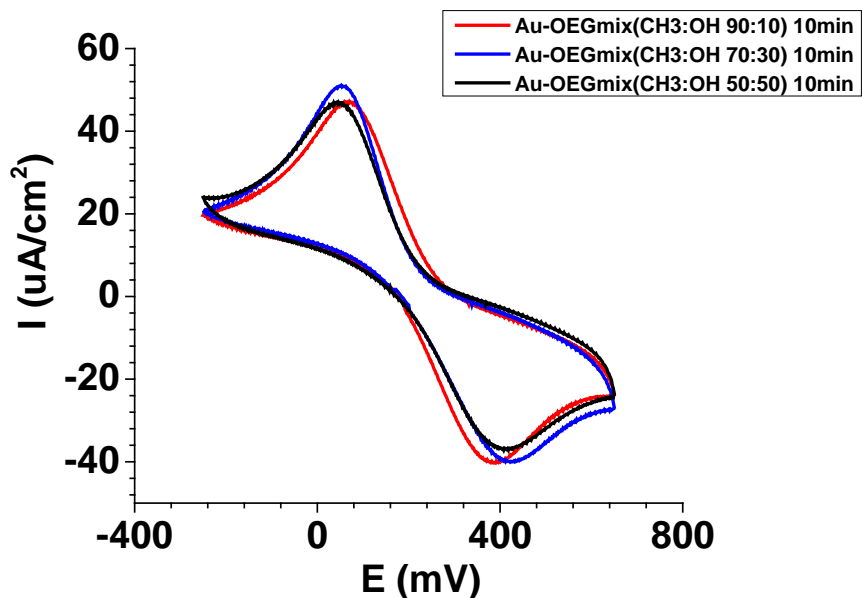


**Figure 3.2.8** Plots of CV curves taken with OEG<sub>mix</sub> covered gold working electrodes of varying composition after incubating in 1 mM K<sub>3</sub>(Fe(CN)<sub>6</sub>) (100 mM PBS, pH 8.0) for 10 min. These current densities are uncorrected for capacitance (e.g. non-Faradaic) effects.

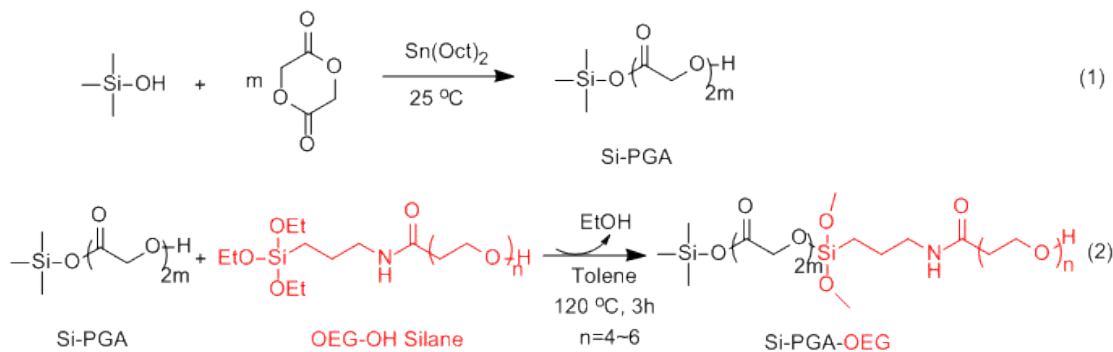
For all three OEG mixture modified gold surfaces, a peak current density of ca. 50  $\mu\text{A}/\text{cm}^2$  was collected. This value is only 20  $\mu\text{A}/\text{cm}^2$  lower than the signal on bare gold surface which is ca. 70  $\mu\text{A}/\text{cm}^2$ , indicating that the accessibility of the electrode surface to the redox probe is not significantly blocked by the coverage of the OEG layer. This is possibly because the employed OEG layer is relatively loosely packed. The result implies that the surface covered with OEG substrate layer is still applicable for electrochemical tests.

**ii. BSA Adsorption on Co-polymer Brushes with OEG as an Outside Layer**

After probing the protein adsorption process on OEG modified substrates, similar experiments were run on co-polymer brushes containing polyester as the first layer and OEG as the outer layer. The preparation procedure is described in Scheme 3.2.1 using Si-PGA-

OEG as an example. These layers were prepared by first grafting polyester brushes from silicon surface via SI-ROP as described previously (eq. 1). This was followed by subsequently grafting OEG-OH to the polyester layer through a condensation reaction between the ethoxysilanes (from OEG) and the hydroxy terminal groups (from the polyester) (eq. 2). BSA adsorption and brush degradation were studied at the same time using ellipsometry. The results are shown in Figure 3.2.9.

**Scheme 3.2.1 Synthesis of PGA and OEG co-polymer brushes with OEG as an outside layer.**



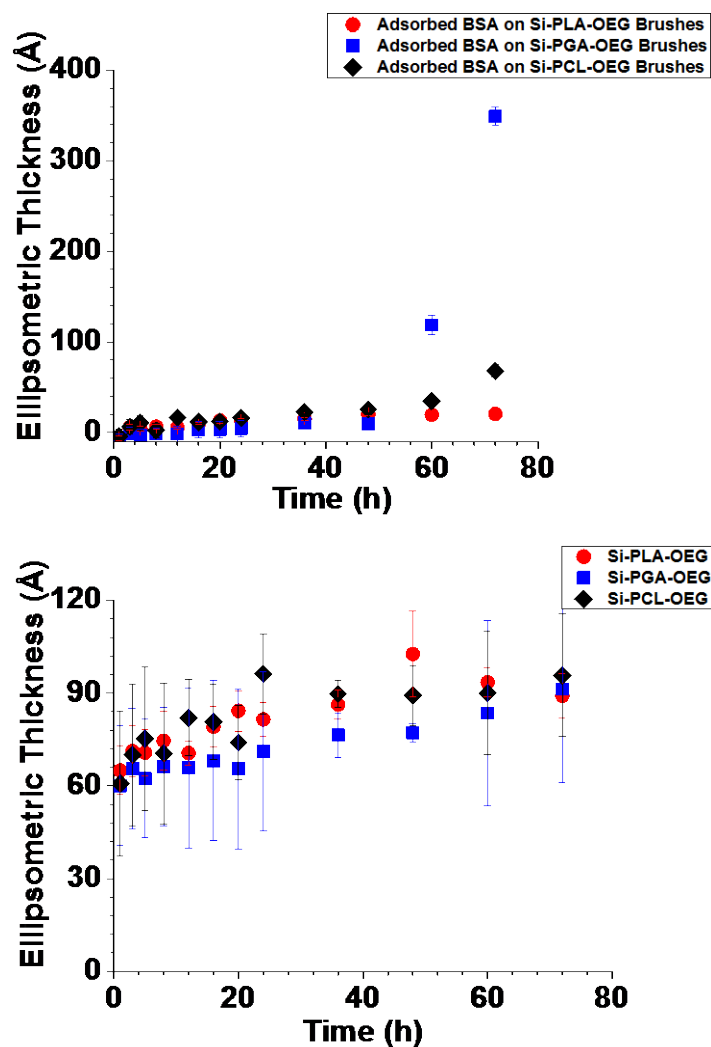


Figure 3.2.9 Plots of ellipsometric thicknesses of (top) adsorbed BSA on Si-PLA-OEG, Si-PGA-OEG and Si-PCL-OEG brushes and (bottom) Si-PLA-OEG, Si-PGA-OEG and Si-PCL-OEG brushes after BSA was removed by sonication in 5 wt% SDS(aq) versus incubation time in 4.5 mg/mL BSA(PBS, pH 7.4, 100 mM ionic strength, 37 °C) solutions. Error bars represent the magnitude of the 90% confidence interval for five measurements on one sample.

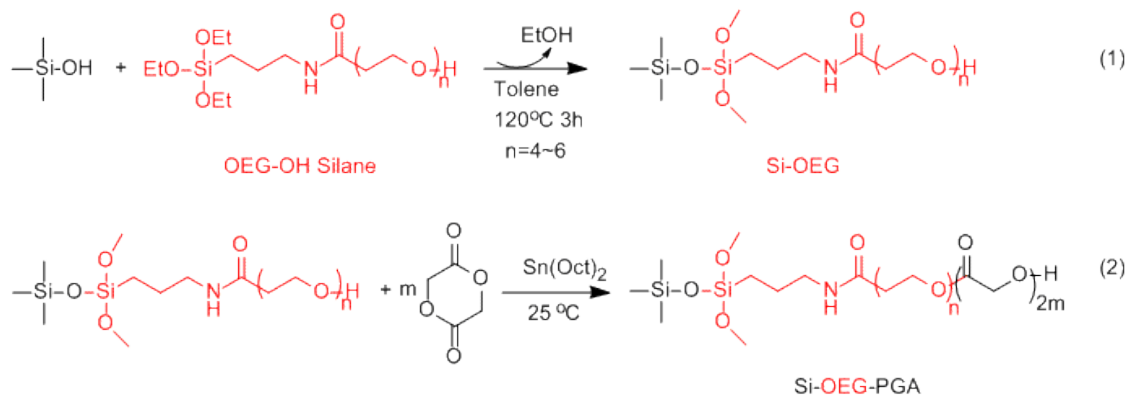
After applying OEG as an outer layer, the brush suppressed protein adsorption up to almost 60 h incubation compared to 20 h for single polyester brush surfaces (Figure 3.2.4). Again, the OEG groups are effective at resisting protein adsorption. The resulting noticeable adsorption on Si-PGA-OEG brushes after 60 h incubation might be caused by the loss of the OEG outer layer due to degradation of the OEG layer or PGA brushes or both. Since PGA brushes have more defects on the surface compared to PLA and PCL brushes (Figure 2.2.19), the deposition of the OEG layer on the PGA brush might be less uniform. Both incomplete coverage with OEG layer and the faster degradation rate of PGA compared to PLA and PCL might increase the opportunity for the removal of OEG outside layer from the brush surface. As a result, exposure of relatively hydrophobic PGA brushes to the protein environment might occur leading to more protein adsorption.

Although the anti-fouling property was greatly improved, degradation of these co-polymer brushes was hindered. No degradation was observed for all three brushes during the 80 h experiment. The inhibition of brush degradation is likely caused by the blocking of the end groups of the brush by the OEG layer which prohibited the proposed backbiting process. During the degradation of Si-PGA-OEG brushes, a large variation in brush thickness was obtained. This result indicates the poor uniformity of the brush surface which might be due to the incomplete coverage with OEG.

### **iii. BSA Adsorption on Co-polymer Brushes with OEG as the Substrate Layer**

The same BSA adsorption experiments were also performed on co-polymer brushes with OEG as a substrate layer. As demonstrated in Scheme 3.2.2, these layers were prepared by first grafting OEG-OH to the silicon substrate through a condensation reaction between the ethoxysilanes (from OEG) and the hydroxy groups (from silicon) (eq. 1). The polyester brushes were then grown from the OEG layer through ROP using the hydroxy terminal groups of OEG-OH as initiators (eq. 2). The results of BSA adsorption and brush degradation are shown in Figure 3.2.10.

**Scheme 3.2.2 Synthesis of PGA and OEG co-polymer brushes with OEG as the substrate layer.**



Evident protein adsorption was noticed on Si-OEG-PLA and Si-OEG-PCL brushes after around 30 h incubation while no adsorption was observed on Si-OEG-PGA brushes during the 72 h experiment. The possible reasons for this behavior might be more accessibility to the underlying OEG moieties and the faster degradation rate of PGA co-polymer brushes compared to PLA and PCL co-polymer brushes. However, the latter explanation is less likely to be the case here since Si-OEG-PGA brushes did not show significant degradation. It is assumed that Si-OEG-PGA brushes are relatively protein resistant due to the incorporated OEG component and the main process on the brush is reversible protein adsorption. The irreversible BSA adsorption behavior on surface is suppressed but brush degradation might be compromised by the BSA adsorption and desorption process.

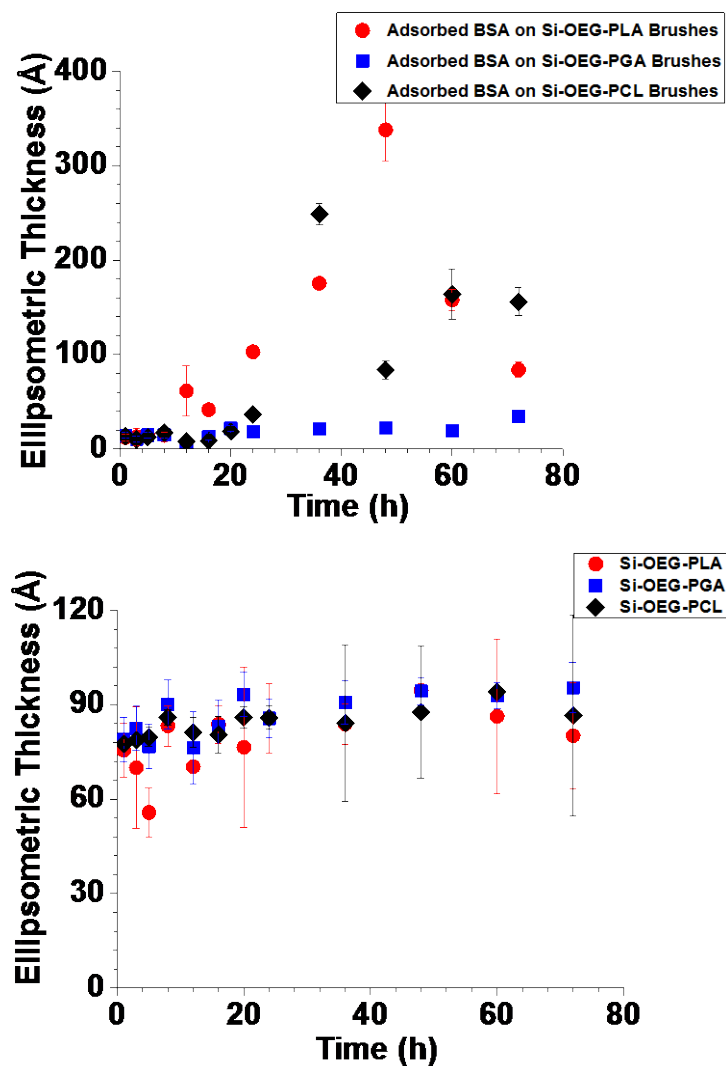


Figure 3.2.10 Plots of ellipsometric thicknesses of (top) adsorbed BSA on Si-OEG-PLA, Si-OEG-PGA and Si-OEG-PCL brushes and (bottom) Si-OEG-PLA, Si-OEG-PGA and Si-OEG-PCL brushes after BSA was removed by sonication in 5 wt% SDS(aq) versus incubation time in 4.5 mg/mL BSA(PBS, pH 7.4, 100 mM ionic strength, 37 °C) solutions. Error bars represent the magnitude of the 90% confidence interval for five measurements on one sample.

The trends in protein adsorption on Si-OEG-PLA and Si-OEG-PCL brushes are similar to those on PLA and PCL brushes as previously shown. This is explained by the relative hydrophobicity of these brushes. The hampered degradation of these brushes is explained by the blocking of the end groups due to the extensive adsorption of BSA molecules on the surface.

#### **iv. BSA Adsorption on Co-polymer Brushes with OEG mixtures as the Substrate Layer**

As demonstrated above, Si-OEG-PGA brushes displayed the best protein resisting ability among the three brushes while the brush degradability was to some extent affected. In order to further increase the accessibility to OEG groups yet still provide a degradable surface, brushes with sub-layers of OEG mixtures were prepared. Two OEG mixtures, containing 50% to 50% and 90% to 10% molar ratio of OEG-OMe and OEG-OH, were deposited as the substrate layers. It is hypothesized that by adjusting the ratio of OEG-OMe and OEG-OH, the amount of subsequently grown PGA and protein resistance can be controlled. BSA adsorption and brush degradation were monitored concomitantly via ellipsometry and results are shown below. (Figures 3.2.11 and 3.2.12).

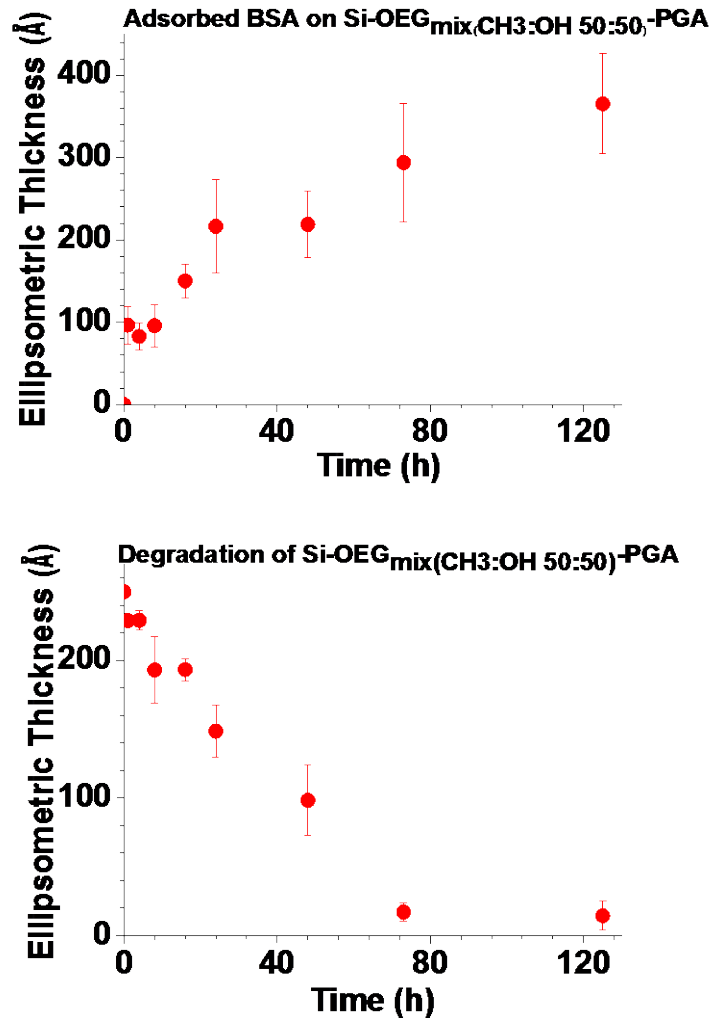


Figure 3.2.11 Plots of ellipsometric thicknesses of (top) adsorbed BSA on Si-OEG<sub>mix</sub>-PGA brushes and (bottom) Si-OEG<sub>mix</sub>-PGA brushes (mixed OEG substrate layer: 50% : 50% methyl and hydroxy terminated OEG) after BSA was removed by sonication in 5 wt% SDS(aq) versus incubation time in 4.5 mg/mL BSA (PBS, pH 7.4, 10 mM ionic strength, 37 °C) solutions. Error bars represent the magnitude of the 90% confidence interval for five measurements on one sample.

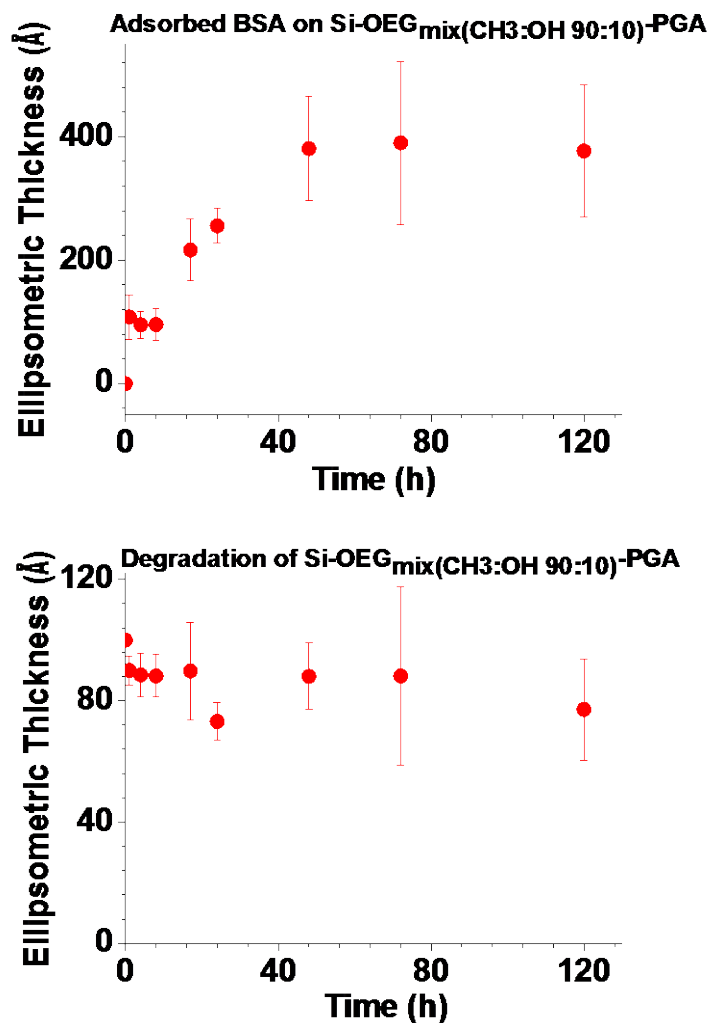


Figure 3.2.12 Plots of ellipsometric thicknesses of (top) adsorbed BSA on Si-OEG<sub>mix</sub>-PGA brushes and (bottom) bare Si-OEG<sub>mix</sub>-PGA brushes (mixed OEG substrate layer: 90% : 10% methyl and hydroxy terminated OEG) after BSA was removed by sonication in 5 wt% SDS(aq) versus incubation time in 4.5 mg/mL BSA (PBS, pH 7.4, 10 mM ionic strength, 37 °C) solutions. Error bars represent the magnitude of the 90% confidence interval for five measurements on one sample.

Gradual BSA adsorption was observed on both brushes which is possibly because these trials were run in the low ionic strength protein solutions. Modified protein buffer was applied in subsequent experiments. Nevertheless, the brush degradability where the sub-layer consisted 50% to 50% OEG-OMe and OEG-OH, was greatly improved as can be seen from the data in Figure 3.2.11. This behavior is rationalized by the increased access to OEG groups. Although protein molecules adsorbed on the PGA grafted domains due to the low ionic strength of the solution, the hydrophilic OEG-OMe regions might still assist in the penetration of water molecules and the resulting degradation of PGA brushes.

Surprisingly, the co-polymer brushes with 90% to 10% OEG-OMe and OEG-OH mixtures as the sub-layer did not show a significant decrease in thickness during the same incubation time. This is possibly because the coverage of PGA is low on the OEG layer. As can be seen from the initial thickness on the degradation curves, with similar growth time, the thicknesses of Si-OEG<sub>mix</sub>-PGA brushes are very different when the ratio of methoxy and hydroxy groups in the OEG mixture layer changes. Surfaces prepared with a higher percentage of OEG-OH have a thicker PGA outer layer because there are more initiators for the growth of PGA brushes. Ellipsometry measures the average thickness of OEG with and without the grafted PGA layer. When the presence of PGA on the OEG substrate layer is sufficiently low, the degradation of the PGA layer might be difficult to determine because there is so little polymer initially present.

In order to reduce the effect of ionic strength on the BSA adsorption process, modified protein solutions were then utilized in repeats of the experiments. In addition, a shorter PGA brush was prepared on mixed OEG layer with 50% to 50% OEG-OMe and OEG-OH as to further increase the access to the underlying OEG groups. Adsorbed protein and brush degradation were monitored by ellipsometry and results are shown in Figure 3.2.13.

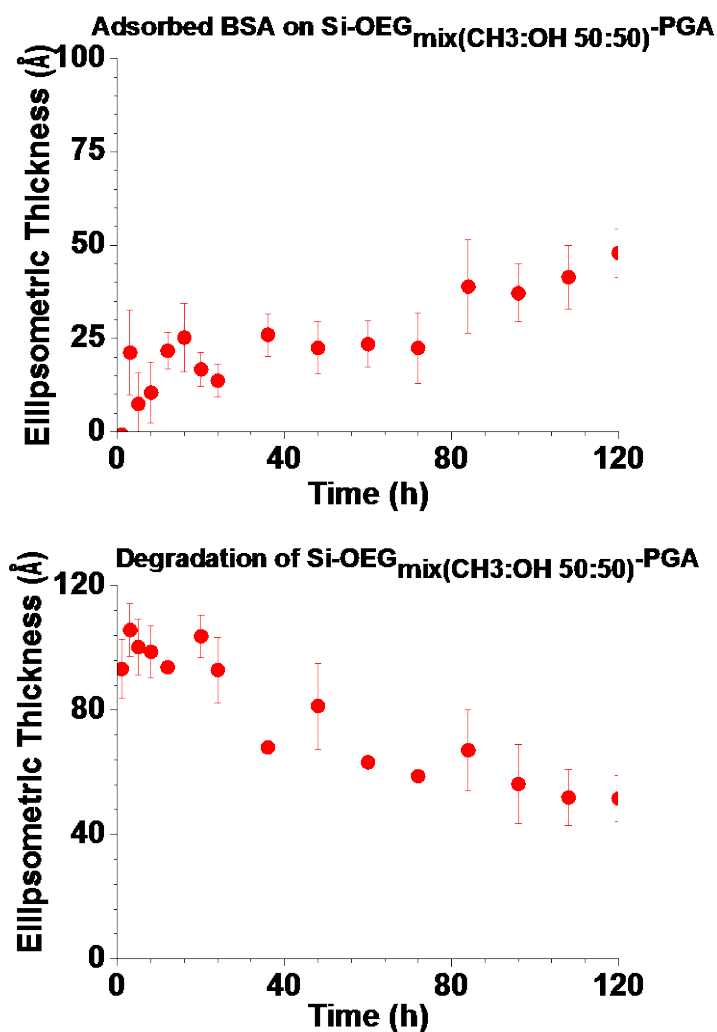


Figure 3.2.13 Plots of ellipsometric thicknesses of (top) adsorbed BSA on Si-OEG<sub>mix</sub>-PGA brushes and (bottom) Si-OEG<sub>mix</sub>-PGA brushes (mixed OEG substrate layer: 50% : 50% methyl and hydroxy terminated OEG) after BSA was removed by sonication in 5 wt% SDS(aq) versus incubation time in 4.5 mg/mL BSA (PBS, pH 7.4, 100 mM ionic strength, 37 °C) solutions. Error bars represent the magnitude of the 90% confidence interval for five measurements on one sample.

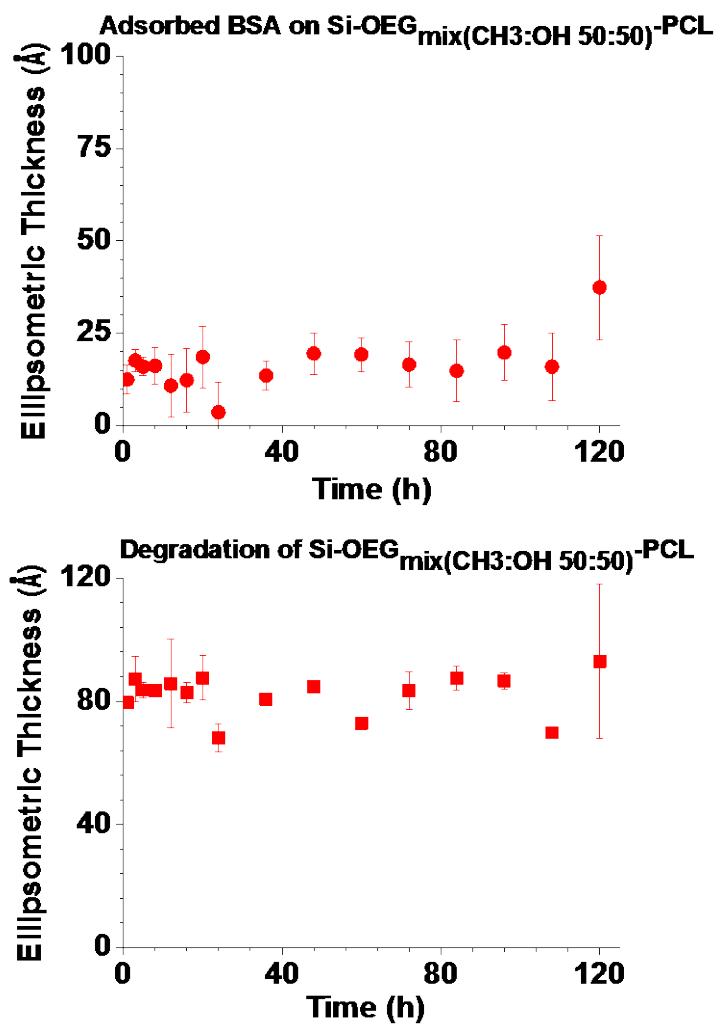


Figure 3.2.14 Plots of ellipsometric thicknesses of (top) adsorbed BSA on Si-OEG<sub>mix</sub>-PCL brushes and (bottom) Si-OEG<sub>mix</sub>-PCL brushes (mixed OEG substrate layer: 50% : 50% methyl and hydroxy terminated OEG) after BSA was removed by sonication in 5 wt% SDS(aq) versus incubation time in 4.5 mg/mL BSA (PBS, pH 7.4, 100 mM ionic strength, 37 °C) solutions. Error bars represent the magnitude of the 90% confidence interval for five measurements on one sample.

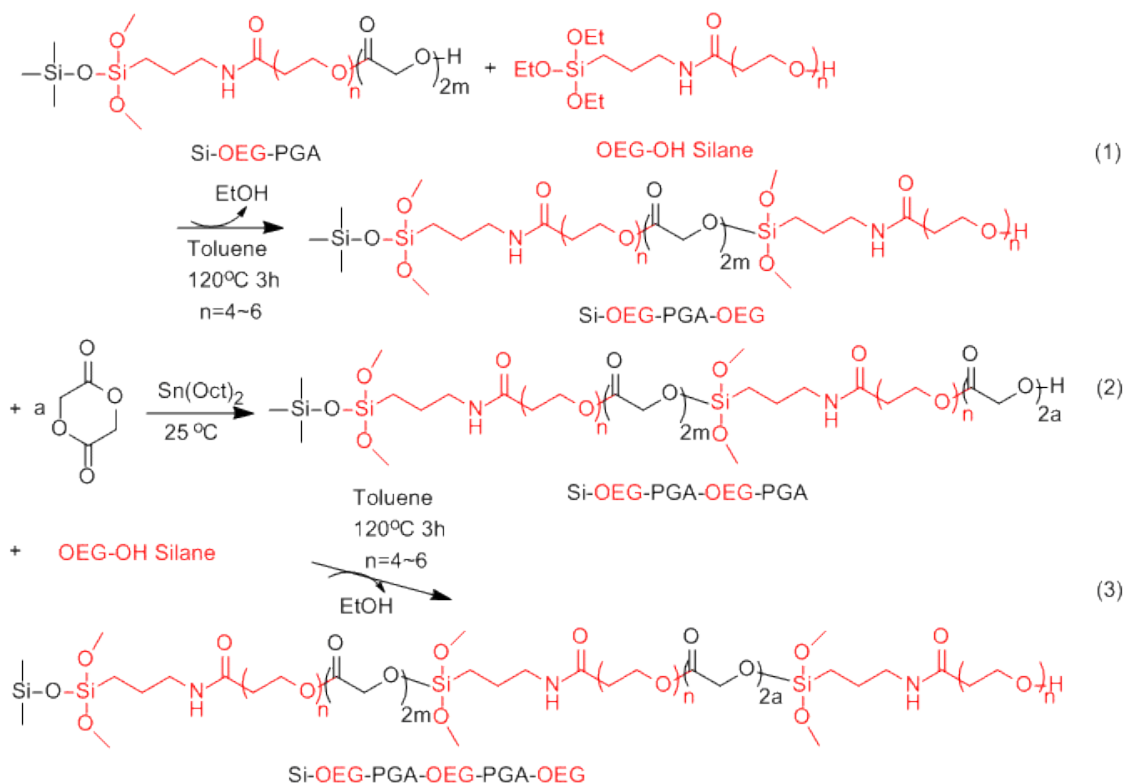
At this ionic strength, reduced BSA adsorption on brush surface concomitant with improved brush degradability were achieved. This result can be attributed to both (1) increased access to OEG moieties by adjusting the relative amount of OEG and PGA components and (2) the better degradability of PGA than PLA and PCL.

The same experiment was repeated on Si-OEG<sub>mix</sub>-PCL brushes. PCL brushes with similar thickness as the PGA brushes discussed above was prepared on mixed OEG layer with 50% to 50% OEG-OMe and OEG-OH. BSA adsorption and brush degradation were monitored by ellipsometry by measuring thickness before and after protein removal with SDS. As can be seen from Figure 3.2.14, although a low-level of protein adsorption was obtained when using PCL as the outer layer on the mixed OEG surface, the degradation of PCL brushes was negligible compared to the Si-OEG<sub>mix</sub>-PGA brushes.

**v. BSA Adsorption on Multilayer Co-polymer Brushes**

BSA adsorption was also investigated on multilayer co-polymer brushes. The sequence for growing such multilayer co-polymer brushes is illustrated in Scheme 3.2.3.

**Scheme 3.2.3 Synthesis of multilayer Si-(OEG-PGA)<sub>2</sub>-OEG co-polymer brushes.**



Similar Si-OEG-PGA brushes were first prepared following Scheme 3.2.2. A second OEG layer was then deposited on top of the brush as shown in Scheme 3.2.3 (eq. 1). Two more layers were further grown followed by the sequence of (1) PGA (eq. 2) and (2) OEG (eq. 3) through the same preparation methods as discussed above. Ellipsometric thickness of each layer is shown in Figure 3.2.15. The aim was to increase the ratio of OEG to polyester as well as the brush hydrophilicity. The ellipsometric thickness of brush after protein adsorption was measured. Degradation of the brush was also conducted in buffer solution without protein under pH 7.4. The results are shown in Figure 3.2.16.

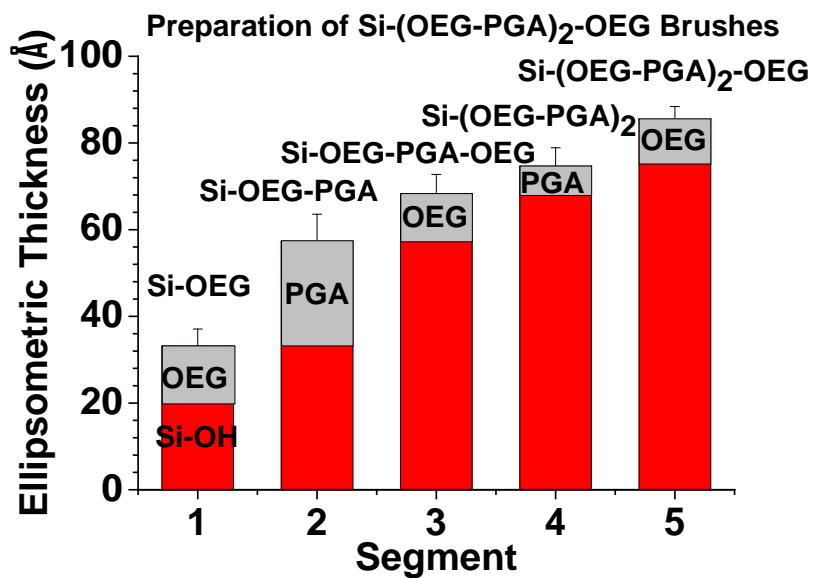
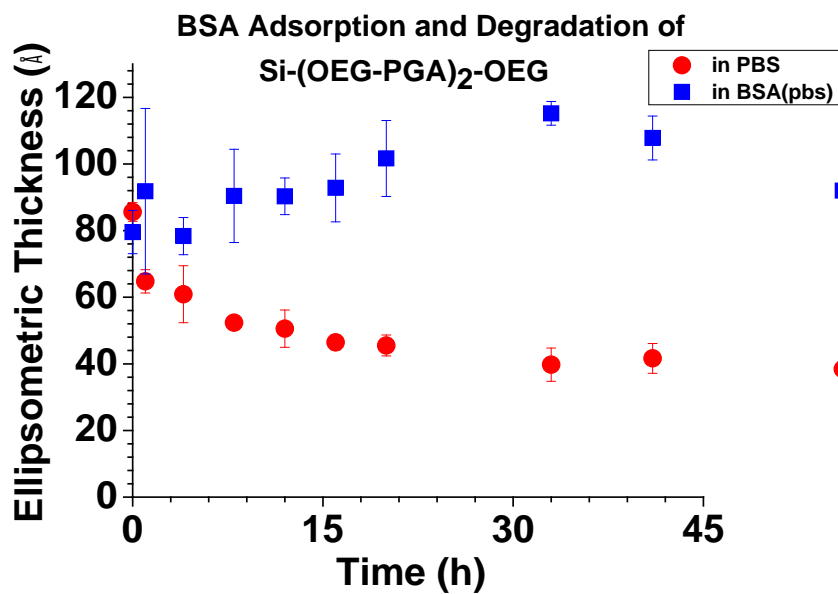


Figure 3.2.15 Plot of ellipsometric thicknesses after the growth of each segment in multilayer Si-(OEG-PGA)<sub>2</sub>-OEG brushes. Error bars represent the magnitude of the 90% confidence interval for ten measurements on two sample.



**Figure 3.2.16** Plots of ellipsometric thicknesses of Si-(OEG-PGA)<sub>2</sub>-OEG brushes versus incubation time in PBS (pH 7.4) and 4.5 mg/mL BSA(PBS, pH 7.4, 10 mM ionic strength, 37 °C) solutions. Error bars represent the magnitude of the 90% confidence interval for five measurements on one sample.

The experiment was carried out under low ionic strength condition. Nevertheless, a very small increase in thickness, less than 4 nm, was obtained after 45 h incubation indicating a substantial anti fouling property of this brush. The brush was degradable in basic buffer solutions while this process was to some extent compromised in buffer solutions containing proteins which might be due to the low salt concentration.

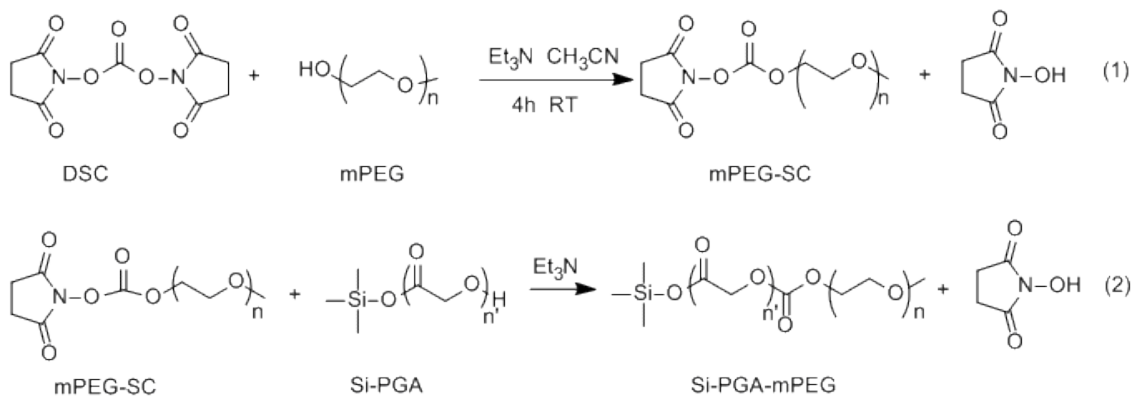
### 3.2.3 BSA Adsorption on PEG Modified Brushes

#### i. PEGylation of Brushes with Synthesized and Commercial PEG Derivatives

As discussed above, short chain OEG was exploited to make co-polymer brushes with polyesters and these co-polymer brushes better suppress protein adsorption than single polyester brushes. Moreover, it is reported that PEG with longer chains demonstrates higher

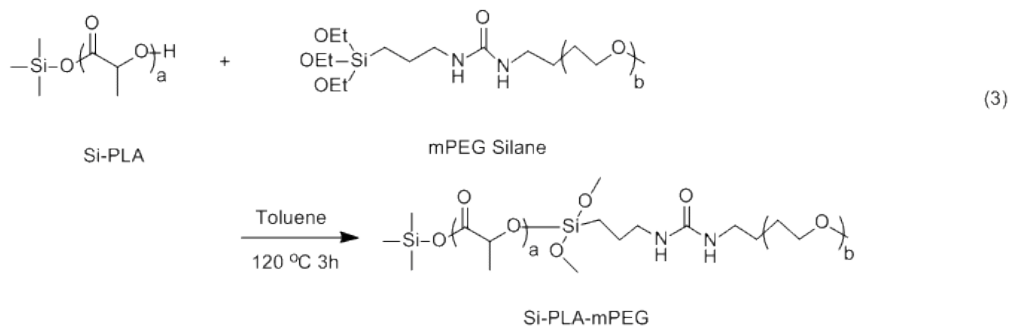
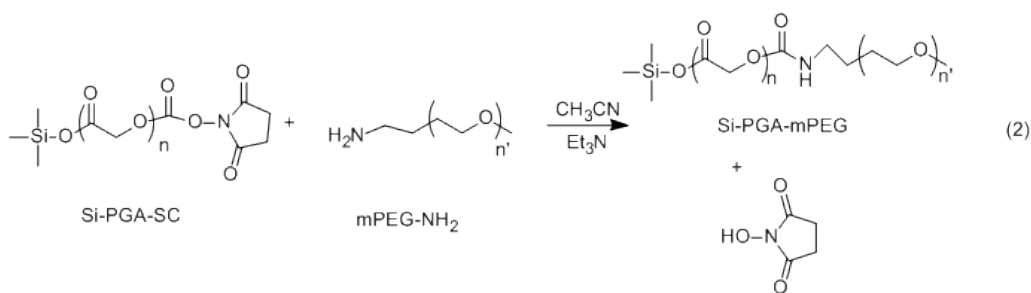
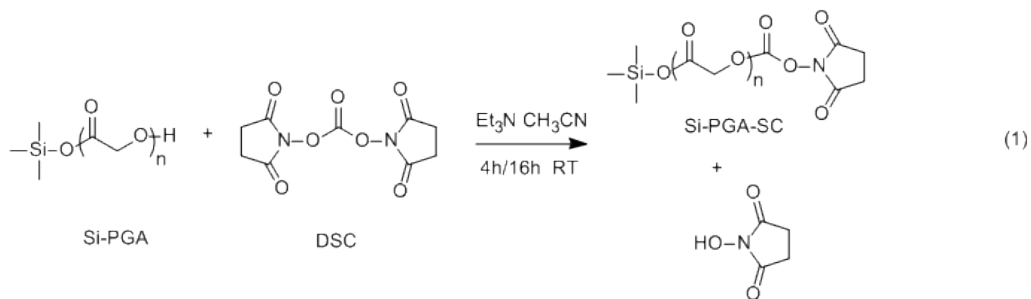
efficiency in resisting protein adsorption than with shorter chains.<sup>11</sup> Thus, some effort was devoted to the modification of polyester brushes with longer chain PEGs.

**Scheme 3.2.4 Synthesis of SC activated mPEG<sub>2000</sub> and PEGylation of PGA brushes with mPEG<sub>2000</sub>-SC.**



Initially, methoxy poly(ethylene glycol)<sub>2000</sub> (mPEG<sub>2000</sub>) was reacted with N,N'-disuccinimidyl carbonate (DSC) to form methoxy poly(ethylene glycol)<sub>2000</sub> N-succinimidyl carbonate (mPEG<sub>2000</sub>-SC) as shown in Scheme 3.2.4 (eq. 1).<sup>12</sup> The PEG derivatives were then applied to modify the PGA brush surface (eq. 2).<sup>13</sup> However, no evident thickness increase was observed under all tested conditions (described in experimental section). This result is likely due to the low reactivity of the PEG derivatives with hydroxy groups since more studies were reported on the PEGylation of these derivatives on amine groups.<sup>12a, 14</sup> Therefore, alternative PEGylation methods were conducted on polyester brush surfaces as described in Scheme 3.2.5.

**Scheme 3.2.5 PEGylation of SC modified PGA brushes with mPEG<sub>5000</sub>-NH<sub>2</sub> and PEGylation of PLA brushes with mPEG<sub>2000</sub> silanes.**



The first alternative PEGylation scheme was performed by modifying a PGA brush with DSC (eq. 1) followed by PEGylating the brush with mPEG<sub>5000</sub>-NH<sub>2</sub> (eq. 2).<sup>15</sup> The second method was carried out by PEGylating the PLA brush with mPEG<sub>2000</sub> silanes (eq. 3).<sup>16</sup> Under all conditions investigated, a maximum of around 2 nm thickness increase of the brush was attained after PEGylation which is very similar to the result of previously

studied OEG modification. This indicates a relatively low grafting density of PEG chains on the polyester brush surface.<sup>16b</sup> The grafting density of both OEG and PEG on brush surface can be calculated using the following equation (eq. 1),

$$Mn \left( \frac{g}{mol} \right) = \frac{h(nm)\rho \left( \frac{g}{cm^3} \right) N_A (mol^{-1})}{\sigma (nm^{-2})} \times 10^{-21} \left( \frac{cm^3}{nm^3} \right) \quad (1)$$

Grafting density of OEG:

$$500 \left( \frac{g}{mol} \right) = \frac{1.7(nm) \times 1.08 \left( \frac{g}{cm^3} \right) \times 6.02 \times 10^{23} (mol^{-1})}{\sigma (nm^{-2})} \times 10^{-21} \left( \frac{cm^3}{nm^3} \right) \quad (2)$$

$$\sigma(\text{OEG}) = 2.21 \text{ nm}^{-2}$$

Grafting density of PEG<sub>5000</sub>:

$$5000 \left( \frac{g}{mol} \right) = \frac{2(nm) \times 1.08 \left( \frac{g}{cm^3} \right) \times 6.02 \times 10^{23} (mol^{-1})}{\sigma (nm^{-2})} \times 10^{-21} \left( \frac{cm^3}{nm^3} \right) \quad (3)$$

$$\sigma(\text{PEG}_{5000}) = 0.26 \text{ nm}^{-2}$$

Grafting density of PEG<sub>2000</sub>:

$$2000 \left( \frac{g}{mol} \right) = \frac{2(nm) \times 1.08 \left( \frac{g}{cm^3} \right) \times 6.02 \times 10^{23} (mol^{-1})}{\sigma (nm^{-2})} \times 10^{-21} \left( \frac{cm^3}{nm^3} \right) \quad (4)$$

$$\sigma(\text{PEG}_{2000}) = 0.65 \text{ nm}^{-2}$$

where Mn is the molecular weight (g/mol), h is the thickness (nm), ρ is the density (g/cm<sup>3</sup>), N<sub>A</sub> is the Avogadro's number (mol<sup>-1</sup>) and σ is the grafting density (nm<sup>-2</sup>). As can be seen from the calculation, PEGylations with long chain PEGs reveal much lower grafting density, ca. 0.26~0.65 nm<sup>-2</sup>, than with short chain OEG which has grafting density around ca. 2.21 nm<sup>-2</sup>. This result presumably is because more space is required by each PEG chain than OEG due to steric hindrance.<sup>16b</sup>

## ii. BSA Adsorption on PEG Modified Brushes

After the PEGylation on silicon and polyester brushes with long chain mPEG<sub>2000</sub> silanes, BSA adsorption was investigated. Ellipsometric thicknesses of adsorbed protein were collected as a function of incubation time. Degradation of PEG modified PLA brushes was also studied. The results are shown in Figure 3.2.17.

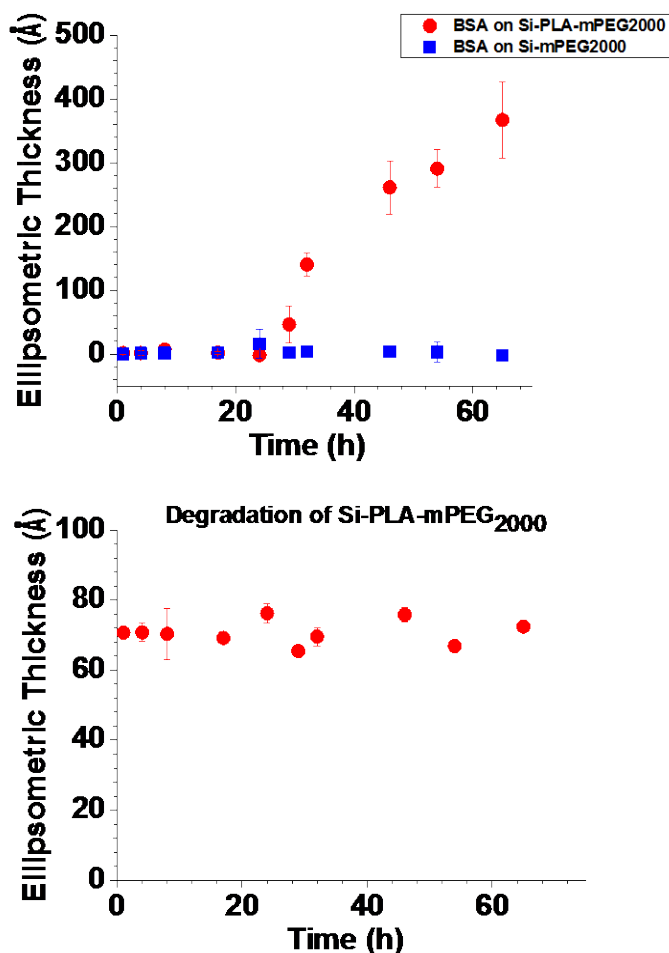


Figure 3.2.17 Plots of ellipsometric thicknesses of (top) adsorbed BSA on mPEG<sub>2000</sub> brushes and mPEG<sub>2000</sub> modified PLA brushes and (bottom) bare mPEG<sub>2000</sub> modified PLA brushes versus incubation time in 4.5 mg/mL BSA (PBS, pH 7.4, 10 mM ionic strength, 37 °C) solutions. Error bars represent the magnitude of the 90% confidence interval for five measurements on one sample.

Protein adsorption on PEG modified PLA brushes started to occur after 24 h while no adsorption was detected on PEG modified silicon surface during 60 h incubation. The

possible explanations for this behavior are (1) the low ionic strength of the buffer used and (2) the low grafting density of PEG on the brush surface.<sup>17</sup> The hydrophilicity of the brush might not be greatly improved compared to using short chain OEG due to the low grafting density of PEG on surface. Furthermore, the low ionic strength might also facilitate the hydrophobic interaction between the protein molecules and the brush surface.

### 3.2.4 Quantitative Characterization of BSA Adsorption on Brushes

#### i. Calculation of Adsorbed Protein using Dry Ellipsometric Thickness

In addition to the study of protein adsorption effect on various brush surfaces, characterization methods were also explored so as to quantify the adsorbed proteins on surface. Ellipsometry was utilized to provide the dry thickness of adsorbed protein layer. In order to use the thickness to calculate the quantity of protein on surface, such as adsorption density  $\sigma$  (molecule/nm<sup>2</sup>), an assumption is made which is described as follows.

It is generally understood that the structure of BSA is prolate ellipsoid (4×4×14 nm<sup>3</sup>).<sup>18</sup> Thus, the volume can be calculated based on its dimension parameters. However, it might be difficult to determine the actual volume if the structure of BSA changes due to denaturation and dehydration. In this work, calculation using ellipsometric thickness is carried out adopting the assumption that the shape of BSA molecule is not changed after adsorption; therefore, the volume of BSA used in the calculation is not the dry volume but the one after solvation. An example using thickness to calculate the adsorption density is illustrated here. If the thickness of adsorbed BSA is around 10 nm, the adsorption density can be calculated using the following equation (eq. 5) which is derived from eq. 1,

$$\sigma \text{ (molecule/nm}^2\text{)} = h \text{ (nm)} \frac{1}{\frac{4}{3}\pi abh} \text{ (nm}^{-3}\text{)} \quad (5)$$

$$\sigma \text{ (molecule/nm}^2\text{)} = 10 \text{ (nm)} \frac{1}{\frac{4}{3}\pi \times 2 \times 2 \times 7} \text{ (nm}^{-3}\text{)} = 0.85 \text{ molecule/nm}^2 \quad (6)$$

where a, b and h represent the three radii along the three axes of the BSA molecule.

#### ii. Calculation of Adsorbed Protein using BCA Protein Assay Measurement

A protein assay is another technique that can offer absolute quantity of adsorbed proteins. A bicinchoninic acid (BCA) protein assay was employed in this work due to its high

resolution (detection limit:  $\sim 0.5 \mu\text{g/mL}$ ).<sup>19</sup> The solution-based characterization method is rarely applied on flat surface because the amount of collected protein is relatively low due to the limited surface area. In order to test the feasibility of the method, the required minimum surface area of brush samples is calculated based on the detection limit.

The minimum surface area of brush samples is calculated using the following equation,

$$m(BSA) (g) = \frac{h (nm)s (nm^2)}{\frac{4}{3}\pi abh (nm^3)N_A (mol^{-1})} \times Mn(BSA) (g/mol^{-1}) \quad (7)$$

where  $m$  is the actual mass of BSA (g) and  $s$  is the surface area of the brush sample ( $\text{nm}^2$ ). Assuming a minimum of 0.5 mL solution is necessary to wash off the adsorbed BSA from each substrate and the thickness of adsorbed BSA is around 10 nm, the area of brush sample can be calculated using the following equation,

$$0.5 \times 10^{-6} \text{ g/mL} \times 0.5 \text{ mL} = \frac{10 (nm)s (nm^2)}{\frac{4}{3}\pi \times 2 \times 2 \times 7 (nm^3) \times 6.02 \times 10^{23} (mol^{-1})} \times 66463 (g/mol^{-1}) \quad (8)$$

$$s = 2.39 (cm^2)$$

where the detection limit of BCA assay,  $0.5 \mu\text{g/mL}$ , is applied. According to the result, square shaped silicon sample with side length at least around 1.5 cm is required. The calculated sample size is within a reasonable scale, so the BCA assay method was deemed to be applicable. Due to the requirement of using small amount detergent to remove proteins from the surface, a small vial for collecting protein was designed (discussed in experimental section).

Before evaluating the amount of surface attached proteins using BCA assay, a calibration was conducted using standard BSA solutions at two concentration ranges, 0-5  $\mu\text{g/mL}$  and 0-2000  $\mu\text{g/mL}$ . Considering that the variance of the data might be affected by the level of analyte, both weighted and non-weighted linear regressions were performed.<sup>20</sup> The results are shown in Figure 3.2.18 and 3.2.19.

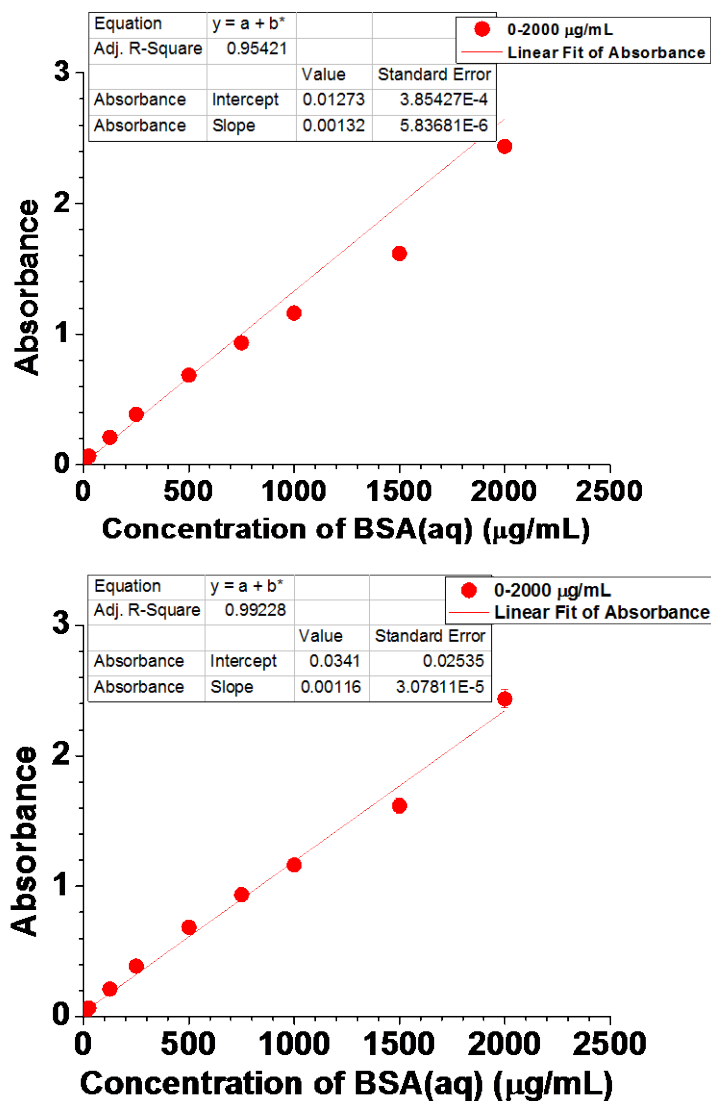


Figure 3.2.18 (top) Weighted with standard errors and (bottom) non-weighted calibration curves of BCA protein assay over 0-2000 ug/mL BSA (aq) range. Error bars represent (top) the relative errors and (bottom) the magnitude of the 90% confidence interval for five readings on one sample.

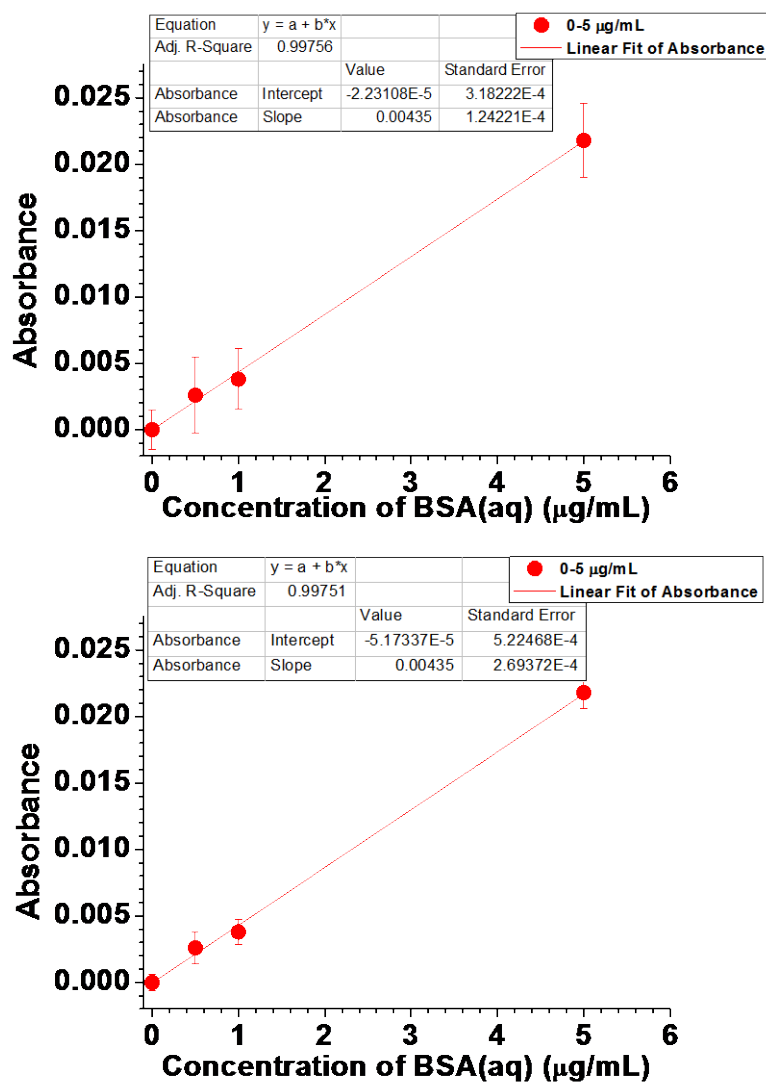
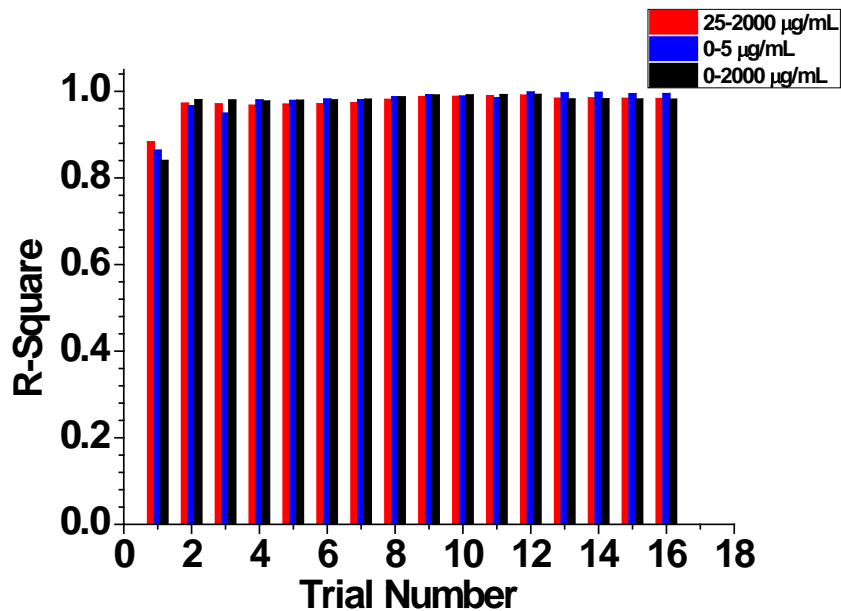


Figure 3.2.19 (top) Weighted with standard errors and (bottom) non-weighted calibration curves of BCA protein assay over 0-5 µg/mL BSA (aq) range. Error bars represent (top) the relative errors and (bottom) the magnitude of the 90% confidence interval for five readings on one sample.

As can be seen from the correlation coefficients of the linear fit curves, calibrations

on both concentration ranges demonstrated good linear relationship between protein concentration and absorbance. The difference between weighted and non-weighted linear regressions over 0-2000  $\mu\text{g/mL}$  range is larger than over 0-5  $\mu\text{g/mL}$  range. This might be related with the higher magnitude of the solution concentration. Taking the analyte associated variance into consideration, the weighted linear regression might be more appropriate (close to the actual relationship between protein concentration and absorbance) for high concentration range since the regression minimized the sum of the (deviation/variance). Nevertheless, in this work, most of the protein samples collected from the surface were in the low concentration range. Thus, the calculation is mainly based on the calibration over 0-5  $\mu\text{g/mL}$  range. Due to the small difference between the weighted and non-weighted linear regressions under this concentration range, the result derived from non-weighted regression is not shown.

While doing the calibrations, it was found that, in addition to the concentration range of the standard protein solutions, the developing time of the BCA assay also influences the goodness of fit of the linear regressions. As can be seen from Figure 3.2.20, at least 20 min is required to obtain a good calibration. Although the best linear fit was obtained after about two hours incubation, the difference between the calibration after 20 min and 2 h incubation is rather small.



**Figure 3.2.20 Linearity of BCA protein assay calibration curves versus incubation time over different BSA (aq) concentration ranges. Measurements were taken every ten minutes until two hours (trial 12) and then every four hours.**

The adsorption density of BSA on PGA brushes was calculated using the BCA method as a function of incubation time. The results are compared with the ellipsometric thickness of adsorbed BSA.

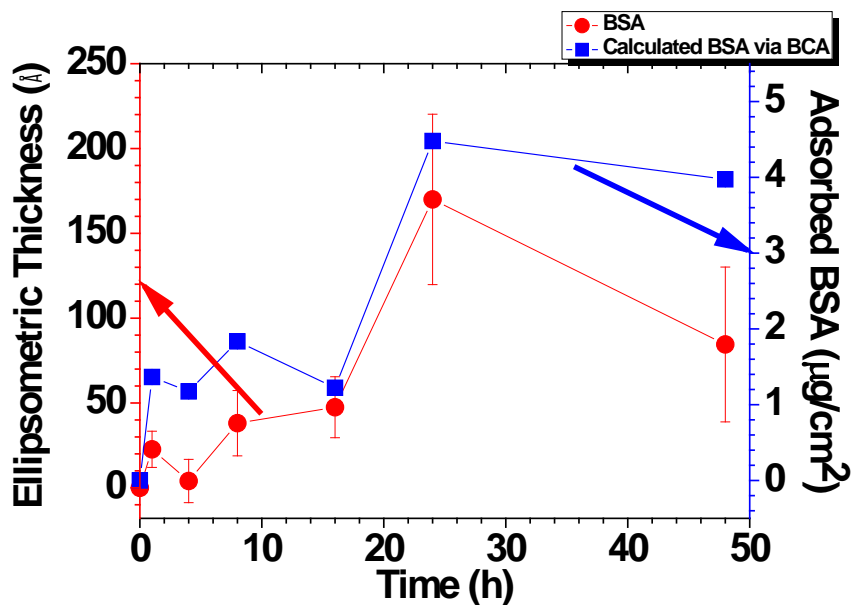


**Figure 3.2.21** Plots of ellipsometric thicknesses and BCA protein assay calculated adsorbed BSA on grafted PGA brushes versus incubation time in 4.5 mg/mL BSA (PBS, pH 7.4, 10 mM ionic strength, 37 °C) solutions. Error bars represent the magnitude of the 90% confidence interval for five measurements on one sample.

As can be seen from the graph above, the two techniques generally indicated similar trends in adsorption. Nevertheless, there is still difference between the results measured by the two methods. The thickness of the adsorbed protein was calculated by subtracting the thickness measured after incubation from the thickness measured after sonication. This value is likely to be higher than the thickness of the actual attached protein since the layer sonicated off might also contain some degraded brush. The different sources of errors might result in variation between two methods.

### iii. Quantitative Characterization Study of Adsorbed Protein with ATR-FTIR

ATR-FTIR is also a potential candidate for characterizing the adsorption process of BSA on polyester brushes.<sup>21</sup> The quantity of adsorbed protein and polyester brushes can be

compared. This can be accomplished by calculating the integration of amide characteristic peaks from BSA and the carbonyl peak from the brush. (Figure 3.2.22) Although both amide peaks (I & II) are well distinguishable from the carbonyl peak of the brush (Figure 3.2.23), amide I region tends to overlap with a water band.<sup>22</sup> This water band is difficult or impossible to remove even on 'dry' samples (Figure 3.2.24). The amide II band of BSA is thus considered to be more suitable for the comparison with the carbonyl peak of the brush than the amide I band. Deconvolution of the spectra and peak fitting were performed to evaluate the peak areas of amide II and carbonyl bands.<sup>21</sup> The ratio of these two peaks was then compared with the results derived from ellipsometry. The results are shown in Figure 3.2.25.

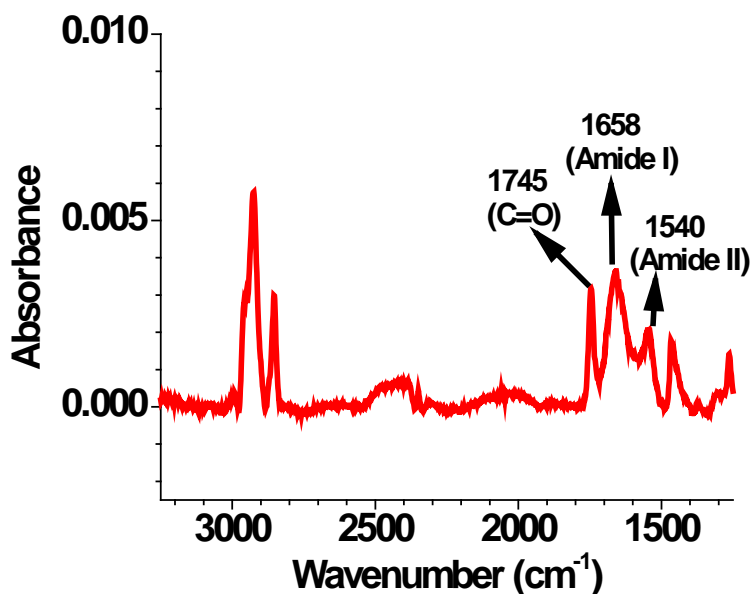


**Figure 3.2.22** Plot of ATR-FTIR spectrum of PLA brushes after adsorption with BSA.

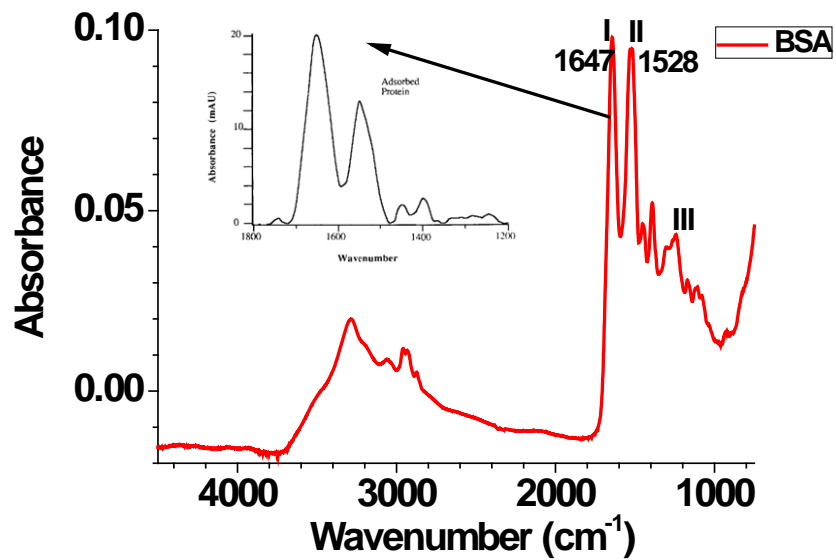


Figure 3.2.23 Plot of ATR-FTIR spectrum of bulk BSA. Inset shows characteristic amide I and II peaks of surface adsorbed BSA from the literature.<sup>22a</sup>

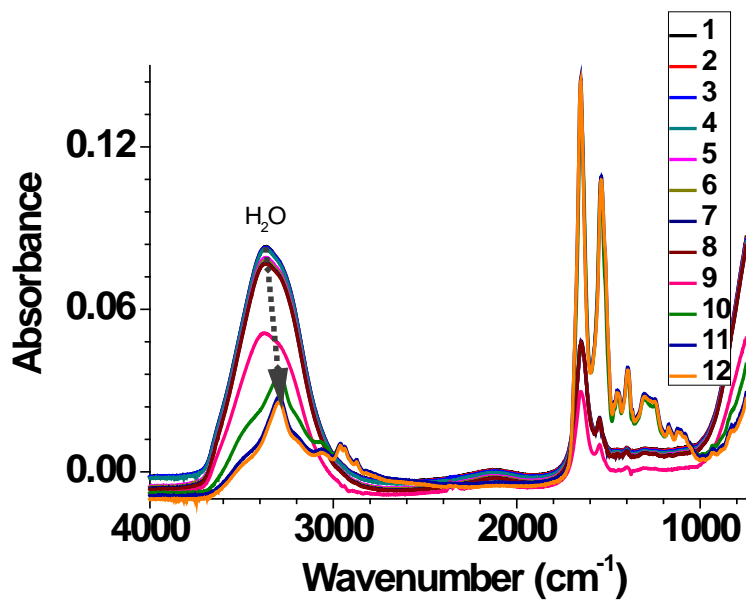
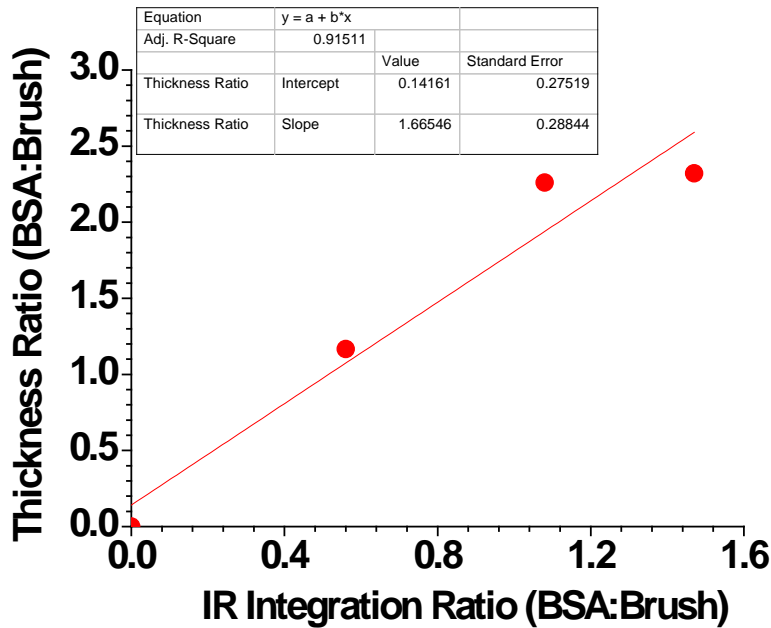


Figure 3.2.24 Plots of ATR-FTIR spectra of BSA from aqueous solution to gelation state.



**Figure 3.2.25 Plot of linear regression of quantity ratio between BSA and PLA brushes calculated based on ellipsometric thickness and ATR-FTIR spectra.**

The regression between the results obtained from the two techniques is not ideally linear which might have resulted from the errors of different methods. Nevertheless, using multiple methods to characterize the protein adsorption process can provide complementary information. Preliminary results suggested these studied techniques are relatively comparable.

### **3.3 Conclusions**

Biofouling and brush degradation were systematically studied using BSA(PBS) as standard protein solutions. It was first found that salt concentration played an important role in the rate of protein adsorption. Immersing samples in protein buffers with low salt concentration (10 mM) resulted in fast and enhanced BSA adsorption. This was explained by the increased affinity between protein molecules and polymer surfaces due to hydrophobic interactions and reduced electrostatic repulsions. BSA buffers with revised ionic strength

(100 mM) were then applied in the study of both protein adsorption and brush degradation in order to obviate the fast fouling caused by low salt concentration.

BSA adsorption was tested on various brush surfaces. PLA, PGA and PCL brushes demonstrated extensive adsorption of BSA after a short incubation time (20 h). The result indicated the relative hydrophobicity of the polyester brush surfaces. Modifications of these brushes to introduce protein resistant components (OEG and PEG) to make co-polymer brushes were conducted. It was found that both brush structure and relative amount of OEG and polyester are essential in adjusting the protein resistance of the brushes. An anti-fouling surface can be obtained by either using OEG or PEG as an outside layer or by increasing the amount of OEG relative to polyester when using OEG-OH and OEG-OMe mixture as the substrate layer.

Degradation of different brushes in protein solution was also thoroughly examined. Degradation of single polyester brushes and their co-polymer brushes using OEG-OH (100%) as a substrate layer was hindered. Similar behavior was also observed on co-polymer brushes using OEG as an outside layer. These two results were rationalized by the inhibition of the proposed backbiting process when the hydroxy end groups of polyester were blocked by protein molecules and OEG molecules respectively. Among all brush surfaces tested, PGA co-polymer brushes using OEG-OH and OEG-OMe mixture as the substrate layer was found to be both protein resistant and degradable. This result was likely due to the relatively large amount of OEG moieties and better degradability of PGA.

Different techniques were investigated for quantitatively characterizing the adsorption of BSA on brush surfaces. The surface density of adsorbed BSA can be estimated using ellipsometric thickness assuming that the shape of BSA molecule is not changed upon adsorption. It was also demonstrated that a BCA protein assay and ATR-FTIR can be applied to quantify the amount of adsorbed BSA. The results were relatively comparable with those obtained by ellipsometry.

## 3.4 Experimental

### 3.4.1 Preparation of Co-polymer Brushes

The preparation of silicon substrates and PLA, PGA and PCL brushes were conducted in the same way as described in the previous chapter. Co-polymer brushes of these polyesters with OEG and PEG were prepared in a dinitrogen-filled dry box. Depending on the structure of the co-polymer brushes (i.e. using OEG as the substrate layer or as an outside layer), PEGylation was performed on bare silicon surfaces or polyester brush surfaces. Each bare silicon or brush sample was placed in a 20 mL glass vial and transferred in to the dry box. To each sample 5 mL of OEG silane (Gelest, USA) solutions (25 mM OEG-OH or OEG-OMe or their mixtures in anhydrous toluene) or PEG silane (Laysan Bio) solutions (25 mM in anhydrous toluene) was added. The sample vials were then sealed tightly with Teflon caps and transferred to an oil bath. Reactions were run at 120 °C for 3 h. After the reaction, samples were thoroughly rinsed with toluene followed by drying under a stream of nitrogen.

### 3.4.2 PEGylation of Brushes with Synthesized PEG Derivatives

#### i. Synthesis of SC activated mPEG<sub>2000</sub> and PEGylation of PGA brushes with mPEG<sub>2000</sub>-SC

mPEG<sub>2000</sub> (1.9 g, 0.95 mmol) was dissolved in anhydrous acetonitrile (4.0 mL). DSC (0.46 g, 1.8 mmol) and anhydrous triethylamine (0.63 mL, 4.6 mmol) were then added under nitrogen. The clear solution was stirred at room temperature for 4 h and then concentrated using a rotatory evaporator. The product (mPEG<sub>2000</sub>-SC) was precipitated, washed several times with diethyl ether and recrystallized from isopropanol twice. The precipitate was then filtered and dried under high vacuum (5 millitorr) to give 1.8 g (yield 88%) white solid. <sup>1</sup>H NMR (CDCl<sub>3</sub> δ in ppm): 4.47 (t, 2H, CH<sub>2</sub>-SC), 3.63 (s, 180H, PEG), 2.83 (s, 4H, SC-group).

PEGylation of PGA brushes with synthesized mPEG<sub>2000</sub>-SC was performed in the dinitrogen-filled dry box. Each sample was placed in a 20 mL glass vial and 20 μL dry triethylamine and 5 mL mPEG<sub>2000</sub>-SC (5~10 mmol/L, in anhydrous chloroform or toluene)

was added. The sample vials were then sealed tightly with Teflon caps and transferred to an oil bath. Reactions were run at a given temperature (40~100 °C) for 2~12 h. After PEGylation, samples were rinsed with excess chloroform or toluene and dried using a stream of nitrogen.

**ii. PEGylation of SC modified PGA brushes with mPEG<sub>5000</sub>-NH<sub>2</sub>**

Modification of PGA brushes with DSC was performed in the dinitrogen-filled dry box. Each sample was placed in a 20 mL glass vial and 0.4 mL of triethylamine and 5 mL of DSC (1 mmol/L, in anhydrous acetonitrile) solution were added. The sample vials were then sealed tightly with Teflon caps and transferred to an incubator with a rotation speed of 100 rpm. Reactions were run at room temperature for 4 h. After modification, samples were rinsed with excess ethanol and dried using a stream of nitrogen.

PEGylation of PGA-SC with mPEG<sub>5000</sub>-NH<sub>2</sub> (Fluka) was also conducted in the dinitrogen-filled dry box. Each sample was placed in a 20 mL glass vial and 10 µL of dry triethylamine and 5 mL of mPEG<sub>5000</sub>-NH<sub>2</sub> (10 mmol/L, in anhydrous chloroform) solution were added. The sample vials were then sealed tightly with Teflon caps and transferred to an oil bath. Reactions were run at a give temperature (40-80 °C) for 24 h. After PEGylation, samples were rinsed with excess chloroform and dried using a stream of nitrogen.

**3.4.3 Adsorption of Protein on Brush Substrates and Degradation of Brushes**

Protein adsorption on various brush surfaces were conducted by immersing the sample in 4 mL of freshly prepared BSA(PBS) with different concentrations at pH 7.4 in a 12-well plastic plate. The ionic strength of the protein buffer was adjusted with sodium chloride. The plate was placed in an incubator at a 37 °C and rotation speed of 100 rpm. At various time points, the sample was removed from the protein buffer and rinsed with excess DI water, then dried with a stream of nitrogen.

**3.4.4 Protein Desorption via Sonication**

The removal of adsorbed protein was carried out by sonicating the samples in 5 wt% SDS(aq) solutions for 1 h. The samples were then rinsed with excess DI water and dried with a stream of nitrogen. When performing BCA protein assays, sonication of brush samples was

conducted in a plastic vial as shown in Figure 3.4.1. Two replicated samples (1.5 cm × 1.5 cm) were inserted in the vial and 0.5 mL of SDS(5 wt%, aq) solution was added. After 1 h sonication, the solution was collected to run the protein assay and the samples were rinsed thoroughly with DI water followed by drying under nitrogen.

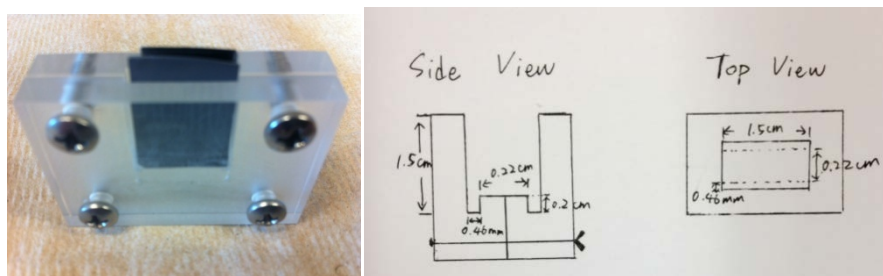


**Figure 3.4.1 Photograph (left) and design scheme (right) of a plastic vial used as a sample container during sonication.**

### 3.4.5 Ellipsometry Measurements

The thickness of brushes was measured using a single-wavelength ellipsometer at a 70 degree angle (AutoEL-III, Rudolph Research, Flanders, NJ). All measurements were taken on dry samples. Five measurements, four at the corners and one at the center, were taken on each sample. Each sample was measured after treatment under UVO, after the growth of polymer brushes, after protein adsorption and after sonication in 5 wt% SDS(aq). The thickness of polymer brush sample was calculated by subtracting the initial value after UVO treatment from that obtained after growth of brush. The thickness of adsorbed protein was calculated by subtracting the value after sonication in detergent solution from that after incubation with protein solution.

### 3.4.6 BCA Protein Assay Measurements

The BCA (Thermo Scientific) working reagent was prepared by mixing reagent A and B under a volume ratio of 50:1. The BSA standards and collected protein solutions were first added to a 96-well microplate with flat bottoms. The mixed BCA working reagent was then added to each sample under a volume ratio of 8:1 (200  $\mu$ L BCA and 25  $\mu$ L BSA

solution). The plate was capped and samples were incubated at room temperature for a given time to allow the color to develop. The readings were taken by a plate reader (Synergy HT) at 562 nm.

#### **3.4.7 ATR-FTIR Measurements**

ATR-FTIR spectra were collected on the Excalibus Series bench (Varian) with the MIRacle Single Reflection ATR kits (PIKE). The ATR crystal was a germanium crystal. The pressure to hold the sample was 530 lb. The background scans were collected in air.

#### **3.4.8 NMR**

NMR spectra were recorded on a 300 Hz Gemini 2300 spectrometer using  $\text{CDCl}_3$  as the solvent.

## REFERENCES

1. (a) Wang, R.; Lajevardi-Khosh, A.; Choi, S.; Chae, J., Regenerative Surface Plasmon Resonance (SPR) biosensor: real-time measurement of fibrinogen in undiluted human serum using the competitive adsorption of proteins. *Biosens Bioelectron* 2011, 28 (1), 304-7; (b) Demneh, S. M. G.; Nasernejad, B.; Modarres, H., Modeling investigation of membrane biofouling phenomena by considering the adsorption of protein, polysaccharide and humic acid. *Colloids Surf., B* 2011, 88 (1), 108-114.
2. (a) Grafahrend, D.; Heffels, K. H.; Beer, M. V.; Gasteier, P.; Moller, M.; Boehm, G.; Dalton, P. D.; Groll, J., Degradable polyester scaffolds with controlled surface chemistry combining minimal protein adsorption with specific bioactivation. *Nat Mater* 2011, 10 (1), 67-73; (b) Grafahrend, D.; Calvet, J. L.; Klinkhammer, K.; Salber, J.; Dalton, P. D.; Moller, M.; Klee, D., Control of protein adsorption on functionalized electrospun fibers. *Biotechnol Bioeng* 2008, 101 (3), 609-21.
3. (a) Molino, P. J.; Higgins, M. J.; Innis, P. C.; Kapsa, R. M.; Wallace, G. G., Fibronectin and bovine serum albumin adsorption and conformational dynamics on inherently conducting polymers: a QCM-D study. *Langmuir* 2012, 28 (22), 8433-45; (b) Mrksich, M.; Sigal, G. B.; Whitesides, G. M., Surface plasmon resonance permits in situ measurement of protein adsorption on self-assembled monolayers of alkanethiolates on gold. *Langmuir* 1995, 11 (11), 4383-4385; (c) Fang, J.; Wang, P.; Du, X.; Zhu, D.-M., Detailed analysis of quartz crystal microbalance and surface plasmon resonance spectroscopy in probing molecular adsorption onto solid-liquid interfaces. *J. Phys. Chem. C* 2009, 113 (36), 16121-16127; (d) Maruyama, T.; Katoh, S.; Nakajima, M.; Nabetani, H.; Abbott, T. P.; Shono, A.; Satoh, K., FT-IR analysis of BSA fouled on ultrafiltration and microfiltration membranes. *J. Membr. Sci.* 2001, 192 (1-2), 201-207.
4. Seyrek, E.; Dubin, P. L.; Tribet, C.; Gamble, E. A., Ionic strength dependence of protein-polyelectrolyte interactions. *Biomacromolecules* 2003, 4 (2), 273-282.
5. (a) Molino, P. J.; Higgins, M. J.; Innis, P. C.; Kapsa, R. M. I.; Wallace, G. G., Fibronectin and Bovine Serum Albumin Adsorption and Conformational Dynamics on Inherently Conducting Polymers: A QCM-D Study. *Langmuir* 28 (22), 8433-8445; (b) Kim J, Y. J., Protein adsorption on polymer particles. In *Encyclopedia of surface and colloid science*, Hubbard, A. T., Ed. Marcel Dekker: New York, 2002; Vol. 4, pp 4373-4381.

6. Kleijn, M.; Norde, W., The adsorption of proteins from aqueous solution on solid surfaces. *Heterogen. Chem. Rev.* 1995, 2 (3), 157-172.
7. Karlsson, M.; Ekeröth, J.; Elwing, H.; Carlsson, U., Reduction of irreversible protein adsorption on solid surfaces by protein engineering for increased stability. *J. Biol. Chem.* 2005, 280 (27), 25558-25564.
8. Xu, L. Poly(lactic acid) Polymer Brushes as Dynamic Surfaces. Ph.D Dissertation, North Carolina State University, Raleigh, NC, 2011.
9. Melander, W.; Horvath, C., Salt effects on hydrophobic interactions in precipitation and chromatography of proteins - interpretation of lyotropic series. *Arch. Biochem. Biophys.* 1977, 183 (1), 200-215.
10. (a) Jo, S.; Park, K., Surface modification using silanated poly(ethylene glycol)s. *Biomaterials* 2000, 21 (6), 605-616; (b) Liu, S. X.; Kim, J. T.; Kim, S., Effect of polymer surface modification on polymer-protein interaction via hydrophilic polymer grafting. *J. Food Sci.* 2008, 73 (3), E143-E150.
11. Ionov, L.; Synytska, A.; Kaul, E.; Diez, S., Protein-resistant polymer coatings based on surface-adsorbed poly(aminoethyl methacrylate)/poly(ethylene glycol) copolymers. *Biomacromolecules* 2010, 11 (1), 233-237.
12. (a) Zalipsky, S.; Brandeis, E.; Newman, M. S.; Woodle, M. C., Long circulating, cationic liposomes containing amino-PEG-phosphatidylethanolamine. *FEBS Lett.* 1994, 353 (1), 71-74; (b) Andresen, T. L.; Davidsen, J.; Begtrup, M.; Mouritsen, O. G.; Jorgensen, K., Enzymatic release of antitumor ether lipids by specific phospholipase A2 activation of liposome-forming prodrugs. *J. Med. Chem.* 2004, 47 (7), 1694-1703; (c) Boden, N.; Bushby, R. J.; Liu, Q. Y.; Evans, S. D.; Jenkins, T. A.; Miles, R. E., N,N'-disuccinimidyl carbonate as a coupling agent in the synthesis of thiophospholipids used for anchoring biomembranes to gold surfaces. *Tetrahedron* 1998, 54 (38), 11537-11548.
13. [http://www.peg-drug.com/peg\\_Application/Application.html](http://www.peg-drug.com/peg_Application/Application.html).

14. (a) Roberts, M. J.; Bentley, M. D.; Harris, J. M., Chemistry for peptide and protein PEGylation. *Adv. Drug Delivery Rev.* 64, 116-127; (b) Veronese, F. M.; Pasut, G., PEGylation, successful approach to drug delivery. *Drug Discovery Today* 2005, 10 (21), 1451-1458; (c) Shailesh T. Prajapati., e. a., Pegylation: an approach for protein and peptide drug delivery systems. *International Journal of Advances in Pharmaceutical Research* 2011, 2 (6), 252-262; (d) Ghosh, A. K.; Duong, T. T.; McKee, S. P.; Thompson, W. J., N,N'-disuccinimidyl carbonate - a useful reagent for alkoxy-carbonylation of amines. *Tetrahedron Lett.* 1992, 33 (20), 2781-2784.
15. Betancourt, T.; Byrne, J. D.; Sunaryo, N.; Crowder, S. W.; Kadapakkam, M.; Patel, S.; Casciato, S.; Brannon-Peppas, L., PEGylation strategies for active targeting of PLA/PLGA nanoparticles. *J. Biomed. Mater. Res., Part A* 2009, 91A (1), 263-276.
16. (a) Norrman, K.; Papra, A.; Kamounah, F. S.; Gadegaard, N.; Larsen, N. B., Quantification of grafted poly(ethylene glycol)-silanes on silicon by time-of-flight secondary ion mass spectrometry. *J. Mass Spectrom.* 2002, 37 (7), 699-708; (b) Cauda, V.; Argyo, C.; Bein, T., Impact of different PEGylation patterns on the long-term bio-stability of colloidal mesoporous silica nanoparticles. *J. Mater. Chem.* 2010, 20 (39), 8693-8699.
17. Sofia, S. J.; Premnath, V.; Merrill, E. W., Poly(ethylene oxide) grafted to silicon surfaces: Grafting density and protein adsorption. *Macromolecules* 1998, 31 (15), 5059-5070.
18. Halperin, A.; Fragneto, G.; Schollier, A.; Sferrazza, M., Primary versus ternary adsorption of proteins onto PEG brushes. *Langmuir* 2007, 23 (21), 10603-10617.
19. Kitano, H.; Kondo, T.; Kamada, T.; Iwanaga, S.; Nakamura, M.; Ohno, K., Anti-biofouling properties of an amphoteric polymer brush constructed on a glass substrate. *Colloids Surf., B* 88 (1), 455-462.
20. Miller, J. C., *Statistics for Analytical Chemistry*. 2nd ed.; Ellis Horwood Ltd.: Chichester, West Sussex, England, 1988; p 227.
21. Giacomelli, C. E.; Bremer, M.; Norde, W., ATR-FTIR study of IgG adsorbed on different silica surfaces. *J. Colloid Interface Sci.* 1999, 220 (1), 13-23.

22. (a) Lenk, T. J.; Ratner, B. D.; Gendreau, R. M.; Chittur, K. K., IR spectral changes of bovine serum-albumin upon surface-adsorption. *J. Biomed. Mater. Res.* 1989, 23 (6), 549-569; (b) Smith, B. M.; Franzen, S., Single-pass attenuated total reflection Fourier transform infrared spectroscopy for the analysis of proteins in H<sub>2</sub>O solution. *Anal. Chem.* 2002, 74 (16), 4076-4080.

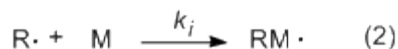
## Chapter 4 Further Study on Microwave Induced Free Radical Polymerization on Nanoparticles

### 4.1 Introduction

#### 4.1.1 Free Radical Polymerization

Free radical polymerization (FRP) has been an important and extensively used method for synthesizing various types of polymers for tens of years. Categorized as a type of chain polymerization, FRP is typically applied for polymerizing monomers containing unsaturated bonds, such as styrene and methyl methacrylate. Similar to other types of chain polymerization methods including ionic (anionic & cationic) and coordination polymerization, polymer with high molecular weight is formed at relatively early stage of polymerization compared to step polymerization.

#### Scheme 4.1.1 Initiation step of free radical polymerization.



FRP usually follows three main steps: initiation, propagation and termination. The first step, initiation, consists of two sub-steps: (1) homolytic dissociation of initiator molecules to form free radicals and (2) transfer of a free radical to the first monomer molecule (Scheme 4.1.1). Since  $k_d$  (rate constant of homolytic dissociation) is in the range of  $10^{-6} \sim 10^{-4} \text{ s}^{-1}$  at temperatures FRP is usually carried out and  $k_i$  (rate constant of initiation) is significantly larger than  $k_d$ , the first sub-step is considered as the rate determining step of initiation process.<sup>1</sup> Radical initiators with bond dissociation energies ranging from 100 kJ/mol to 170 kJ/mol are frequently applied to generate carbon centered and oxygen centered free radicals during initiation step. Organic and inorganic peroxides, azo compounds

and redox systems are the most important classes of radical initiators. For example, benzoyl peroxide (BPO) and 2,2'-azobisisobutyronitrile (AIBN) are commonly used in bulk and organic solution polymerization because they are soluble in most organic solvents.<sup>2</sup> Hydrogen peroxide with iron (II) salts and potassium persulfate ( $K_2S_2O_8$ ) can be used in aqueous solution and in emulsion polymerization due to their good solubility in water.<sup>3</sup>

Radical initiators can be dissociated through different activation approaches including thermal, photochemical and redox methods. Among these, thermal, homolytic dissociation is the most widely used.<sup>4</sup> The value of  $k_d$  can be affected by various factors such as the structure of initiators or the radicals generated, the nature of the solvent and temperature. Taking azo initiators ( $R_1-N=N-R_2$ ) as an example,  $k_d$  is larger when the R groups on the initiator are more bulky and the generated carbon radicals are more stable (i.e. R: tertiary > primary).<sup>5</sup> Azo initiators such as AIBN is usually considered to be more superior than peroxides initiators due to their similar reactivity in different solvent systems.<sup>6</sup> Although  $k_d$  is not determined by a single factor, it is most frequently associated with temperature. According to the Arrhenius equation ( $\ln k_d = \ln A_d - \frac{E_d}{RT}$ ),  $\ln k_d$  is directly correlated with  $-1/T$ . The activation energy of dissociation ( $E_d$ : kJ/mol) and the frequency factor ( $A_d$ :  $s^{-1}$ ) of an initiator can be calculated based on experiment determined rate constants at different temperatures.

**Table 4.1.1 Rate constant of dissociation and half lives of initiators in benzene.<sup>7</sup>**

Initiator	Solvent	Temperature (°C)	$k_d$ ( $10^{-6} \text{ s}^{-1}$ )	$t_{1/2}$ (h)	$E_a$ (kJ/mol)
AIBN <sup>a</sup>	Benzene	50	2.6	74	128.4
		70	40	4.8	
		100	$1.6 \times 10^3$	0.12	
BPO <sup>b</sup>	Benzene	60	2.0	96	124.3
		80	25	7.7	
		92	$1.9 \times 10^2$	1	

a, b:  $k_d$  of AIBN and BPO was calculated under the condition of using  $\alpha$ ,  $\alpha$ -diphenyl  $\beta$ -picrylhydrazyl and styrene respectively to inhibit induced decomposition.

As can be seen from Table 4.1.1, rate constant of dissociation of AIBN is almost fourteen times larger when the temperature is increased from 50 °C to 70 °C.<sup>7</sup> The reactivity of an initiator is also frequently expressed as  $t_{1/2}$ , the half life of an initiator. It is defined as the time required to reduce the concentration of an initiator by half as shown in the following equation

$$t_{1/2} = \frac{\ln 2}{k_d} = \frac{0.693}{k_d}$$

where  $t_{1/2}$  is inversely proportional to  $k_d$ . The corresponding half lives of AIBN at 50 °C and 70 °C are 74 h and 4.8 h. Although increasing the temperature can lead to a faster dissociation of an initiator, the rate constant is still much smaller compared to propagation and termination ( $10^2 \sim 10^4 \text{ L} \cdot \text{mol}^{-1} \cdot \text{s}^{-1}$  and  $10^6 \sim 10^8 \text{ L} \cdot \text{mol}^{-1} \cdot \text{s}^{-1}$ ). Usually, the actual initiation rate ( $v_i$ ) is even slower than the dissociation rate because the initiator efficiency ( $f$ ) is less than one which can be affected by induced decomposition and a cage effect:  $v_i = 2fk_d [I]$ . Therefore, the slow initiation process is one of the main reasons leading to a wider molecular weight distribution of polymer synthesized by FRP.<sup>8</sup>

Chain propagation takes place until all monomer is consumed or termination occurs. The rate constant of propagation  $k_p$  ( $10^2 \sim 10^4 \text{ L} \cdot \text{mol}^{-1} \cdot \text{s}^{-1}$ ) is mainly governed by temperature, the type of monomer and the reactivity of the propagating radical.<sup>9</sup> Chain termination can occur by a combination of two modes: (1) recombination of two chain radicals to yield a longer single chain which can no longer propagate; and (2) disproportionation where a hydrogen atom on one chain is abstracted by another chain radical to give two stable chains with unsaturated and saturated ends respectively. The mode of termination is dependent on the structure of monomer and temperature. For example, the possibility of disproportionation is higher at elevated temperatures for methyl methacrylate.<sup>10</sup> The mode of termination can affect the molecular weight distribution (polydispersity index: PDI) of the resulting polymer, which is defined as the following equation:

$$\text{PDI} = \frac{M_w}{M_n}$$

where  $M_w$  is the weight average molecular weight and  $M_n$  is the number average molecular weight. The theoretical PDI values of FRP with recombination and disproportionation terminations are 1.5 and 2.0 respectively.<sup>4</sup>

In addition to the three main steps, chain transfer is also an important process during the FRP reaction. In general, chain transfer process has a similar effect to termination. The chain radical is deactivated through abstracting a hydrogen or other atom and transferring the radical to other species in the system such as solvent, monomer and initiator. This behavior usually results in low degree of polymerization and can also influence the molecular weight distribution. The rate constant of chain transfer ( $k_{tr}$ ) is usually compared with that of propagation to give the transfer constant  $C = k_{tr}/k_p$ , which is usually small for most monomers<sup>11</sup>, initiators<sup>12</sup> and solvents. Some solvents with relative high transfer constant, such as carbon tetrabromide<sup>13</sup> which has weak carbon halogen bonds and stable radicals due to resonance, are used as chain transfer agents to control the molecular weight of polymer than solvents.

As stated above, the major disadvantage of FRP, the poor control of molecular weight distribution is mainly due to the slow initiation step.<sup>14</sup> Other methods such as atom transfer radical polymerization (ATRP) and reversible addition-fragmentation chain transfer (RAFT) have been widely studied recently to better control the properties of synthesized polymers.<sup>15</sup> However, these methods usually require additional steps to remove the catalyst.<sup>16</sup> In this chapter, effort has been mainly focused on controlling the initiation process of FRP through microwave irradiation.

#### **4.1.2 Conventional Heating and Microwave Heating**

Conventional heating is a widely used method to provide heat for chemical reactions. Usually, an external heating source such as a hot plate is required. By placing the reaction vessel in an oil or water bath on the hotplate, heat generated by the hotplate can be transferred to the reaction system following a complex path (through the oil or water bath, the glass walls of the vessel and then the reactants in the vessel). This method is relatively slow due to the multiple steps of heat transfer. Time is required to reach a thermal equilibrium between the heating source and the reaction system. Furthermore, there are many other factors rendering this method inefficient, such as different thermal conductivities of various materials that are involved in the heat transfer process, temperature differentials and the loss of heat during the transfer process. In order to stop the reaction or reduce the system temperature, the external heating source needs to be removed and cooling methods are sometime employed.

Different from conventional heating, microwave heating is directly related to the inherent microwave absorbing ability of substances. This method is more efficient because it does not involve a complicated heat transfer process. The frequencies of microwaves range from 0.3 to 300 GHz with corresponding wavelengths of 1 m to 1 mm. The most widely used frequency for commercially available microwave ovens and reactors is 2.45 GHz. Under this functional frequency, the electric field cycles  $4.9 \times 10^9$  times per second. The resulting fast reorientation of polar and ionic species under this fast changing electric field is the main source of microwave heating.

The interaction between microwave and different materials is mainly dependent on the properties of the material. For instance, when a conducting material such as a piece of metal is exposed to the electric field of microwave irradiation, an induced current can be generated. This behavior is due to the responsive movement of electrons or ionic species that can lead to a fast temperature rise. This heating mechanism is usually referred as conduction polarization.<sup>17</sup>

While dielectric materials are placed under the electric field of microwave, the resulting heat is mainly due to the rotation of permanent or induced dipoles. The rate of this heating process is dependent on the loss tangent ( $\tan \delta$ ) value of the substance as shown in the following equation:

$$\tan \delta = \frac{\epsilon''}{\epsilon'}$$

where  $\epsilon'$  is real permittivity and  $\epsilon''$  is the dielectric loss factor. Similar to dielectric constant (relative permittivity  $\epsilon_r$ ), real permittivity describes the ability of a material to be polarized under the electric field (microwave absorbing ability). The dielectric loss factor indicates the ability of the substance to convert microwave energy to heat. Good insulators and nonpolar solvents with low  $\tan \delta$  (i.e. quartz and benzene) are usually transparent to microwaves with negligible heating effect under microwave irradiation. In contrast, polar solvents such as water and alcohols with relatively high  $\tan \delta$  can be heated quickly under microwave irradiation.<sup>18</sup> Although  $\tan \delta$  of some materials is higher at high frequencies ( $\gg 2.45$  GHz), most microwave reactors employ a low frequency (2.45 GHz) in order to heat the substance more efficiently because the penetration depth ( $D_p$ ) of microwave on the substance is inversely proportional to  $\tan \delta$ .<sup>19</sup> If a substance is heated with a maximum heating rate (with high  $\tan \delta$ ) under high frequencies, the microwave energy is mostly absorbed by the outer layer.

According to the heating mechanisms discussed above, the heating process of a reaction can be controlled by adjusting the power of the microwave generator. The desired temperature and reaction time can be set on the machine without physically adding and

removing heating sources. Most of the recent commercial microwave reactors are incorporated with an automatic cooling function, under which the reaction can be cooled rapidly. Comparing to conventional heating, microwave heating is apparently more convenient and efficient.

#### 4.1.3 Microwave Assisted Polymerization

Due to the advantages of microwave heating compared to conventional thermal heating, it has been used to synthesize various types of polymers. For example, microwave assisted FRP was demonstrated with either high monomer conversion under the same reaction time or faster reaction rate compared to conventional heating.<sup>20</sup> The enhanced reaction rate during microwave irradiation raises questions as to which mechanisms for heating dominate in this case. It is generally concluded that thermal and nonthermal effects (specific microwave effects) are the two main mechanisms for heating.<sup>21</sup>

The thermal effect is attributed to the instant heating (sometimes uncontrollable local heating) by microwave irradiation following the heat transfer mechanisms discussed in the last section. Since the rate constant of the reaction increases at elevated temperature according to the Arrhenius equation ( $k = Ae^{-\frac{E}{RT}}$ ), the rapid temperature rise by microwave heating can lead to a faster increase in reaction rate than conventional heating.<sup>17</sup> In contrast, the nonthermal effect is more controversial and a detailed mechanism is still not fully understood. One of the proposed mechanisms is also derived from the Arrhenius equation.<sup>22</sup> The nonthermal effect was proposed to be related with the frequency factor  $A$  ( $s^{-1}$ ). The enhanced molecular vibrations by microwave irradiation might result in an increase of the  $A$  value which in turn leads to a faster reaction rate constant. Another thought is that the activation energy ( $E$ ) of a reaction might be decreased if the more polar transition state is more effectively stabilized under microwave irradiation compared to the ground state (Figure 4.1.1).<sup>21, 23</sup> However, a recent result indicates that this so-called nonthermal effect is misleading and is actually also a thermal effect.<sup>24</sup> It is thought that the nonthermal effect was proposed under conditions where inaccurate system temperatures were measured. Therefore,

the existence of nonthermal effect is very debatable and further experiments need to be carried out to clarify it. For instance, comparisons could be made between reactions performed at the exact same temperatures under conventional and microwave heating using accurate temperature characterization methods.

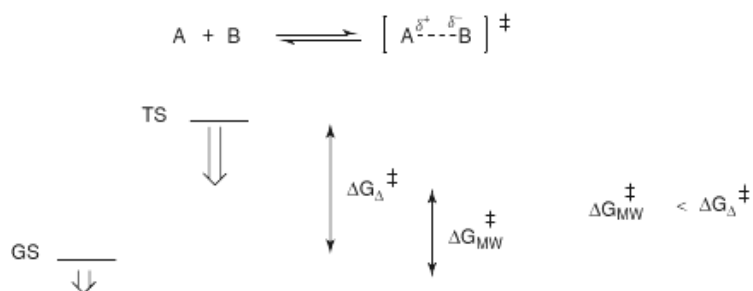


**Figure 4.1.1 Depiction of a more efficient stabilization of a more polar transition state compared to the ground state under microwave irradiation.<sup>21</sup>**

Although the mechanism for accelerating the rate of reactions performed under microwave irradiation is not completely and clearly understood, this heating method has already been applied frequently in both step and chain polymerizations. For example, it was shown that the reaction between 3,3-bis(chloromethyl)oxetane and bisphenol A is faster under microwave irradiation compared to conventional heating at similar temperatures to achieve same yield.<sup>25</sup> Another research group reported slightly higher yield of poly( $\epsilon$ -caprolactam-co- $\epsilon$ -caprolactone) synthesized from  $\epsilon$ -caprolactam and  $\epsilon$ -caprolactone by anionic catalyzed ring opening polymerization under microwave heating compared to conventional heating after the same amount of reaction time.<sup>26</sup> It is worth mentioning that the temperature of the first reaction was monitored using a thermovision infrared camera and the latter case was measured by an inserted grounded thermocouple. The thermovision infrared camera measures the surface temperature; therefore, any nonuniform heat gradient in the reaction mixture leading to a local high temperature spot might not be detectable by the

camera. The different reaction time required to achieve equal yield under *similar temperatures* by the two heating method might be lack of accuracy in measurement of temperature. However, for the second case, the reaction temperature recorded by the thermocouple inserted in the mixture might be relatively close to that of the reaction heated by the conventional method. Therefore, the result obtained by the two heating methods might be more comparable than in the first case where an infrared camera was used.

In addition to traditional polymerization synthesis, microwave irradiation has also been utilized in assisting surface initiated polymerization (SIP). For instance, microwave assisted SIP of  $\epsilon$ -caprolactone on magnetite nanoparticles was reported to be much faster than using a conventional heating method.<sup>27</sup> In the presence of these superparamagnetic nanoparticles, the reaction temperature (200 °C) was reached within 100 s and reaction was completed in 7 min under 200 W by microwave heating. When using a conventional heating method, a much longer reaction time (5 h) was required. However, only general explanations were given for this result. The fast reaction rate was proposed to be due to the enhanced chain propagation rate by microwave irradiation. In this work, the reaction temperature was monitored by an external IR sensor which only measured the bulk temperature of the outside wall of the reaction vessel. Therefore, it is difficult to rule out any local heating effect caused by the strong microwave absorber (magnetite nanoparticles). The actual reaction temperature under microwave heating might be much higher than the apparent value resulting in an increased reaction rate. As can be seen from this and other reported work,<sup>27-28</sup> besides the general application of good solid microwave absorbers to enhance the heating process, they can also be employed in speeding up reaction rates and may improve polymer properties as hypothesized in this chapter.

#### **4.1.4 Other Applications of Microwave Heating**

Microwave assisted polymer synthesis is one application. In addition, microwave has also been used in various types of organic synthesis,<sup>22</sup> in sample preparation such as sample drying,<sup>29</sup> in enzymatic digestions<sup>30</sup> and in other heating processes.<sup>31</sup> In this chapter, microwave heating was mainly introduced in assisting SI-FRP in order to attain controlled

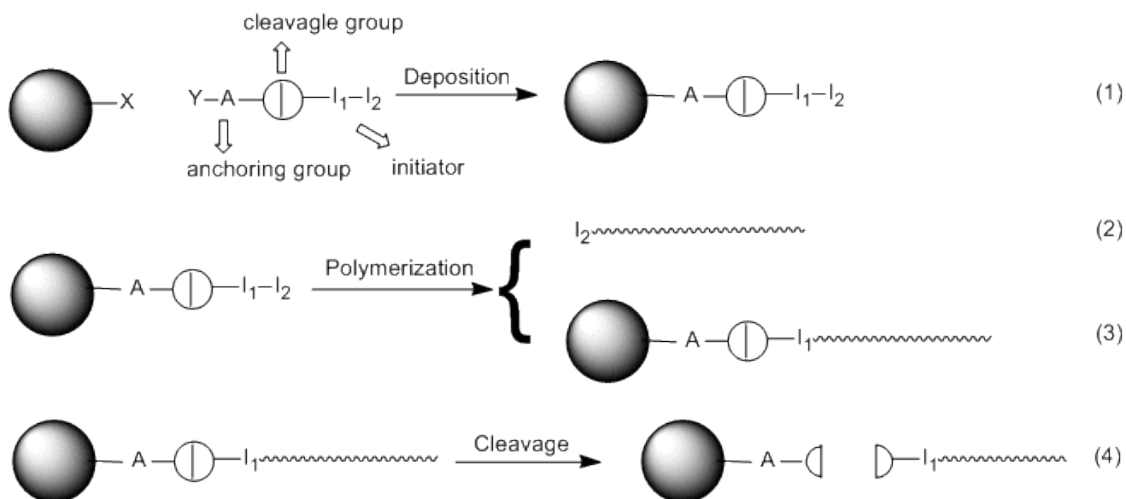
properties such as molecular weight and molecular weight distribution of the resulting polymers. A detailed hypothesis is provided in the following section.

#### 4.1.5 Our Hypothesis

Here, the concept of localized, microwave heating is explored. Specifically, it was sought to determine whether initiation from a microwave absorbing substrate can occur under a large temperature gradient that increases the rates of initiation (close to the surface) relative to the rates of propagation (presumably farther from the surface). It was hypothesized that, if this occurred, it might be possible to achieve lower PDI values for polymer grown under these conditions.

To explore this, an azo initiator<sup>32</sup> was synthesized and bonded to iron oxide magnetic nanoparticles. The particle bonded initiators were added to solvent and monomer. By applying microwave irradiation, surface grafted polymer was formed by FRP. The resulting surface grafted polymer was collected by a subsequent cleavage reaction. A cartoon of this approach is described in Scheme 4.1.2.

**Scheme 4.1.2 Proposed mechanism for SI-FRP under microwave irradiation.**



Following previous work,<sup>32</sup> the synthesized azo initiator consisted an anchoring group (mono- or tri-chlorosilane) at one end, a cleavable group (ester) in the middle and an azo initiator having similar structure with AIBN at the other end. Covalent bonds were formed between the initiator and metal oxide particles (eq. 1). Since magnetic iron oxide nanoparticles are good microwave absorbers, it was hypothesized that the surface temperature can be raised quickly under microwave irradiation. If a poor microwave absorbing solvent ( $\tan \delta = 0.04$ ) such as toluene is used,<sup>24</sup> it was hypothesized that the surface temperature of nanoparticles might be much higher than that of the solution within a short time under microwave irradiation. The existence of this local heating effect before complete heat dissipation from surface to bulk solution might result in an increased rate constant of the dissociation step ( $k_d$ ) which in turn will lead to a fast initiation step. During this process, it is assumed that the heat generated on the particle surface can be efficiently transferred to the bonded azo initiators. After homolytic dissociation, two types of radical initiators can be generated, surface bonded radicals and radicals in solution. These two types of radical initiators can then initiate polymerization both on particle surface and in solution (eq. 2&3). The surface bonded polymer can then be cleaved off from the surface through an acid catalyzed hydrolysis of the ester group on the azo initiator (eq. 4). The collected polymer can then be characterized. Through improving the rate of initiation, it is expected that the molecular weight distribution can be relatively controlled.

## **4.2 Results and Discussion**

### **4.2.1 Preliminary Results**

#### **4.2.1.1 Microwave Absorbing Effect of Different Materials**

Tests to determine the microwave absorbing effect of various surfaces were initially conducted on different substrates by heating them in the same amount of solution under different powers, ranging from 10 W to 100 W for 10 min. The heat generated by the substrates was expressed by subtracting the temperature of the solution in the absence of substrate from that after adding the substrates. A magnetic stir bar used in the microwave tube was first tested. The results are shown in Figure 4.2.1.

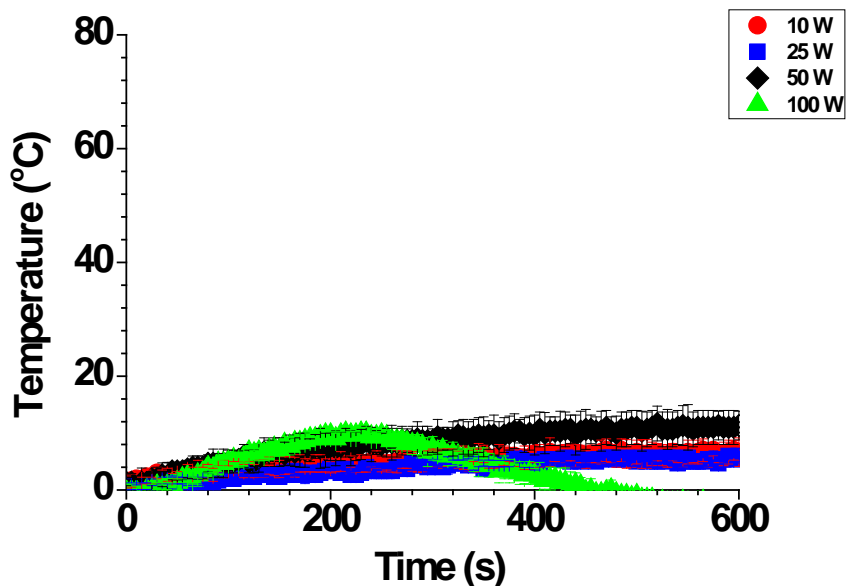


**Figure 4.2.1** Plots of temperature profiles of toluene containing a stir bar versus time under different powers induced by microwave heating measured by the microwave IR sensor. Error bars represent the standard deviation of three measurements over three samples.

After adding the stir bar to the solution, an approximately 10 °C increase in temperature was observed at each applied power comparing with bare solution without stir bar. This result is mainly attributed to the stirring effect instead of the heating effect of the stir bar. Therefore, it was concluded that the microwave absorbing effect of the stir bar is negligible and it was used in the following tests.

The microwave absorbing effect was then studied on particles with different sizes under the same conditions. Figures 4.2.2 and 4.2.3 show the net heating effect of Fe<sub>2</sub>O<sub>3</sub> and SiO<sub>2</sub> particles with two different sizes respectively. As can be seen, only nanometer sized Fe<sub>2</sub>O<sub>3</sub> particles exhibited a large temperature change due to a microwave absorbing effect.

An increase in temperature, around 40 ~ 50 °C was obtained by adding Fe<sub>2</sub>O<sub>3</sub> nanoparticles. The micron-sized particles did not show an evident enhancement in the solution temperature (less than 10 °C). This is possibly due to the limited heat transfer from much smaller surface area of micron-sized particles compared to nanoparticles. When same mass was used for both types of particles, the surface area of micron-sized particle is computed to be 10<sup>3</sup> times smaller than that of the nanoparticles. As a result, the heating area on micron-sized particle surfaces is smaller resulting in different efficiency of temperature enhancement compared to nanoparticles. For example, same sized alumina was heated under microwave irradiation. A faster temperature increase was detected when more alumina was used.<sup>33</sup> Under the same conditions, SiO<sub>2</sub> particles demonstrated a very small temperature increase due to a low microwave absorbing effect. Around a 20 °C temperature increase was detected in the presence of SiO<sub>2</sub> nanoparticles while almost no temperature increase was observed with micron-sized particles of SiO<sub>2</sub>.

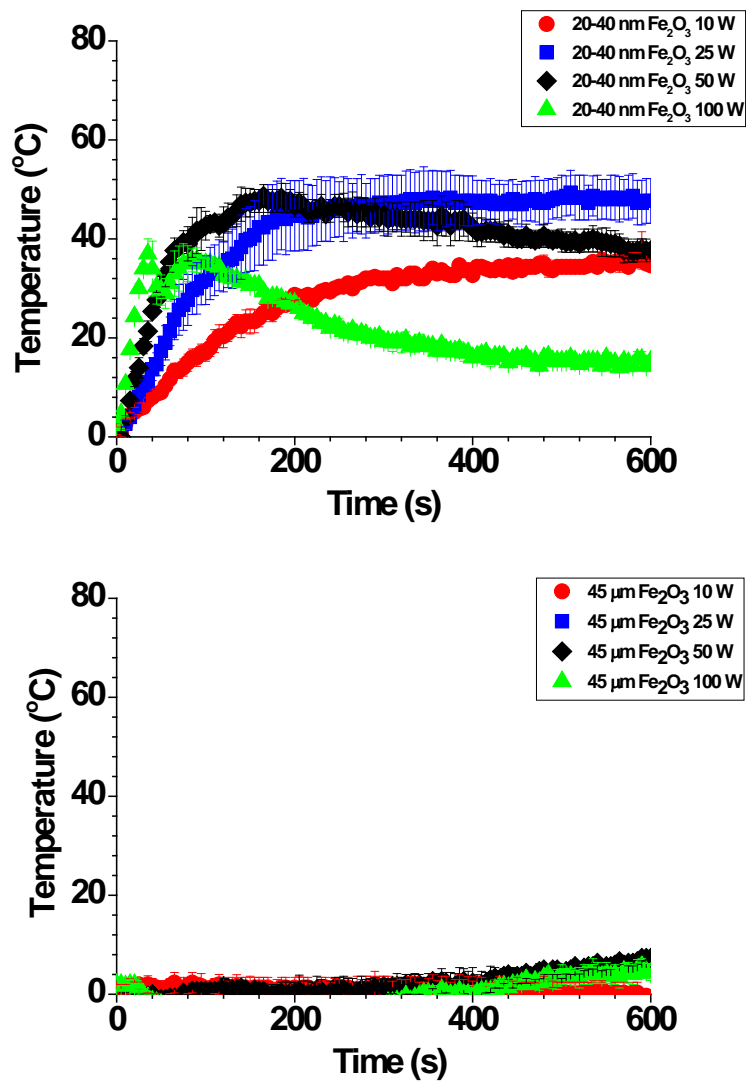


Figure 4.2.2 Plots of temperature profiles of toluene containing  $\text{Fe}_2\text{O}_3$  particles with different sizes versus time under different powers induced by microwave heating measured by microwave IR sensor. Error bars represent the standard deviation of three measurements over three samples.

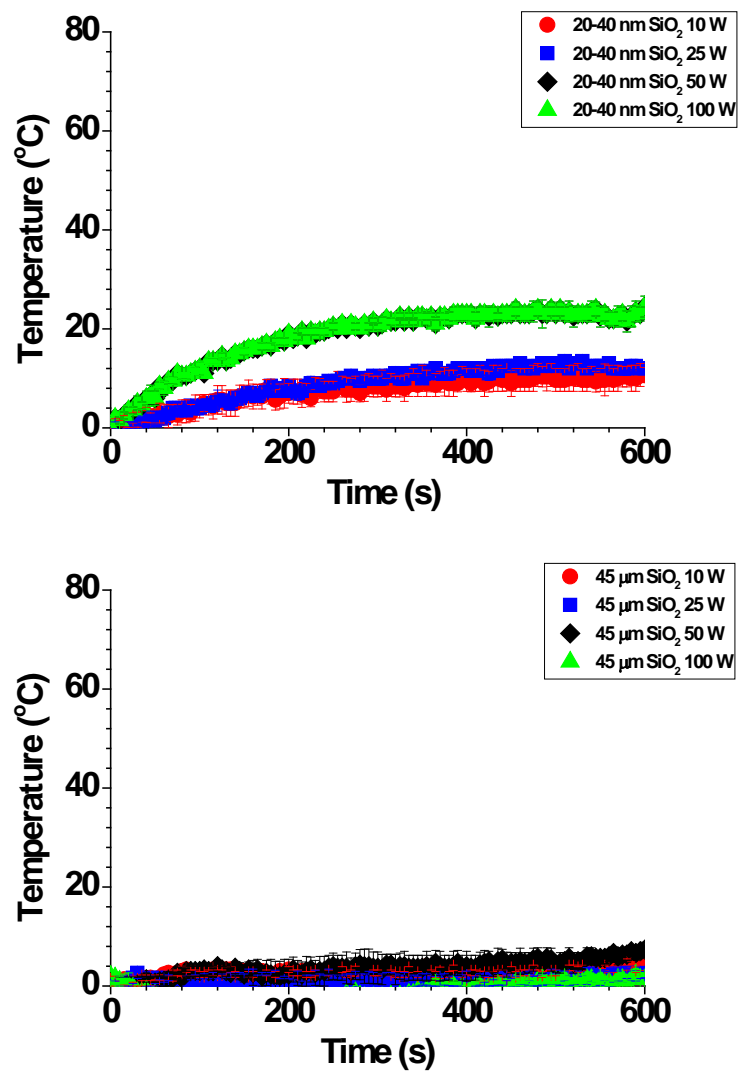
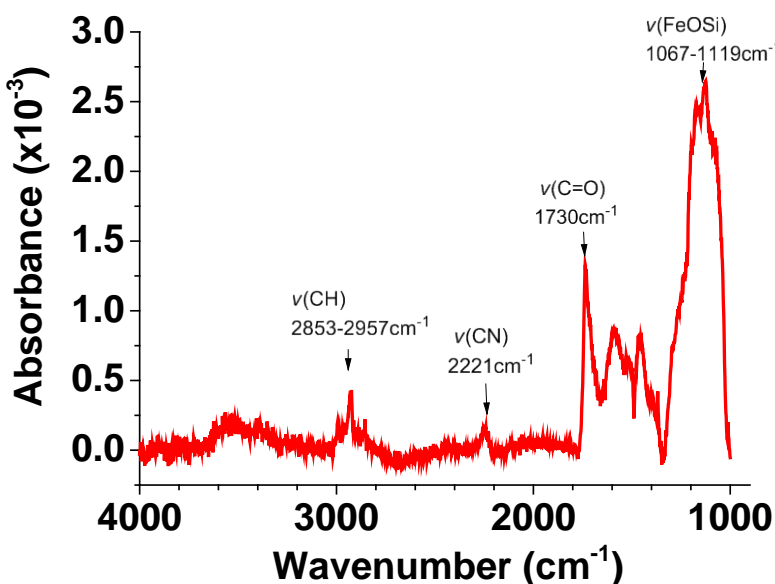


Figure 4.2.3 Plots of temperature profiles of toluene containing SiO<sub>2</sub> particles with different sizes versus time under different powers induced by microwave heating measured by microwave IR sensor. Error bars represent the standard deviation of three measurements over three samples.

#### 4.2.1.2 Deposition of Azo Initiator on Fe<sub>2</sub>O<sub>3</sub> Nanoparticles

Two types of azo initiators, azomono-chlorosilanes (AMCS) and azotrichlorosilanes (ATCS), were synthesized and deposited on Fe<sub>2</sub>O<sub>3</sub> nanoparticles. ATR-FTIR was performed on the modified particles subsequently to confirm the successful attachment of the azo initiators (Figure 4.2.4). Absorbance peaks at 1730 cm<sup>-1</sup>, 2221 cm<sup>-1</sup> and 2853-2957 cm<sup>-1</sup> correspond to the vibrations of the carbonyl, nitrile and C-H groups of the initiators respectively.



**Figure 4.2.4** Plot of ATR-FTIR spectrum of ATCS modified Fe<sub>2</sub>O<sub>3</sub> nanoparticles.

To further verify the immobilization efficiency of the azo initiators, FRP of styrene was carried out in the presence of both AMCS and ATCS modified Fe<sub>2</sub>O<sub>3</sub> nanoparticles under thermal heating (60 °C) for 17 h. Since there are two types of polymer produced during the reaction (particle bonded and nonbonded polymers) as described in section 4.1.5, the two fractions were first separated through centrifugation. Afterwards, the bonded polystyrene was

cleaved off from the particles through hydrolysis of the ester groups from the initiators catalyzed by *p*-toluenesulfonic acid (*p*-TsOH). This was followed by separating the particles from the polymer solution through centrifugation. Detailed procedure was discussed in the experimental section. Both bonded and nonbonded polymer was then collected through precipitation into methanol and characterized with GPC. The results are shown in Table 4.2.1 below.

**Table 4.2.1 GPC results for polystyrene synthesized in the presence of azo initiator modified Fe<sub>2</sub>O<sub>3</sub> nanoparticles using thermal heating (60 °C, 17 h ).**

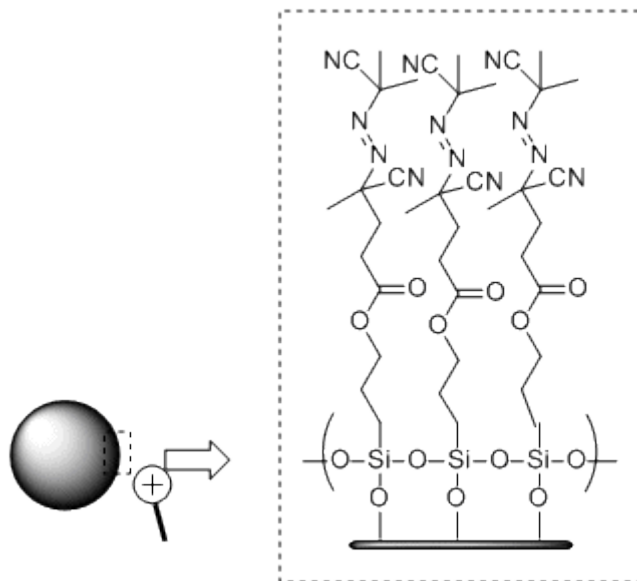
Initiator	Polymer	M <sub>n</sub> (× 10 <sup>5</sup> Da)	M <sub>w</sub> (× 10 <sup>5</sup> Da)	PDI	Monomer Conversion (%)
ATCS	Nonbonded	1.84	5.10	2.77	8.98
ATCS	Bonded	3.23	9.10	2.81	3.82
ATCS	Nonbonded*	1.83	9.90	5.40	8.98
ATCS	Bonded*	1.38	4.86	3.52	3.59

\*large scale reactions

Reactions with ATCS modified nanoparticles demonstrate detectable monomer conversions of styrene for polymerizations both in solution and on particles. Monomer conversion was roughly estimated by dividing the mass of the obtained polymers by the mass of monomer used initially. However, the amounts of both types polymers collected from the reactions with AMCS modified nanoparticles was too low for characterization with GPC. This result suggests that the efficiency of immobilization with ATCS on the substrates was relatively higher than that with AMCS. As illustrated in Scheme 4.2.1, the cross linking among the ATCS molecules might form a more stable and uniform monolayer on the surface than AMCS. This monolayer would lead to more initiation sites on the particles. Monomer

conversion of polymerization in solution is higher than that on particle surface which might be due to the effect of auto-polymerization of styrene in solution.

#### Scheme 4.2.1 Deposition of ATCS on Fe<sub>2</sub>O<sub>3</sub> nanoparticles.



#### 4.2.1.3 FRP of Styrene under Microwave Irradiation

It is hypothesized that the local temperature of the Fe<sub>2</sub>O<sub>3</sub> nanoparticles under microwave irradiation is significantly higher than the bulk solution over a short time scale. However, the IR sensor of the CEM microwave is only able to measure the temperature at the surface of the glass vessel which is presumably very close to the bulk temperature. The local temperature at the surface of the nanoparticles is difficult to determine. Nevertheless, it is important to know the surface temperature because it can provide information about the kinetics of initiation and comparison experiments can be run through thermal heating under similar conditions. Therefore, a model calculating the local temperature on particle surface was built and will be discussed in a separate section. Preliminary experiments, however, were

carried out before the completion of the model under different working modes of the microwave.

**i. FRP of Styrene under Duty Cycle Mode**

FRP of styrene using particle bonded azo initiators was first conducted using the duty cycle mode of the microwave synthesizer. In this mode, a fixed power is set and the power is manually turned on and off for a given number of cycles. Experiments were run under this working mode in order to avoid getting extremely high local temperature that might cause initiator decomposition before initiation of polymerization. The first set of experiments were performed under the conditions listed in Table 4.2.2.

**Table 4.2.2 Conditions for FRP of styrene in the presence of ATCS modified Fe<sub>2</sub>O<sub>3</sub> nanoparticles using duty cycle mode (1<sup>st</sup> set). Values in the parenthesis represent the standard deviation of measured temperatures between two samples.**

Power (W)	30	40	50	70	100
Power On/Off time (s)	5/10	5/10	5/10	5/10	5/10
Cycles	40	40	40	40	40
Maximum Temperature (°C)*	60(0.7)	56(4.2)	78(1.4)	74(15.6)	102(9.2)

\*Recorded near the vessel surface using the IR sensor of the microwave

After the reactions under the above conditions, both bonded and nonbonded polystyrene was collected using the same procedure as described above. However, very little amount of both types of polymer was collected through precipitation into methanol. Therefore, the polymer solutions were evaporated to separate the polymer from the solvent and residual monomer. Based on the GPC results, only low molecular weight materials ( $10^2$ ~ $10^3$  Da) were produced under these conditions. A possible reason for this result might be that the local temperature was too high and most of the initiators decomposed before they initiated the polymerization reaction. Therefore, another set of reactions was performed by

reducing the power-on time to decrease the temperature at the surface. The conditions used for these reactions are listed in Table 4.2.3.

**Table 4.2.3 Conditions for FRP of styrene in the presence of ATCS modified Fe<sub>2</sub>O<sub>3</sub> nanoparticles using duty cycle mode (2<sup>nd</sup> set). Values in the parenthesis represent the standard deviation of measured temperatures between two samples.**

Power (W)	30	50	70	90
Power On/Off time (s)	2/10	2/10	2/10	2/10
Cycles	50	50	50	50
Maximum Temperature (°C)*	42(2.8)	55(2.1)	57(3.5)	69(5.7)

\* Recorded near the vessel surface using the IR sensor of the microwave

Similar results were obtained compared to the first set of experiments. Only low molecular weight products were detected by GPC. Two reasons are proposed. First, the local temperature was still very high and resulted in the decomposition of azo initiators. Second, the reaction time was not long enough to grow polymers with reasonable molecular weight. To test whether lower temperature and longer reaction time might assist in producing high molecular weight polymer, a revised mode of microwave irradiation was investigated and is described below.

#### **ii. FRP of Styrene under Single-Mode Peptides Synthesis (SPS) Condition**

Under SPS mode, several parameters can be adjusted on the CEM microwave, including power (W), maximum temperature (°C), delta temperature (°C) and time (h). The microwave will heat the reaction under the set power until the measured temperature reaches the maximum temperature. The power will then be turned off automatically to cool down the system by a set delta temperature. At that time, the power will turn on again to heat up the reaction system. Using this loop method, the bulk temperature of the reaction can be automatically controlled within a smaller oscillating range compared to the duty cycle mode.

Experiments were first run in this way at 20 W power for 1 h and GPC results of the resulting polymer are shown in Table 4.2.4.

**Table 4.2.4 GPC results for polystyrene synthesized in the presence of ATCS modified Fe<sub>2</sub>O<sub>3</sub> nanoparticles using SPS mode. Values in the parenthesis represent the standard deviation of results between two samples.**

Max T/Delta T (°C)	Polymer	M <sub>n</sub> (× 10 <sup>4</sup> Da)	PDI	Monomer Conversion (%)
45 / 2	Bonded	4.59 (3.80)	1.00 (0.01)	1.04(0.12)
45 / 2	Nonbonded	5.77 (1.79)	1.40 (0.14)	1.83(0.18)
50 / 2	Bonded	5.78 (6.23)	1.11(0.11)	0.845(0.03)
50 / 2	Nonbonded	5.53 (3.42)	1.25(0.02)	1.93(0.18)

According to the GPC results, both particle bonded and nonbonded polymer with molecular weight of around 10<sup>4</sup> Da were obtained. Interestingly, the PDI of surface bonded polymer was lower than nonbonded polymer in solution. Furthermore, comparison experiments using ATCS modified SiO<sub>2</sub> nanoparticles revealed that almost no polymer was collected from either particles or in solution under the same conditions. The above results were initially very encouraging and seem to indicate a local heating effect of Fe<sub>2</sub>O<sub>3</sub> nanoparticles. However, the amount of polymer produced under these conditions was rather small as can be seen from the low monomer conversions. These low conversions were possibly due to the low concentration of initiators. Up to this point, the amount of ATCS modified Fe<sub>2</sub>O<sub>3</sub> nanoparticles used in the reactions was calculated based on the amount of SiO<sub>2</sub> particles with same size reported by Ruhe et al, assuming that the surface area of the two types of particles was similar.<sup>34</sup> However, due to the porous structure, the surface area of SiO<sub>2</sub> particles is actually larger than Fe<sub>2</sub>O<sub>3</sub> particles. Therefore, reactions with revised

amount of Fe<sub>2</sub>O<sub>3</sub> nanoparticles were performed using SPS mode under conditions listed in Table 4.2.5.

**Table 4.2.5 Conditions for FRP of styrene in the presence of ATCS modified Fe<sub>2</sub>O<sub>3</sub> nanoparticles using SPS mode.**

Max T (°C)	35	40	45	50	55	60	70	80	90
Delta T (°C)	1	1	1	1	1	1	1	1	1
Power (W)	20	20	20	20	20	20	20	20	20
Time (h)	1.5/3/4.5	1.5/3/4.5	1.5/3/4.5	1.5	1.5	1.5	1.5	1.5	1.5

As can be seen from the GPC results shown in Figure 4.2.5, only reactions under maximum temperatures ranging from 45 °C to 60 °C for 1.5 h produced polymers with relatively reasonable molecular weights (~10<sup>4</sup> Da). Combined with the results shown in Table 4.2.4, almost all polymer, both bonded and nonbonded, presented very low PDI values ranging from 1.0 to 1.2. This is uncommon since the PDI of polymers synthesized through FRP is usually between 1.5 and 2.0. PDI values under 1.5 for free radical polymerized polystyrene have never been reported before.<sup>35</sup>

Comparison experiments were then performed under same conditions (50 °C to 60 °C for 1.5 h) using an equivalent amount of AIBN as initiator. GPC results are shown in Figure 4.2.6. The molecular weight of the polymer produced under these conditions is similar to those using particle bonded initiators. More importantly, the PDI of the polymers (around 1.2), is still very low. This result suggests the presence of Fe<sub>2</sub>O<sub>3</sub> nanoparticles might not be necessary to produce low PDI polymer. However, all the reactions resulting in low PDI polymer had very low monomer conversions (less than 10%). Therefore, the resulting polymer with low PDI might be dependent on the yield or monomer conversion instead of local heating effect.

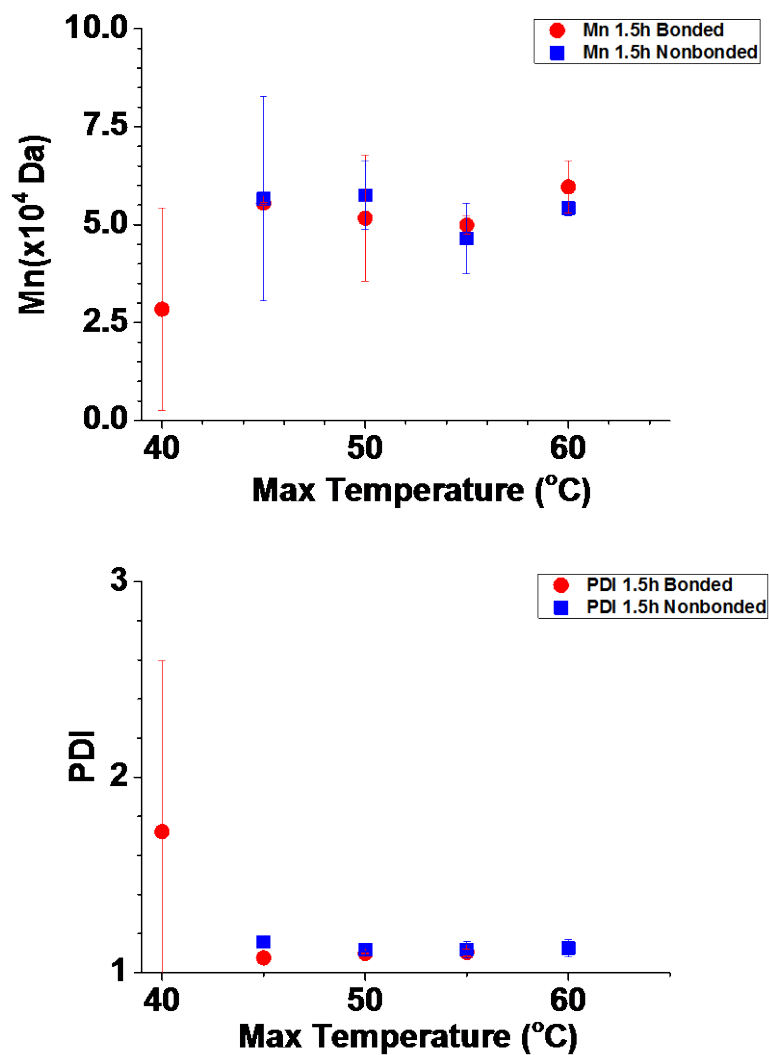
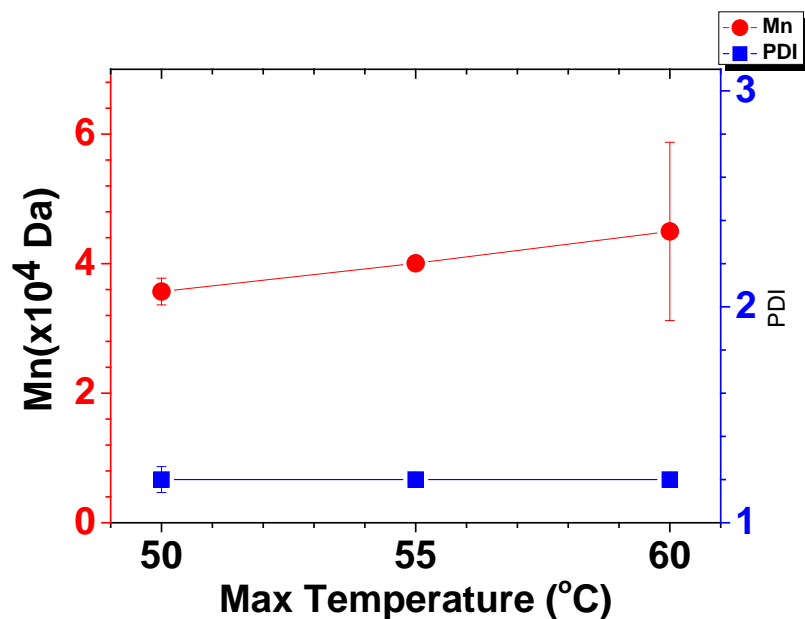


Figure 4.2.5 Plots of GPC results ( $M_n$  & PDI versus reaction temperature) for polystyrene synthesized using SPS mode in the presence of ATCS modified  $\text{Fe}_2\text{O}_3$  nanoparticles. Error bars represent the standard deviation of two measurements over two samples.



**Figure 4.2.6** Plots of GPC results ( $M_n$  & PDI versus reaction temperature) for polystyrene synthesized using SPS mode using free AIBN as initiators. Error bars represent the standard deviation of two measurements over two samples.

In order to determine the relationship between monomer conversion and PDI values, experiments with free AIBN in solution were conducted using SPS mode under conditions listed in Table 4.2.6. Comparison reactions were carried out in parallel under same conditions (same time and temperature) via thermal heating. GPC results are shown in Figure 4.2.7 and 4.2.8. Here, only results at the same temperature are comparable since the time scale is over the half life of AIBN. At different temperatures, AIBN has different half lives. Thus, the length of reaction time using the same half life scale is very different at different temperatures.

**Table 4.2.6 Conditions for FRP of styrene in the presence of free AIBN using SPS mode.**

Max T (°C)	60				70			
Delta T (°C)	1				1			
Power (W)	20				20			
Time ( $\times t_{1/2}$ of AIBN)	0.1	0.6	1	2	0.1	0.6	1	2
Time (h)	2.15	12.9	21.5	43	0.4	2.4	4	8

Under these conditions, polystyrene synthesized by microwave heating demonstrated a lower PDI (around 1.4) than thermal heating (1.6~1.8). The monomer conversion of reactions using microwave heating is also smaller than that using thermal heating under both temperatures (Figure 4.2.9). One possible explanation for this phenomenon is that the formation of radical initiators under microwave irradiation might be faster than thermal heating due to the instant heating of initiator molecules by fast dipole rotation under the rapidly changing electric field. At the very beginning of the reaction, the concentration of radicals might be higher under microwave irradiation compared to thermal heating. However, this behavior might also increase the opportunity for recombination of radicals resulting in decomposition of the initiators due to a possible cage effect. If the amount of reactive initiators decreases very quickly, the propagation rate (eq. 1) might be reduced resulting in low monomer conversion. Under the situation of low monomer conversion, the possibility for chain transfer step is reduced<sup>14</sup> which might result in polymers with low PDI.

$$v_p = k_p[M][M \cdot] \quad (1)$$

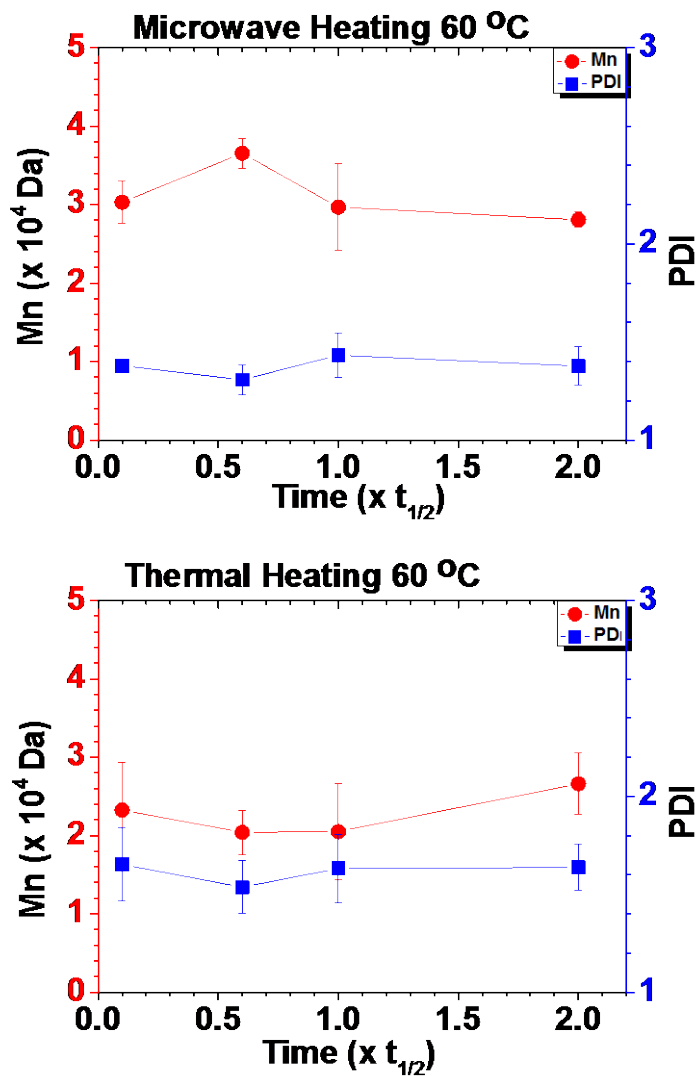


Figure 4.2.7 Plots of GPC results ( $M_n$  & PDI versus reaction time) for polystyrene synthesized at 60 °C using (top) microwave heating and (bottom) thermal heating with free AIBN as initiators. Error bars represent the standard deviation of two measurements over two samples.

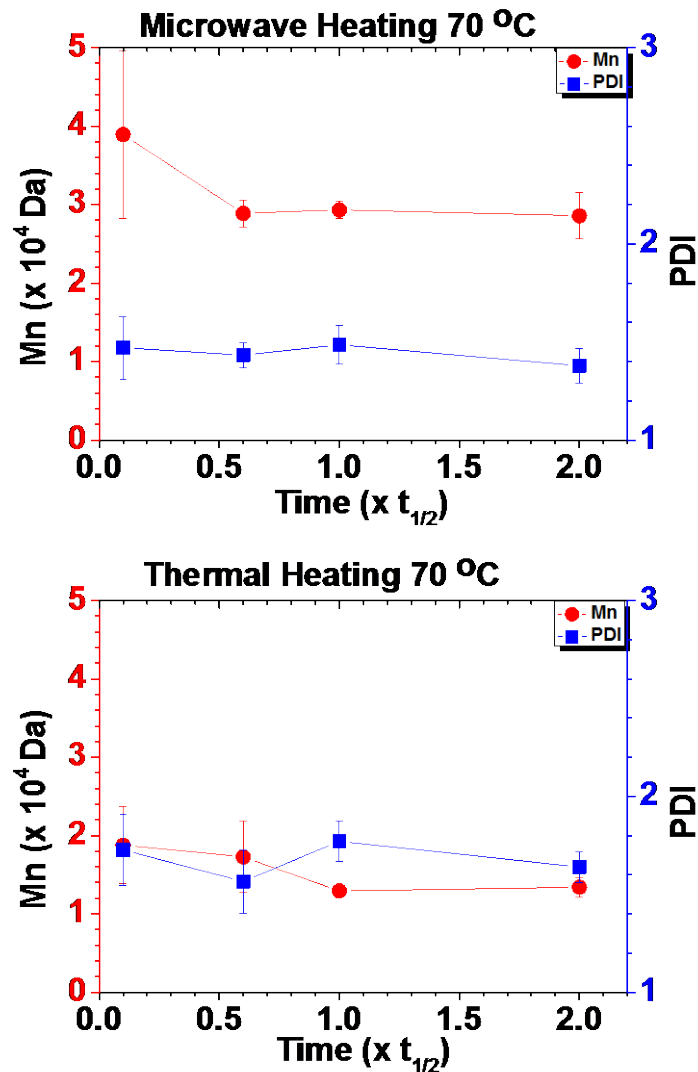
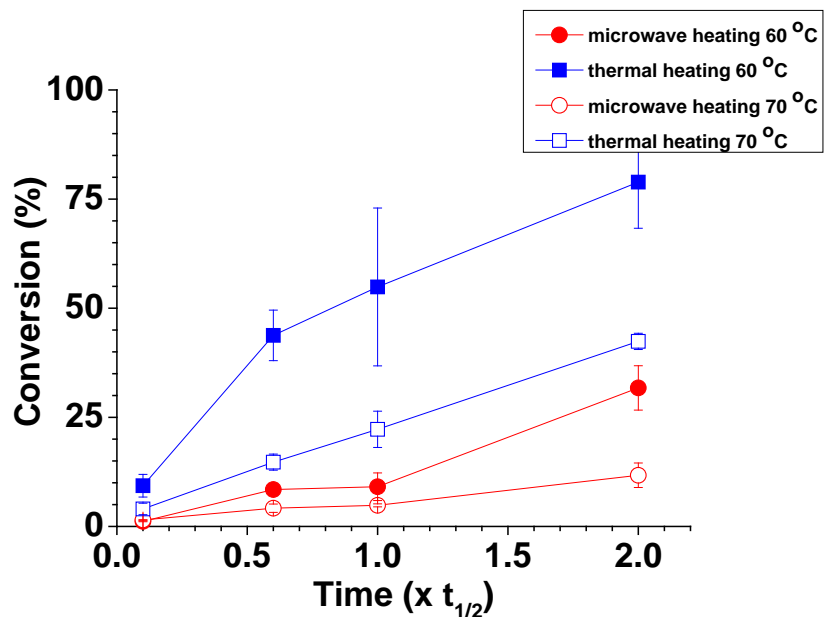


Figure 4.2.8 Plots of GPC results ( $M_n$  & PDI versus reaction time) of polystyrene synthesized at 70 °C using (top) microwave heating and (bottom) thermal heating with free AIBN as initiators. Error bars represent the standard deviation of two measurements over two samples.



**Figure 4.2.9** Plots of monomer conversions at different temperatures versus reaction time using different heating methods with free AIBN as initiator. Error bars represent the standard deviation of two measurements over two samples.

From the results obtained so far, it can be generally concluded that free radical polymerization of styrene under microwave heating had lower monomer conversion as well as smaller PDI compared to thermal heating under the same conditions. This result might be only attributed to microwave irradiation since thermal heating produced polymers with higher PDI even when monomer conversion was low. However, it is not possible to conclude that the local heating effect of  $\text{Fe}_2\text{O}_3$  nanoparticles was the main reason for the resulting low PDI because both reactions assisted by microwave with and without the presence of the nanoparticles produced similar results.

#### 4.2.1.4 Modeling of the Microwave Heating Process using Fe<sub>2</sub>O<sub>3</sub> Nanoparticles

(This work was done in collaboration with Erich Bain)

##### i. The Absorption Rate of Microwave Irradiation by Fe<sub>2</sub>O<sub>3</sub> Nanoparticles

A model to estimate the surface temperature of Fe<sub>2</sub>O<sub>3</sub> nanoparticles in solution heated by microwave was computed and is discussed below. Assumptions made in order to build a heat (or energy) balance of the reaction system were that (1) the applied microwave energy was mainly absorbed by the magnetic Fe<sub>2</sub>O<sub>3</sub> nanoparticles and (2) the resulting instant heat was transferred in the sequence of solution, the vessel and then the outside wall of the vessel where the temperature was measured by an IR sensor (Figure 4.2.10).

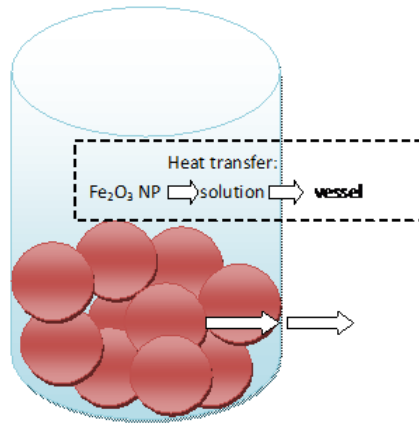


**Figure 4.2.10** Picture of heat transfer process of microwave irradiated reactions

This heat balance of the system can be described as

$$\dot{Q} = m_f C_{pf} \frac{dT}{dt} + m_v C_{pv} \frac{dT}{dt} + hS_v(T - T_0) \quad (2)$$

where  $\dot{Q}$  is defined as the absorption rate of microwave irradiation by the nanoparticles ( $\text{J} \cdot \text{s}^{-1}$ ),  $m_f$  is the mass of solution inside the vessel (g),  $m_v$  is the mass of the vessel (g),  $C_{pf}$  and  $C_{pv}$  are heat capacities of the solution and the vessel respectively ( $\text{J} \cdot \text{g}^{-1} \cdot ^\circ\text{C}^{-1}$ ),  $h$  is the heat

transfer coefficient of unit area between the outside surface of the vessel and the air at temperature  $T_0$  ( $\text{W}\cdot\text{m}^{-2}\cdot^\circ\text{C}^{-1}$ ) and  $T$  is the temperature of the system ( $^\circ\text{C}$ ). Equation 2 can be rearranged as

$$T = T_0 + \frac{\dot{Q}}{hS_v} - \frac{m_f C_{Pf} + m_v C_{Pv}}{hS_v} \times \frac{dT}{dt} \quad (3)$$

where

$$A = \frac{\dot{Q}}{m_f C_{Pf} + m_v C_{Pv}}$$

$$B = \frac{hS_v}{m_f C_{Pf} + m_v C_{Pv}}$$

and  $\frac{A}{B} = \frac{\dot{Q}}{hS_v}$  are set to simplify equation 3 to get equation 4.

$$T = T_0 + \frac{A}{B} - \frac{1}{B} \times \frac{dT}{dt} \quad (4)$$

Equation 4 can then be solved as follows:

$$T - T_0 - \frac{A}{B} = -\frac{1}{B} \times \frac{dT}{dt} \quad (5)$$

$$Bdt = -\frac{dT}{T - T_0 - \frac{A}{B}}$$

$$\int Bdt = \int -\frac{dT}{T - T_0 - \frac{A}{B}}$$

$$Bt = -\ln\left(T - T_0 - \frac{A}{B}\right) + C' \quad (6)$$

Since  $T=T_0$  when  $t=0$ ,  $C'$  can be solved as follows:

$$0 = -\ln\left(-\frac{A}{B}\right) + C'$$

$$C' = \ln\left(-\frac{A}{B}\right)$$

Therefore, equation 6 can be written and rearranged as follows to give equation 7:

$$Bt = -\ln\left(T - T_0 - \frac{A}{B}\right) + \ln\left(-\frac{A}{B}\right) = -\ln\frac{T - T_0 - \frac{A}{B}}{-\frac{A}{B}}$$

$$e^{-Bt} = \frac{T - T_0 - \frac{A}{B}}{-\frac{A}{B}}$$

$$T = T_0 + \frac{A}{B}(1 - e^{-Bt}) \quad (7)$$

where  $A=0.42 \pm 0.03 \text{ } ^\circ\text{C}\cdot\text{s}^{-1}$  and  $B=0.54 \times 10^{-2} \pm 0.07 \times 10^{-3} \text{ s}^{-1}$  are obtained by fitting equation 7 to experimentally measured temperature profiles of reactions under condition of 10 W, 10 min.  $\dot{Q}$  can then be calculated by using use  $m_f=6 \text{ g}$ ,  $C_{Pf}=1.65 \text{ J}\cdot\text{g}^{-1}\cdot^\circ\text{C}^{-1}$ ,  $m_v=16 \text{ g}$  and  $C_{Pv}=0.75 \text{ J}\cdot\text{g}^{-1}\cdot^\circ\text{C}^{-1}$ .<sup>28b</sup> The resulting value is  $9.11 \text{ J}\cdot\text{s}^{-1}$ . The result indicates 91.1% of the energy per unit time applied by microwave irradiation is absorbed by  $\text{Fe}_2\text{O}_3$  nanoparticles.

## ii. Temperature Gradient at the Particle Surface

As was studied by Merabia et al.,<sup>36</sup> the surface temperature gradient of gold nanoparticles (1.3 nm) follows classical continuum heat transfer equations. Therefore, heat conservation inside the  $\text{Fe}_2\text{O}_3$  nanoparticle (Figure 4.2.11) can be accounted for using the following equations.

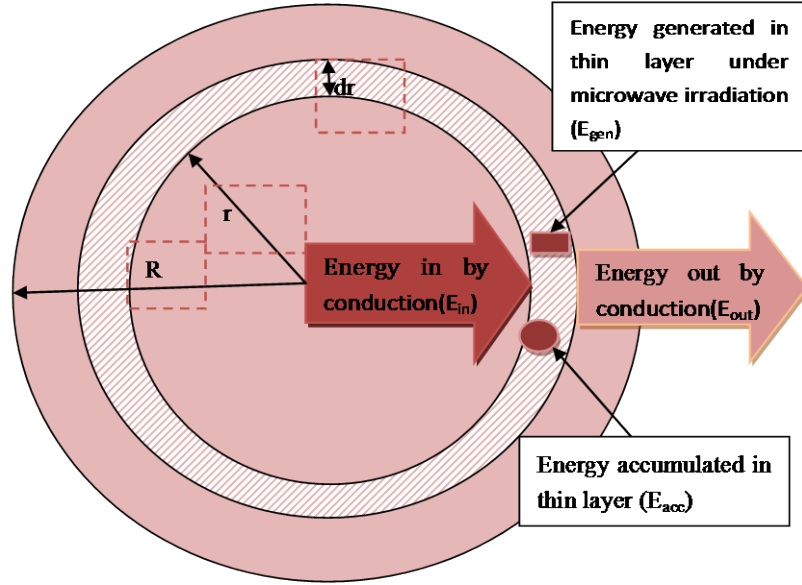


**Figure 4.2.11 Picture of heat conservation in Fe<sub>2</sub>O<sub>3</sub> nanoparticles**

Given that:  $E_{in} + E_{gen} = E_{acc} + E_{out}$ , detailed form of this heat conservation is written in equation 8

$$-k_p \frac{dT}{dr} \times 4\pi r^2 - H_v 4\pi r^2 dr = c_{pp} \rho 4\pi r^2 dr \frac{dT}{dt} - k_p \frac{dT}{dr} \times 4\pi (r + dr)^2 \quad (8)$$

where  $k_p$  is thermal conductivity of Fe<sub>2</sub>O<sub>3</sub> nanoparticles ( $\text{J} \cdot \text{s}^{-1} \cdot \text{m}^{-1} \cdot \text{°C}^{-1}$ ),  $c_{pp}$  is the heat capacity ( $\text{J} \cdot \text{g}^{-1} \cdot \text{°C}^{-1}$ ),  $\rho$  is the density ( $\text{g} \cdot \text{cm}^{-3}$ ) and  $H_v$  is the rate of energy per unit volume input to the nanoparticles by microwave irradiation ( $\text{J} \cdot \text{s}^{-1} \cdot \text{m}^{-3}$ ). Equation 8 can be rearranged as follows.

$$-k_p 4\pi [(r + dr)^2 - r^2] \frac{dT}{dr} = -H_v 4\pi r^2 dr - c_{pp} \rho 4\pi r^2 dr \frac{dT}{dt}$$

$$-k_p \frac{d\{[(r + dr)^2 - r^2] \frac{dT}{dr}\}}{dr} = -H_v r^2 - c_{pp} \rho r^2 \frac{dT}{dt} \quad (9)$$

Here, a steady state temperature inside the particle was assumed:  $\frac{dT}{dt} = 0$ . Under this assumption, equation 9 can be simplified as follows.

$$-k_p \frac{d\left\{[(r+dr)^2 - r^2] \frac{dT}{dr}\right\}}{dr} = -H_v r^2$$

$$-k_p \frac{d\left(r^2 \frac{dT}{dr}\right)}{dr} = -H_v r^2$$

$$-\int d\left(r^2 \frac{dT}{dr}\right) = -\int \frac{H_v}{k_p} r^2 dr$$

$$r^2 \frac{dT}{dr} = \frac{H_v}{3k_p} r^3 + C_1$$

$$\int dT = \int \left(\frac{H_v}{3k_p} r + \frac{C_1}{r^2}\right) dr$$

$$T = \frac{H_v}{6k_p} r^2 - \frac{C_1}{r} + C_2 \quad (10)$$

Two boundary conditions are used here to solve equation 10:

$$(a) \left. \frac{dT}{dr} \right|_{r=0} = 0;$$

$$(b) T|_{r=R} = T_s$$

to give

$$C_1 = 0, \quad C_2 = T_s + \frac{H_v}{6k_p} R^2$$

$$T = T_s + \frac{H_v}{6k_p} (r^2 - R^2) \quad (11)$$

Equation 11 can then be simplified to give  $T \approx T_s$  by neglecting  $\frac{H_v}{6k_p}(R^2 - r^2)$  since  $H_v(R^2 - r^2)$  is small relative to  $k_p$ . A third boundary condition is then applied in order to solve  $T_s$  as shown in the following equation

$$-k_p \left. \frac{dT}{dr} \right|_{r=R} = G(T_s - T_B) = \frac{H_v R}{3} \quad (12)$$

where heat flux at the surface of the particle is set to be proportional to the temperature gradient between the surface ( $T_s$ ) and bulk ( $T_B$ ). Here  $G$  is the interfacial thermal conductance  $G$  ( $J \cdot s^{-1} \cdot m^{-2} \cdot ^\circ C^{-1}$ ). It is assumed that the heat transfer from the particle to the bulk solution first occurred by conduction in a thin laminar layer with thickness of  $x$  since the size of particles are small compared to the length scale of currents in the stirred fluid. This is described in equation 13.

$$-k_p \left. \frac{dT}{dr} \right|_{r=R} = \frac{k_f (T_s - T_B)}{x} \quad (13)$$

where  $k_f$  is the thermal conductivity of the fluid ( $J \cdot s^{-1} \cdot m^{-1} \cdot ^\circ C^{-1}$ ). The temperature profile is assumed to be linear in this thin laminar layer, the thickness of which is on the order of the particle radius.<sup>36</sup> Therefore, by combining equation 12, 13 and using  $k_f = 0.14 J \cdot s^{-1} \cdot m^{-1} \cdot ^\circ C^{-1}$ , the approximated value of  $G$  can be calculated as follows.

$$x \approx R$$

$$G \approx \frac{k_f}{R} \approx 4.67 \times 10^6 J \cdot s^{-1} \cdot m^{-2} \cdot ^\circ C$$

Given that  $H_v = \frac{\dot{Q}}{\frac{4}{3}\pi R^3 N_p}$ , and a particle radius of 30 nm and a density of  $5.24 \text{ g} \cdot \text{cm}^{-3}$  for

$\text{Fe}_2\text{O}_3$ , the number of particles is approximately  $1.13 \times 10^{15}$  by calculation. As a result, the temperature difference between the surface of nanoparticles and the bulk solution can be calculated as follows.

$$T_s - T_B = \frac{H_V R}{3G} = \frac{\dot{Q}}{4\pi R^2 N_p G} = \frac{9.11}{4\pi(30 \times 10^{-9})^2 \times 1.13 \times 10^{15} \times 4.67 \times 10^6} = 1.53 \times 10^{-9} \text{ } ^\circ\text{C} \quad (14)$$

Disappointingly, the calculated result indicates that almost no temperature difference exists between the surface of nanoparticles and that of bulk solution.

The relationship between the temperature difference and the size of the particles is shown in equation 14. Given that  $\dot{Q}$ ,  $m$  and  $k_f$  are constant, the temperature difference can be adjusted by changing the size of the particles. According to the result shown in equation 15 and Figure 4.2.12, millimeter sized particles can result in a temperature difference of more than 100 °C. However, if millimeter sized particles are used under the same mass scale, the number of the particles will be reduced by the magnitude of  $10^{18}$ . This scale is larger than the amount of particles that was used in reactions ( $1.13 \times 10^{15}$ ), so this result cannot be practically obtained. However, if mass is changed to be a variable, the temperature gradient can be rearranged to give equation 16. This equation indicates that only smaller particle size and a smaller amount of particles can result a greater temperature gradient. Given that the particles used now are of nanometer scale, the amount of particles needs to be less than  $10^8$  to result in a temperature gradient of around 51 °C. The mass of ten million nanometer sized  $\text{Fe}_2\text{O}_3$  is around  $10^{-12}$  g which also is not practical to realize.

$$T_s - T_B = \frac{H_V R}{3G} = \frac{\dot{Q}}{4\pi R^2 N_p G} = \frac{\dot{Q}}{4\pi R^2 \times \frac{m}{\frac{4}{3}\pi R^3 \rho} \times \frac{k_f}{R}} = \frac{9.11}{\frac{0.72}{\frac{1}{3}R^2 \times 5.24 \times 10^6} \times 0.14} = 1.58 \times 10^8 R^2 \quad (15)$$

$$T_s - T_B = \frac{H_V R}{3G} = \frac{\dot{Q}}{4\pi R^2 N_p G} = \frac{\dot{Q}}{4\pi R^2 \times N_p \times \frac{k_f}{R}} = \frac{\dot{Q}}{4\pi R \times N_p \times k_f} = \frac{9.11}{4\pi R \times N_p \times 0.14} = \frac{5.18}{RN_p} \quad (16)$$

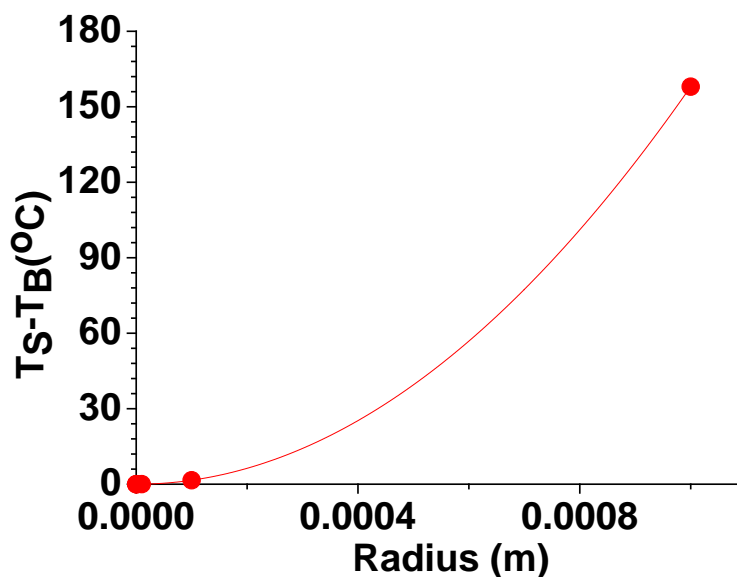


**Figure 4.2.12 Plot of radius of particles versus temperature gradient.**

The computed model nanoparticle system provided information about local temperature under a steady state assumption (eq. 9). This omission of a time factor might affect the final result of the modeling. Combining the model and the experimental result, it is still difficult to determine the existence local heating effect of magnetic nanoparticles under microwave irradiation without further study. Therefore, efforts in subsequent studies were focused on flat substrates. A local heating effect was proposed on silicon wafers previously, and this hypothesis is tested further here.<sup>37</sup>

## **4.2.2 Further Study**

### **4.2.2.1 Calculation of Monomer Conversion Using UV-Vis Spectroscopy**

Previously, monomer conversion was calculated by dividing the mass of insoluble materials after evaporation under high vacuum by the mass of monomer used initially. The calculation is relatively inaccurate since evaporation might not be sufficient to remove substances trapped in polymers such as solvent and residual monomer. Therefore, the

calculated conversion might be higher than the actual value. Here, UV-Vis spectroscopy is investigated for determining monomer conversions.

**i. Calibration with Styrene/Toluene Solution System**

As can be seen from Figure 4.2.13, the absorption band of styrene overlapped with toluene from 190 nm to 280 nm and almost no difference in intensity can be detected when varying the concentration of each substance (Figure 4.2.14).<sup>38</sup> Over the range of 280 nm~296 nm, styrene showed increased absorption intensity when the concentration increased. However, both toluene and polystyrene had very low absorbance over the same range.<sup>39</sup> Therefore, calibration and monomer conversion might be evaluated by measuring the absorbance over this region (280 nm~296 nm). Here, an assumption is made that the volume of the solution is not changed after the reaction. Thus, the monomer conversion might be calculated by simply measuring and calculating the difference between the absorbance of solution before and after reaction without removing polymer.

Before assessing the monomer conversions, calibration was performed by measuring the absorbance at 290 nm using a set of standard styrene/toluene solutions. The standard solutions were prepared by keeping the total volume the same but varying the volume ratios of styrene and toluene mixtures, ranging from 0.5 mL styrene/9 mL toluene to 4 mL styrene/6 mL toluene. The highest molar concentration of styrene (3.49 mol/L) is the concentration used in experiment before polymerization. The absorption of the standards was measured by UV-Vis spectroscopy as is demonstrated in Figure 4.2.14.

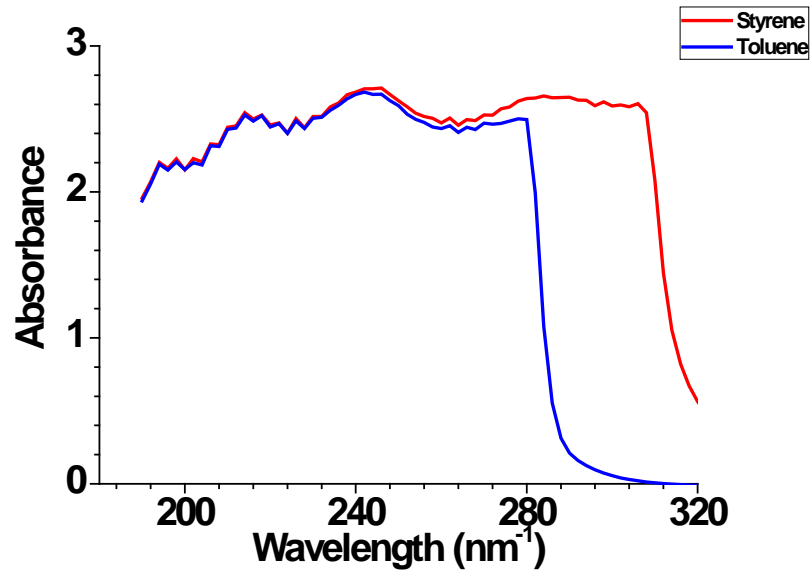


Figure 4.2.13 Plots of UV-Vis spectra of styrene and toluene.

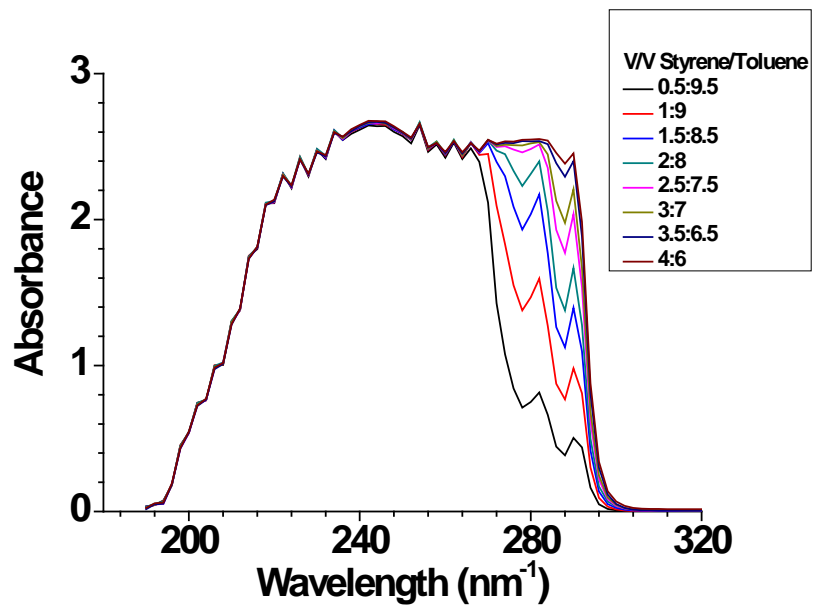


Figure 4.2.14 Plots of UV-Vis spectra of styrene/toluene solutions at different volume ratios.

## ii. Linear Dynamic Range of Calibration Curve

Calibration curve of styrene standards was first generated over the entire concentration range tested. Both weighted and non-weighted linear regressions were performed (Figure 4.2.15). As can be seen from the correlation coefficients of both linear fits, the linearity was off especially in the high concentration range. This deviation from linearity is possibly caused by the saturated absorbance ( $>1$ ) over high styrene concentrations. Therefore, a revised calibration was conducted over a small concentration range (0.43~1.41 mol/L) in order to get a better linear relationship between the concentration of styrene and absorbance. The results are shown in Figure 4.2.16.

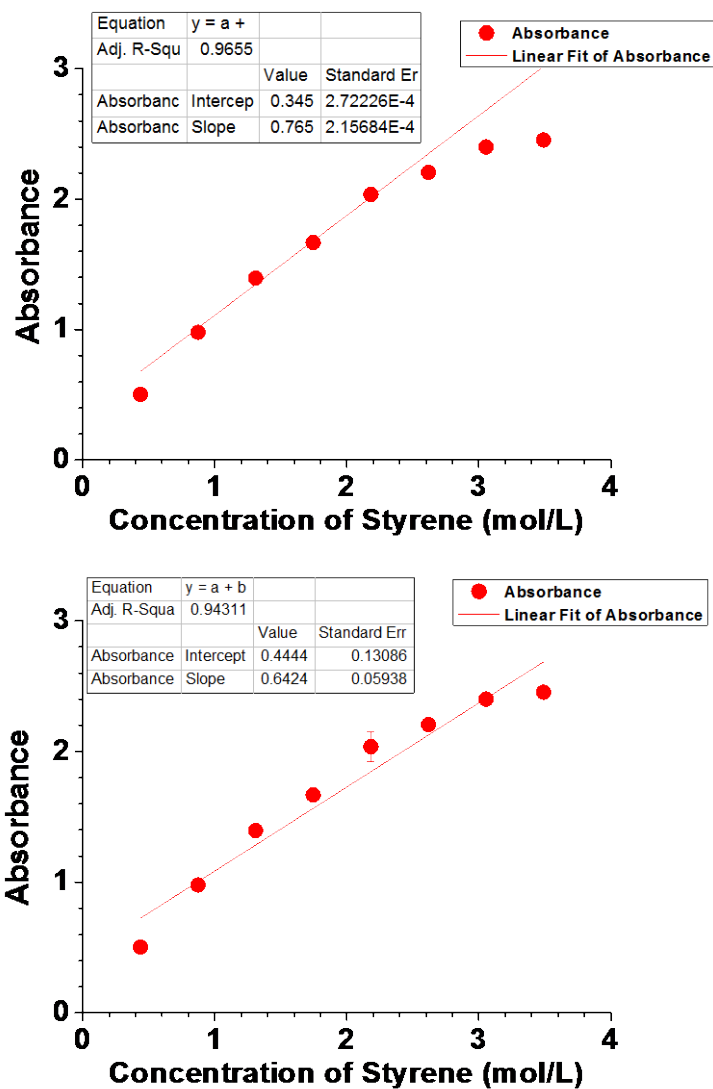
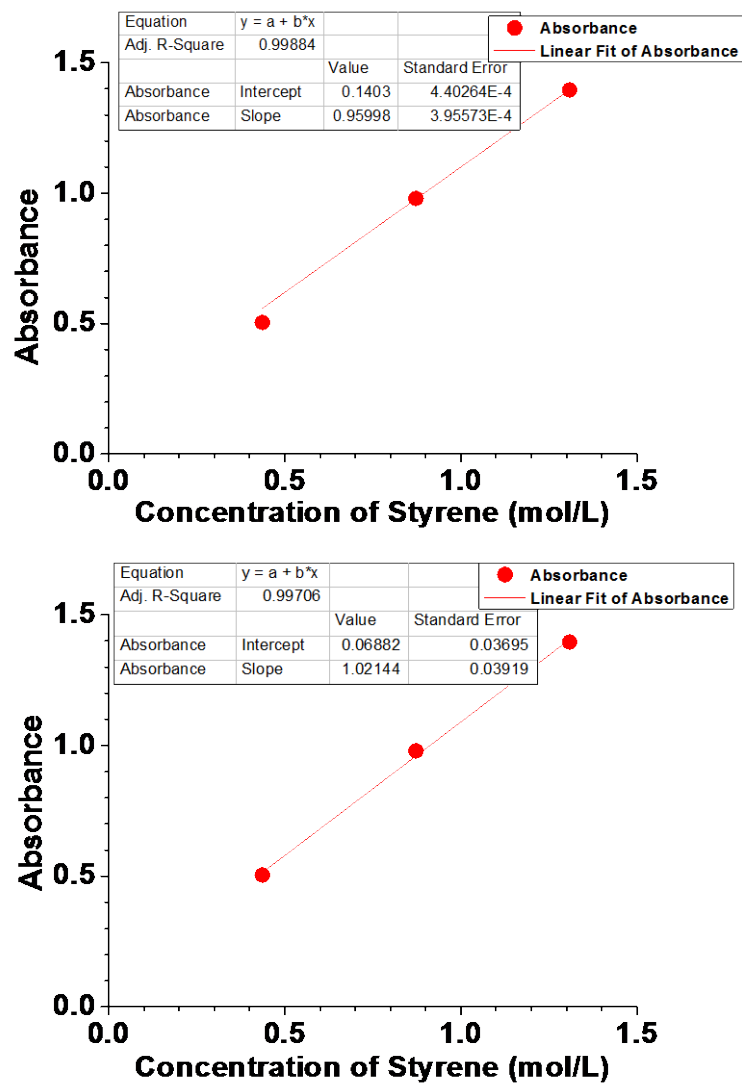


Figure 4.2.15 (top) Weighted with standard errors and (bottom) non-weighted calibration curves of UV-Vis spectra using styrene/toluene solution system. Error bars represent (top) the relative errors and (bottom) the magnitude of the 90% confidence interval for five readings on one sample.



**Figure 4.2.16** Linear range of calibration curves of UV-Vis spectra (top) weighted with standard errors and (bottom) non-weighted using styrene/toluene solution system. Error bars represent (top) the relative errors and (bottom) the magnitude of the 90% confidence interval for five readings on one sample.

According to the correlation coefficients, calibration over a low concentration range

showed better linearity than those obtained over a wider range. Nevertheless, previous results indicate that most monomer conversion of microwave irradiated FRP of styrene was in a relatively low percent range (0~20%). The concentration of residual styrene is thus in the high concentration range where the calibration shows a deviation from linearity. Therefore, this UV method is not precise enough for determining monomer conversions and it was not used further.

#### **4.2.2.2 Calculation of Monomer Conversion Using GC Measurement**

In addition to UV spectroscopy, GC was also investigated to determine the monomer conversion. In order to use the GC method, it is necessary to remove the polymer from the solutions before taking measurements. Therefore, precipitation was performed and polymer was thoroughly washed with methanol. All fractions of the solutions were collected and the final volume was fixed also using methanol with volumetric flasks. The concentration of styrene monomer could then be determined using a calibration based on an internal standard. The conversion of monomer can be evaluated by calculating the difference between the concentrations of styrene before and after the reaction.

Before assessing the monomer conversions, calibration was first conducted using a set of standards. Two internal standards, benzene and benzyl chloride were tested respectively. The solutions were prepared by fixing the amount of internal standard (1 mL) but varying the volume of styrene (0.5~2.5 mL). The final volume was adjusted with methanol using 100 mL volumetric flasks which is the same as actual preparation of reaction samples. The ratio of peak integration of styrene to internal standard was compared with the volume ratio of the two substances. Calibrations with two internal standards are discussed below.

##### **i. Calibration of GC with Benzene as an Internal Standard**

Initially, benzene was applied as an internal standard, and the results of calibration are shown in Figure 4.2.17. Both weighted and non-weighted linear regressions were performed. Both calibration curves showed good linearity between the peak integrations from the chromatogram and the actual volume ratio of styrene and internal standard. Therefore, using benzene as an internal standard is applicable for determining monomer conversion.

Considering the toxicity of benzene, calibration using another internal standard, benzyl chloride, was also tested.

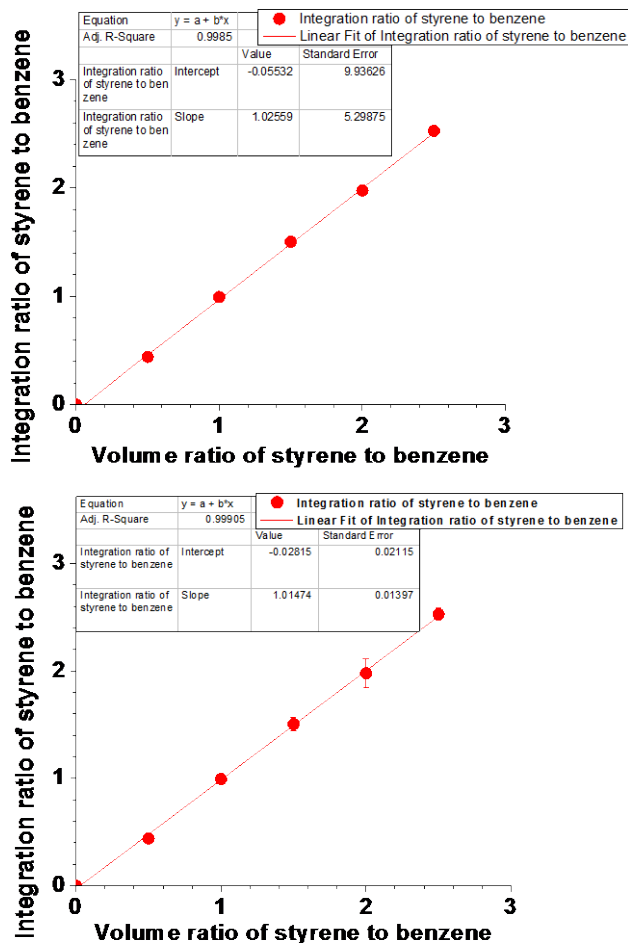


Figure 4.2.17 (top) Weighted with standard errors and (bottom) non-weighted calibration curves of GC using styrene/methanol solution system with benzene as the internal standard. Error bars represent (top) the relative errors and (bottom) the magnitude of the 90% confidence interval for six readings on one sample.

ii. Calibration of GC with Benzyl Chloride as an Internal Standard

Both weighted and non-weighted calibrations with benzyl chloride as the internal standard were carried out and results are shown in Figure 4.2.18. Again, good linear relationships between calculated peak integrations and volume ratios were obtained from both curves. This calibration method was thus applied in calculating monomer conversions of subsequent reactions due to the good linearity and lower toxicity of the internal standard compared to benzene.

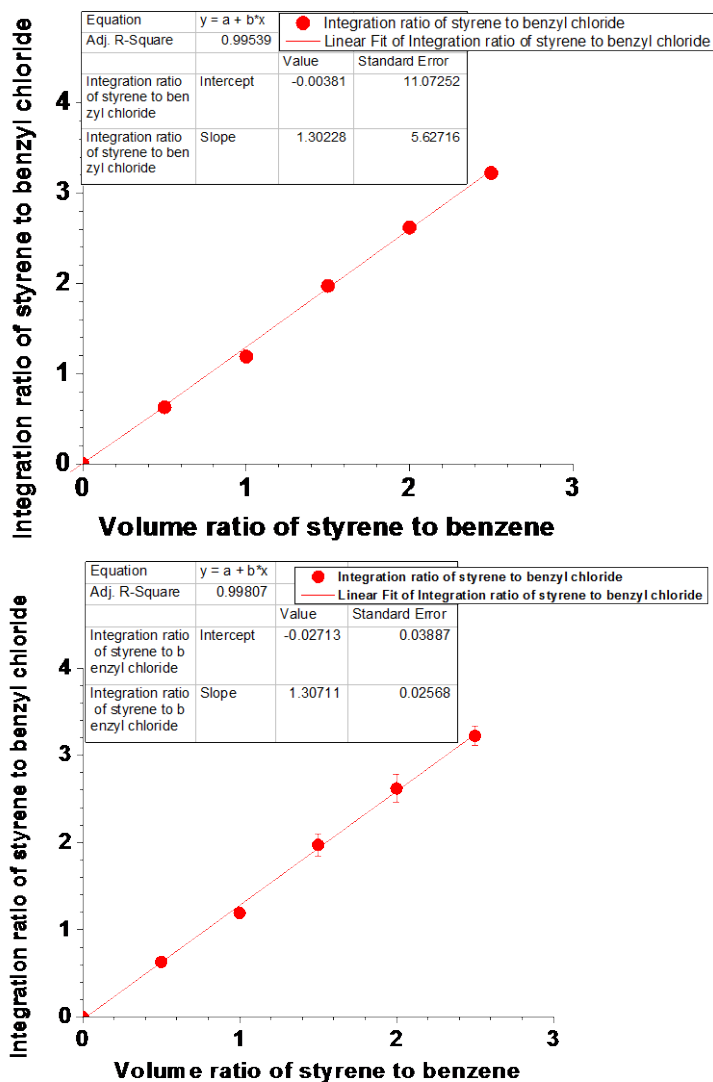
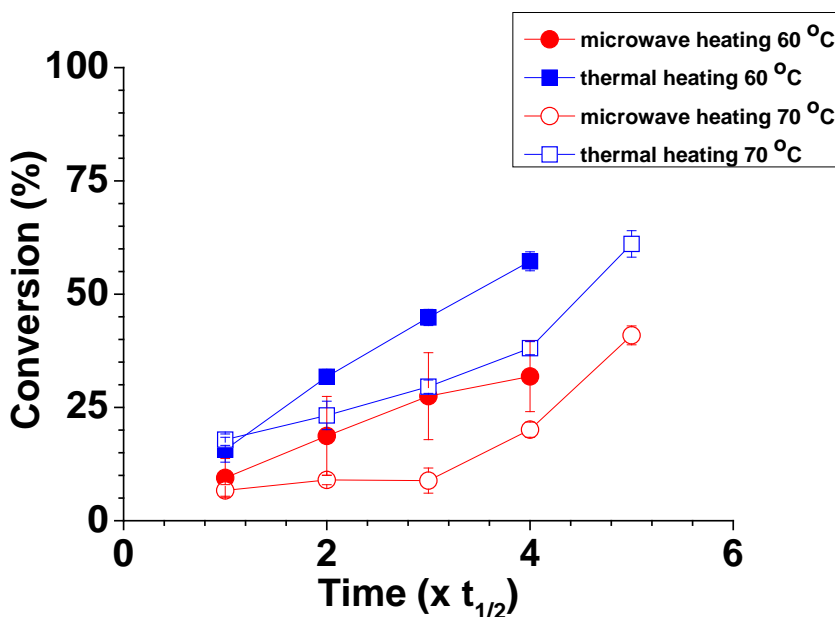


Figure 4.2.18 (top) Weighted with standard errors and (bottom) non-weighted calibration curves of GC using styrene/methanol solution system with benzyl chloride as the internal standard. Error bars represent (top) the relative errors and (bottom) the magnitude of the 90% confidence interval for four readings on one sample.

### iii. Calculation of Monomer Conversion of Microwave and Thermally Assisted FRP

Previously, experiments with free AIBN in solution were conducted using both microwave and thermal heating. Monomer conversions were determined by calculating the mass of materials after evaporating the solvent and residual monomer under high vacuum. Here, another set of similar experiments were carried out and monomer conversions were evaluated using the GC method. The results are shown in Figure 4.2.19.



**Figure 4.2.19** Plots of styrene monomer conversions calculated by GC calibration curve versus reaction time for microwave and thermal induced FRP at different temperatures. Error bars represent the magnitude of the 90% confidence interval for nine readings on three sample.

Microwave assisted FRP of styrene displayed lower monomer conversion compared to thermal heating under the same conditions. However, compared to the previous results (Figure 4.2.9), the GC method demonstrated lower monomer conversions under most

conditions. For example, previous result showed that the monomer conversion under 60 °C,  $2 \times t_{1/2}$  using thermal heating was around 75% while the GC method revealed a conversion of 30%. The obvious difference between the two methods indicates the lack of accuracy of the previous method as mentioned before. Evaporation might not be sufficient to remove substances trapped in polymer. Therefore, the calculated conversion was higher than the actual value when the polymer was collected and weighted. The GC method is more accurate and precise as can be seen from the smaller error bars compared to the previous results.

#### **4.2.2.3 Reproducibility of Microwave Induced Polymerization on Flat Substrate**

Since both previous experimental results and the model calculation indicate the local heating effect of Fe<sub>2</sub>O<sub>3</sub> nanoparticles is not likely, the focus was transferred back to polymerizations on flat substrates. As discussed in previous work, microwave irradiation can assist SI-FRP within very short reaction time (30 s~2 min) indicating a local heating effect of the silicon substrate. Therefore, repeat experiments were first performed using azo initiator modified silicon substrates under the same conditions as reported previously.<sup>37</sup>

##### **i. Reproducibility of Microwave Induced FRP on Silicon under Previously Used Conditions**

Microwave irradiated FRP of both methyl methacrylate and styrene was carried out on silicon substrates. The same microwave working mode (power time mode) and reaction time were used. Reactions were run under different powers, ranging from 20 W to 100 W as described previously.<sup>37</sup> The thickness of polymer was determined by ellipsometry. The results are shown below.

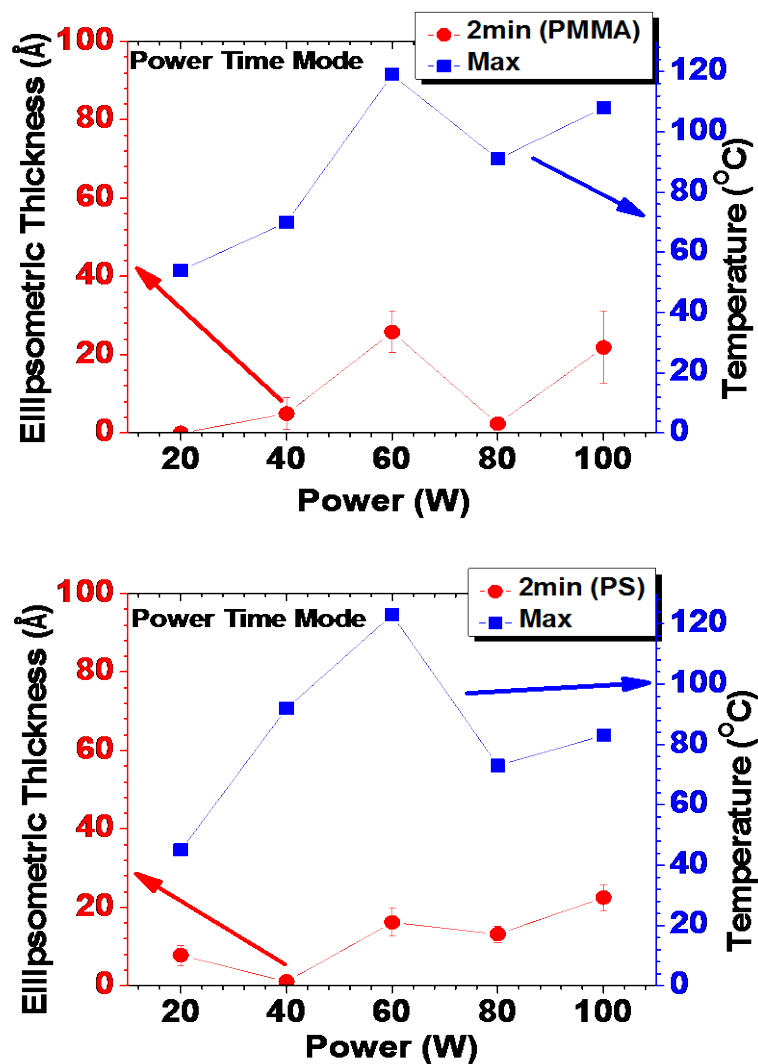


Figure 4.2.20 Plots of ellipsometric thickness of (top) PMMA and (bottom) PS and maximum system temperature versus reaction power for microwave induced FRP on silicon surface using power time mode. Error bars represent the magnitude of the 90% confidence interval for ten measurements on two samples.

Under all conditions, almost no growth of polymers were detected on the silicon

substrates. This result contradicts the previous results, that at least 8 nm thick polymer can be grown on the surface even at low power, such as 25 W within 2 min. During the experiments, it was observed that reproducible control of system temperature under the same power is very difficult. The above plots only represent the temperature of one trial due to the large variation of maximum temperatures between runs. In order to further check the reproducibility and accuracy of the previous results, reactions were carried out under modified conditions using SPS mode.

**ii. Microwave Induced FRP on Silicon under Modified Conditions**

Under SPS working mode, the maximum reaction temperatures were set to be 100 °C and 120 °C at different powers for the polymerization of both methyl methacrylate and styrene. Longer reaction times were used than the power time mode. These ranged from 5 min to 30 min. The ellipsometric thickness of the grafted polymer was determined and results are shown in Figure 4.2.21 and 4.2.22.

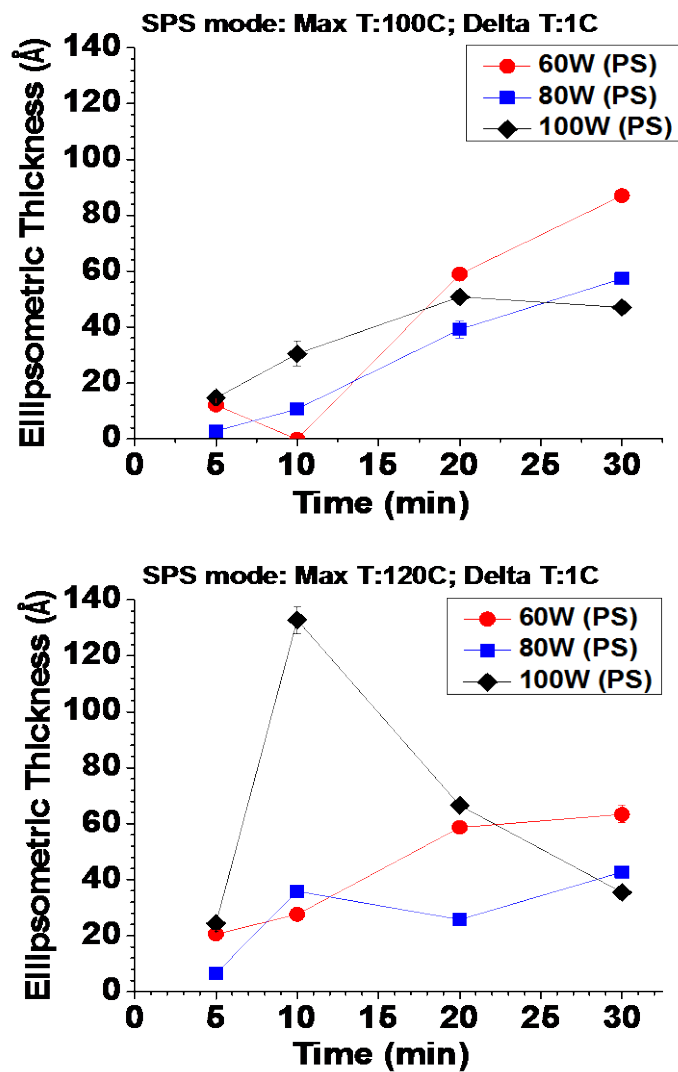


Figure 4.2.21 Plots of ellipsometric thickness of PS versus reaction time at (top) 100 °C and (bottom) 120 °C using different powers for microwave induced FRP on silicon surfaces using SPS mode. Error bars represent the magnitude of the 90% confidence interval for ten measurements on two samples.

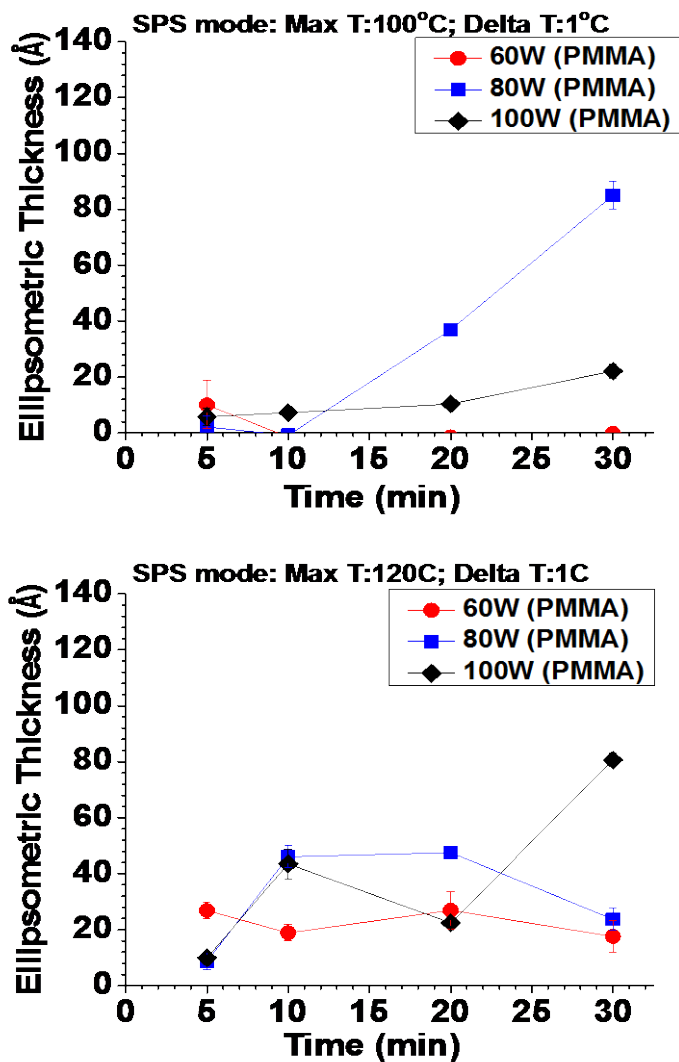


Figure 4.2.22 Plots of ellipsometric thickness of PMMA versus reaction time at (top) 100 °C and (bottom) 120 °C using different powers for microwave induced FRP on silicon surfaces using SPS mode. Error bars represent the magnitude of the 90% confidence interval for ten measurements on two samples.

The thickness of PS increased under most of the conditions tested using SPS mode as

a function of reaction time. A thickness of around 13 nm was observed under only one condition (120 °C, 100 W after 10 min). Nevertheless, under all conditions tested, only 6~8 nm layer of PS is detected after 30 min reaction. Under the same conditions, almost no growth or very thin layer (8 nm) of PMMA was detected. Both the low thickness of the grafted polymers and the requirement for long reaction time are different from the previous results. The poor reproducibility in the results is most likely caused by the large variation of system temperature as mentioned above. Therefore, in the subsequent sections, the reproducibility of system temperature was further studied by using the microwave IR sensor and an external IR camera.

#### **4.2.2.4 Reproducibility of Temperature Measurement by Microwave IR Sensor**

Initially, the reproducibility of temperature reported using the microwave IR sensor was tested. Toluene solutions with and without the presence of different substrates were heated at different powers, ranging from 10 W to 300 W for 5 min. Three trials were run under each conditions as indicated in different colors in the graphs. The results are shown and discussed below.

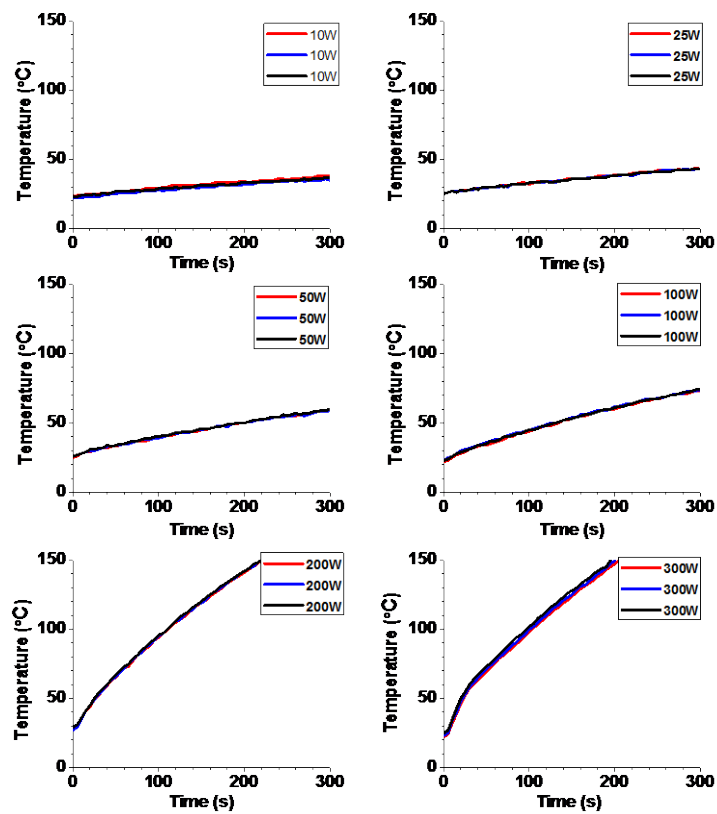


**Figure 4.2.23** Plots of temperature profiles of a toluene solution versus time at different powers induced by microwave heating measured by a microwave IR sensor.

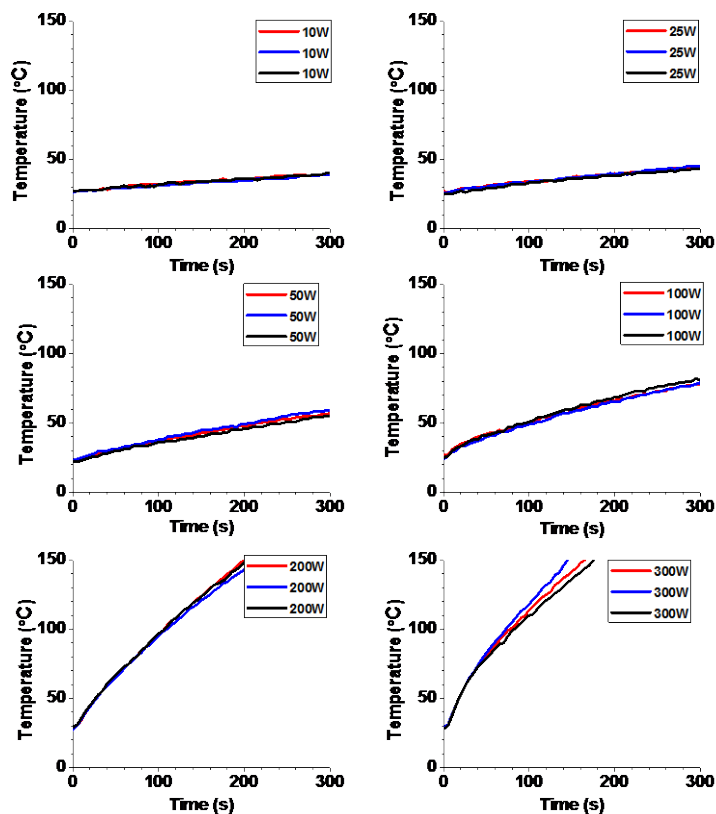


**Figure 4.2.24** Plots of temperature profiles of a toluene solution containing a quartz substrate versus time at different powers induced by microwave heating measured by a microwave IR sensor.

As can be seen from Figure 4.2.23, the heating of a toluene solution under microwave irradiation displayed very good consistency between runs under each condition. After the addition of a quartz sample in toluene, similar temperature profiles with good reproducibility under most conditions were also obtained (Figure 4.2.24). Only small temperature deviations between runs at 300 W was observed. The results are attributed to the low  $\tan \delta$  of quartz ( $6 \times 10^{-5}$ )<sup>17</sup> which results in negligible heating under microwave irradiation.

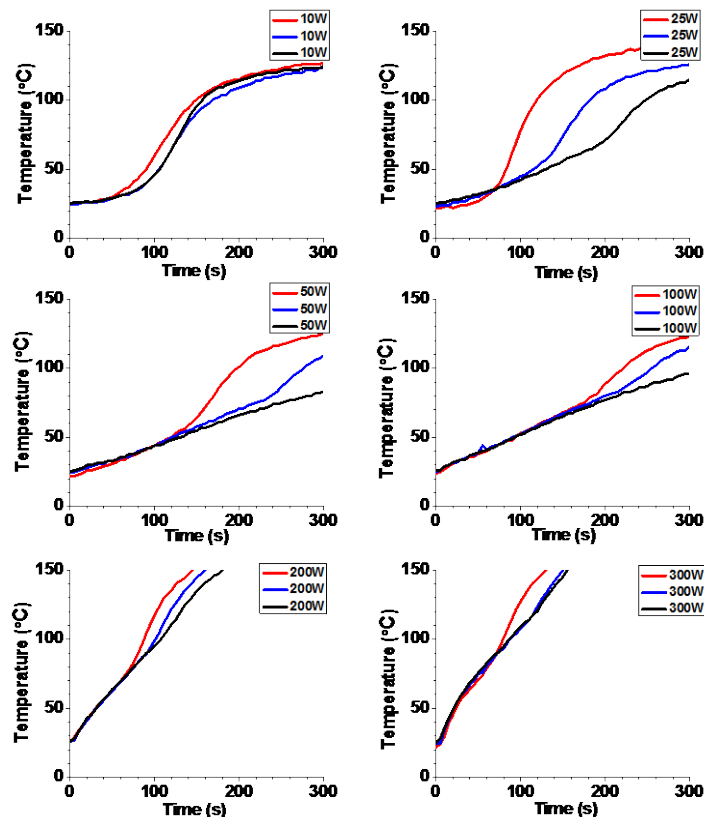


**Figure 4.2.25** Plots of temperature profiles of a toluene solution containing a silicon substrate versus time at different powers induced by microwave heating measured by a microwave IR sensor.

After adding a silicon substrate to the solution, the system temperature increased much faster under the same conditions compared to bare solution and solution containing the quartz substrate (Figure 4.2.25). For example, the temperature of the solution with silicon reached to 100 °C within 3 min under 10 W while the temperature of toluene with and without the quartz sample only raised to 50 °C after 5 min under 10 W. This result is explained by the higher microwave absorbability of silicon due to the larger dielectric constant (11.7~12.9) than quartz (3.8~4.2).<sup>40</sup>

Furthermore, obvious variation in temperature was detected among the three runs of toluene solution containing a silicon substrate under most conditions tested. Although same silicon sample was used in all experiments, the microwave absorption efficiency of the substrate and the resulting heating profile of the system might still vary. This hypothesis is examined more closely in the next section by using an IR camera.

#### **4.2.2.5 Comparison of Temperature Measurement by IR Sensor and IR Camera**

In order to further test the reproducibility and probe the local heating effect, an external IR camera was used to monitor the surface temperature of the system in parallel with the microwave IR sensor. Here, an open vessel system was employed and temperature profiles of silicon sample with different orientations inside the glass tube were tested. The IR camera was placed on top of the microwave tube as shown in Figure 4.2.26. When a silicon sample was placed in a microwave tube without adding solvent, the IR camera measures the surface temperature of the silicon sample. Here, it is worth mentioning that the IR camera might underestimate the surface temperature of silicon due to temperature-dependent emissivity of silicon, but the measurement might still provide information about the uniformity of heat generated on the surface.<sup>41</sup> When silicon sample was completely immersed in the solvent, the IR camera measured the temperature of the solvent at the air-solvent interface. For all the tests, the microwave IR sensor measured the surface temperature of the glass tube from the bottom.

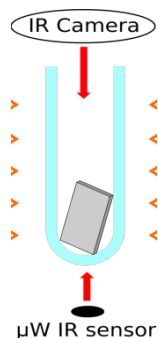


**Figure 4.2.26** Depiction of a setup where a tilted silicon sample was placed in a microwave tube and the temperature profile was monitored by an IR camera from the top and a microwave IR sensor from the bottom in parallel.

**i. Temperature Profiles of Tilted Inserted Silicon Wafer in Air and Toluene Monitored by IR sensor and IR Camera**

Initially, a silicon sample was tilted placed in the microwave tube with and without addition of toluene. The system was heated by microwave under 10 W and 25 W for 1 min. Three trials were run under each condition as indicated in different colors in the graphs. The temperature profiles monitored by both IR camera and microwave IR sensor are shown in Figure 4.2.27.

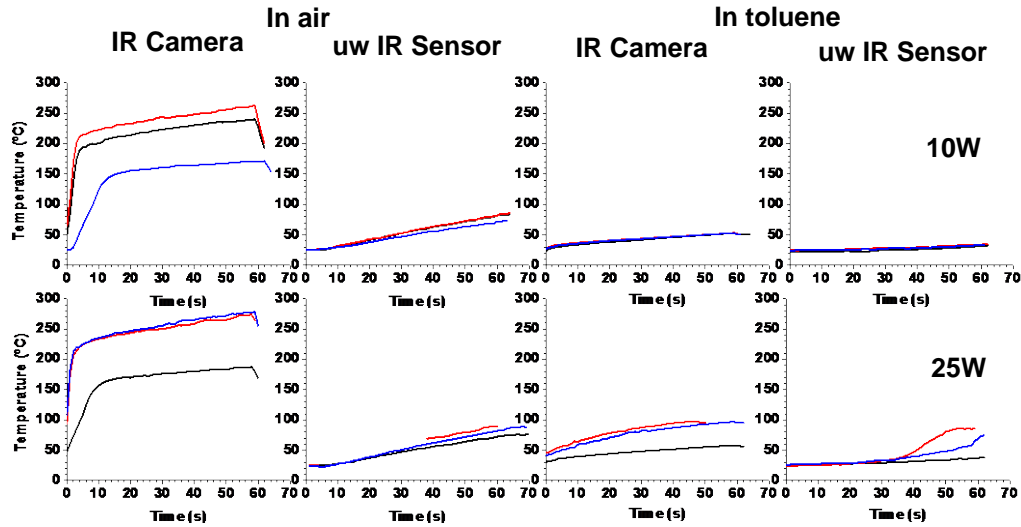


**Figure 4.2.27** Plots of temperature profiles of tilted silicon substrates in air and toluene versus time at different powers induced by microwave heating measured by an IR camera and a microwave IR sensor.

When the silicon sample was heated in air, the temperature profiles of a single point (on the silicon surface) monitored by IR camera under the same conditions were different between different runs. This variability of temperature on the same silicon wafer under microwave heating might result in the difficulty in reproducing the SI-FRP on the substrate as discussed previously. Furthermore, the microwave IR sensor provided very different temperature profiles than the IR camera for the same system (silicon heated in air). Much lower temperatures were observed under both conditions. This is because the IR sensor measured the temperature of the glass tube and the temperature rise of the glass tube was mainly caused by the heat transfer from the silicon wafer. Due to the small contacting area between silicon and the glass tube, the efficiency of heat transfer is presumably low leading to a mild temperature rise. When the silicon sample was heated in toluene, the temperature profiles reported by IR camera and microwave IR sensor were similar. Variation of temperature between runs was seen under 25 W.

**ii. Temperature Profiles of Crushed Silicon Wafer in Air and Toluene Monitored by IR sensor and IR Camera**

Pieces of crushed silicon wafer were then placed in the microwave tube with and without addition of toluene and heated under the same conditions (Figure 4.2.28). The temperature profiles monitored by IR camera and microwave IR sensor are shown in Figure 4.2.29.

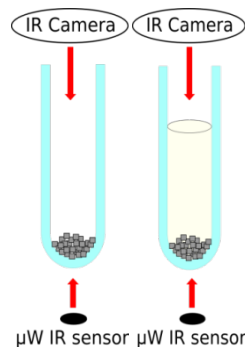


**Figure 4.2.28 Depiction of a setup where pieces of crushed silicon wafer were placed in a microwave tube (right) with and (left) without addition of toluene. The temperature profile was monitored by an IR camera from the top and a microwave IR sensor from the bottom in parallel.**

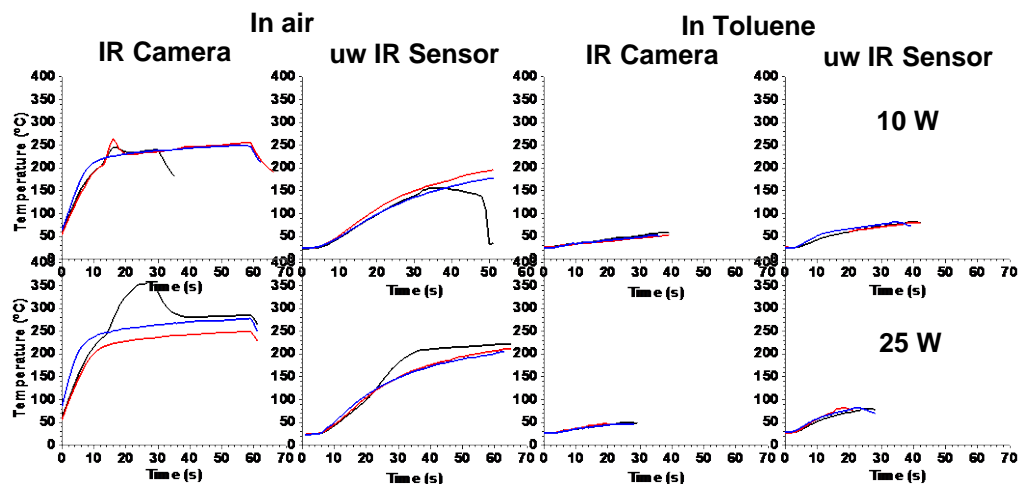


**Figure 4.2.29** Plots of temperature profiles of crushed silicon substrates placed in air and toluene versus time at different powers induced by microwave heating measured by an IR camera and a microwave IR sensor.

Similar to silicon sample that was heated in air as shown in Figure 4.2.27, the temperature of the crushed silicon wafer (monitored by IR camera) heated in air under both conditions also reached above 200 °C within 1 min. The variation in temperature was smaller but still detectable compared with the tilted silicon sample. The temperature reported by microwave IR sensor was higher than that of silicon tilted placed in the tube (Figure 4.2.27). This is possibly due to the larger contacting area between the crushed silicon and the glass vessel leading to more efficient heat transfer.

When toluene was added to the crushed silicon wafer, the temperature of both toluene (monitored by IR camera) and the bottom of the glass tube (monitored by microwave IR sensor) reached 50 °C very quickly (less than 1 min). Small variations in temperature between runs was obtained. This result is also explained by the large contacting area between silicon and toluene resulting in efficient and uniform heat transfer. In this set of experiments, the power was manually turned off when the temperature reached above 50 °C in order to

prevent condensation of toluene on the camera lens caused by evaporation.

### iii. Temperature Profiles of Horizontally Placed Silicon Wafer in Air and Toluene Monitored by IR sensor and IR Camera

A silicon wafer was also heated by placing it horizontally in a microwave tube in air and in toluene as shown in Figure 4.2.30. Both IR methods were employed to measure the temperature and same conditions were used. When the sample was heated in air, temperature was measured at two different points on the same wafer (monitored by IR camera) as indicated in the solid and dotted lines (Figure 4.2.31). Obvious differences in temperature between the two points on the wafer were observed which indicates irreproducible temperature profiles across the same silicon wafer under microwave heating. The temperature profile monitored by the IR sensor was similar to that of silicon tilted placed in the tube which might be due to the similar heat transfer efficiency in both cases (Figure 4.2.27). The temperature profiles of silicon in toluene examined by the two methods were alike except that more variation of temperature was measured by the IR sensor.

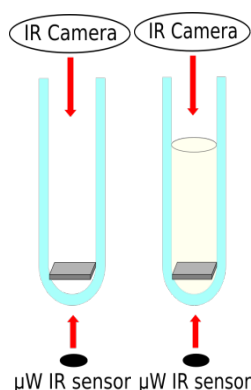


**Figure 4.2.30** Depiction of a setup where silicon wafer was horizontally placed in a microwave tube (right) with and (left) without addition of toluene. The temperature was monitored by an IR camera from the top and a microwave IR sensor from the bottom in parallel.

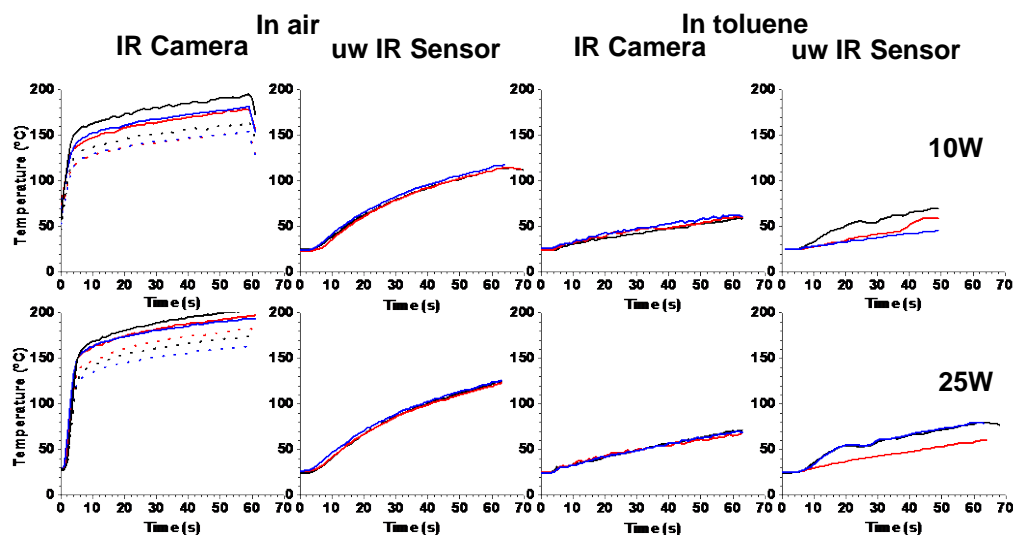


**Figure 4.2.31** Plots of temperature profiles of silicon substrates horizontally placed at bottom of microwave tube in air and toluene versus time at different powers induced by microwave heating measured by an IR camera and a microwave IR sensor.

From the results above, it can be generally concluded that variation in temperature across the same silicon sample can be seen regardless of how the sample was oriented. The reason for this phenomenon is not very clear. A preliminary interpretation is that the microwaves are randomly reflecting passing through the reactor vessel, and this might lead to difficulty to control homogeneous heating on different spots on the surface. This might be one of the reasons for the irreproducible FRP on silicon surface as mentioned previously. Furthermore, the IR camera might underestimate the surface temperature of silicon when it was placed in air due to its low emissivity. Therefore, if local heating exists, the high surface temperature of silicon might lead to fast decomposition of surface bonded initiators which might also be the reason for the poor reproducibility of SI-FRP. In the following section, the IR camera is utilized to further probing the local heating of silicon in solution.

#### **iv. Study of Local Heating using IR Camera**

In order to better understand the surface temperature gradient of a silicon sample in

solution, a silicon substrate was coated with a layer of tetraethoxysilane (TEOS) (~100 nm) as a heat insulator. The sample was heated by microwave irradiation to see if a different temperature profile (reduced surface temperature) can be obtained. The temperature profile of this coated silicon sample ( $\text{Si}/\text{SiO}_x$ ) was tested using the IR camera by horizontally placing the sample in different positions: (1) in air, (2) above toluene with the bottom face of the sample in contact with toluene (3) and with the sample immersed just 1~2 mm into the toluene. Figure 4.2.32 illustrates these three positions. The sample was heated for 1 min during which an IR camera placed on top of the tube recorded the top surface temperature (i.e. silicon or toluene). Two power conditions, 10 W and 25 W were employed and three trials were run for each condition as indicated in the different colors in the graphs. The results are shown in Figure 4.2.33.

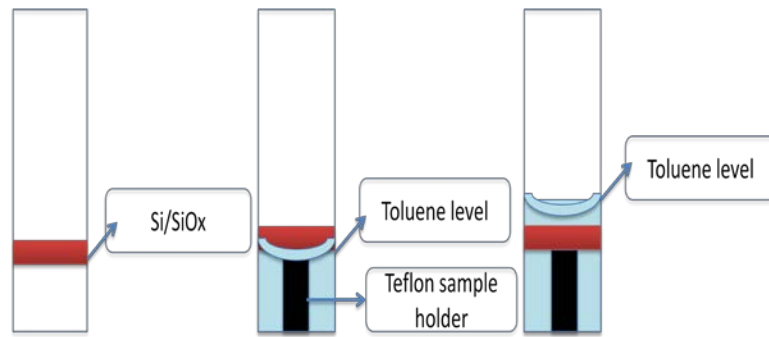


**Figure 4.2.32 Depiction of a TEOS coated silicon sample placed (1) in air, (2) above toluene with the bottom face contacting with toluene (3) and below toluene for just 1~2 mm in a microwave tube.**

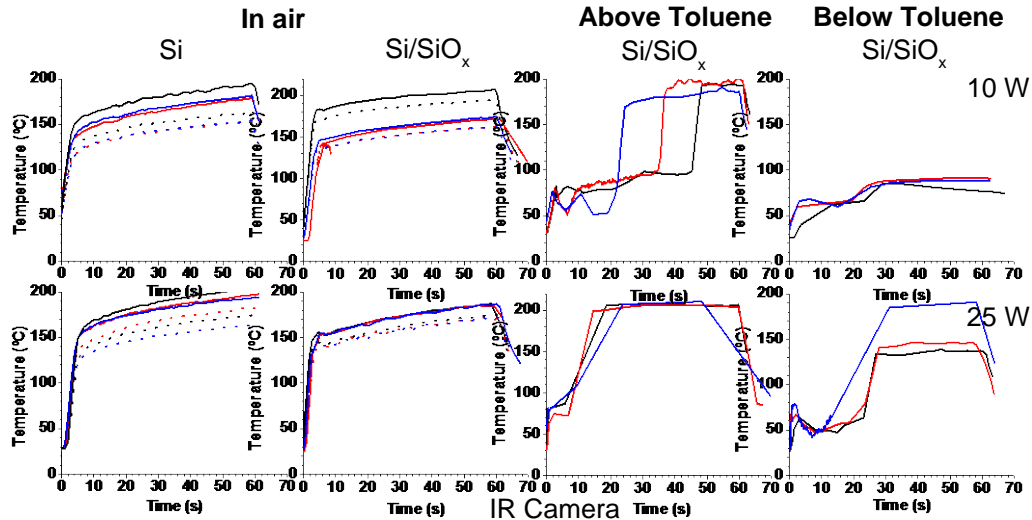


**Figure 4.2.33 Temperature profiles of microwave heated (1) Si in air, (2) Si/SiO<sub>x</sub> in air, (3) Si/SiO<sub>x</sub> above toluene with the bottom face contacting with toluene (4) and Si/SiO<sub>x</sub> below toluene for just 1~2 mm at different powers monitored by an IR camera.**

When Si/SiO<sub>x</sub> was heated in air, the temperature of two different spots on the same sample for each run were recorded as indicated in the solid and dotted lines on graphs (second column of graphs). The temperature profile of Si/SiO<sub>x</sub> in air was very similar to the previously measured silicon sample heated in air (first column of graphs). Surface temperatures increased instantly and variation of temperature on different spots on the surfaces were seen. Although both Si and Si/SiO<sub>x</sub> reached similar temperature (~200 °C) after 1 min, the temperature of Si/SiO<sub>x</sub> might be closer to the real surface temperature than silicon due to the higher emissivity of silica than silicon.<sup>42</sup>

When Si/SiO<sub>x</sub> was placed above toluene as indicated in Figure 4.2.32, different results were obtained. As can be seen from the graphs in the third columns in Figure 4.2.33, the temperature did not increase as instantly as when Si/SiO<sub>x</sub> was heated in air (the second column of graphs). There is a lag time before the large temperature rise. This lag time is more obvious at 10W than 25 W when the sample was placed above toluene.

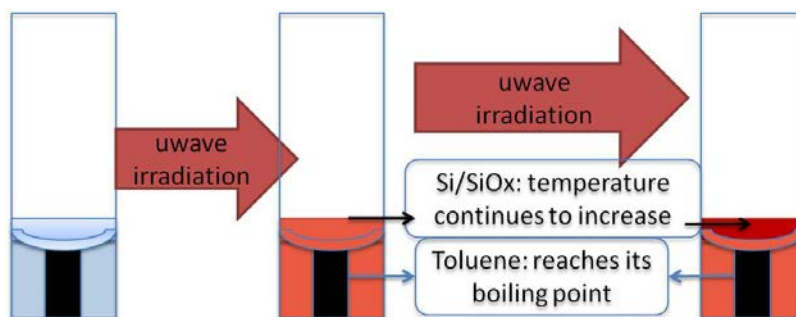


**Figure 4.2.34 A cartoon illustrating the "saturation of heat transfer" between Si/SiO<sub>x</sub> and toluene under unpressurized atmosphere.**

The lag time for the temperature increase might be due to the fast heat transfer from Si/SiO<sub>x</sub> to toluene. When the sample was above toluene (the third column of graphs), the heat could transfer from the bottom face of the sample to the toluene below. The IR camera measured the temperature of top-surface of Si/SiO<sub>x</sub> in this case. During the first 10~20 s, the surface temperature was low which might indicate that most of the heat generated by Si/SiO<sub>x</sub> during this time was rapidly transferred to the toluene below. The surface temperature soon increased to 200 °C. Since all these tests were run in an open vessel, the temperature of toluene (liquid) should not be able to reach above the boiling point. Therefore, in this case, it is reasonable to conclude the surface temperature of Si/SiO<sub>x</sub> is higher than the surrounding liquid after reaching the heat transfer saturation (Figure 4.2.34). The temperature difference (~90 °C) can be calculated by subtracting the value of boiling point of toluene (111 °C) from the maximum temperature on Si/SiO<sub>x</sub> (~200 °C). However, SI-FRP experiments were mostly performed in a closed vessel where pressure can build; so toluene can be heated beyond its normal boiling point. This would lead to difficulty in interpreting the exact temperature difference between the surface temperature of Si or Si/SiO<sub>x</sub> and bulk solution.

When the sample was immersed in toluene (1~2 mm below the air-toluene interface) and heated at 10 W, the temperature only reached around 100 °C within 1 min. Under 25 W, however, the temperature increased to ~200 °C after about 20 s of heating (the fourth column

of graphs in Figure 4.2.33). In this case, the IR camera measured the temperature of the toluene at the air-toluene interface. The temperature of toluene (liquid) should not be able to exceed its boiling point in this open system. One possible explanation for this result might be that the top-layer of toluene solution was heated very fast by heat transfer from Si/SiO<sub>x</sub> resulting in evaporation of toluene. The temperature measured by the IR camera in this case (25 W) might be the temperature of toluene gas layer instead of toluene liquid surface. However, when the sample was examined after the experiment was concluded, liquid toluene was observed on top of the silicon, so the toluene must have re-condensed.

Comparing the temperature profile of Si/SiO<sub>x</sub> placed above and below toluene at 10 W, the temperature of toluene in the first case was able to reach the boiling point of toluene within 1 min which then result in the saturation of heat transfer and a temperature increase (to 200 °C) on the Si/SiO<sub>x</sub> surface. However, in the latter case, the temperature of toluene was not able to reach above 100 °C within 1 min heating. The differences between these two samples are (1) the heat-transfer interface (first case: silicon bottom surface and toluene; second case: top silica surface and toluene) and (2) the amount of toluene. The thermal conductivities of silicon and silica are very different (130 and 1.4 W/m·K respectively);<sup>43</sup> therefore the different temperature profile is likely caused by the different interfaces through which heat had to transfer. The addition of more toluene to the vessel might also result in a reduced temperature rise at low heating powers considering the higher heat capacity of toluene (1.71 J/g·°C) than silicon (0.75~0.8 J/g·°C).<sup>43a, 44</sup>

**Table 4.2.7 Heat capacity of different solvents.**<sup>44</sup>

	CCl <sub>4</sub>	Toluene	Water
c <sub>p</sub> (J/g·K)	0.85	1.71	4.18

The temperature profile of the same TEOS coated silicon sample (Si/SiO<sub>x</sub>) was also tested by placing the sample in solvents with different heat capacities as listed in Table 4.2.7.

The Si/SiO<sub>x</sub> was placed above the solvents similarly as mentioned above. The same conditions were used and the results are shown in Figure 4.2.35.

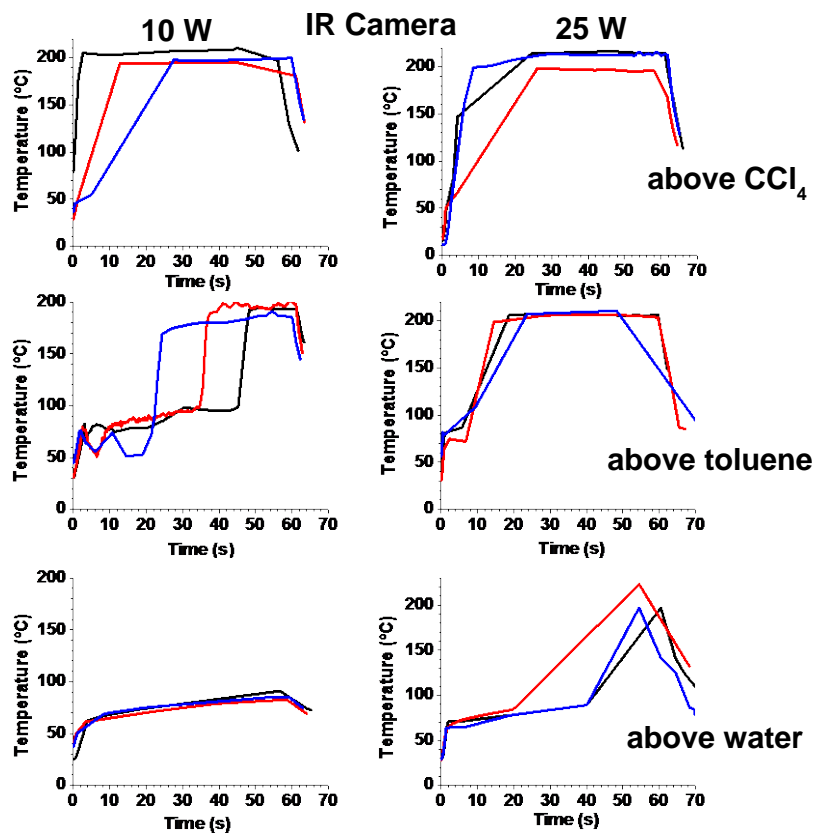


**Figure 4.2.35** Temperature profiles of microwave heated Si/SiO<sub>x</sub> sample placed above CCl<sub>4</sub>, toluene and water with the bottom face contacting with solvents at different powers monitored by an IR camera.

As can be seen from the temperature profiles of Si/SiO<sub>x</sub> when it was placed above various solvents, the lag time for the rise in surface temperature was different presumably due to the different  $c_p$  of these solvents. CCl<sub>4</sub> has the smallest  $c_p$  so the heat-transfer from

Si/SiO<sub>x</sub> to CCl<sub>4</sub> reached a "saturation" (the boiling point of CCl<sub>4</sub>) fastest resulting in a quick surface temperature rise on Si/SiO<sub>x</sub>. Water has the highest c<sub>p</sub> so the heat-transfer "saturation" occurred slower resulting in longer lag time for the rise in temperature on sample surface. Again, in these cases, it is reasonable to believe the surface temperature of Si/SiO<sub>x</sub> is higher than the surrounding liquid after reaching the heat transfer saturation. However, it is unknown if this difference still exists when these tests are performed in a closed vessel.

Considering the possible underestimation of the surface temperature of silicon in air by the IR camera, the local heating of silicon when it is coated with silica or placed in solution, is difficult to interpret. Also, other factors including the thermal conductivity of the coating or solution, the thickness of the coated layer and the amount of solution might also affect a well-controlled temperature gradient of the coated layer on the silicon. This thought was further probed by testing the temperature profile of a silicon sample with a layer of PDMS (1 mm) placed on top was heated by microwave at 10 W for 1 min. Three trials were run under this condition as indicated in the different colors in Figure 4.2.36.

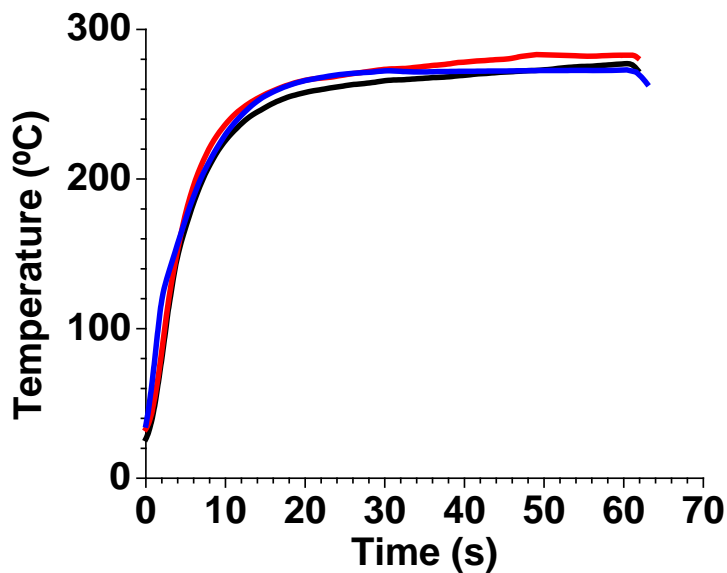


**Figure 4.2.36 Temperature profiles of microwave heated silicon sample with a PDMS layer attached to the surface monitored by an IR camera.**

As can be seen from the result, when a layer of PDMS was employed as an insulator, the surface temperature of PDMS reached 280 °C within 1 min which is even higher than the temperature of the bare silicon as shown in Figure 4.2.33. This result indicates that the surface temperature measured previously is very likely to be inaccurate because PDMS has a higher emissivity (~0.9) than silicon.<sup>45</sup> If a steady-state ( $\frac{dT}{dt} = 0$ ) of this coated layer is assumed, and the input power of microwave (10 W) is assumed to be the same power transferred from the silicon substrate to the PDMS layer, the temperature difference between the silicon surface and the PDMS surface can be estimated using the following equation,

$$\Delta T = \frac{P \times d}{\kappa \times A} \quad (17)$$

where P (W) is heat transferred per unit time, d (m) is the thickness of PDMS,  $\kappa$  (0.15 W/m·°C) is the thermal conductivity of PDMS which is similar to toluene and A (m<sup>2</sup>) is the contact area between the substrate and PDMS. The temperature difference between the two surfaces is calculated to be more than 1000 °C which means the silicon surface is more than 1200 °C. Even by reducing the power to the minimum (1 W), the temperature difference is still computed to be above 100 °C. The high temperature is not suitable for the SI-FRP due to the fast decomposition of initiator. These results suggest that it might be impractical to generate a reasonable surface temperature on silicon under these conditions and it might be necessary to use a much thicker insulator layer with poor thermal conductivity to obtain a lower surface temperature. However, this idea needs to be further tested. Furthermore, if there is a temperature gradient across an insulator coated silicon sample in solution, it is still hard to conclude how this will change when going from an open vessel system to a closed vessel system.

### 4.3 Conclusions

SI-FRP of styrene was performed on ATCS modified Fe<sub>2</sub>O<sub>3</sub> nanoparticles by microwave irradiation. Different working modes and conditions for microwave irradiation were explored in order to better control the local heating effect of the particles as hypothesized in the beginning of this chapter. Among all the working modes, including duty

cycle mode, power time mode and SPS mode, SPS mode was demonstrated to give better control of the system temperature. Under this working mode, FRP of styrene with and without the presence of the ATCS modified nanoparticles displayed both lower monomer conversion (<20%) and smaller PDI (<1.5) compared to thermal heating under the same conditions. The low monomer conversion was explained by the fast formation and decomposition of radical initiators leading to reduced propagation rate. The small PDI was reasoned by the reduced chain transfer effect under low monomer conversion. The experimental results did not support the local heating effect since reactions under microwave heating without Fe<sub>2</sub>O<sub>3</sub> nanoparticles also produced low PDI polymer. Furthermore, a model calculation of the surface temperature gradient also indicated small temperature difference between Fe<sub>2</sub>O<sub>3</sub> nanoparticle surface and bulk solution.

Upon further study, GC was demonstrated to be a relatively precise method for determining monomer conversion. The reproducibility of SI-FRP on silicon surface was found to be poor using the previously tested conditions under power time mode. Although revised conditions under SPS mode were applied, it was still difficult to obtain a thicker polymer on a microwave absorbing surface compared to a microwave transparent surface within a short time as reported before.<sup>37</sup> By using microwave IR sensor and an external IR camera, the reproducibility of system temperature was examined. The results show variation of temperature across both Si and Si/SiO<sub>x</sub> samples under same conditions which is likely to be one of the reasons for the poor reproducibility of SI-FRP on these substrates. The surface temperature of silicon was likely to be underestimated by the IR camera due to the low emissivity of silicon which might also be a reason for the irreproducible SI-FRP. The local heating effect of the flat Si and Si/SiO<sub>x</sub> sample was probed by placing the sample in different positions. From the results, the surface temperature of the sample was thought to be higher than the bulk solution due to a saturation of heat transfer. Solvents with a low or moderate  $c_p$  such as CCl<sub>4</sub> and toluene can lead to a relatively fast temperature rise of the bulk solution which might reduce the temperature gradient from surface to bulk relatively quickly. However, all the temperature tests were performed in an open vessel system which might be

deviate from results obtained under the actual experimental conditions where the system was sealed. Therefore, further study needs to be carried out in order to get a more precise temperature gradient for silicon sample in solution in a closed vessel system. Furthermore, a reasonable surface temperature of silicon was shown to be lack of control under practical conditions and a thick insulator layer might be necessary to attach to the silicon surface. The layer properties including thermal properties and thickness still require further investigation.

## 4.4 Experimental

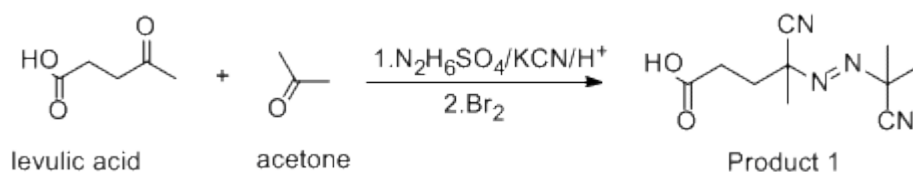
### 4.4.1 Materials

Iron (III) oxide nanoparticles (FW 159.69 g/mol, 20-40 nm, S.A. 30-60 m<sup>2</sup>/g) and silica nanoparticles (FW 60.09 g/mol, 20-40 nm, S.A. 180 m<sup>2</sup>/g) were dried overnight under high vacuum (5 millitorr) before use. Toluene was distilled under a nitrogen atmosphere from sodium using benzophenone as an indicator. Dichloromethane was distilled under a nitrogen atmosphere from phosphorus pentoxide. Styrene was passed through a neutral alumina column, distilled under reduced pressure and stored under nitrogen at -20 °C. All the other solvents and chemicals were used as received. A microwave system (CEM corp, Discover focused<sup>TM</sup>, single mode, self-tuning, magnetron frequency 2450 MHz, maximum power output 300 W, temperature control range 10-250 °C, *in situ* magnetic variable stirring speed) was used as the heating source.

### 4.4.2 Synthesis of Asymmetric Azo Initiators

#### i. Synthesis of Product 1

##### Scheme 4.4.1

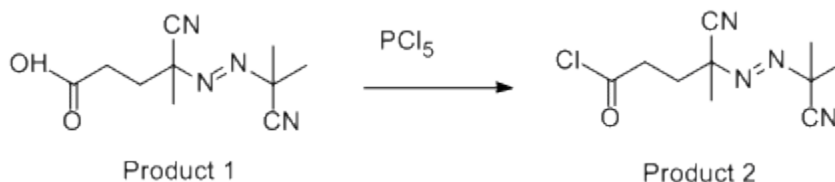


Levulinic acid (62.50 g, 0.54 mol) was first dissolved in 65.00 mL deionized (DI) water. To this stirring solution, sodium bicarbonate (45.41 g, 0.54 mol) was gradually added to neutralize the solution and the carbon dioxide produced was released. The solution was stirred overnight until the pH value reached 7.00. In a 3 L three-necked round bottom flask, hydrazine sulfate (70.05 g, 0.54 mol), potassium cyanide (70.07 g, 1.08 mol) and 950 mL DI water were added. This mixture was heated to 50 °C for 40 min to dissolve all of the solids. The neutralized levulinic acid (filtered if solid sodium bicarbonate remained) and 40 mL of acetone was mixed and added dropwise to the three-necked flask. This process took more than 30 min. The solution was stirred at 50 °C for 3 h and then cooled in an ice bath. The solution was then acidified with hydrochloric acid (2 N) to pH 4.00 (from pH 8.00) which was tested with a pH meter. At this temperature (0 °C), bromine (50 mL, 0.97 mol) was added dropwise to the mixture until the solution remained dark red. The solution needed to be stirred strongly during this process. After the addition of bromine, the solution was stirred for 30 min. Sodium bisulfite was then added to react with the excess bromine until the red color disappeared. The solution was then stirred overnight at room temperature to let the entire released hydrogen cyanide escape. After this, the solution was filtered. The precipitate was washed twice with DI water and suspended in about 35 mL sodium hydroxide solution (1 N), stirred for 30 min and then filtered. The insoluble part consisted of azobisisobutyronitrile (AIBN) which was kept for future use. After filtration, the solution was acidified with concentrated hydrochloric acid and a white precipitate formed (Product 1). The filtered solid was dried under high vacuum (5 millitorr) and 8.25 g of product 1 was obtained. The filtrate was extracted twice with dichloromethane (DCM), washed with DI water and dried over anhydrous sodium sulfate. The filtered solution was concentrated using a rotatory evaporator and then dried under high vacuum (5 millitorr). A second portion of product 1 (29.45 g) was obtained as yellow oil. This yellow oil was recrystallized in a mixture of methanol/water (1/5, v/v) at room temperature for three days and 4.20 g of product 1 was obtained. The recrystallization can take longer if there are more impurities

(when the oil is dark yellow). Combined yield of product 1 was 12.45 g, 10.41%.  $^1\text{H NMR}$  ( $\text{CDCl}_3$   $\delta$  in ppm): 2.36-2.64 (m, 4H,  $\text{CH}_2$ ), 1.72, 1.73 and 1.76 (s, 3H each,  $\text{CH}_3$ )

## ii. Synthesis of Product 2

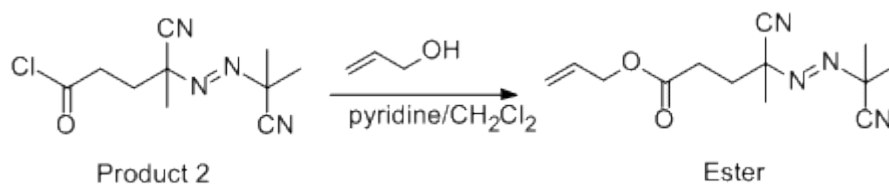
### Scheme 4.4.2



To a 250 mL round bottom flask, phosphorus pentachloride (12.11 g, 58.08 mmol) in 15 mL DCM was added. This solution was placed in an ice bath under a nitrogen atmosphere. Product 1 (3.00 g, 13.51 mmol) in 15 mL DCM was added dropwise to the solution. The mixture was then allowed to warm to room temperature and stirred overnight. The excess of phosphorus pentachloride was filtered off under nitrogen. The remaining solution was concentrated using a rotatory evaporator. The resulting phosphorus pentachloride precipitate was removed by filtration and the solution was concentrated further until no more solid precipitated. A few drops of DCM were added to the concentrated solution and this solution was added dropwise to hexane cooled in dry ice/acetone bath. A white precipitate was obtained, filtered and dried to give 2.78 g of product 2 (85% yield).  $^1\text{H NMR}$  ( $\text{CDCl}_3$   $\delta$  in ppm): 2.91-3.20 (m, 2H,  $\text{CH}_2\text{COCl}$ ), 2.40-2.62 (m, 2H,  $\text{CH}_2\text{C}$ ), 1.71, 1.72 and 1.75 (s, 3H each,  $\text{CH}_3$ )

## iii. Synthesis of Allylic ester

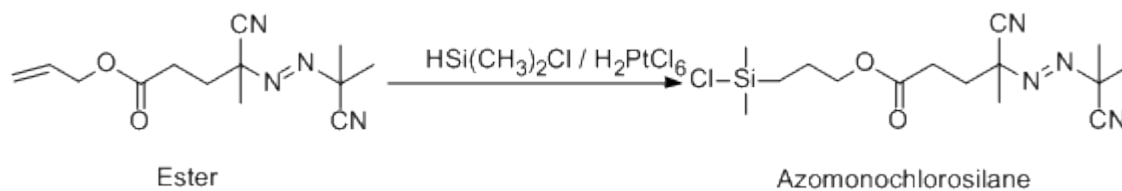
### Scheme 4.4.3



To a 250 mL flask, allyl alcohol (0.95 mL, 13.94 mmol) and pyridine (2.26 mL, 28.09 mmol) were added to 17.39 mL DCM. This solution was placed in an ice bath under a nitrogen atmosphere. To this solution, a mixture of product 2 (2.78 g, 11.56 mmol) in 17 mL DCM was added dropwise. The solution was then allowed to warm to room temperature and stirred overnight. The solution was then washed twice with sulfuric acid (2 N), sodium bicarbonate saturated solution and water respectively. The organic layer was dried over anhydrous sodium sulfate and the filtered solution was concentrated using a rotatory evaporator. The resulting pale yellow oil was dissolved in a small amount of DCM and poured into 100 mL hexane cooled in dry ice/acetone bath. A white to yellowish solid was obtained, filtered and dried to give 1.72 g of allylic ester (57% yield).  $^1\text{H NMR}$  ( $\text{CDCl}_3$   $\delta$  in ppm): 5.88-5.97 (m, 1H, =CH-), 5.25-5.36 (m, 2H,  $\text{CH}_2=$ ), 4.60-4.62 (d, 2H,  $\text{CH}_2\text{O}$ ), 2.38-2.57 (m, 4H,  $\text{CH}_2\text{CH}_2$ ), 1.72, 1.74, 1.76 (s, 3H each,  $\text{CH}_3$ )

#### iv. Synthesis of Azochlorosilane

**Scheme 4.4.4**

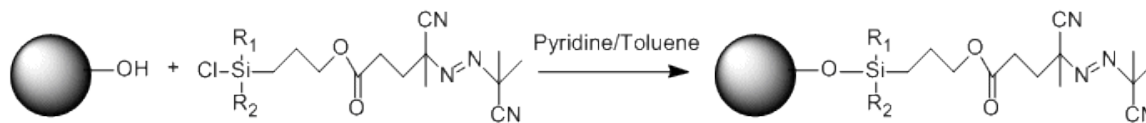


A solution of hexachloroplatinic acid (17.2 mg, 0.04 mmol) in 0.29 mL of dimethyl ether/ethanol (1/1, v/v) was added to a suspension of 1.72 g of the allylic ester and 17.2 mL of either monochlorosilane or trichlorosilane. The mixture was heated to reflux for 3 h until the entire solid was dissolved indicating the completion of the reaction. The excess silane was removed under high vacuum (5 millitorr) with a liquid nitrogen cooled trap. The product was concentrated and a small amount of DCM was added to the product and the solution was filtered over anhydrous sodium sulfate under flowing nitrogen to remove the residual platinum catalyst. The product was dried under high vacuum (5 millitorr) to obtain 1.85 g of

pale green oil (79% yield).  $^1\text{H}$  NMR ( $\text{CDCl}_3$   $\delta$  in ppm): 4.10 (t, 2H,  $\text{OCH}_2$ ), 2.36-2.53 (m, 6H,  $\text{CH}_2$ ), 1.71-1.75 (s, 3H each,  $\text{CH}_3$ ), 0.81-0.92 (m, 2H,  $\text{SiCH}_2$ ), 0.44 (s, 6H,  $\text{SiCH}_3$ )

#### 4.4.3 Initiator Deposition

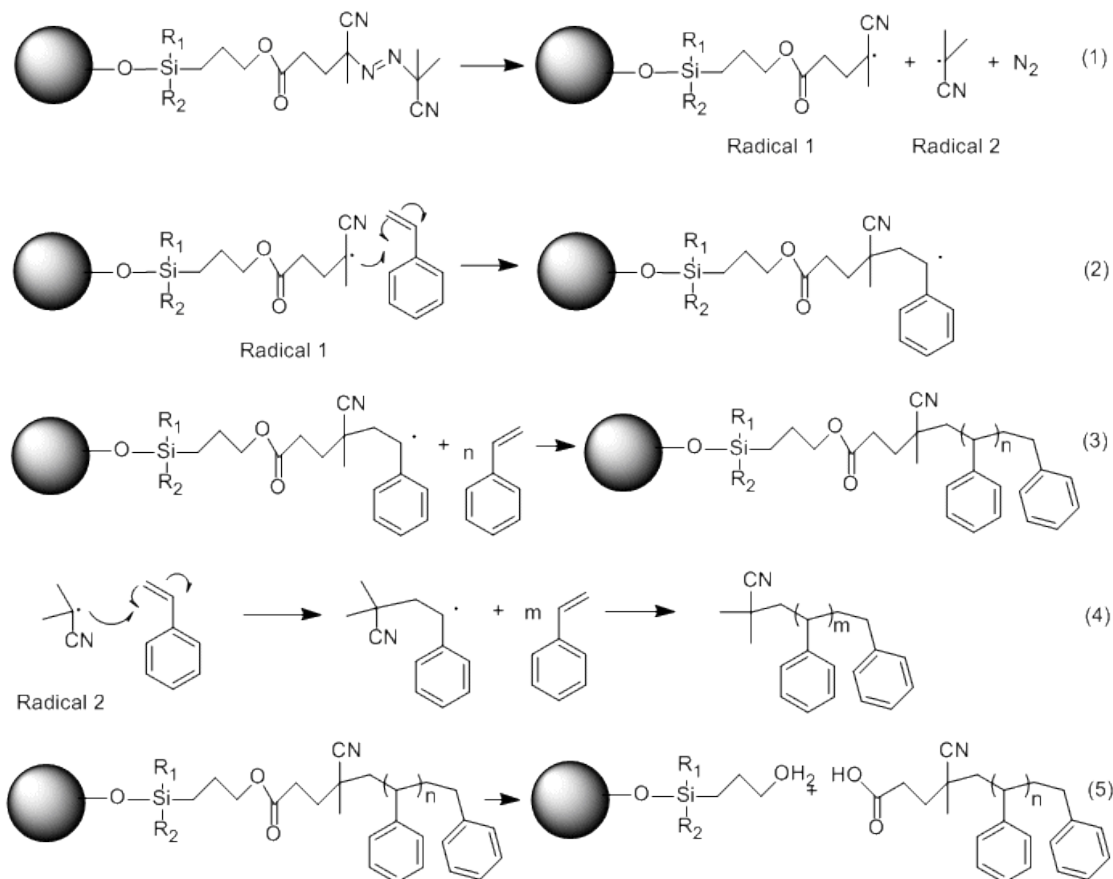
Scheme 4.4.5



Under a nitrogen atmosphere, a solution of 1.50 g of the azo- mono- or tri- chlorosilane in 50 mL of toluene was added to a suspension of 3 g silica or 12 g iron (III) oxide nanoparticles in 100 mL of toluene. A total of 3 mL of pyridine was added and the mixture was stirred for 12 h. Then the modified nanoparticles were centrifuged and washed with toluene, ethanol, acidified ethanol/water (1/1, v/v, pH 3), ethanol/water (1/1, v/v), ethanol and diethyl ether respectively. The remaining solids were dried overnight at under high vacuum (5 millitorr).

#### 4.4.4 Microwave Induced and FRP on Substrate

Scheme 4.4.6



In a 10 mL microwave tube, 2 mL/4 mL styrene/toluene mixture was added to 720 mg iron (III) oxide or 120 mg silica nanoparticles. The mixture was degassed under vacuum through repeated freeze-pump-thaw cycles. The microwave tube was then placed in the chamber of the microwave reactor. Different conditions for conducting the microwave irradiation were explored as described in the results and discussion section. Two types of active radicals are formed during the activation process of the initiators on the particles (eq. 1). Radical 1 is bound to nanoparticles and radical 2 is dissolved in the solution. These two types of radicals can then initialize free radical polymerization of styrene.

Radical 1 can react with styrene monomer to form polymer brushes bonded to the particles (eq. 2&3). At the same time, radical 2 can initiate polymerization of styrene when the temperature of the bulk solution is high enough for propagation (eq. 4). As a result, there are expected to be two types of polymers after the reaction, nanoparticle bound and nonbonded polymers. The particles and the solution can be separated by centrifugation. The supernatant contained nonbonded polymers. The particles were washed with toluene several times and all the supernatant was collected. If a large amount of polymer was produced, nonbonded polymer could be precipitated out in methanol and then collected. If the amount of polymer produced was very small (less than 100 mg), the solution was placed under high vacuum to evaporate all the solvent and monomer residuals. The non-volatile residue contained nonbonded polymer.

After separating the nanoparticles from the nonbonded polymer solution, the polymer modified particles were suspended in 24 mL of toluene and 2.4 mL methanol and 12 mg of *p*-toluenesulfonic acid (eq. 5) were added. The mixture was heated to reflux overnight. This process has been shown to cleave the ester linkage and free the polymer from the particles. The products were isolated by the same procedures as described above for the nonbonded polymer.

#### **4.4.5 Thermal FRP on Substrate**

In a 10 mL glass tube, 2 mL/4 mL styrene/toluene mixture was added to 720 mg iron (III) oxide or 120 mg silica initiator modified nanoparticles. The mixture was degassed under vacuum through repeated freeze-pump-thaw cycles. The glass tube was then placed in an oil bath at a given temperature. After the reaction, same procedures as mentioned above were followed to collect the bonded and nonbonded polymers.

#### **4.4.6 Characterization**

ATR-FTIR spectra were collected on the Excalibus Series bench (Varian) with the MIRacle Single Reflection ATR kits (PIKE). The ATR crystal was a germanium crystal. The pressure to hold the sample was 530 lb. The background scans were collected in air. NMR spectra were recorded on a 300 Hz Gemini 2300 spectrometer using CDCl<sub>3</sub> as the solvent.

The molar mass and PDI values of polymers were determined by gel permeation chromatography (GPC) on a Waters Lambda-Max Model 481 using THF as the solvent. The column used for GPC was Jordi-gel DVB 1000 Å. Monomer conversion was determined by UV-Vis spectroscopy (Hewlett Packard 8452 A, Diode Array Spectrophotometer) and GC (Hewlett Packard 5890 Series II, Column: J&W Scientific Cat No. 123.5032) with a flame ionization detector (FID).

## REFERENCES

1. Dossi, M.; Storti, G.; Moscatelli, D., Initiation kinetics in free-radical polymerization: prediction of thermodynamic and kinetic parameters based on ab initio calculations. *Macromol. Theory Simul.* **2010**, *19* (4), 170-178.
2. (a) Braun, D., *Polymer Synthesis :Theory and Practice : Fundamentals, Methods, Experiments*. 4th ed.; Springer: Berlin ; New York, 2005; p 172; (b) Gasper;, J. D.; Lombardi, R. A., Acrylic Polymers. In *Coatings Technology Handbook*, 3rd ed.; Tracton., A. A., Ed. CRC Press: New York : Marcel Dekker, 2005; pp 46-2.
3. (a) Sarac, A. S., Redox polymerization. *Prog. Polym. Sci.* **1999**, *24* (8), 1149-1204; (b) Bovey, F. A.; Kolthoff, I. M., *Emulsion Polymerization*. Interscience: New York, 1955.
4. Odian, G. G., *Principles of Polymerization*. 4th ed.; Wiley: Hoboken, N.J., 2004.
5. Minamii, N.; Yamada, B., In *Polymeric Materials Encyclopedia*, Salamone, J. C., Ed. CRC Press: 1996; Vol. 1, p 435.
6. (a) Lewis, F. M.; Matheson, M. S., Decomposition of aliphatic azo compounds. *J. Am. Chem. Soc.* **1949**, *71* (2), 747-748; (b) Raley, J. H.; Rust, F. F.; Vaughan, W. E., Decompositions of DI-T-alkylperoxides. 1. Kinetics. *J. Am. Chem. Soc.* **1948**, *70* (1), 88-94; (c) Moad, G.; Solomon, D. H., *The Chemistry of Free Radical Polymerization*. Pergamon, Oxford, 1995; p 67.
7. Brandrup, J.; Immergut, E. H.; Grulke, E. A.; Abe, A.; Bloch, D. R., *Polymer Handbook* 4th ed.; John Wiley & Sons: p II/2 & II/34.
8. (a) Iwasaki, T.; Yoshida, J., Free radical polymerization in microreactors. Significant improvement in molecular weight distribution control. *Macromol* **2005**, *38* (4), 1159-1163; (b) Nabifar, A.; McManus, N. T.; Vivaldo-Lima, E.; Lona, L. M. F.; Penlidis, A., Thermal polymerization of styrene in the presence of TEMPO. *Chem. Eng. Sci.* **2009**, *64* (2), 304-312.
9. Pojman, J. A.; Willis, J.; Fortenberry, D.; Ilyashenko, V.; Khan, A. M., Factors affecting propagating fronts of addition polymerization-velocity, front curvature, temperature

profile, conversion, and molecular-weight distribution. *Journal of Polymer Science Part a-Polymer Chemistry* **1995**, *33* (4), 643-652.

10. (a) Zammit, M. D.; Davis, T. P.; Haddleton, D. M.; Suddaby, K. G., Evaluation of the mode of termination for a thermally initiated free-radical polymerization via matrix-assisted laser desorption ionization time-of-flight mass spectrometry. *Macromol* **1997**, *30* (7), 1915-1920; (b) Bamford, C. H.; Eastmond, G. C.; Whittle, D., Network formation. 3. Influence of organometallic initiator on network structure. *Polymer* **1969**, *10* (9), 771-&.

11. (a) Kukulj, D.; Davis, T. P.; Gilbert, R. G., Chain transfer to monomer in the free-radical polymerizations of methyl methacrylate, styrene, and alpha-methylstyrene. *Macromol* **1998**, *31* (4), 994-999; (b) Kapfenstein-Doak, H.; Barner-Kowollik, C.; Davis, T. P.; Schweer, J., A novel method for the measurement of chain transfer to monomer constants in styrene homopolymerizations: The pulsed laser rotating reactor assembly. *Macromol* **2001**, *34* (9), 2822-2829.

12. (a) Braks, J. G.; Huang, R. Y. M., Polymerization mechanisms and molecular weight distribution. 2. AIBN initiated polymerization of styrene at 60 degree C. *J. Appl. Polym. Sci.* **1978**, *22* (11), 3111-3120; (b) May, J. A.; Smith, W. B., Polymer studies by gel permeation chromatography. 2. Kinetics parameters for styrene polymerizations. *J. Phys. Chem.* **1968**, *72* (1), 216-&.

13. Gleixner, G.; Breitenbach, J. W.; Olaj, O. F., Kettenübertragung durch tetrabromkohlenstoff bei der polymerisation von styrol und von vinylacetat. *Die Makromolekulare Chemie* **1977**, *178* (8), 2249-2255.

14. Matyjaszewski, K., *Handbook of Radical Polymerization*. Wiley-Interscience: Hoboken, N.J., 2003.

15. (a) Patten, T. E.; Matyjaszewski, K., Atom transfer radical polymerization and the synthesis of polymeric materials. *Advanced Materials* **1998**, *10* (12), 901-915; (b) Matyjaszewski, K.; Xia, J., Atom transfer radical polymerization. *Chem. Rev.* **2001**, *101* (9), 2921-2990; (c) Chiefari, J.; Chong, Y. K.; Ercole, F.; Krstina, J.; Jeffery, J.; Le, T. P. T.; Mayadunne, R. T. A.; Meijs, G. F.; Moad, C. L.; Moad, G.; Rizzardo, E.; Thang, S. H., Living free-radical polymerization by reversible addition-fragmentation chain transfer: the RAFT process. *Macromol* **1998**, *31* (16), 5559-5562.

16. Tsarevsky, N. V.; Matyjaszewski, K., Environmentally benign atom transfer radical polymerization: Towards “green” processes and materials. *Journal of Polymer Science Part A: Polymer Chemistry* **2006**, *44* (17), 5098-5112.
17. Bogdal, D.; Prociak, A., *Microwave-Enhanced Polymer Chemistry and Technology*. Wiley: 2008; p 280.
18. Mingos, D. M. P.; Baghurst, D. R., Tilden lecture. Applications of microwave dielectric heating effects to synthetic problems in chemistry. *Chem. Soc. Rev.* **1991**, *20* (1), 1-47.
19. Metaxas, A. C.; Meredith, R. J., *Industrial Microwave Heating*. Peter Peregrinus Limited: London, 1983.
20. (a) Chia, H. L.; Jacob, J.; Boey, F. Y. C., The microwave radiation effect on the polymerization of styrene. *Journal of Polymer Science Part A: Polymer Chemistry* **1996**, *34* (11), 2087-2094; (b) Jacob, J.; Chia, L. H. L.; Boey, F. Y. C., Microwave polymerization of poly(methyl acrylate): Conversion studies at variable power. *J. Appl. Polym. Sci.* **1997**, *63* (6), 787-797.
21. Perreux, L.; Loupy, A., *Microwaves in Organic Synthesis*. 3rd ed.; Wiley: New York, NY, USA, 2013.
22. Lidström, P.; Tierney, J.; Wathey, B.; Westman, J., Microwave assisted organic synthesis—a review. *Tetrahedron* **2001**, *57* (45), 9225-9283.
23. Miklavc, A., Strong acceleration of chemical reactions occurring through the effects of rotational excitation on collision geometry. *ChemPhysChem* **2001**, *2* (8-9), 552-555.
24. Kappe, C. O., How to measure reaction temperature in microwave-heated transformations. *Chem. Soc. Rev.* **2013**.
25. Hurduc, N.; Abdelylah, D.; Buisine, J.-M.; Decock, P.; Surpateanu, G., Microwave effects in the synthesis of polyethers by phase transfer catalysis. *Eur. Polym. J.* **1997**, *33* (2), 187-190.

26. Fang, X.; Hutcheon, R.; Scola, D. A., Microwave syntheses of poly( $\epsilon$ -caprolactam-co- $\epsilon$ -caprolactone). *Journal of Polymer Science Part A: Polymer Chemistry* **2000**, *38* (8), 1379-1390.
27. Nan, A.; Turcu, R.; Craciunescu, I.; Pana, O.; Scharf, H.; Liebscher, J., Microwave-assisted graft polymerization of  $\epsilon$ -caprolactone onto magnetite. *Journal of Polymer Science Part A: Polymer Chemistry* **2009**, *47* (20), 5397-5404.
28. (a) Guo, W.; Hensarling, R. M.; LeBlanc, A. L.; Hoff, E. A.; Baranek, A. D.; Patton, D. L., Rapid synthesis of polymer brush surfaces via microwave-assisted surface-initiated radical polymerization. *Macromol. Rapid Commun.* **2012**, *33* (9), 863-868; (b) Holzwarth, A.; Lou, J.; Hatton, T. A.; Laibinis, P. E., Enhanced Microwave Heating of Nonpolar Solvents by Dispersed Magnetic Nanoparticles. *Ind. Eng. Chem. Res.* **1998**, *37* (7), 2701-2706.
29. Hesek, J. A.; Wilson, R. C., Practical analysis of high-purity chemicals. X. Use of a microwave oven in in-process control. *Anal. Chem.* **1974**, *46* (8), 1160-1160.
30. Chen, W.-Y.; Chen, Y.-C., Acceleration of microwave-assisted enzymatic digestion reactions by magnetite beads. *Anal. Chem.* **2007**, *79* (6), 2394-2401.
31. Rao, M. V.; Shah, J. J.; Geist, J.; Gaitan, M., Microwave Dielectric Heating of Fluids in Microfluidic Devices. In *The Development and Application of Microwave Heating*, 2012.
32. Prucker, O.; Ruhe, J., Polymer Layers through Self-Assembled Monolayers of Initiators. *Langmuir* **1998**, *14* (24), 6893-6898.
33. Bram, G.; Loupy, A.; Majdoub, M.; Gutierrez, E.; Ruiz-Hitzsky, E., Alkylation of potassium acetate in "dry media" thermal activation in commercial microwave ovens. *Tetrahedron* **1990**, *46* (15), 5167-5176.
34. Prucker, O.; Ruhe, J., Mechanism of radical chain polymerizations initiated by azo compounds covalently bound to the surface of spherical particles. *Macromol* **1998**, *31* (3), 602-613.

35. Huang, R. Y. M.; Westlake, J. F.; Sharma, S. C., Molecular weight distribution in radiation-induced polymerization. I.  $\gamma$ -radiation-induced free-radical polymerization of liquid styrene. *J. Polym. Sci., Part A-1: Polym. Chem.* **1969**, 7 (7), 1729-1747.
36. Merabia, S.; Shenogin, S.; Joly, L.; Keblinski, P.; Barrat, J. L., Heat transfer from nanoparticles: A corresponding state analysis. *Proc. Natl. Acad. Sci. U. S. A.* **2009**, 106 (36), 15113-15118.
37. Behof, W. Progress Towards the Synthesis of Novel Graphite Derivatives from a Solution Processable Poly-Cyano Precursor Polymer. Ph.D. Dissertation, North Carolina State University, Raleigh, NC, 2010.
38. (a) Kimura, K.; Nagakura, S., Vacuum ultraviolet spectra of styrene, benzaldehyde, acetophenone, and benzonitrile. *Theor. Chim. Acta* **1965**, 3 (2), 164-173; (b) Ramart, M.; Bertucat, S., Deformation de la structure electronique du carbone par effet steique (serie de la pyridine). *Bull. Soc. Chim. Fr.* **1951**, 18, 212-214.
39. Li, T.; Zhou, C. L.; Jiang, M., UV absorption-spectra of polystyrene. *Polymer Bulletin* **1991**, 25 (2), 211-216.
40. (a) Dielectric Constant, Strength, & Loss Tangent. <http://www.rfcafe.com/references/electrical/dielectric-constants-strengths.htm>; (b) Relative Dielectric Constants. [http://cp.literature.agilent.com/litweb/pdf/genesys200801/reference.htm#elements/substrate\\_tables/tableer.htm](http://cp.literature.agilent.com/litweb/pdf/genesys200801/reference.htm#elements/substrate_tables/tableer.htm).
41. Nulman, J.; Antonio, S.; Blonigan, W., Observation of silicon wafer emissivity in rapid thermal processing chambers for pyrometric temperature monitoring. *Appl. Phys. Lett.* **1990**, 56 (25), 2513-2515.
42. Infrared Thermometer Emissivity tables [http://www.scigiene.com/pdfs/428\\_InfraredThermometerEmissivitytablesrev.pdf](http://www.scigiene.com/pdfs/428_InfraredThermometerEmissivitytablesrev.pdf).
43. (a) <https://en.wikipedia.org/wiki/Silicon>; (b) Silica - Silicon Dioxide (SiO<sub>2</sub>). <http://www.azom.com/article.aspx?ArticleID=1114>.

44. Parameters for Common Solvents Used in Photothermal and Photoacoustic Spectrometry. <http://ion.chem.usu.edu/~sbialkow/Research/Tablevalues.html>.
45. Samy, R.; Glawdel, T.; Ren, C. L., Method for microfluidic whole-chip temperature measurement using thin-film poly(dimethylsiloxane)/Rhodamine B. *Anal. Chem.* **2008**, *80* (2), 369-375.